Trinity College Dublin
Coláiste na Tríonóide, Baile Átha Cliath
The University of Dublin

A 3D printed acoustic metamaterial liner to reduce low-frequency aeroengine noise.

Eoghan P. Ross

Supervisor: Prof. Gareth J. Bennett

Co-Supervisor: Prof. Scott C. Morris

Department of Mechanical, Manufacturing & Biomedical Engineering

School of Engineering

Trinity College Dublin, *the University of Dublin*

D02 PN40

Ireland

March 2023

A dissertation submitted to the University of Dublin in partial fulfilment of the requirements for the degree of Ph.D.

Declaration

I declare that this thesis has not been submitted as an exercise for a degree at this or any other university and it is entirely my own work.

I agree to deposit this thesis in the University's open access institutional repository or allow the library to do so on my behalf, subject to Irish Copyright Legislation and Trinity College Library conditions of use and acknowledgement.

Your name, Month Year

Abstract

As the level of air travel continues to increase, so too does the demand for better noise-reduction technologies for aircraft. The environmental noise produced by aircraft has been shown to have a significant adverse effect on the health and well-being of communities living near airports and along flight paths. Engine noise is one of the two main sources of aircraft noise. The current trend in engine design to increase the nacelle radius and reduce the nacelle length adds constraints to the size and weight of novel acoustic treatments. The use of additive manufacturing allows novel acoustic materials to be developed which would not be feasible using traditional manufacturing techniques. This holds significant promise for the development of novel acoustic liners for aircraft engine nacelles, which are able to meet the growing size and weight concerns.

This works follows the development of an acoustic metamaterial from the initial design optimisation up to an assessment of the liner's performance in NASA's Advanced Noise Control Fan (ANCF) rig, now located at the University of Notre Dame, which has a Technology Readiness Level (TRL) of 3. The design optimisation utilised numerical and analytical techniques to maximise the absorption of the liner under normal incidence. The design was made possible by the use of additive manufacturing which allowed geometries to be explored and implemented that would not have been possible using traditional manufacturing techniques. The optimised geometry of the liner was assessed in grazing incidence in Trinity College Dublin (TCD) and the Laboratoire d'Acoustique de l'Université du Mans (LAUM) at a range of SPL and flow conditions. These preliminary assessments identified the frequencies and flow conditions at which the liner performed well.

The acoustic metamaterial was printed in 237 parts which were installed in the ANCF rig. The liner was tested as a function of RPM and reduced both the broadband noise and tonal noise amplitudes, particularly in the region of 1000 Hz. In this region, the first harmonic of the blade passing frequency was reduced by 18.5 dB when the ANCF was tested at its

nominal operating speed of 1800 RPM. At this speed, an overall PWL reduction of 2.7 dB was achieved across all harmonic bands.

Acknowledgements

I would like to thank my supervisor, Prof. Gareth Bennett, for his good humour, support and guidance during the course of my PhD, for enabling and supporting me and my research, and for giving me so many unique opportunities. I would also like to extend my appreciation to my co-supervisor, Prof. Scott Morris, for his support during our time working together.

Thank you to Dr. John Kennedy, for your constant willingness to help and share knowledge and information. To Dr. Dan Sutliff who's wealth of knowledge made so much of this work possible.

To the technical staff in Trinity College Dublin, in particular Mick, Brendan and Alex for your assistance. To the technical staff at the University of Notre Dame, without whom so much of my testing would not have been possible. In particular, my thanks go to Mark Ross, for the kindness and support during my time in ND. Our conversations in the warehouse and during testing truly made the time fly.

Lara, I don't think I would have made it through these last few years without you. You were always such a source of support and comfort and were always so generous with your time when I needed help. Kelvin, to have been paired on a project with someone who would become such a close friend was an unbelievable stroke of luck. It is such a shame that we are no longer going to be coworkers. The adventures I have had with the two of you by my side have been amazing.

To the friends and amazing people I have met in my time in the fluids office. In particular, Robiul who has been with me every step of the way, Morgan who made sure I was fed when I was too focused to pay attention to the world around me, Karina I don't know what I'd have done without you.

To Shauna, who was always there to have a much-needed coffee break but more significantly helped keep me sane during the months of lockdowns and uncertainty. To my old housemates Katelin and David, who were always so patient in listening to the woes of research

and supported me regardless. To my housemates in SB, Kelvin (again) and Carlos, my time with ye was an amazing experience which I wish could have lasted longer.

To the friends who have encouraged me over the years. To Amy, Meadhbh and Ian who I saw far less than I would have liked but were always so understanding when I did get to see them. To Megan, Rhiannon, Leon, Ronan and Santiago, whose antics when we would meet up kept me sane. To Tallon, who has influenced me in so many ways these last few years without even realising it.

Finally, I would like to thank my parents and siblings. To my mother who was always there with words of encouragement and support when I needed them. To my father whose influence from a very early age led to my love of science which has led me to where I am today. To my sister, Aisling whose help and insights were always appreciated. To my grandparents, who have always encouraged me and believed in me when I might not have. And to my aunt Fionnuala, your constant support meant so much.

Contents

List of Figures

List of Tables

Nomenclature

Acronyms

AM	Additive Manufacturing	
AMM	Acoustic Metamaterial	
$ANCF$	Advanced Noise Control Fan	
BPF	Blade Passing Frequency	
$DDOF$	Double Degree of Freedom	
FEM	Finite Element Modelling	
FML	Foam Metal Liner	
$GFIT$	Grazing Flow Impedance Tube	
$GIIT$	Grazing Incidence Impedance Tube	
ICD	Inlet Control Device	
IGV	Inlet Guide Vane	
IPP	Interior Perforated Panel	
L_{den}	Day-evening-Night Noise Indicator	dB(A)
$MDOF$	Multi Degree of Freedom	
MPP	Micro-perforated Panel	
NRA	Narrow Region Acoustics	
$OASPL$	Overall Sound Pressure Level	dB
OD	Optical Duct	
OTR	Over The Rotor	
$POHC$	Perforated Panel Over Honeycomb Core	
PWL	Sound Power Level	dB
RPM	Revolutions per Minute	
$SDOF$	Single Degree of Freedom	
SPL	Sound Pressure Level	dB

TL	Transmission Loss	dB
TRL	Technology Readiness Level	
TV	Thermoviscous	

Greek Symbols

α	Absorption Coefficient	
ν_0	Kinematic Viscosity of Air	$\mathrm{m^2 s^{-1}}$
ω_0	Angular Frequency	$\mathrm{rads^{-1}}$
$\overline{\alpha}$	Mean Absorption Coefficient	
ϕ	Porosity	
$\Psi\,(\Phi)$	Fok Function	
ρ	Density	$\mathrm{kgm^3}$
ρ_0	Density of Air	$\mathrm{kgm^3}$

Roman Letters

$\#P$	Faceplate Perforation Count	
$\langle p_t \rangle$	Averaged Total Pressure	Pa
$\langle v_z \rangle$	Averaged Velocity in the Vertical Direction	$\mathrm{ms^{-1}}$
A	Area of Opening	m^2
B	Number of Blades	
b_1	Duct Internal Width	mm
b_2	Duct Total Width	mm
c	Speed of Sound	m/s
c_0	Speed of Sound in Air	$\mathrm{ms^{-1}}$
D	Diameter of Cylinder	m
D	Faceplate Perforation Diameter	mm
d	Septum Perforation Diameter	mm
H	Total Liner Height	mm
h	Total Cell Height	mm
$h_{1,Rn}$	Upper Duct Height Row n	mm
$h_{2,Rn}$	Lower Duct Height Row n	mm
J_n	n^{th} Order Bessel Function	
k_0	Wavenumber	$\mathrm{m^{-1}}$
l_m	Momentum Length Scale	m

N	Harmonic Band Number	
r	Reflection Coefficient	
T	Faceplate Thickness	mm
t	Septum Thickness	mm
x_1	Intra-cell Perforation Spacing (Length)	mm
x_2	Inter-cell Perforation Spacing (Length)	mm
y_1	Intra-cell Perforation Spacing (Width)	mm
y_2	Inter-cell Perforation Spacing (Width)	mm
Z	Acoustic Impedance of Air	$\mathrm{Pasm^{-1}}$
z	Specific Acoustic Impedance	$\mathrm{kgm^{-2}s^{-1}}$
Z_0	Characteristic Acoustic Impedance of Air	$\mathrm{Pasm^{-1}}$
z_0	Characteristic Specific Acoustic Impedance of Air	$\mathrm{kgm^{-2}s^{-1}}$

Chapter 1

Introduction

1.1 Concept and Motivation

As air travel continues to become more frequent, the industry-led demand to improve the efficiency of aircraft increases. While the aviation industry was significantly impacted by restrictions implemented during the pandemic, as discussed by Toru Hasegawa [1], it is expected that annual numbers of air passengers will return to 88% of the 2019 levels by the end of 2022, and will exceed the 2019 levels by 2024 [2]. For those living in close proximity to airports and aviation centres, the return to normal air traffic levels and the anticipated increases will see a return of high levels of noise pollution. These levels of noise pollution have been seen to have a significant impact on the environment and populations in the surrounding areas. In recent years aircraft noise has been the subject of numerous studies which have linked noise to numerous health problems including cardiovascular diseases, Non-Hodgkin lymphoma and hypertension, as well as learning and developmental problems in young children [3–6]. The European Union introduced several regulations to reduce the impact of aviation on surrounding communities. Vision 2020, for example, required that by 2020 the perceived noise level from aircraft must be reduced by 50% compared to standard levels in 2000. Flightpath 2050 continues on from the success of Vision 2020 and seeks to reduce the perceived noise emissions from aircraft by 65% compared to 2000 standard levels by 2050 [7].

Approaches to reducing aircraft noise are typically split into two categories: air-frame noise reduction and engine noise reduction. The introduction of the turbofan brought a significant reduction to the noise produced by the conventional jet engines of the time. A turbofan engine achieved this by adding a secondary airflow in the engine around the turbojet. Made possible by the introduction of the external nacelle and fan, the secondary flow adds a slower-moving mass of air through the engine. As a result of the greater mass in the engine, the turbofan is capable of producing the same level of thrust as a turbojet with less energy, which results in less noise being produced and greater fuel efficiency. Additionally, acoustic liners can be installed in the walls of the nacelle, further improving the noise reduction capabilities [8]. However, the turbofan also introduced a new source of noise from the compressor fan. While the overall noise profile is significantly reduced, the fan noise is predominately in the broadband, low-frequency range and produces tonal noise which is more noticeable and irritating than non-tonal noise at the same frequency [9]. At the same time, higher bypass ratios are currently being used when designing engines to improve fuel efficiency and reduce emissions. To compensate for the increase in the diameter of the nacelle, the thickness of

the nacelle and length are being reduced, so the technologies employed must be small and lightweight. The increase in the fan diameter additionally results in the fan being operated at lower RPMs, which shifts the noise profile of the engine towards lower frequencies which are harder to reduce using conventional acoustic liners.

The current industry standard for nacelle liners is a perforated panel over honeycomb liner [10, 11]. The design is lightweight and strong due to the structural strength of the honeycomb core. This single-degree-of-freedom (SDOF) design acts as a quarter-wavelength resonator, a Helmholtz resonator, or a combination of both, and is limited in its ability to target the broad range of noise generated by the engine. The characteristic absorption curve of the liner is dependent on the depth of the resonator [12]. To achieve low-frequency attenuation, the depth of the liner must be increased. However, as the depth of the liner is increased the frequency response of the liner narrows. This is illustrated in Fig. 1.1 which shows the absorption curve for four different cavity depths of an SDOF liner. The cavity with a depth of 50 cm has its first absorption peak at 170 Hz, while the 5 cm cavity has its first absorption peak at 1440 Hz. Combined with the growing constraints on the size of the liners, an alternative approach to engine liner development must be explored.

Acoustic metamaterials (AMMs) hold significant promise as the next generation of engine nacelle liners. Artificially designed and engineered, AMMs typically exhibit effective properties different to those expected from their physical properties. A variety of different approaches are used when designing AMMs including space coiling, lattice structures such as Kelvin cells, decorated membranes, acoustic plates and hybrid technologies. These different approaches each have a focus that allows a specific property to be obtained by manipulating the effective properties of the material. Many of these approaches have been investigated in the case of normal incidence, in which the incident acoustic wave is normal to the active surface of the metamaterial [13–17]. However, for use as a nacelle liner, the performance of the material in grazing incidence is of greater interest as the liner must not interfere with the airflow through the engine. The application of multi-degree of freedom liners and similar technologies in grazing incidence has been investigated in NASA Langley using the Grazing Flow Impedance Tube, as well as a number of other laboratories including KTH, DLR and JAXA [18–21]. However, to the author's best knowledge, testing of such technologies in an engine nacelle has yet to be published.

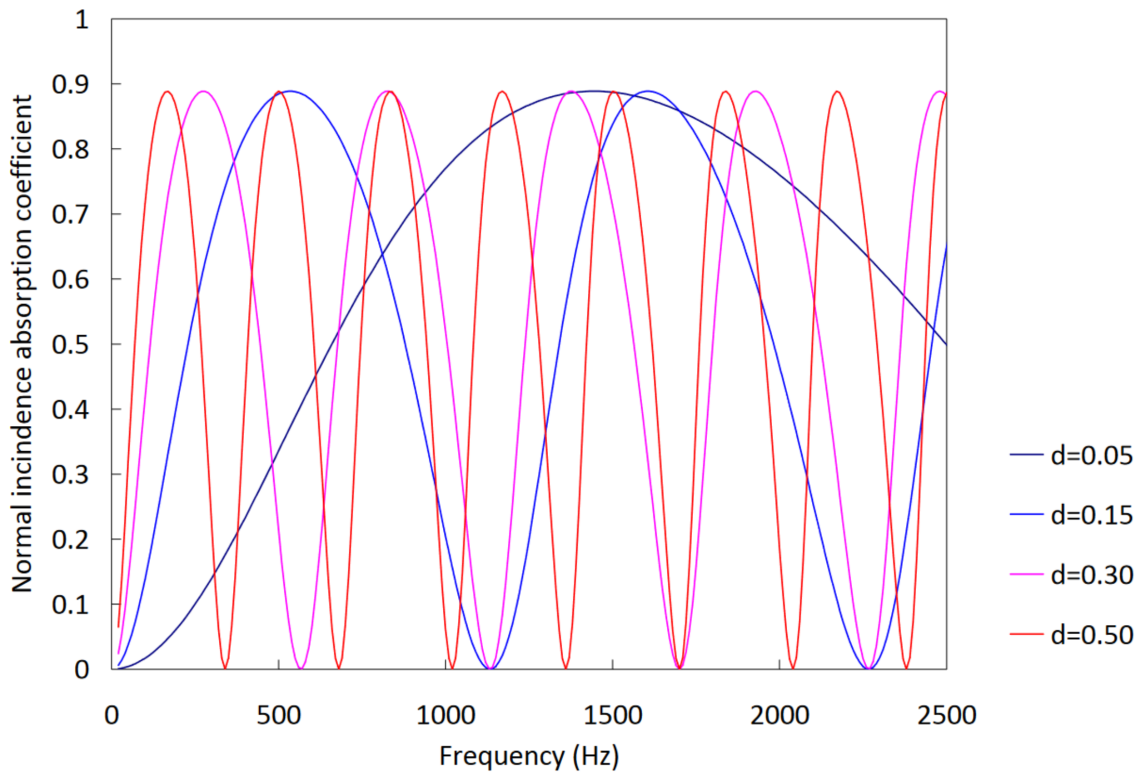

Figure 1.1: Absorption coefficient as a function of frequency for four single-degree-of-freedom liners for a range of cavity depths. The depth, d, of the cavity is in meters (m) [12]

Though the current perforated panel over honeycomb liners are limited in their ability to target the noise generated by the fan, a multi-degree of freedom liner based on design has potential as a next-generation liner. Tang et al. [22–25] proposed a modified perforated panel over a honeycomb core liner design. Their design features a secondary perforated panel embedded in the honeycomb core. This is achieved by adding a diagonal septum which divides individual cells at different heights. This division creates a number of acoustic resonators which are able to target a number of different frequencies, and additional losses are achieved by the micro-perforations in the second perforated panel. A similar premise was explored by Palani et al. [26] who investigated the performance of a single duct with a microperforated faceplate and slanted, perforated septum, and multiple, folded cavity liners.

1.2 Scope and Research Objectives

The aim of this project is to design a novel acoustic liner capable of low-frequency attenuation of aircraft fan noise. The material, designed for use in the inlet of an engine nacelle, must

therefore be lightweight and have a small size to comply with the growing limitations of the space available in the nacelle casing. This is achieved by following these objectives:

1. To determine a viable acoustic metamaterial liner design that is able to meet the noise profile targets while maintaining a small footprint.
2. To optimise the design for low-frequency noise reduction that is also capable of reducing the blade passing frequency and harmonics of the turbofan engine.
3. To characterise the performance of the optimised design in grazing incidence.
4. To produce a liner designed for the curved test section of the ANCF using additive manufacturing
5. To evaluate the performance of the additive manufacturing.
6. To assess the performance of the acoustic metamaterial liner in the ANCF.

The liner being developed in this project is based on the designs by Tang et al. [22]. This liner concept builds on the performance of the perforated panel over honeycomb liner which is currently the most common nacelle acoustic liner. By splitting the cell of the backing structure of the liner, the liner is converted from a single-degree of freedom liner to a multi-degree of freedom liner. Additionally, the septum used to divide the cells in the liners contains a second row of micro-perforated holes which broadens the range of frequencies that are targeted by the liner.

The concept of Tang is shown in Fig. 1.2. As can be seen in Fig. 1.2(a) the honeycomb core structure has a square cross-section and is divided by the diagonal septum. The diagonal septum also contains sub-millimetre perforations that are in line with the perforations on the top micro-perforated panel. Figure 1.2(b) shows a single unit cell consisting of 6 ducts, and the septum traces a path across the six cells, dividing the second, third, fifth and sixth cells. As indicated in the elevation view, the thickness and hole diameter of the faceplate and septum are not the same. During the design of the material Tang et al. [25] proposed to produce the material using traditional manufacturing methods. In order to produce the liner, the square honeycomb section was cut into trapezoidal sections to follow the path of the septum. A metal sheet was folded to produce the corrugations and the holes were created in the corrugated sheet using a high-power laser. Finally, the trapezoidal sections, corrugated sheet and faceplate were combined using brazing.

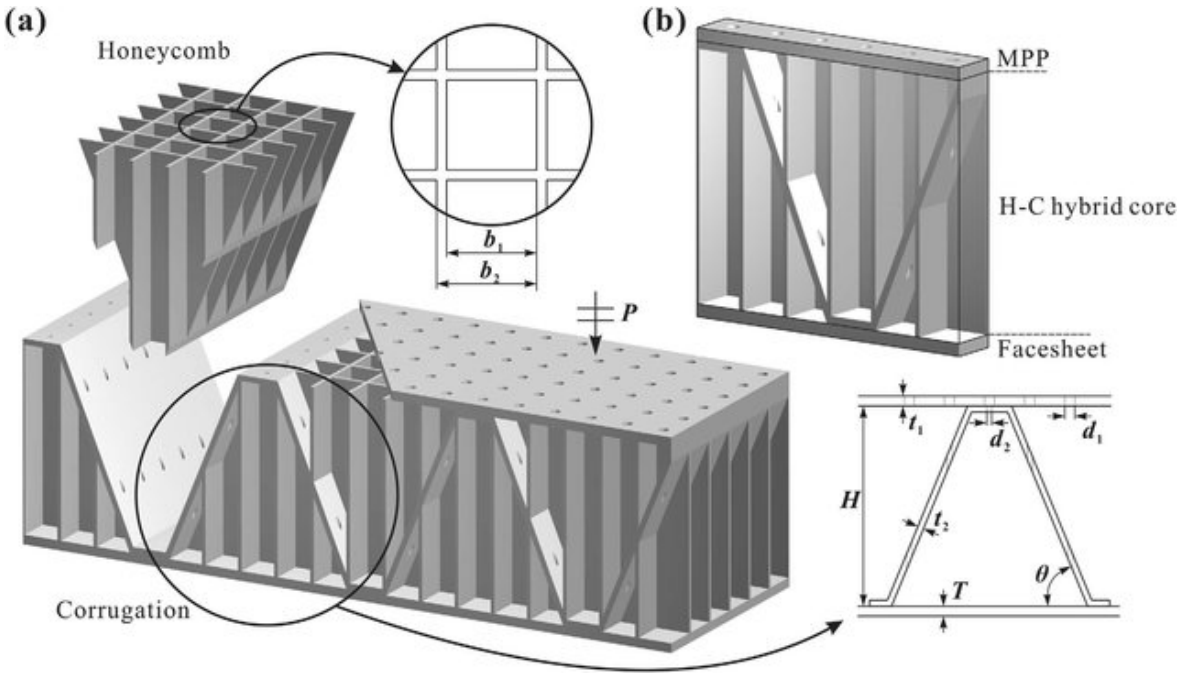

Figure 1.2: Schematic of the acoustic liner concept proposed by Tang et al. [22]. (a) The full technology is a micro-perforated panel over a "honeycomb core" structure. (b) An individual unit cell of the technology is shown in both isometric and elevation views.

Due to the decision to use these traditional methods, a number of limitations were introduced. One of the most significant limitations was the forced path of the septum. By choosing to cut the core structure and insert the septum as a folded sheet, the septum could only be made diagonally. This in turn meant that the perforations in the septum had a reduced effective length and the depth of the cavities was fractionally reduced. This resulted in the total footprint of the technology being underutilised.

This study proposes to further the work performed, designing a material that is optimised for use in grazing incidence which has not been explored previously and produced using additive manufacturing. By choosing to use additive manufacturing, there are fewer limitations applied. Without the need to fold and recombine the honeycomb structure and septum together, it is possible to investigate the performance of a backing structure which has horizontal septums instead of diagonal septums. This opens the possibility of further combinations of cavity depth and septum heights. In this work, prior to the design optimisation, the design concept is referred to as the liner or MDOF liner. However, after the design is optimised it is referred to as the T-Liner. The "T" is to represent Trinity College Dublin, where the design optimisation process was performed.

Additionally, this study will evaluate the performance of the manufacturing process that is used to produce the liner. The methods of additive manufacturing used in the study are methods primarily during design conceptualisation and prototyping. If acoustic liners were to be manufactured using additive manufacturing, alternative means of additive manufacturing would be used which are capable of producing materials in more durable and temperature-resistant materials such as titanium or cobalt chrome. However, the quality of the samples and the impact of the manufacturing process's reliability on the final liner's performance will be evaluated.

Chapter 2

Literature Review

2.1 Background

In Section 1.1, the health problems associated with aircraft environmental noise were discussed. These problems provide a very strong motivation to reduce the level of aircraft noise generated. For decades the level of civilian air travel has been increasing. Modern aircraft, and in particular aircraft engines [27, 28], are significantly quieter than they were 30 years ago. BDL [27], the German Aviation Association, reported that since the 1960s, the noise of an aircraft has been reduced by up to 88%, a reduction of 30 dB. In Fig. 2.1 it can be seen that the newest generation of the Airbus A319neo is nearly 30 dB quieter than the Boeing 707 released almost 60 years prior, amounting to an 88% decrease to the effective perceived noise.

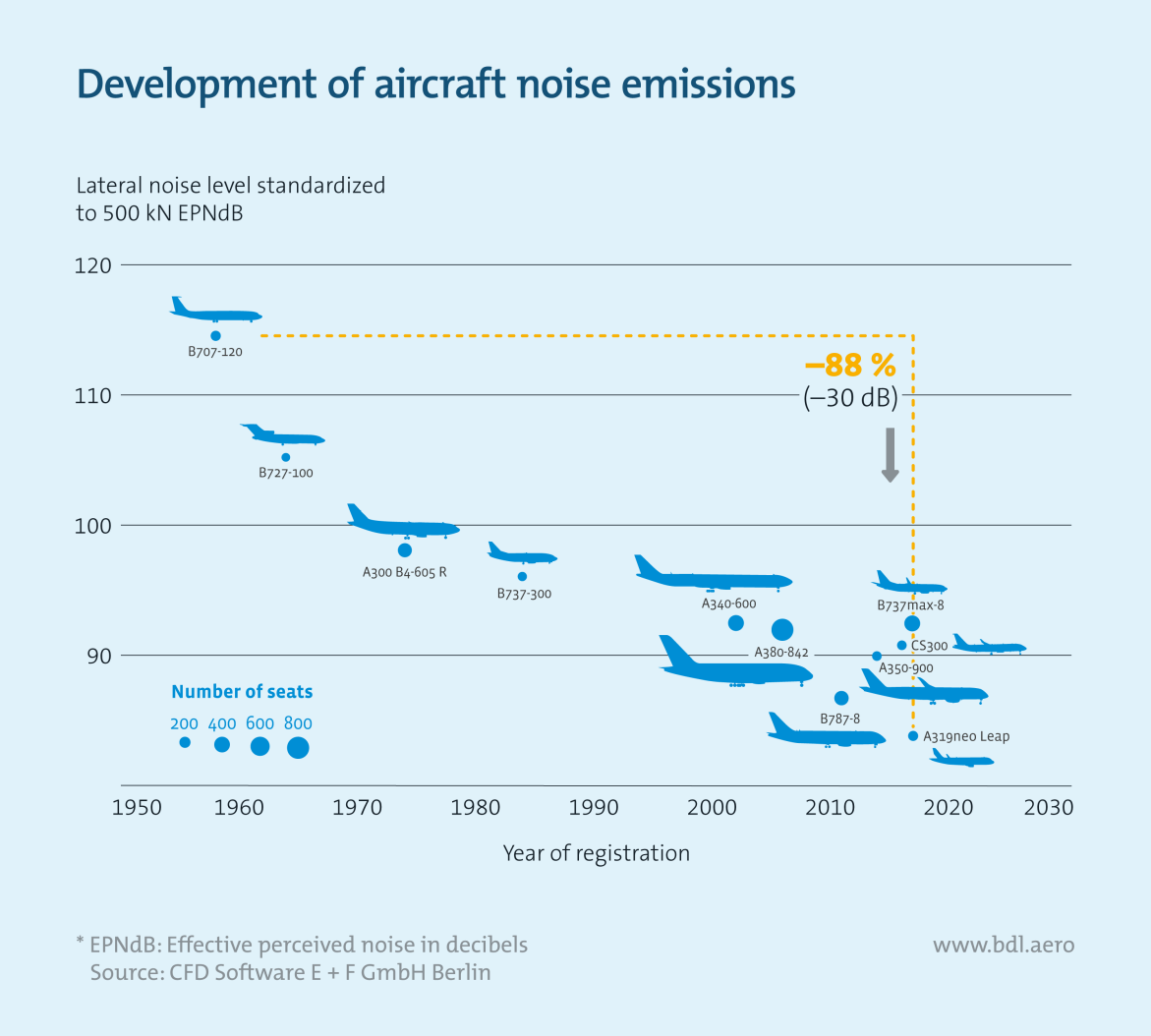

Figure 2.1: Reducing in aircraft noise emissions from a selection of aircraft produced between 1960 and 2020 [27].

In June 2016, EU aviation rules came into effect which apply to over 50,000 civil aircraft movements annually [29]. These rules are in line with the approach created by the International Civil Aviation Organisation. The rules are focused on cost-effective ways of reducing aircraft noise at individual airports. The four points of focus of the rules are; reducing noise through the use of modern aircraft, proper maintenance of the land around the airport, adapting operation procedures to reduce the noise impact and introducing operational restrictions [30].

While the impact and significance of the COVID-19 pandemic on the aviation industry may not be understood for several years, it did provide an opportunity to better understand the impact of aircraft noise on those regularly exposed to it. A study was carried out in 2015 which looked at the impact of long-term exposure to aircraft noise on blood pressure [31]. The study looked at those who live near Cracow Airport and were exposed to high (>60 dB) aircraft noise, and an unexposed group (<55 dB). It was determined that long-term aircraft noise resulted in significant impacts on cardiac health. A follow-up study was conducted in June 2020, 4 months after the COVID-19 pandemic restrictions were introduced which surveyed 75% of the original participants from both the high exposure and unexposed groups [32]. The second study found significant reductions in the previously observed cardiac health impact of the exposed groups when compared to the unexposed group.

Given the significant impact of aircraft noise on the health of those exposed, it is in the interest of the public from both a health and economic viewpoint to address the issue. Fingal County Council [33] reported that between 2011 and 2016 the number of people exposed to noise levels greater than 55 dB(A) L_{den} grew by 7,900. Of this, 6,600 more people were exposed to noise levels between 55 to 59.9 dB(A) L_{den}, 1,200 more people were exposed to noise levels between 60 to 64.9 dB(A) L_{den} and 100 more people were exposed to noise levels between 65 to 69.9 dB(A) L_{den}. The areas covered by each of these brackets can be seen in Fig. 2.2.

A report by the European Aviation Safety Agency [34] predicted in 2016 that air traffic could see an increase of 45% compared to the 2014 level. While this report predates the impact that the COVID-19 restrictions had on the aviation industry, the return to air travel has been rapid [1, 2] as was discussed in Section 1.1. Based on the predicted increase in air traffic, the population in Europe who would be exposed to the >55 dB L_{den} contour region could reach between 2.58 and 4.29 million by 2035. In order to prevent this, aircraft noise

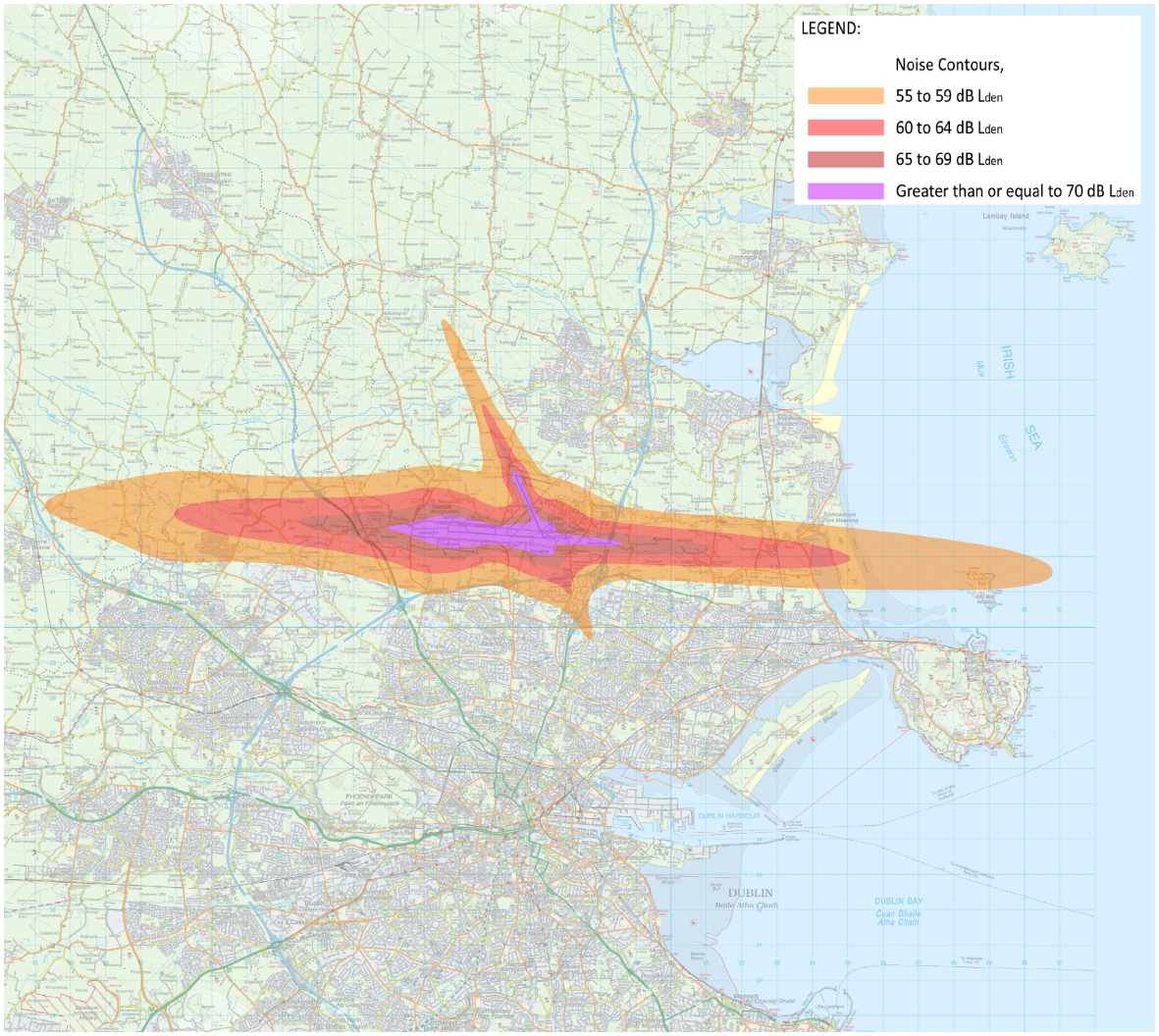

Figure 2.2: Noise Exposure Map of Dublin airport showing the L_{den} contour regions surrounding the airport along the runway flight paths. Adapted from [33].

must be reduced by 0.1 - 0.3 dB per annum on new aircraft in order to see a net decrease compared to the 2014 level for the 2035 timeframe. Significant breakthroughs are therefore necessary to address the sources of aircraft noise.

2.2 Aircraft Noise Sources

In order to reduce the perceived noise generated by the aircraft, the main areas of noise generation had to be identified and targeted. There are three primary categories for the classification of aircraft noise generation: airframe noise, engine noise and airframe-engine noise interactions [35]. The airframe noise is comprised of a number of sources including landing gears and landing gear cavities, high lift devices, and trailing edge shedding. Similarly,

engine noise is generated in a number of ways, with each type of noise having different noise profiles. The areas on the aircraft which generate these forms of noise can be seen in Fig. 2.3.

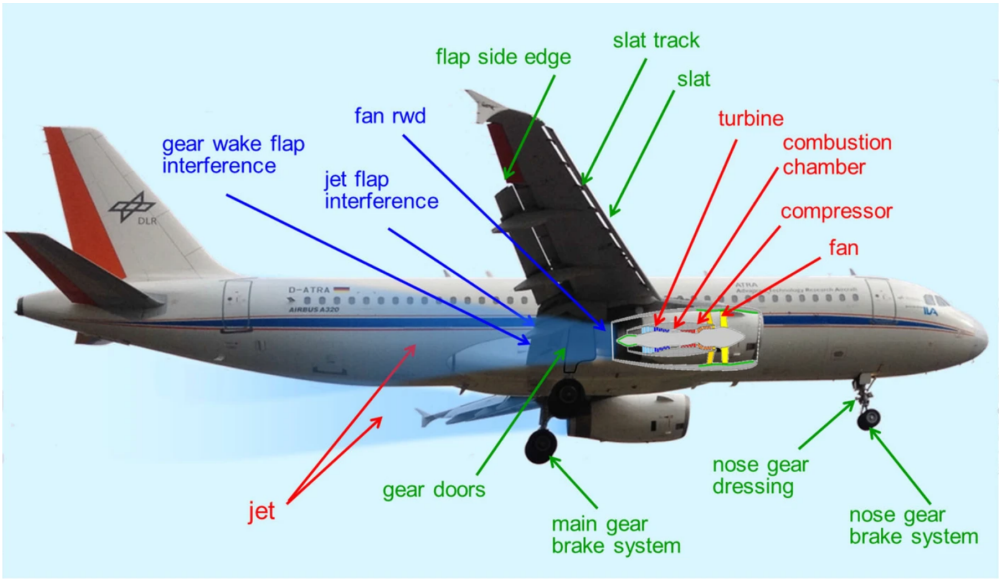

Figure 2.3: Sources of aircraft noise; sources listed in green are airframe noise sources, sources in red are engine noise sources and blue are noise sources caused by interactions between the airframe and engine noise sources, ©Henri Siller and Jan Delfs, DLR, 2019 [35].

The combination of the engine and airframe noise contributes to the total noise generated by the aircraft. The noise produced by aircraft is a problem at all stages of flight for both passengers inside the plane, and people outside the plane along the flight path. While flight at high altitudes generally limits the effect of aircraft noise on civilian populations, the noise produced by the sonic boom was a significant restraint on the use of supersonic aircraft. However, this is a lesser concern than the noise produced during take-off and landing.

During take-off, the primary source of noise emitted from the plane is engine noise [36]. This is due to the high levels of thrust required to produce the necessary lift to make the aircraft airborne. Once the plane is in the air, the power is reduced to 25% of the maximum. During approach and landing, the engine operates at low thrust and as a result, the airframe contributions during landing are much more significant [37]. This can be seen in Fig. 2.4.

The airframe noise is sound that is generated as a result of interactions between the airflow over the aircraft and features on the body of the aircraft that disturb the flow [38–44]. These features can be intrusions or recesses from the mean surface and the fuselage. Depending on the feature, the noise can be radiated directly, as is seen in the case of struts, wheels, braces and flaps, or it can be generated as a result of shear layer interactions, as is seen in

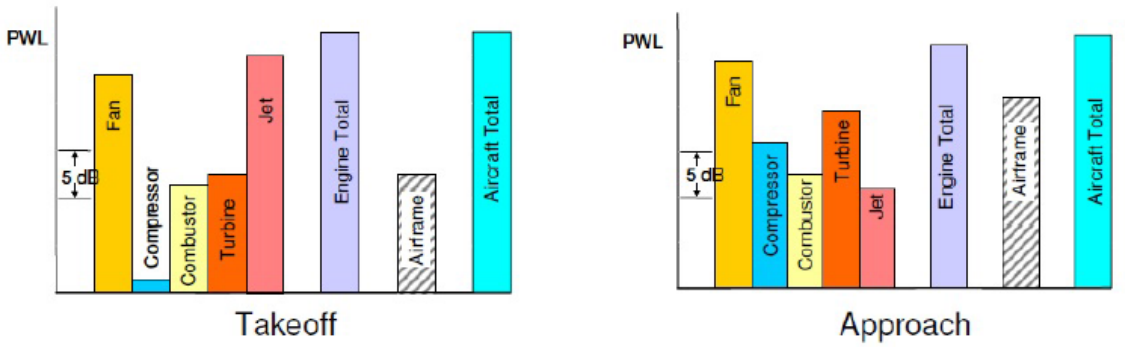

Figure 2.4: Comparison of the PWL of engine and airframe noise contributions at takeoff and approach [36].

the case of the landing-gear cavity. As is often the case in aviation, the addition of noise control measures for airframe noise is constrained by concerns relating to the effect on the performance of the aircraft, safety and cost.

The airframe noise generated by the landing gear mechanism is one of the most prominent airframe noise sources during take-off and landing [45]. There are a number of ways in which the landing gear mechanism generates noise, mostly related to the geometry of the landing gear. Of the noise sources, one of significant concern is the cavity noise generated by the landing gear bay which is exposed when the landing gear is deployed. Not only does the cavity noise increase the total noise emission of the aircraft, but the pressure fluctuations within the cavity can also cause damage to instruments and equipment located in the landing gear bay [46–48]. The noise generated in the cavity is due to the shear layer interactions which occur over the mouth of the cavity. A number of active and passive methods are considered to reduce cavity noise. Passive approaches such as trailing edge have been added to the edge of the cavity which has seen noise reductions of 7 EPNdB [49], while active methods such as the use of a fluidic spoiler at the edge of the cavity have been used to prevent shear layer formations [50].

2.2.1 Aeroengine Noise

In the 1950s, the first passenger planes that were powered by turbojet engines instead of piston engines began to enter service. The popularity of turbojets increased quickly for many reasons from improved range and reliability to reduced interior noise. Following a test flight of a turbojet plane, Wing Commander Maurice A. Smith said:

"Piloting a jet aircraft has confirmed one opinion I had formed after flying as a passenger in the Lancastrian jet test beds, that few, if any, having flown in a jet-propelled transport, will wish to revert to the noise, vibration and attendant fatigue of an airscrew-propelled piston-engine aircraft" [51].

However, despite the perceived improvements inside the aircraft, noise levels measured externally would often be over 120 dB. These turbojets only had one flow of air through the engine, which would leave the engine at very high speeds. When the high-speed jet left the engine and interacted with the relatively low speed of the air outside of the engine, the interaction of the two streams generated very high noise levels [28]. Additionally, in these early designs, there was a limited number of areas in the engine where noise-attenuating materials could be employed. Many of the methods involved modifying the end of the jet to reduce the noise produced by jet mixing without compromising the thrust of the engine [52]

In the late 1960s, the turbofan engine was introduced which reduced the noise emitted by the engine. The turbofan engine has a very similar core to a turbojet engine, with an additional fan at the front of the engine and a secondary airflow around the turbine engine. The design of both engines can be seen in Fig. 2.5. The secondary flow around the engine is referred to as the bypass, and depending on the ratio of the amount of air that bypasses the engine, turbofans are categorised as low-bypass or high-bypass engines [28].

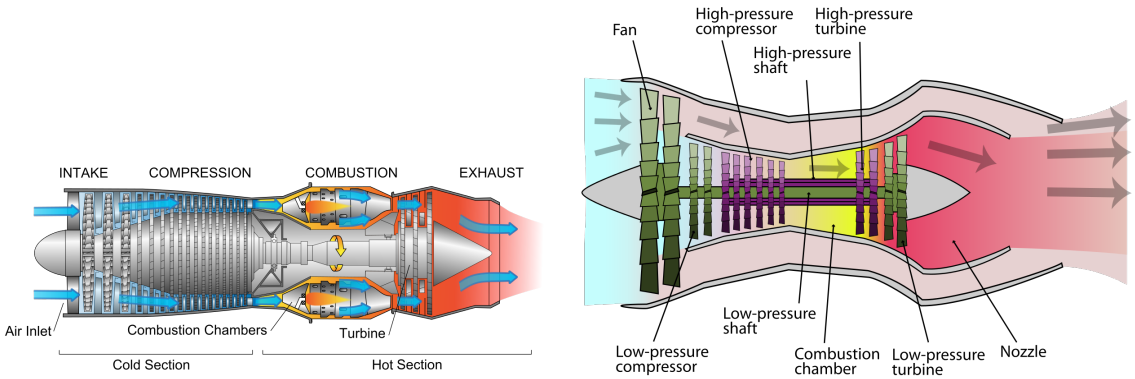

(a) Turbojet Engine (b) Low Bypass Ratio Turbofan Engine

Figure 2.5: Design comparison of the (a) turbojet engine [53] and (b) turbofan engine which has a low bypass ratio [54].

The reduction in noise emissions was initially small [55]. However, as the design of the turbofan engines changed over the decades so did the ability of the engines to reduce the level of noise emitted. Figure 2.6 shows a general reduction of approximately 20 dB between

the late 1950s and 2000. The first generation of turbofan engines typically had a low-bypass ratio of 1-2:1 in the 1960s but when the second generation engines started to be introduced higher bypass ratios of 4-6:1 were starting to be used [28]. Higher bypass ratios have been seen entering use in more recent years with some modern aircraft having bypass ratios as high as 12:1 [56]. However, the reduced noise from the engines was not the primary motivation for these changes. The main motivation for the transition to higher bypass ratios was their lower fuel consumption and high propulsion efficiencies.

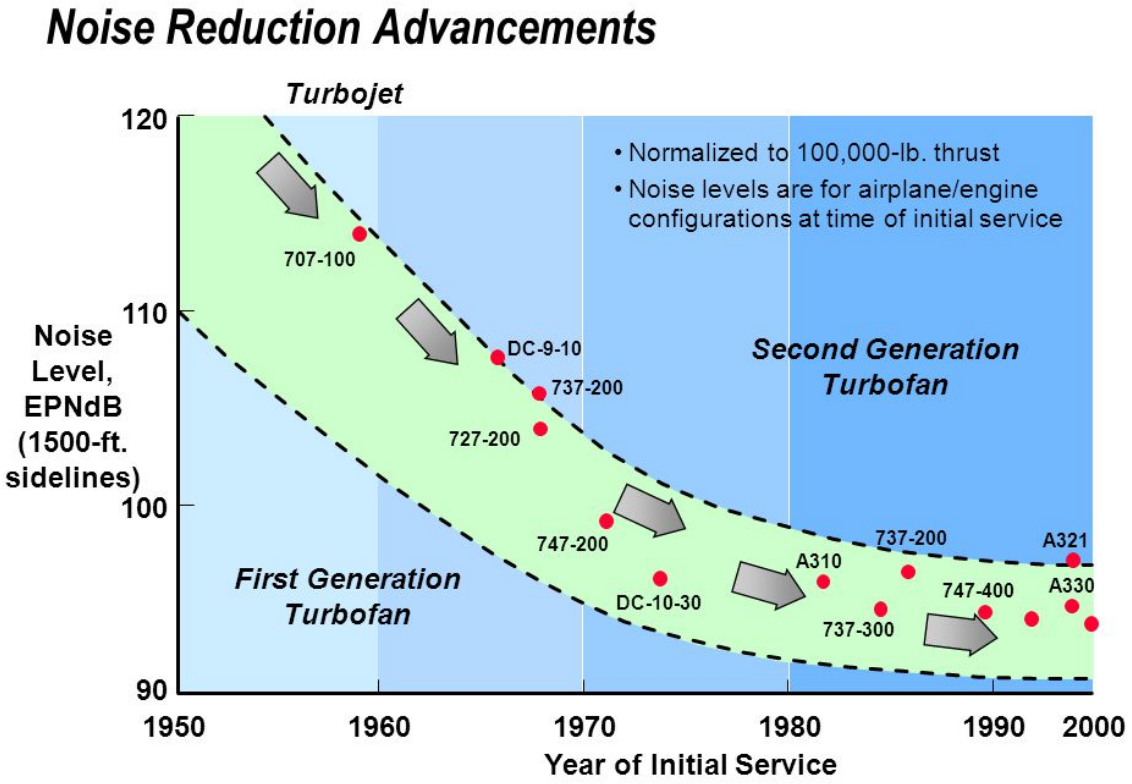

Figure 2.6: Reduction of the noise by different generations of aircraft engines [57].

The decrease in noise produced by these turbofan engines was largely due to the speed of the secondary flow through the engines reducing the impact of jet mixing. The bypass flow through the engines moved at an intermediate velocity compared to the velocity of the jet and the free stream velocity outside the engine [58]. However, the fan also brought with it a new source of the noise. As can be seen in Fig. 2.7 while the introduction of the turbofan significantly reduced the noise emission from the engine, it introduced a new source of noise, fan noise. There are two different types of fan noise; fan broadband noise and fan

tonal noise [59]. Figure 2.8 shows these contributions in greater detail for a typical turbofan engine on approach. The fan broadband noise has a relatively low contribution to the overall sound pressure level (OASPL) at lower frequencies but steadily increases with the frequency, dominating over 1000 Hz. It additionally introduces tonal noise. Tonal noise contributions of the engine are present across the frequency range, above 1250 Hz. While broadband noise has a more constant contribution to the overall sound pressure level than tonal noise, the first few tones have a significantly higher SPL than broadband noise at the same frequency. The tonal noise is additionally more irritating to those exposed than the broadband noise of the same frequency.

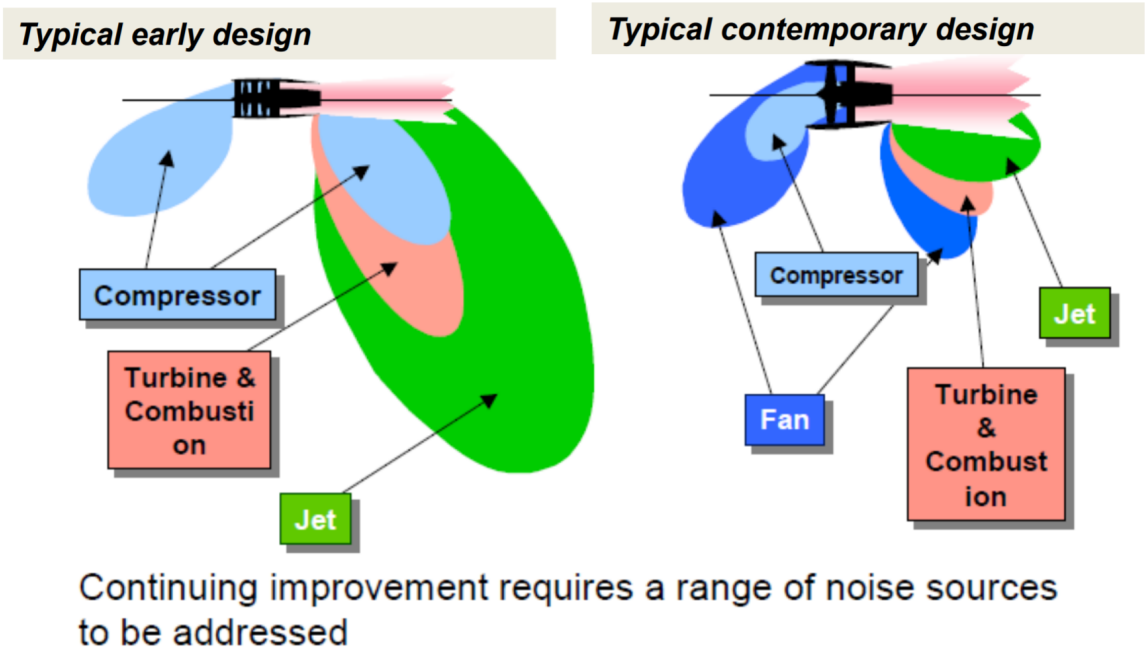

Figure 2.7: Comparison of noise sources between a turbojet engine and a turbofan engine [60]. The noise sources present in the turbojet engine were significantly reduced by the turbofan engine design but added fan noise.

Fan noise, in particular tonal fan noise, is a function of the fan pressure ratio and the rotational tip speed of the fan blades [58]. The engine shaft rotational frequency, related to the fan rotational tip speed, produces harmonics known as engine orders which make up the tonal noise. The tonal noise has a number of contributing sources including spectral peaks at integer multiples of the shaft speed, integer multiples of the blade passing frequency (BPF) and buzzsaw noise, which occurs when the fan blade tip speed goes supersonic. It is particularly prominent during takeoff when the fan speed is higher [61].

In addition to the noise generated by the fan, the nacelle in the turbofan design resulted in the introduction of duct modes. As discussed in Sutliff [62], the generation of these duct modes is governed by the cylindrical wave equation. Both axial and radial modes may be produced in the duct which will propagate when the frequency of the fan noise is greater than the cut-off frequency. For a high-speed fan found in a turbofan engine, this can result in several hundred propagating modes. When these duct propagation modes are coupled to the rotor-stator, and similar interactions, they produce the tonal component of the far-field fan noise.

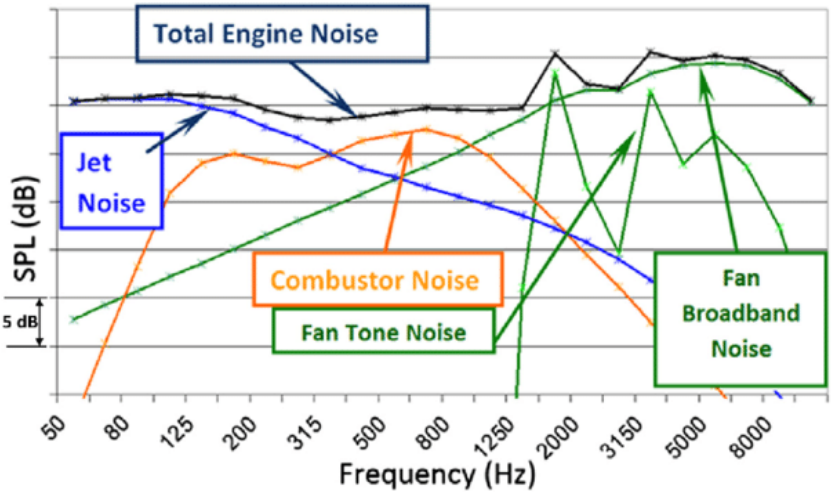

Figure 2.8: Contributions of different noise sources within the turbofan engine to the overall noise generated by the engine. Source: SAFRAN Snecma [9].

As the design of the turbofan moves to higher bypass ratios, the internal diameter of the engine increases and with it the size of the engine nacelle. The size and weight of new components in aviation are always design constraints. In an effort to reduce the size and weight of new engines, the size of the nacelle is beginning to be restricted. This means that additional technologies that can be added to the engine must have a small thickness and be lightweight. This presents significant difficulties as the technologies must target large acoustic wavelengths [61, 63].

2.2.2 Aeroengine Noise Abatement

To reduce the noise that is emitted from turbojet engines passive and active methods of noise reduction are used. Active methods use the addition of external energy into the system to reduce the noise. Passive methods aim to reduce noise that is generated without the addition of more energy [64]. Passive methods are difficult to design and implement in aircraft

engines as a result of the limited space available to target large wavelengths. Designers have implemented noise targeting technologies in other areas of the aircraft such as the linings of the fuselage which reduces the cabin noise for passengers. However, improvements must be made in order to reduce environmental noise. The three main methods of passive noise control identified by Gorj Bandpy and Azimi [61] are swept and leaned stators, bifurcated inlets and acoustic liners.

Rotor-stator interactions are a significant source of noise generation in the engine. The rotor and rotor-stator interactions in the engine result in the formation of wakes in the airflow. The periodic fluctuations in smooth wakes result in the generation of tones at multiples of the rotor BPF, while the random fluctuations arising from the turbulent wake of the rotor-stator interaction generate broadband noise [65]. The conventional means of reducing rotor-stator interaction noise are to modify the ratio of rotors to stators or increase the axial spacing between them [66, 67]. However, these methods were seen to reduce the aerodynamic performance of the engine, while also increasing the weight. Woodward et al. [68] reported that using a swept and leaned stator instead of the standard radial stators, could reduce the rotor-stator interactions, leading to a noise reduction of 3 EPNdB.

A bifurcated inlet is a proposed change to the geometry of the nacelle inlet similar to the inlet design of supersonic aircraft engines. The bifurcated 2D inlet design has a rectangular cross-section at the mouth which gradually changes to a circular cross-section at the fan plane. Early tests of the variable geometry using the bifurcated design reported significant boundary layer separation at the cowl lip which could be reduced by using a bell-mouth inlet [69, 70]. Although inlet guide vanes (IGVs) are generally found to introduce additional noise, by using IVGs in the bifurcated inlet design the choking effect in the inlet could be controlled. It was observed that this resulted in a reduction of the engine noise [71]. Li et al. [72] discovered in ground static tests that the distance between the bifurcated inlet trailing edge and the fan plane had a minimal impact on the noise attenuation of the inlet. This would mean that the aerodynamics and performance of the engine could be the primary focus of the inlet design without affecting its noise attenuation capabilities. They also reported that the inlet noise reduction is related to the spacing between the IGV and the fan.

Acoustic liners are the most common form of passive noise reduction. Acoustic liners reduce the noise radiated from the engine by absorbing the acoustic energy. They are most commonly found in the wall of the nacelles of the engines, although there are a number of

other areas inside an engine where they can be placed, shown in Fig. 2.9. Most acoustic liners that are installed in engines are manufactured in sections and are joined together once installed in the nacelle. The joins are longitudinal strips known as splices.

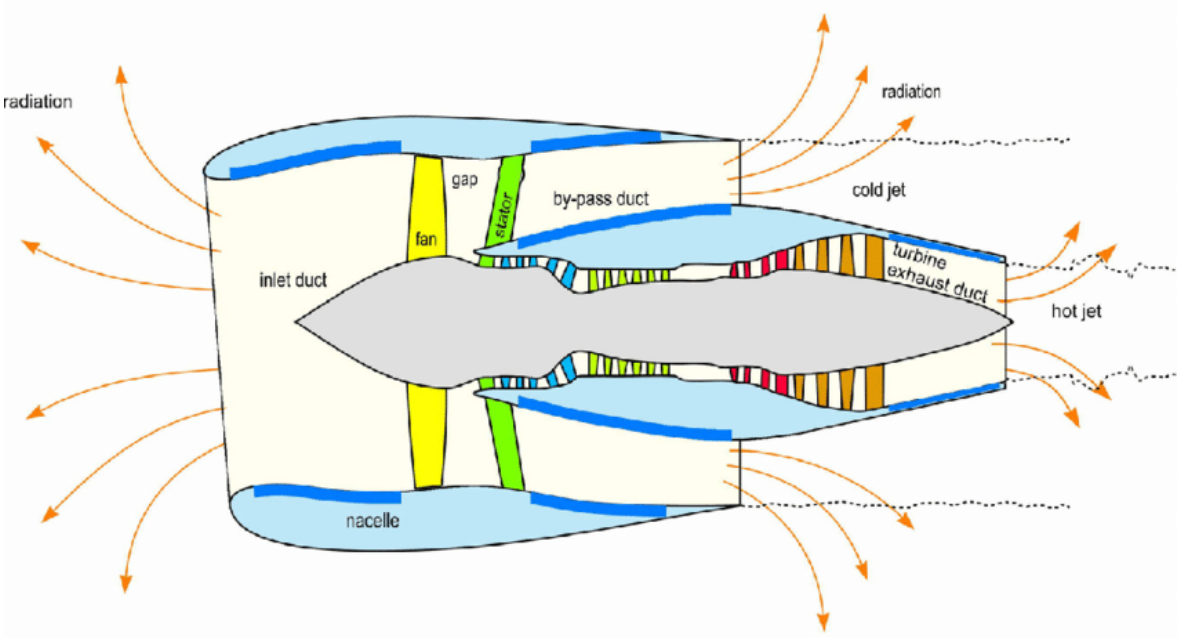

Figure 2.9: Locations used for an acoustic liner in turbofan engines are shown in dark blue [73].

These splices are hardwall surfaces which produce discontinuities in the overall acoustic impedance of the nacelle wall. A study conducted by Airbus in 1997 determined that the splices generated additional noise in the engine. The fan noise modes are scattered by the splices which in turn produces more modes [37]. The modes that are generated as a result of the rotor-splice interactions can be predicted by the Tyler-Sofin relationship[66] for rotor-stator interactions. By reducing the number and thickness of the splices, the number of modes excited is reduced. Fig. 2.10 shows the difference in thickness of splices between two generations of spliced liners. Hervé and Airbus [74] conducted numerical studies which showed that the use of a zero-splice liner, also known as a spliceless liner, could achieve reductions of more than 3 EPNdB compared to a 2 thin-splice lining. In the course of this study, Batard also found that it is possible for a spliced acoustic liner to have an adverse effect on the noise level of the engine if the noise scattering from the splices is not controlled. Further, Gantie et al. [75] showed that for a spliceless liner to be effective, it must be truly spliceless as a splice of only 15-20 mm was sufficiently large to scatter the first BPF and negate the benefit of the spliceless liner. Despite the difficulties of producing an acoustic liner that can

be readily installed in an engine nacelle without any splice, teams in Rolls-Royce [76] and Bombardier [77] have achieved it as part of their next generation engines and aircraft.

Figure 2.10: Representation of the size of the acoustic liner splice between two generations of engine liners [78].

The standard acoustic liner that is used in nacelles is an SDOF liner. It consists of a perforated panel over a honeycomb core (POHC) which has a hardwall backing [10, 11]. The honeycomb core behaves as a quarter wave resonator and the perforated panel attenuates noise due to viscous losses in the holes. The perforated plate serves a second purpose; as it is a relatively smooth surface it allows the flow over the wall of the nacelle to remain as smooth as possible. These traditional liners can have unfortunately narrow absorption spectra as described in Section 1.1. In some cases instead of having a single degree of freedom, a double-degrees-of-freedom (DDOF) liner is used instead. In DDOF liners, there is a second layer of honeycomb and a second perforated panel. The parameters of the two layers are different to increase the number of frequencies that the liner is able to target different wavelengths [79]. The difference in composition of the designs can be seen in Fig. 2.11 which features a schematic of both an SDOF and DDOF liner. More recently there are other proposed configurations based on the standard POHC design including the use of micro-perforated panels, fine wire mesh or Kevlar treatments over the surface of the honeycomb and variable depth honeycomb cores [79].

A study by Sutliff et al. [80] which took place over a 10-year period followed the progression of an acoustic liner from initial conception to a test flight. The study provided insight into how the performance of an aeroengine acoustic liner can change over the course of a design

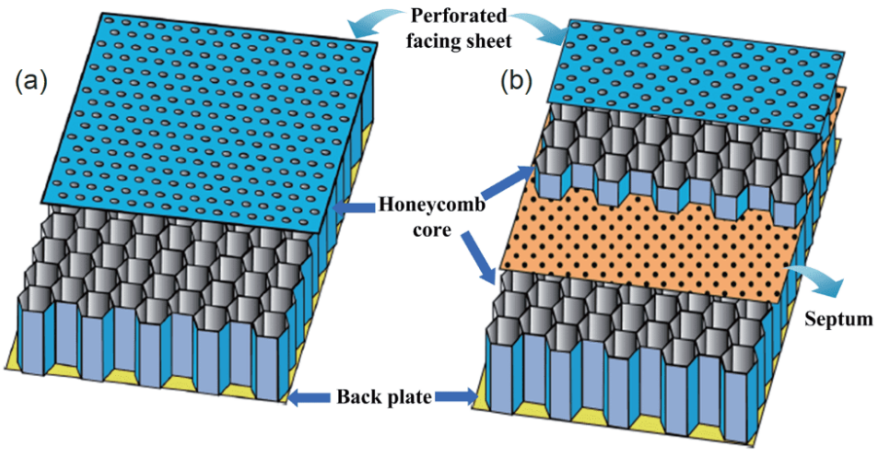

Figure 2.11: Schematics of the composition of a (a) SDOF and (b) DDOF liner [79]

campaign as the level of sophistication of the testing advances. The initial test inception and characterisations were performed on the NIT and GFIT impedance tubes at NASA Langley which has a NASA Technology Readiness Level (TRL) of 2. Adaption of the material for testing on the ANCF low-speed duct fan and FMD high-speed duct fan followed which have a TRL 3 and TRL 4 respectively. The first turbofan test was conducted on DART which has a TRL of 5. Finally, the material achieved a TRL 7 on a test flight when the liner was installed in a LEAP 1B turbofan engine on a Boeing 737 MAX-7. A full description of the NASA TRL can be found in Appendix D with a comparison to the ESA TRL.

The design of the liner employed in the different phases of the study depended on the test environment being employed [80]. The premise of the liners utilised was the SDOF liner which was adapted into DDOF and MDOF liners. The DDOF and multi-degree-of-freedom (MDOF) liners featured fine mesh caps which were installed in individual honeycomb cells creating two and three-layer systems. Additional MDOF configurations were also used in which the depth of the mesh cap was varied from cell to cell creating a large number of cell depths.

As a result of the study, Sutliff et al. [80] noted that as the TRL of the test increased, the performance of the liner decreased. This is attributed to the growing complexity and presence of other sources in successive stages. In the low-TRL tests, the liners achieved SPL reductions on the order of 50 dB. In mid-TRL tests, reductions of 15-5 dB PWL were reported. In the high-TRL test flight at the end of the campaign, reductions on the order of 2 EPNdB component, ∼0.5 EPNdB total, were reported. It was further noted that coupling

the predictions and test evaluations throughout the process increased confidence in the design procedure and helped reduce the chance of a one-off liner design.

2.2.3 Advanced Noise Control Fan

The Advanced Noise Control Fan (ANCF), formerly called the Active Noise Control Fan, is an experimental testbed that was designed by NASA. It was designed in the early 1990s and envisaged as a testbed for fan noise reduction technologies. It was designed to be a low-cost, low-technology readiness-level experimental rig. In addition to its role in aiding the development of fan noise reduction technologies, it has also served to further the understanding of aeroacoustic physics and code validation. In the over 20 years of its lifetime, the ANCF has been upgraded a number of times and most recently relocated from NASA Glenn Research Center to the Turbomachinery Laboratory at the University of Notre Dame [81].

The ANCF was operated by NASA from 1994 until 2016 when it was transferred to the University of Notre Dame [81]. The ANCF was envisaged as a low-cost experimental testbed that could be used for the design and evaluation of noise reduction technologies, as well as for code verification, acoustic database enlargement and the advancement of noise measurement technologies. Figure 2.12 shows the ANCF in location in the Aero-Acoustic Propulsion Laboratory (AAPL) at the NASA Glenn Research Center where it was operated until the transfer in 2016.

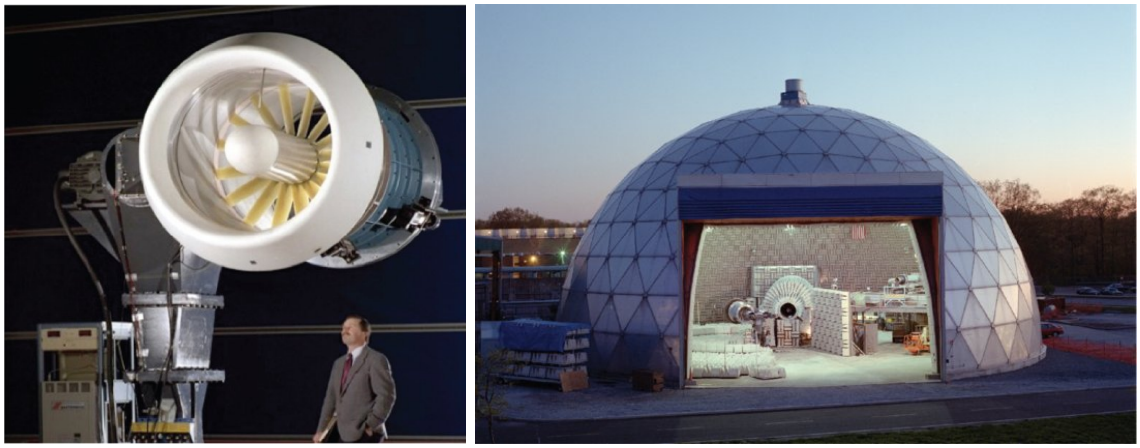

(a) The Early Days of the ANCF (b) The ANCF in location in the AAPL

Figure 2.12: The ANCF in its early days in location at NASA Glenn Research Center[81].

Over the course of its time at NASA, the ANCF went through several periods of testing and research emphasis. As previously mentioned, the ANCF was initially called the “Active”

Noise Control Fan as one of the first significant research campaigns was on methods of active noise control, alongside database development and code validation. Other major campaigns of the ANCF include research into unique fan noise reduction technologies, array development and rotating rake enhancement. In the early 2010s, the ANCF was used in the development of novel acoustic liners [81]). The timeline of the research emphasis can be seen in Fig. 2.13

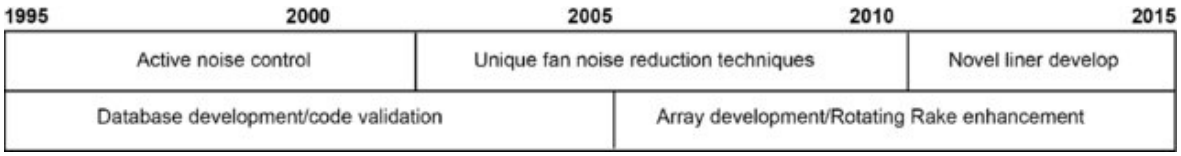

Figure 2.13: Timeline of the research emphasis while located at NASA AAPL [81]

2.2.3.1 Novel Acoustic Liner Development

The ANCF has a nominal operating speed of 1886 revolutions per minute corrected (RPMc). The resulting tip speed of the ∼1.22 m fan is approximately 122 cm/s, with an inlet Mach number of ∼0.15 [81]. The fan has a variable speed capable of speeds varying from 100 to 2500 RPMc, though the usual range of operation is 1500 to 2000 RPMc [82]. The operational frequency range of the ANCF is 250 Hz to 2.5 kHz. This frequency range is of particular concern for community noise, as assessed by the Effective Noise Perceived Level (EPNL) metric. As a result, the ANCF is well suited to the development of novel liners for implementation in aircraft engines.

To understand the performance of liner location on noise generation and attenuation, a study was performed which used six different nacelle treatments in both inlet and OTR locations [83, 84]. The six treatments used in the study were (I) hardwall, (II) hardwall with grooves, (III) grooves with an empty chamber and thin facesheet, (IV) empty chamber and thick facesheet, (V) expansion chamber and thin facesheet and (VI) metal foam and thin facesheet. In configurations (II) to (VI) the grooves are 1/2" deep with an axial length of 2.5" and in (III) to (VI) the acoustic treatment below the grooves are 1" deep. A detailed description of each configuration is available in Gazella et al. [83]. The testing showed that the acoustic treatments had a minimal impact when installed in the inlet. When installed in the OTR location the configurations which featured a thin facesheet recorded attenuation of up to 3 dB in the mid-frequency range. However, there were additionally a number of instances in which the noise was increased. These treatments were further used to study the difference between rotor-only and rotor-stator configurations. The results indicated that

the attenuation was a combination of noise source modification and a reduction of the wave propagation from the rotor-stator interactions [84].

A foam metal liner (FML) was designed based on absorption characteristics that were determined in normal incidence testing [85]. The FML was tested in two configurations; as an inlet duct liner, and as an over-the-rotor (OTR) liner. As an inlet liner, the measured attenuation of the FML matched the predicted performance of the liner well. The subsequent tests in the OTR position performed significantly better than predicted and better than in the inlet location. Additionally, in the OTR position, the performance of the FML was seen to be equivalent to that of a standard SDOF liner. However, the FML achieved this with an axial length of 9", while the SDOF liner was 18" in length and needed to be installed in the nacelle inlet, nacelle aft and the aft centre-body, meaning the FML achieved an equivalent performance with one-sixth the length. A comparison of the SDOF in the inlet, to the FML in both the inlet and OTR locations is shown in Fig. 2.14. The high OTR performance indicated that the replacement of the conventional OTR rub strip with OTR liners could eliminate the need for inlet liners. This would allow the size of engine ducts to be reduced, cutting down on the weight of engine nacelles [81, 84, 86].

A system of Herschel-Quinche (HQ) tubes was installed in the ANCF with a high-resistance liner. The design of the HQ tubes was performed by Virginia Tech using a Goodrich analytical model [87]. The tubes were tuned to the 2BPF tone and broadband component around them. This was to complement the high-resistance liner which was tuned to 2.5 to 5.5 BPF. The combined system of the HQ tubes and the liner performed well, with HQ operating well at low frequencies where the liner was not effective. The system was tested at a range of speeds from 1500 RPM to 1800 RPM. At 1500 RPM the system had an overall power reduction of 3.5 dB which increased in each test point up to an overall reduction of 4.5 dB at 1800 RPM. The power reduction caused by the HQ tubes was similar for each fan speed, with the majority of the increase in performance coming from the high-resistance liner at the higher fan speeds. The success of this combined approach resulted in the decision to continue the HQ system and later adaptations [81].

As discussed in Section 2.2.2, the ANCF was additionally used in a comprehensive study which followed the evolution of an MDOF liner design from the initial concept to a high-TRL test flight [80]. The design tested in the ANCF was first explored in Sutliff et al. [88] in which the performance of a variable impedance liner (VIL) is investigated. The VIL is

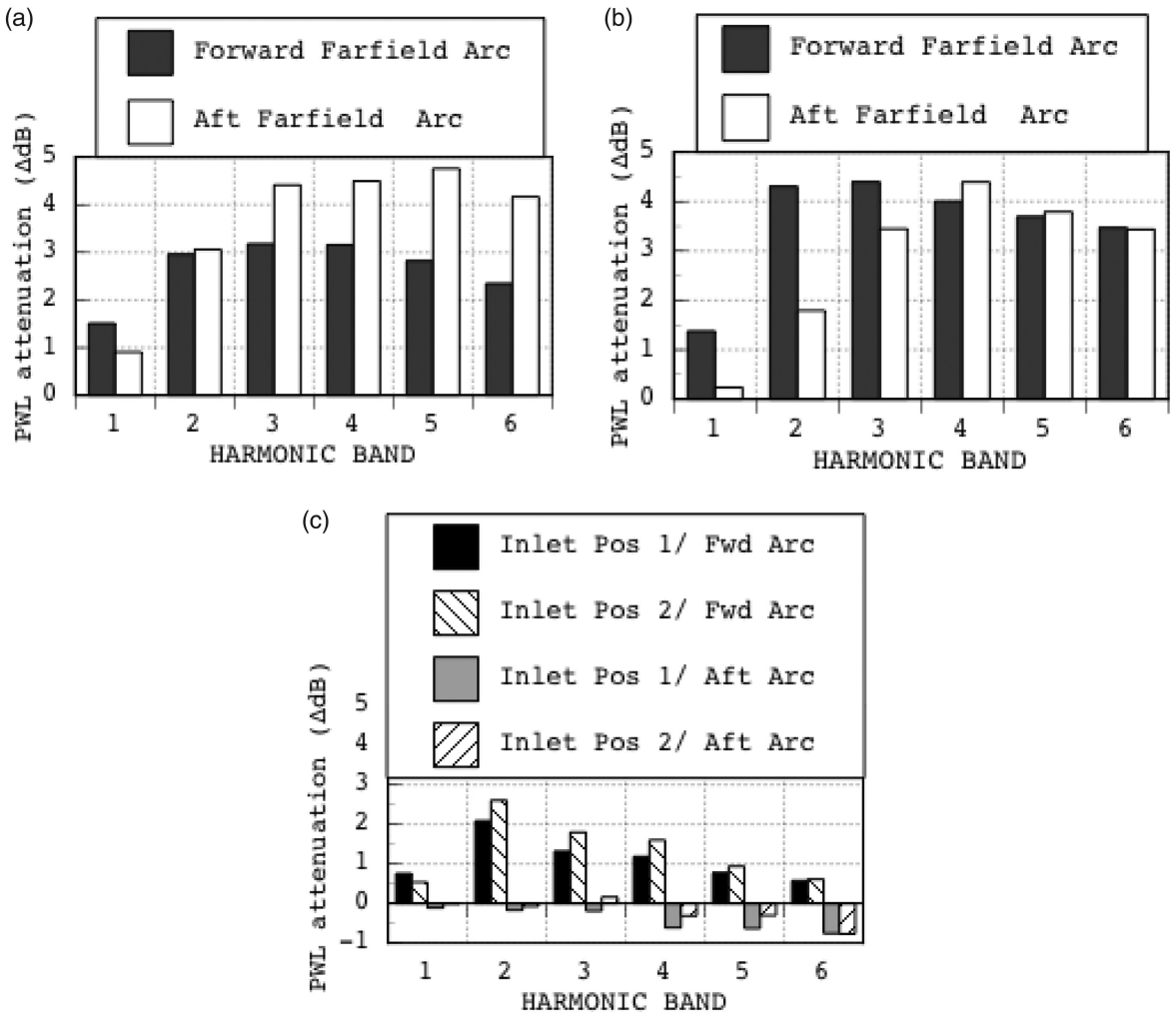

Figure 2.14: Comparison of the far-field attenuation relative to hardwall for foam metal liner compared to a traditional SDOF liner (a) SDOF located in both inlet and exhaust ducts of ANCF (b) FML located OTR of ANCF (c) FML located in inlet duct of ANCF. [84]

made possible by a unique variable depth design. The variable depth is created by installing mesh caps into individual ducts of a honeycomb structure at predetermined heights and the samples had an axial length of 16". The VIL was tested in an aft configuration. The VIL achieved PWL attenuation of 5 dB up to 15 dB across the first three harmonic bands for a range of fan speeds. This performance was in agreement with predictions, validating the prediction capabilities for the liner. The tests proved that the liner fabrication process was viable as a means to produce inlet liners with difficult configurations, an important aspect due to the strong curvature of the DART test rig which was intended as a future test bed of the liner. In high-speed duct fans the VIL continued to perform as predicted and during the testing on the test flight achieved a reduction on the order of 2 EPNdB as previously

discussed. This study shows the benefit of the ANCF as both a test rig for the current state of a liner and an indicator of a liner's future potential [80, 81].

2.2.4 Liner Optimisation

Following the identification of a potential liner design, the optimisation of the design geometry is essential to the development of a high-performing liner. The general approach to liner optimisation involves determining the value of geometric parameters through either numerical or analytical means that will maximise the performance of the liner for a desired frequency range.

To optimise a design, a cost function is defined which relates the geometric variables that can be changed to the parameter being optimised. This parameter depends on the specific study being conducted but is often the absorption coefficient or impedance of the liner in a given frequency range [89, 90]. The final value of this parameter can either be maximised or minimised.

McKay et al. [89] describes the optimisation of a two-chambered device in which the chambers are coupled. To model the physics, an equivalent circuit model of the device is generated based on the electroacoustic theory [91]. Using this model in the cost function as the geometric input, the mean absorption of the device can be analytically maximised within the target frequency. This approach works well for a relatively simple geometry, however, for a more complex device with many coupled parameters a more robust approach is necessary. In Davis et al. [92], a graph-theory approach to the model is introduced. This approach uses the impedance of individual equivalent circuits to create a Laplace matrix representation of the model. As the matrix can be expanded to include more input impedance, it allows a much more complex device to be defined and used as in the cost function that the optimisation routine uses.

The defined cost function is used by an optimisation scheme to automate the variable selection. This optimisation can be performed numerically in many FEM programmes including COMSOL, ACTRAN and ANSYS or analytically using programming languages such as MATLAB and Python, many of which include built-in optimisation packages. These optimisation packages can use either single-objective optimisation or multi-objective optimisation, depending on the design being optimised [26].

In a single objective optimisation, the optimisation algorithm is applied to a single cost function which may in turn have a number of variables. The algorithm will either minimise

or maximise the cost function, depending on the desired outcome, in order to determine the best value for the variables. This is done iteratively by solving the function for a combination of variables. An example of such an algorithm is the *fmincon* algorithm, which is a gradient-based multi-object solver which aims to minimise the cost function. The algorithm begins by solving the function for an initial set of variables and storing the result. The algorithm then solves the next data set and compares the result with the previous result, rejects the larger result and stores the smaller one. This process repeats until the preset tolerance is met for the difference between two results [26, 93].

In multi-objective optimisation, instead of the algorithm solving a single cost function, it solves for multiple cost functions which may in turn have multiple variables. An example of when this would be of use is for a device which is being designed for use at two different frequency ranges. The multi-objective optimisation will evaluate the conflicting cost functions in order to determine an optimal solution for both. Both cost functions are evaluated and the result of the functions is combined into a single solution. If none of the individual cost functions can be improved without negatively impacting the other objective values, the solution is called a non-dominated solution. There may exist many possible solutions in a multi-objective optimisation which are considered equally good and result in the same overall value for the solution, even if the result for the individual cost functions may not be the same [94].

2.3 Metamaterials

Metamaterials are artificially engineered materials that have particular properties and behaviours that are not seen in naturally occurring materials. There are many different definitions of the word metamaterials used in the scientific community. Indeed as Kshetrimayum [95] states even the name metamaterial can be used as a definition as the "meta" comes from the Greek word which means beyond and "material" is derived from the Latin word *materia* meaning matter, alluding to a material that behaves as more than its constituent parts. More formal definitions have also been given. Cui et al. [96] state: "a metamaterial is a macroscopic composite of periodic or non-periodic structure, whose function is due to both the cellular architecture and the chemical composition." This definition provides a strong basis for the understanding of metamaterials. The geometries that are used to produce these unique materials are fundamental to their behaviour. While the chemical composition of the

materials can play a role in the materials' performance, it is secondary to the geometry and structures used.

The first instances of metamaterials were seen in the field of electromagnetism. In the early 1900s, the possibility of negative phase velocities, group velocities and left-handed materials was first explored. In 1968, Veselago [97] demonstrated analytically that a material can have a negative refractive index if the effective permeability and effective permittivity of the material are negative. This became the first model of a metamaterial. However, the concept was not experimentally proven for over three decades. In 2000, Smith et al. [98] developed a lens that exhibited a negative refractive index. This "superlens" was capable of focusing all Fourier components of a 2D image to a point smaller than its wavelength. This was achieved by combining two material designs described by [99, 100]. The first component was a periodic structure made of thin wire which allowed previously unobserved superconducting properties of GHz electromagnetic waves [99]. The second component was a flat, split ring micro-structure of non-magnetic conducting sheets which, in certain configurations, was capable of concentrating electromagnetic energy in a small region [100]. Though this demonstration of the superlensing effect was performed in microwave wavelengths, Pendry [101] showed that a similar effect was possible in optical wavelengths which could allow objects on nanometer length scales to be resolved.

Having been successfully demonstrated in the field of electromagnetism, researchers in other fields of study including acoustics began to grow more interested in the possibilities metamaterials presented.

2.3.1 Acoustic Metamaterials

When metamaterials were proposed in electromagnetism, the primary focus of the research was to generate materials that had a negative refractive index. In order to achieve this, a material would need to have simultaneously negative permeability and permittivity. When researchers began to explore the possibility of metamaterials in acoustics, they began with a similar approach of trying to create a material with a negative refractive index. To pursue this, acoustic analogies of the permittivity and permeability were required. As the mathematical form of electromagnetic waves and acoustics waves is the same, Li and Chan [102] were able to show that it is possible to design an acoustic metamaterial if the material exhibited a negative mass density (ρ) and negative bulk modulus (β). When both of these values are negative, the energy of the system will flow in the opposite direction to the propagation of

the acoustic wave [13]. This allows materials exhibiting a negative refractive index to be used in applications such as superlensing [103, 104], similar to what Pendry [101] demonstrated in electromagnetism.

A superlens is not the only unnatural phenomenon that can arise from atypical values for the mass density and bulk modulus. In Fig. 2.15, the effect of changing the effect parameters of the material can be seen [105]. In the top-right quadrant, both the mass density and bulk modulus of the material are positive which corresponds to the behaviour seen in conventional materials. In all other quadrants, behaviour only possible with a metamaterial is seen. In the bottom-left quadrant, both effective parameters of the material are negative which results in a negative refractive index. Materials that are found in this region are called double-negative materials and display behaviours such as superlensing.

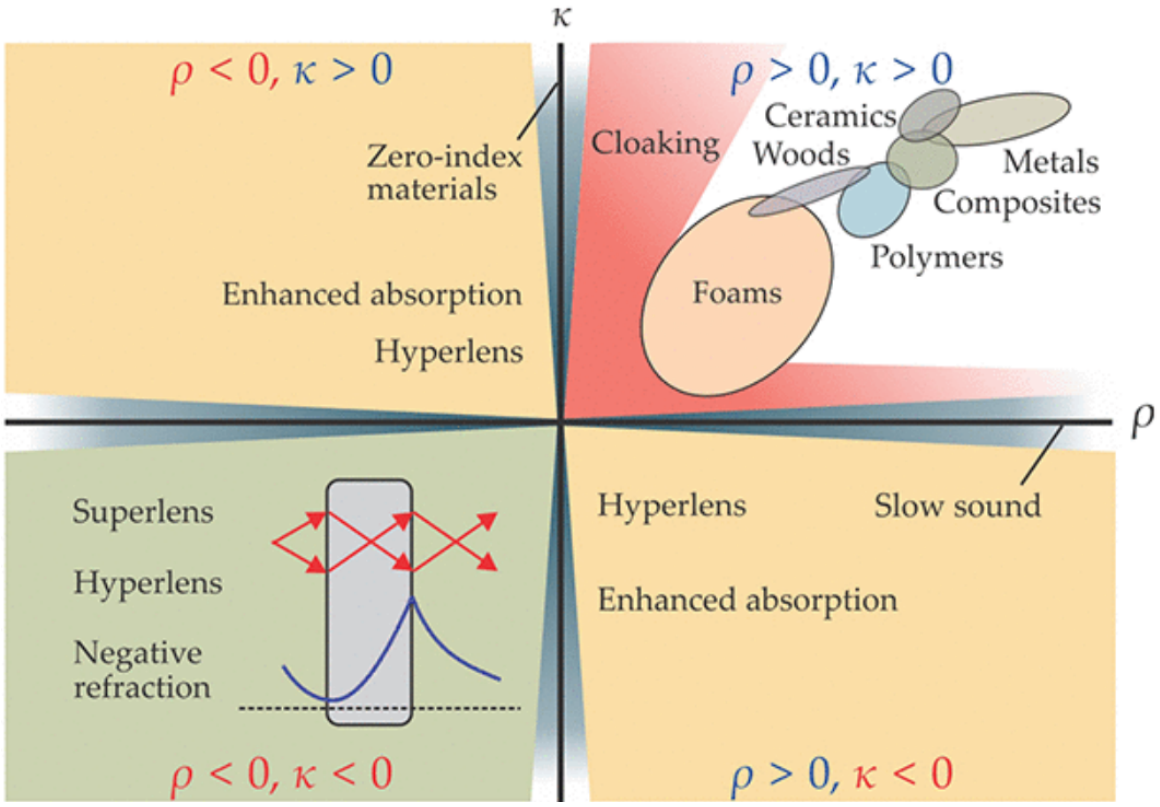

Figure 2.15: Behaviour of the acoustic wave for positive and negative effective properties of the material [105].

The materials in the top-left and bottom-right quadrants are single negative materials which occur when the bulk modulus or the mass density is negative. These single negative materials are not capable of supporting acoustic wave propagation and in these regions, the acoustic wave will decay exponentially [105]. Materials that have a negative bulk modulus

and a positive mass density are found in the top-left region, while materials that have a negative mass density and positive bulk modulus can be found in the bottom-right region.

A material that has a negative bulk modulus will expand when an external force is applied to it. Fang et al. [106] experimentally demonstrated this in the ultrasonic regime with a series of Helmholtz resonators. As the wave propagated along the array of Helmholtz resonators, the propagating wave became an evanescent wave resulting in almost no transmission at the resonant frequency of the Helmholtz resonators. At the resonant frequency, the cavity produces an outward restoring force. If the bulk modulus was positive, the cavity would shrink instead of expand under the external force.

Negative mass density is used to describe materials for which the effective mass ratio of the material is negative and is based on the idea of a locally resonant micro-structure [107]. Milton and Willis [108] described this system by changing Newton's second law so the relationship between the force and the acceleration was non-local in time. They used an analogy of a mass-spring system where there is a mass M_2 located within a cavity of mass M_1 which are coupled together by a spring with a spring constant k. An external force with an angular frequency ω is applied to mass M_1 which causes the mass to vibrate. By solving the constituent equations for the force, it is possible to describe the mass of the system in the following form:

$$M_{eff} = M_1 + \frac{k}{\omega_0^2 - \omega^2} \tag{2.1}$$

where M_{eff} is the effective mass of the system and ω_0 is the resonant frequency of the system. It can therefore be seen that it is possible for the effective mass of the system to become negative in the situation where the force applied is near the resonant frequency of the system. The effective mass density of the system is obtained by dividing the effective mass by the total volume of the system. While the spring-mass system is the most common analogy used to explain the behaviour of the effective mass density, in practice these systems can be realised in other systems, including membrane and plate-type metamaterials.

Between each of these regions seen in Fig. 2.15, another form of behaviour can be found. at the boundary between the four regions, one or both of the effective parameters can have near-zero values. Theoretically, metamaterials located within these regions would have a zero-refractive index with infinity phase velocity. This can allow the metamaterials to exhibit total transmission or total reflection by carefully modifying the parameters [109]. These effective

properties can be employed in material design in a wide variety of ways, varying greatly in complexity and application.

In the field of acoustics, two of the most desirable types of acoustic metamaterials are acoustic cloaks and metasurfaces. An acoustic cloak is a material that is used to hide an object from an incident sound wave by preventing the object from scattering the incident wave. An acoustic metasurface is a collective term used for a metamaterial device which has a thickness under one-tenth of the working wavelength [13]. This ratio of thickness to working wavelength is of significant interest in fields where noise reduction is required with limited space available such as in the aerospace industry. Metasurfaces can operate on a number of principles including phase shifting and local resonances depending on the design approach used. The design of metasurfaces typically consists of an array of unit cells which can be based on a number of different technologies including Helmholtz resonators, space coiling and membranes.

These technologies and approaches to acoustic metamaterial design are discussed in more detail below.

2.3.1.1 Helmholtz Resonators

A Helmholtz resonator-type liner is normally a form of locally reacting liner [110]. The SDOF liner is an example of a Helmholtz resonator-type liner. The behaviour of a single Helmholtz resonator can be modelled using the mass-spring damping system analogy in the frequency range of interest. Using this analogy, the normalised specific impedance of the system can be written as

$$\zeta = \Theta + i\frac{\chi_m - \chi_s}{\rho c} \tag{2.2}$$

in which Θ is the resistance due to the viscous wall losses of the neck, χ_m is the reactance due to the mass, χ_s is the reactance due to the spring, and ρ and c are the density and speed of sound in the fluid [111]. This impedance is not dependent on the angle of incidence of the acoustic wave and as a result, the characterisation of a Helmholtz resonator can be easily carried out in normal impedance.

However, in certain situations, such as when neighbouring cells are interconnected or the cell width is too large compared to the incident wave, the resonator is nonlocally reacting [110]. This is often the case in applications such as aircraft liners where drainage holes

resulted in cells being interconnected [112]. In these cases, the impedance of the material is modelled as an array of Helmholtz resonators

$$\zeta(\omega) = \zeta_{fp} - icot\left(\frac{\omega d}{c}\right) \tag{2.3}$$

in which ζ_{fp} is the resistance of the faceplate, and $icot\left(\frac{\omega d}{c}\right)$ is the reactive component, determined by the cavity depth d.

The use of an array of Helmholtz resonators is particularly interesting as these arrays are able to achieve near-total transmission or total loss of the acoustic waves incident on the array by carefully selecting materials that will result in impedance matching or mismatching. As previously mentioned, Haberman and Guild [105] used an array of Helmholtz resonators to create a negative bulk modulus material that would cause exponential wave decay resulting in near-total transmission loss. However, Gong et al. [113] demonstrated that the Helmholtz resonator could be used for acoustic focusing. By tuning the width of the resonator slits to allow for impedance matching, a focal point that was 12.3 to 17.6 times the size of the incident wave could be achieved while maintaining high transmission.

2.3.1.2 Space Coiling

Space coiling is a form of double negative metamaterial which uses labyrinth-style paths to increase the path length of the acoustic wave. By changing the path length of the wave, the material causes a phase delay in the wave propagation. By careful selection of the path geometry, this phase delay can be anywhere in the range of 0 to 2π [26, 114, 115]. Space coiling was first investigated by Liang and Li [116] in 2012 who proposed a single unit which had the path curled up in a zig-zag pattern. The dispersion relations they determined showed that at different frequencies the material would behave as though it had a negative and higher relative refractive index with respect to the background medium. Liang and Li [116] deemed the use of zig-zag patterns is necessary to minimise thermo-viscous losses in the structure. Liang et al. [117] experimentally showed the capabilities of these space-coiling approaches to achieve double negative and zero-index metamaterials. They further went on to demonstrate the same principle for microwaves.

A number of alternative approaches to space coiling have since been proposed, using different methods of manipulating the coiled path in order to achieve different goals. Xie et al. [118] used a curled approach to design a space coiling metasurface capable of steering

an incident acoustic wave. The metasurface was also capable of propagating the surface wave mode, beam-steering and negative refraction.

Ghaffarivardavagh et al. [119] proposed a "horn-like" method of space coiling. In the zig-zag approach, the path has a constant width throughout the material. This results in the path having an equivalent model of the same depth and path width, which has been filled with a medium of a different refractive index. This can be seen in Figs. 2.16a and 2.16b. In the case of the horn-like approach, the width of the path is incrementally increased while moving farther into the material; at each turn, the aperture of the turn is equal to the width of the next section of the path as seen in Fig. 2.16c. The resulting equivalent model, seen in Fig. 2.16d, is of a material with a greater effective depth that curves along the length, gradually getting wider. The refractive index of both media are the same in the horn-like model. This approach to space coiling enables amplitude manipulation in addition to phase manipulation. The ability of these materials to modify acoustic radiation patterns has been experimentally validated, allowing complete acoustic wave manipulation of the target acoustic waves.

In an attempt to improve the performance of existing acoustic liner design approaches, Chambers et al. [120] proposed a space coiling technology which incorporated folded core geometries and spiralled geometries into conventional cavity backings. Both circular and square spiral designs were investigated which could be inserted into the ducts of honeycomb-style backings. The spiralled and folded paths could create longer effective lengths than the straight backings. An optimised design was seen to have an absorption coefficient greater than 0.6 below 400 Hz. However, the fixed path lengths can result in the absorption coefficient exhibiting drop-out at frequencies without a corresponding tuned duct.

2.3.1.3 Membranes

Decorated membrane metamaterials, often called decorated membrane resonators (DMR), are a type of metamaterial that displays mass density and bulk modulus frequency dispersion [16]. DMRs can be used as a single cell or part of an array, though the latter is most commonly seen. The general form of these materials is an elastic membrane that is typically submillimetre to a millimetre in thickness and is attached to a rigid frame. The membrane is attached to the rigid frame to maintain the desired tension on the membrane and rigid platelets are subsequently attached to the centre of the membrane. The desired working frequency of the DMR is used to determine the mass of the platelet that is attached.

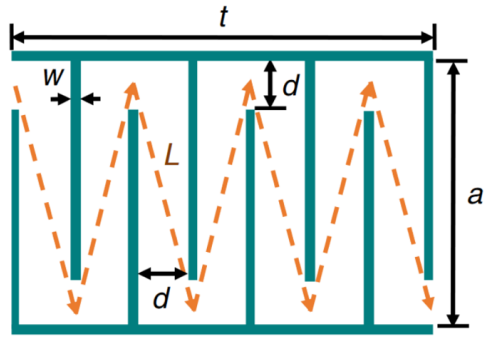

(a) Path of a zig-zag space coiling design

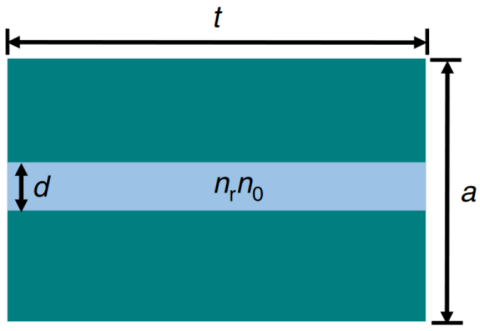

(b) Equivalent model of a zig-zag space coiling design

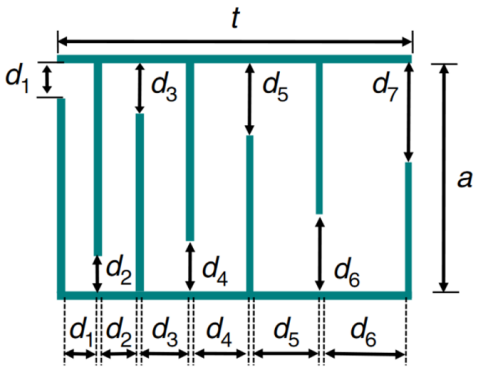

(c) Path of a horn-like space coiling design

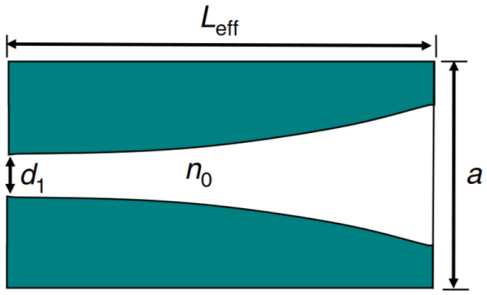

(d) Equivalent model of a horn-like space coiling design

Figure 2.16: A unit cell of (a) a traditional space coiling method and (b) the equivalent model with the same length which has a different refractive index, compared to a unit cell of (c) a horn-like space coiling method and (d) the equivalent model with the same effective length [119].

Mei et al. [121] showed that by using several layers of the decorated membrane metamaterial, near unity absorption could be achieved for wavelengths three orders of magnitude larger than the membrane thickness. This high level of attenuation was attributed to the energy lost by the elastic motion of the membrane around the moving platelets. Yang et al. [122] used a membrane with a rigid boundary and central mass to successfully achieve near unity absorption for two of the eigenmodes in their test range. Naify et al. [123] successfully used coaxial rings attached to a locally resonant acoustic metamaterial (LRAM) to increase the transmission loss peak of the material.

Additionally, Zhao et al. [124] discussed the use of a magnet that would act on the central platelet and allow the frequency of the transmission loss to be tuned. Using this method, they

were able to experimentally obtain different transmission loss peaks at frequencies ranging from 100 Hz to 800 Hz.

2.3.1.4 Cloaking

The concept of metamaterial cloaking was first proposed by Pendry [125] in 2006. The original proposal of a metamaterial cloak was an electromagnetic cloak as opposed to an acoustic cloak. A number of approaches were described that would allow electromagnetic cloaking to occur. However, each of these proposals depended on the symmetry of Maxwell's equations which allowed for transformation-based solutions, as Maxwell's equations are invariant under coordinate transformations. Milton et al. [126] showed that these approaches are not directly applicable in acoustics as the equations of motion are not invariant under the transformations.

However, in 2007, Cummer and Schurig [127] showed that in a 2D representation, the acoustic equation in a fluid has the same form as the single polarization of Maxwell's equations for an anisotropic material. It was shown that an anisotropic "meta-fluid" with an inhomogeneous bulk modulus and inhomogeneous mass density would be able to direct a compression acoustic wave around an object without reflection or detectable scattering. In order to create a material capable of being placed around an object to cloak it, it would be necessary to create an object that is solid but behaves like a fluid. Following this, Norris [128, 129] furthered the understanding of acoustic cloaking by showing that the effect of "inertial cloaking" is a specific case of the theory that the anisotropy of the material can be distributed across both the density and the bulk modulus of the material [13].

To achieve this, Kadic et al. [130] proposed a pentamode-material. This material would have a lattice structure that could behave like a fluid. Here, pentamode refers to a 3D mechanical material engineered to have one none-zero and five vanishing eigenvalues in the elasticity tensor of the material [131]. Using this premise, it was shown numerically that a pentamode microstructure could be designed that has a ratio of the bulk modulus to the shear modulus of nearly 1000. Kadic et al. [132] further went on to manufacture a number of the proposed designs. However, due to size and scaling limitations with their manufacturing process, they have not been able to experimentally measure the performance of these materials. Seen in Fig. 2.17, the lattice structure is created on a length scale of 100 μm, with individual features ranging in size from 19 μm to 0.45 μm.

As outlined by Norris [133] and Giorgio Palma et al. [13] there are alternative approaches to acoustic cloaking being explored, however, these are largely conceptual at this point with

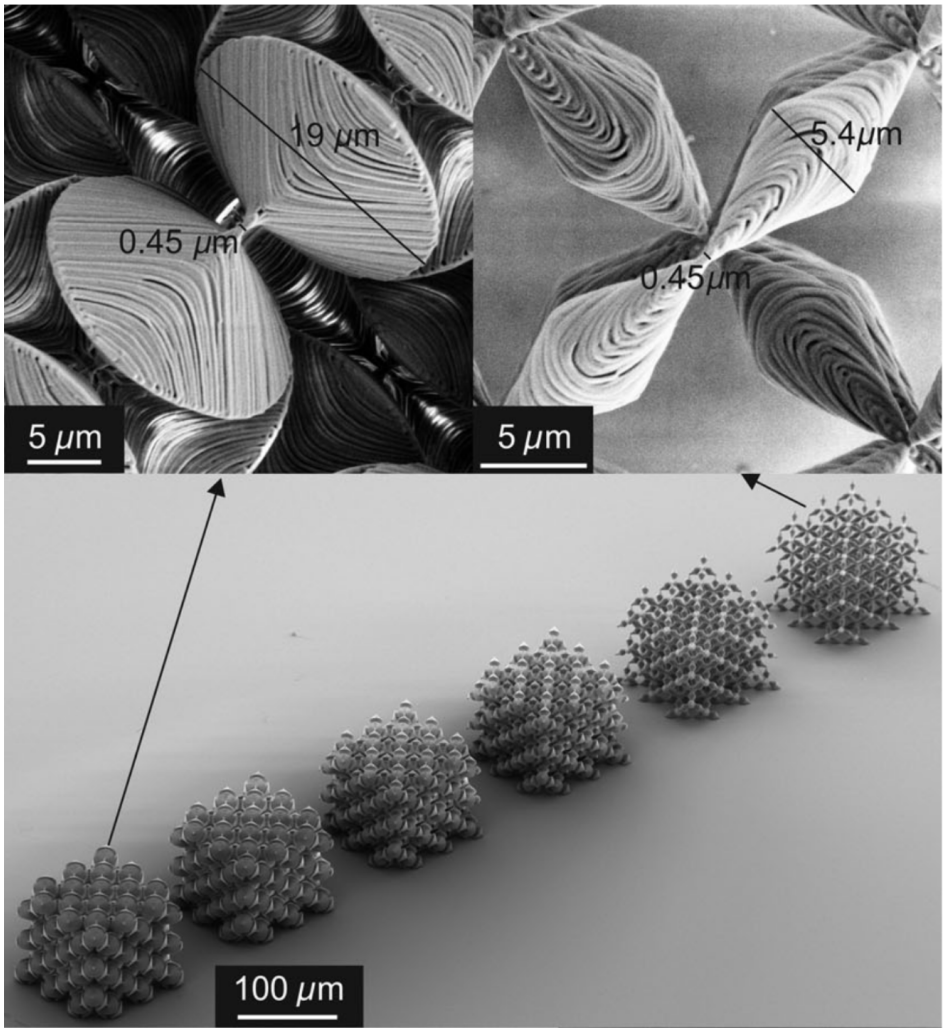

Figure 2.17: Electron micrographs of fabricated polymer lattice structures. These structures are examples of designs that could be modified to create pentamode metamaterials for acoustic cloaking [132].

limited practical realisation. Transformation acoustics, the ability to shink a cloaked object and make it appear vanishingly small from the perspective of an observer, has only been shown to work for a quiescent medium. Using transformation acoustics, a number of attempts have been made to create a "carpet cloak" [134–136]. Zigoneanu et al. [136] presented a 3-dimensional, omnidirectional cloak design which rendered a region of space three wavelengths wide almost invisible to an incident 3 kHz sinusoidal wave. While there has been a number of studies that attempt to apply the transformation acoustics theory to work when there is a flow present, it has yet to be achieved practically [137, 138].

2.3.2 Acoustic Metamaterials in Aeronautics

In aeronautics, acoustic metamaterials are a particularly attractive solution to the problems posed by the noise generation discussed in Section 2.2. Metamaterials are capable of high levels of noise attenuation at a low-frequency range, but are still able to meet the size and weight restrictions that limit the viability of other noise reduction technologies.

The wide range of areas on an aircraft can be met with an equally wide range of metamaterials, each one selected for the specific requirements of that area of the aircraft. Within the landing gear bay, the cavity noise generated is a result of the shear layer interactions. However, by using a DMR that is tuned to target the range of noise dynamically using methods discussed in Naify et al. [123], Zhao et al. [124]. A combination of these approaches would theoretically allow the metamaterial to have high transmission loss peaks, while also being adaptable and able to respond to the changing mode excitation that occurs as a result of the aircraft acceleration.

However, the area on the aircraft where the issue of noise abatement is greatest is also the area where the technologies used are the most limited: in the aircraft engines. The problems associated with the current methods of noise abatement were discussed in Section 2.2.2. The broadband, low-frequency noise is difficult to attenuate ordinarily and the space available for noise treatments to be installed is being restricted by modern aircraft design. Coupled with the weight concern that is ever present in the aviation industry and the need for a robust design there are a lot of considerations present.

The majority of the work that has been done in the field of acoustic metamaterials has been tested in normal incidence. While the results of many of these tests have achieved promising results such as high absorption across broad frequency ranges [139], many of these metamaterials cannot be used in the engine as they would have a significant impact on the airflow through the engine. Ghaffarivardavagh et al. [140] designed a metamaterial in normal incidence which they described as being an "ultra open acoustic metamaterial silencer". The material is a ring that is inserted into a tube in normal incidence. The ring structure is hollow, with a spiral path through the ring. A transmission loss of up to 94% was reported. Unfortunately, though it is claimed that this material is ultra-open, the open area of the design is only 60% which is significantly too low for use in as an aircraft liner.

Given the impracticality of using a normal incidence metamaterial as a new form of nacelle acoustic liner, the attention must instead be turned to grazing incidence metamaterials.

The Grazing Flow Impedance Tube (GFIT) in NASA Langley has been producing interesting results in this area with multi-degree of freedom liners, as well as a number of other laboratories such as KTH, DLR and JAXA [18–21]. However, to date, there are a limited number of materials tested in this manner with the purpose of being implemented in an engine nacelle where there is a demand for high transmission loss under grazing incidence.

Tang et al. [22] proposed a new form of acoustic liner based on a combination of the perforated panel over honeycomb core and the honeycomb-corrugated hybrid core, which they called a perforated honeycomb-corrugated hybrid core (PHCH). The PHCH honeycomb core has individual cells with a square cross-section, as opposed to the more traditional hexagonal grid. The core structure is divided at various heights by diagonal corrugations throughout the material. In addition to a micro-perforated faceplate, the corrugated sheet has perforations which are coaxial with the perforations in the faceplate. Using this design, the impedance of the material is significantly improved over the design of both the SDOF and DDOF discussed in Section 2.2.2. Due to the different cavity heights and coupling effects present along the length of the liner, this system is a multi-degree-of-freedom liner.

Similar concepts were explored by Palani et al. [26] who investigated the performance of three cavity liner designs. Two of the designs featured a perforated, slanted septum within a cavity which had a perforated faceplate. In the first design, seen in Fig. 2.18a, the septum had a perforated region with a fixed percentage open area (POA) and a hard wall region. The second design, in Fig. 2.18b, features a septum with a variable POA, achieved by adding perforations to the hard-wall section of the septum in the previous design. The two sections have different POAs. The third design was a cavity liner that features multiple folded channels to create channels with different effective lengths. This is seen in Fig. 2.19 and was based on patents from Pool et al. [141] and Murray et al. [142]. Unlike the design presented by Tang et al. [22], these designs were for single cavity liners. The liners demonstrated an average of 10 - 14 dB of sound absorption from a normally incident wave of 150 dB. The frequency range of each liner varied for each geometry. While the design has not been tested in grazing incidence, Palani et al. [26] indicated that faceplate optimisation would follow in order to access the liner's capabilities as an aeroengine liner.

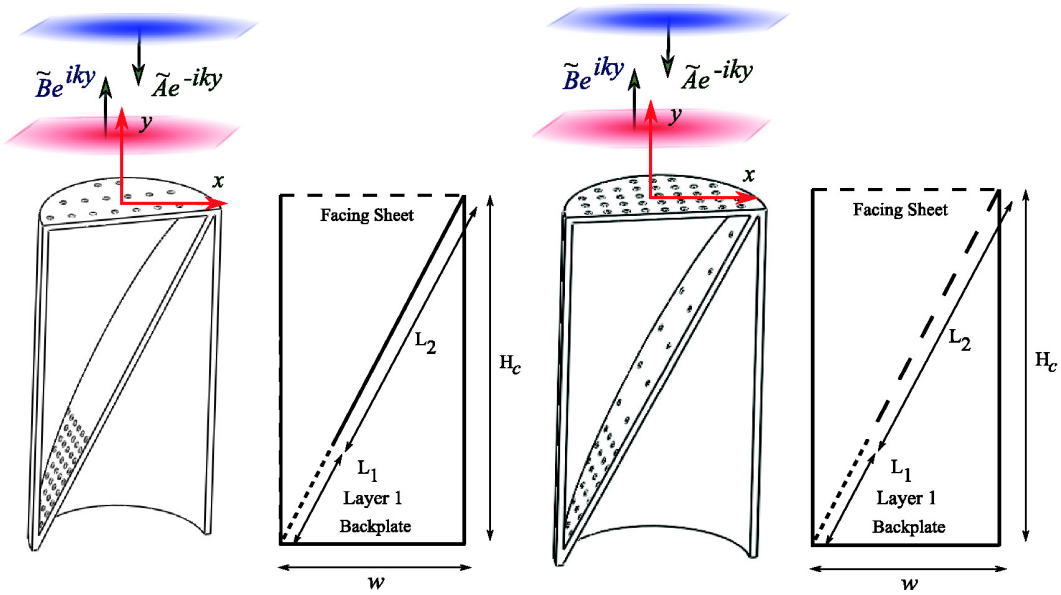

(a) Slanted septum design with a single POA (b) Slanted septum design with a variable POA

Figure 2.18: Design of the slanted septum cavity liner [26].

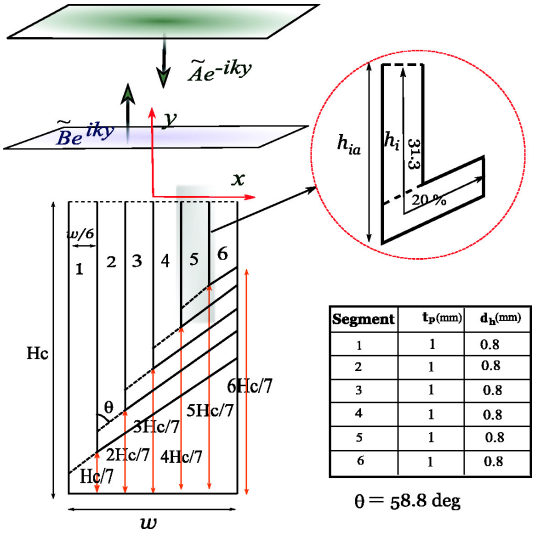

Figure 2.19: Design of the MultiFOCAL concept [26].

2.4 Additive Manufacturing

Additive manufacturing (AM), also referred to as three-dimensional (3D) printing, is a method of manufacturing in which an object is produced by successively creating layers or slices of the object. Traditional methods of manufacturing are subtractive in nature, where the material is removed to produce the final object [143]. The details of how different methods of additive manufacturing create a layer, and eventually the final component, can

vary significantly. However, the general concept and workflow that is followed to produce the object are very similar across all technologies. The four phases of additive manufacturing are

1. Model generation: a 3D model is generated using a CAD programme or other computer-based 3D modelling software.

2. Pre-process: the model is adapted to improve the chances of a successful print. Some printing technologies, in particular powder-based systems, do not require support structures as the unused build media can support the structure as it is produced. Slicing is the process which breaks the design into individual layers that are printed, and the sliced model is converted into a format that is readable by the printer.

3. Additive manufacturing process: the component is printed by printing each layer incrementally.

4. Post-process: the printed component is removed from the printer build plate, and supports are removed if present. The cleaning and curing process vary depending on technology. Some technologies require little to no cleaning, while others involving liquid build media can require cleaning to remove excess media and final curing to complete the component.

The full workflow, seen in Fig. 2.20 can involve a number of additional steps within these phases as described above.

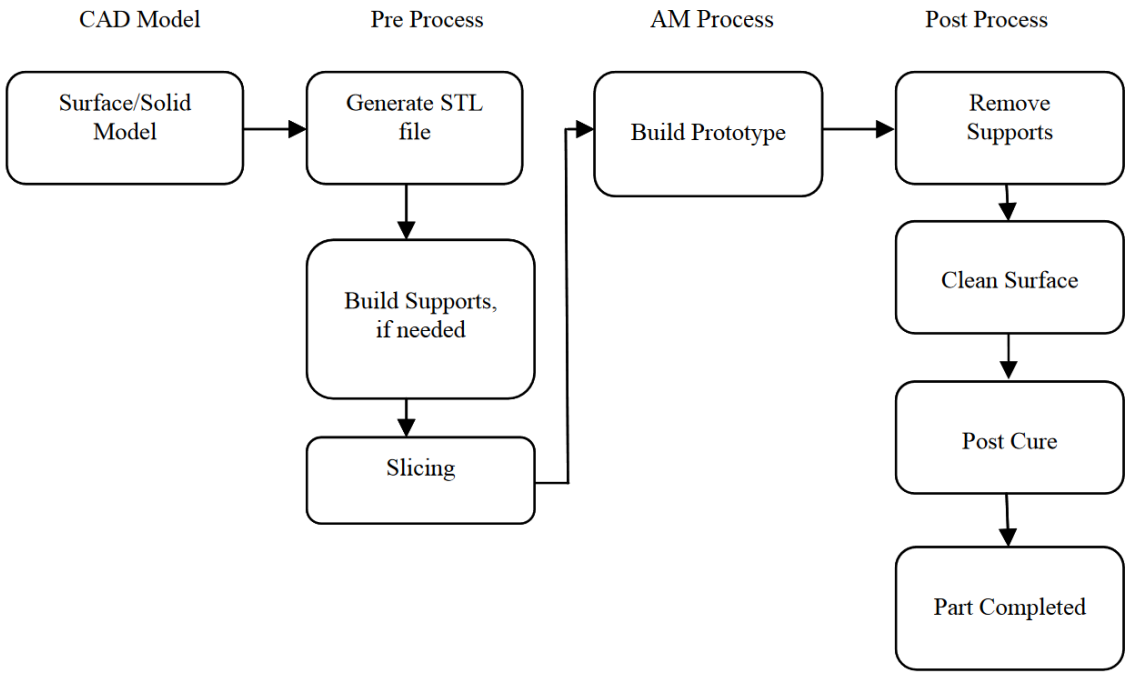

Figure 2.20: Additive manufacturing workflow [144].

2.4.1 Additive Manufacturing in Aviation

Over the last decade, the aerospace industry has become one of the largest sectors involved in additive manufacturing, accounting for 18.2% of the additive manufacturing market share in 2017 [145, 146]. Both metallic and non-metallic AM methods have been of interest in the sector, where metallic processes and materials are of interest for critical components, and non-metallic materials are of interest for non-critical components. Over 20,000 non-metallic 3D printed components were installed in aircraft globally between the 1990s and 2018 [146]. It is estimated that the aerospace AM market will be in excess of $ 31.8 Billion by 2030, with a compound annual growth rate of 20.24% between 2020 and 2030 [147].

For years, the reliability of metallic components has prevented their wide-scale adaption in the aerospace market [143]. As metallic materials are primarily used in critical components, the parts produced must meet strict quality criteria. However, the potential to reduce the number of parts required to build complex systems and the potential to reduce raw material scrap ratios from 80-90% down to 10% resulted in companies continuing to develop the technology [143, 148].

GE Aviation, a subsidiary of General Electric, is one of the largest manufacturers of aircraft engines. In 2016 the company announced a $ 1.6 Billion acquisition of two AM

companies in an effort to realise the full potential of AM in the aerospace industry. Since the acquisition, GE has developed their own AM processes, including the GE Additive's Concept Laser M2 Series 5 which is used in the production of these parts for their newest generation of engines [149]. The M2 uses dual lasers in layer production, allowing for faster and more uniform energy distribution. As discussed by Dowling [150] the energy distribution of the laser in SLM printing is a significant factor in the print quality and the performance of the printed components. One of the areas in which GE have implemented AM components is in the fuel nozzle of the GE LEAP LM9000 engine, reducing 20 parts into a single component. This reduced the overall weight of the nozzle by 25%. Similarly, in their next-generation turboprop, AM allowed 855 parts to be consolidated into 10 components [151].

Airbus and Boeing have also both begun to incorporate AM components into their aircraft design. Airbus used AM to create a hydraulic housing tank as a single part, which was previously a 126-part assembly. They have also reported using AM metal brackets on the A320neo [145]. Boeing has incorporated four AM components into the 787 Dreamliner, with plans to expand this up to 1,000 parts [152]. Airbus has also reported that it is using AM in the development of liquid rocket engine injectors [153] and has plans to send a metal 3D printer to the International Space Station in the coming year [154].

2.4.2 Additive Manufacturing for Aircraft Noise Reduction

While AM has been a significant area of interest in the aerospace sector and in the development of acoustic liners, there has been a more limited implementation of AM in aircraft noise reduction. A number of acoustic liner designs and acoustic treatments have been proposed which could see the implementation in aircraft noise reduction, however, the majority are still in the early stages of development or have not explored the potential of AM to progress the technology [22–26].

Jones and Howerton [86] discussed two different approaches to implementing AM noise reduction technologies in aircraft design; a soft vane concept [155, 156] and external liners [157, 158]. The soft vanes concept incorporates noise reduction technologies into the internal structure of the engine vanes. This was achieved by placing a porous surface over four resonant chambers in the internal volume of the vanes. Noise reductions of 1 - 2 dB were observed over a two-octave range. The authors note that the study was conducted when AM was still in its early days and did not have the level of sophistication or precision that is seen today. Despite this limitation, it still provided significant insight into the adaptation of

internal structures using AM. Further, it is noted that the porous surface should not extend beyond half of the chord.

The external liner was designed for implementation in two locations; in the structure of the wings and in the elevons. The liners had internal channels incorporated into the structure. The length of these ducts varied across the length of the liner. This is similar to methods employed in the design of acoustic metasurfaces and space coiling discussed in Section 2.3.1. The designs were capable of a 0.7 EPNdB cumulative reduction and were identified as having potential applications in open rotor systems. However, to achieve these results the design needed to extend across the entire available surface. Prior to implementation, the liners need to be capable of working while covering a smaller surface area, as there are potential drawbacks to structural performance and the aerodynamics of the system in its current form [86, 157, 158].

Pierre et al. [159] recently presented a noise-reducing, sandwich acoustic liner. The backing structure of the liner is a complex system of five different Helmholtz resonators which were produced using material extrusion additive manufacturing. Each of the five Helmholtz resonators was tuned to a specific frequency and was experimentally validated. When the five cells were tested together as a single sample, a coupling effect between the individual absorption curves was observed. As can be seen in Fig. 2.21, this coupling effect increased the absorption peak of the individual cells and produced a high absorption curve above 0.9 across a 500 Hz frequency range.

For installation in aircraft, the structural performance of a liner is also a significant factor. Damage to a liner could not only result in poor acoustic performance but also poses a risk to the engine if parts of the liner were to be injected into the engine. During the study, the structural strength of the material was also investigated [159]. It was determined that the liner design had a stiffness of up to 10% higher than equivalent honeycomb materials. This shows the potential of AM materials for application in aircraft, as stronger and higher-performing acoustic liners.

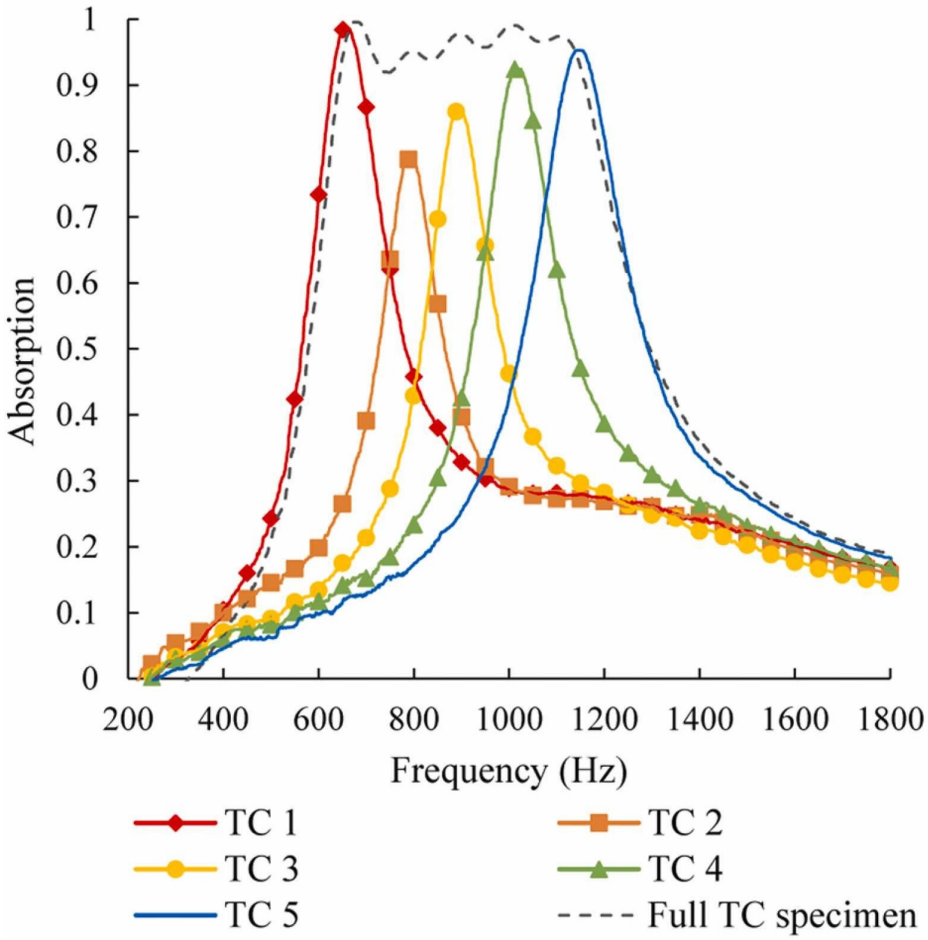

Figure 2.21: Absorption curve of the individual Helmholtz resonators and the performance of the full liner sample [159].

2.5 Conclusions and Contribution of the Thesis

Given the literature review reported in the previous sections, a number of conclusions can be drawn:

- Due to the rising levels of global air travel, new and innovative approaches to aircraft noise reduction are required. For communities living in proximity to airports, there are a number of health problems which can be directly linked to higher noise exposure levels. While several of these problems can be reversed over time, it requires noise exposure levels to be reduced to below 55 dB L_{den}. Air travel forecasts predict up to 4.3 million people in Europe would be exposed to levels greater than this by 2035, showing the urgent need to reduce aircraft noise.

- One of the primary sources of aircraft noise is engine noise. The current trends in aircraft engine design are increasing the engine by-pass ratio which in turn increases the overall size of the engines. This has the adverse effect of increasing their weight. As a result, there is a growing need to reduce the duct length and thickness of the nacelle which in turn reduces the space where conventional liners can be installed. Therefore, novel, lightweight acoustic liners are required that can reduce the broadband noise generated by the aircraft engines during take-off and landing. Additionally, the ability to target tonal noise which is produced at the blade passing frequencies is of particular interest.

- Acoustic metamaterials have demonstrated impressive acoustic performance that is beyond the capabilities of more conventional acoustic treatments which have a similar size. This area holds significant potential for the development of a liner that is able to meet both the acoustic performance required to address aircraft engine noise, and also meet the growing size and weight constraints. Key design elements and concepts have been identified which could provide the basis for the next generation of nacelle liners.

- In the aerospace sector, additive manufacturing has been proven to be a very powerful tool that provides breakthroughs in how aircraft are manufactured. Both Boeing and Airbus have begun to use AM parts in the construction of their aircraft, reducing the number of parts, weight and time to manufacture complex systems. As many acoustic metamaterial designs involve complex geometries, the implementation of AM is well-suited to the design and manufacturing of acoustic liners. Early studies have seen not only impressive acoustic performance from liners produced using AM but also improved structural performance.

Based on the points discussed above, a novel acoustic liner has been produced using additive manufacturing, and its performance has been assessed in a TRL 3 duct fan. The contributions of this thesis include:

- determining a viable acoustic liner design;

- optimisation of the liner design for broadband noise reduction from low-frequency sources at reasonable depths;

- utilising additive manufacturing in the production of the optimised liner;

- providing assessments of the performance of the liner at each stage to validate the predicted performance;
- verifying the performance of the liner in the ANCF duct fan which has a TRL 3.

Chapter 3

Experimental Facilities

A number of experimental facilities were used in the design and assessment of the acoustic liner presented in this thesis. The initial design, optimisation and final design testing were conducted using the Grazing Incidence Impedance Tube (GIIT) at Trinity College Dublin (TCD). Following the assessment in TCD, the liner underwent further testing in the Optical Duct (OD) grazing flow impedance tube at the Laboratory of Acoustics of Le Mans Université (LAUM). The GIIT and OD have a NASA TRL 2.

Finally, the liner was tested in the ANCF rig at the University of Notre Dame to assess its capacity to perform as an aeroengine acoustic liner. The ANCF duct fan is a NASA TRL 3 test rig. The incident noise field is considered more complex than that of the two impedance tubes due to tonal peaks caused by the blade passing frequency. The primary objective of the large-scale test in the ANCF was to evaluate the design which, if successful, could lead to further research into more suitable materials for aeroengines.

3.1 Grazing Incidence Impedance Tube - TCD

The Grazing Incidence Impedance Tube (GIIT) in Trinity College Dublin is designed for transmission loss testing in accordance with ASTM E2611-09 [160]. Additionally, it is capable of measuring reflection and absorption coefficients of samples mounted in normal incidence in accordance with ISO 10534-2:2001 [161].

The GIIT is designed for high SPL testing of up to 130 dB. The walls of the tube are aluminium, measuring 0.015 m in thickness. The tube has an internal rectangular cross-section with a width of 0.05 m and a height of 0.08 m to allow for ease of test sample design and mounting. The tube measures 1.75 m from the acoustic source to the termination. The acoustic source is two loudspeakers mounted opposite each other in the top and bottom walls of the tube. There are twenty-two microphone mounts in the upper wall of the tube; twenty microphone mounts are for grazing incidence tests and the final two located near the termination are for normal incidence tests. Of the twenty grazing incidence microphone mounts, sixteen are located directly above the test section and four are offset from the test section. The central sixteen microphones have a spacing of 0.03 m and the four offset microphones have a spacing of 0.12 m. The normal incidence microphone mounts are located 0.16 m and 0.23 m from the termination. In normal incidence testing, the acoustic samples are mounted in the place of the acoustic termination. The design of the GIIT including all microphone locations can be seen in Fig. 3.1 in the grazing incidence configuration.

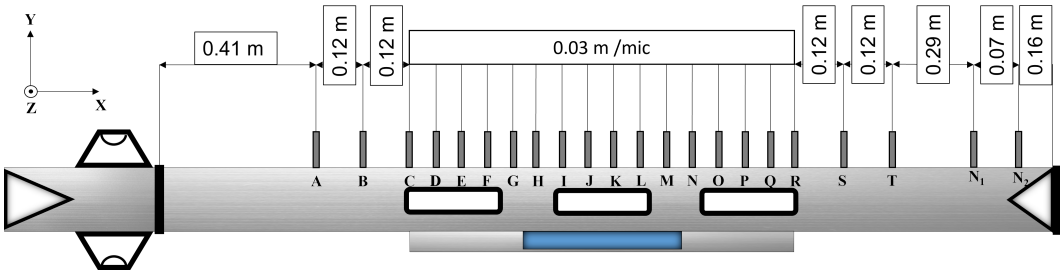

Figure 3.1: Design of the GIIT in grazing acoustic incidence configuration.

In normal incidence testing, samples are installed in the place of the downstream anechoic termination as seen in Fig. 3.2a. Samples can have a surface area that is the same size as the cross-section of the GIIT. Samples are installed in a holder which attaches to an external flange on both side walls. An example of a sample attached to the GIIT can be seen in Fig. 3.2b.

There is a 0.45 m long x 0.05 m wide cut-out centred in the lower panel of the tube to facilitate grazing acoustic incidence testing. Samples are installed in an aluminium holder that is attached to an external flange. This external flange is part of the lower panel. The holder has an internal depth of 0.035 m, so samples with a height of 0.05 m will be flush with the internal wall when attached due to the added 0.015 m wall thickness. If the sample installed is not 0.45 m in length, blanking inserts can be used to fill the empty space. For samples that have a depth greater than 50 mm, a spacer can be added to the upper surface of the sample holder. A solid aluminium insert is also available, which can be installed to facilitate calibration and hardwall testing. Additionally, poly-carbonate windows are present in both sidewalls along the length of the test section to allow PIV measurements to be performed. The windows are separated into four sections, separated by aluminium columns.

A National Instruments PXI-1044 DAQ chassis is used to control the I/O of the test rig. The DAQ is connected to an external amplifier which is used to drive the acoustic source. Two BMS 4591 2” compression drivers are used as the acoustic source. The frequency range of the drivers is between 200 Hz and 9 kHz. The loudspeakers are mounted vertically opposite each other in the upper and lower panels of the GIIT. The anechoic terminations at both the upstream and downstream locations are made from Basotect G+ melamine resin foam. The foam is cut into a wedge to target a wide range of frequencies.

The microphones used in the measurements were G.R.A.S 40PH microphones. The 40PH has a flat frequency response from 20 Hz to 20 kHz, in excess of the frequency range of

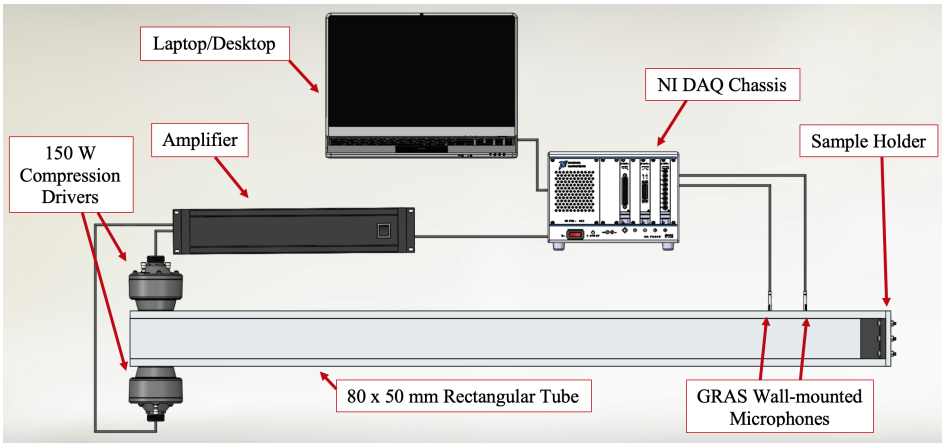

(a) Schematic of the GIIT

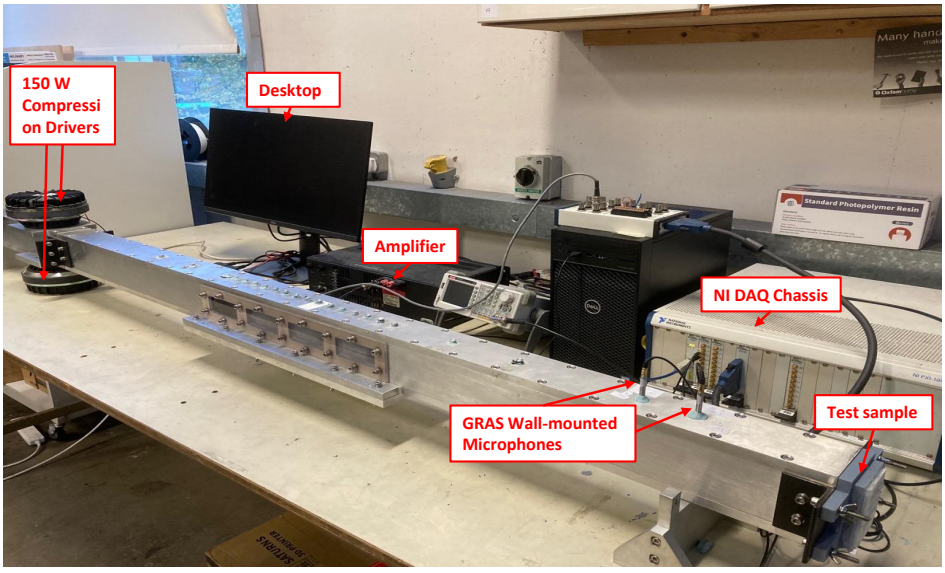

(b) Photo of GIIT and Data acquisition system.

Figure 3.2: GIIT set-up for normal incidence testing.

the acoustic drivers and the GIIT. The microphones are connected to NI PXI-4472B cards mounted in the DAQ chassis. The data acquisition and analysis is performed in MATLAB.

3.1.1 Reflection and Absorption Coefficients

In normal incidence, the reflection coefficient is determined using the transfer function method as outlined in British Standards ISO 10534-2:2001 [161]. The sound pressure at the two microphones locations N_1 and N_2 are recorded as p_1 and p_2 respectively. The transfer function, H_{12}, can be expressed as the ratio between these two pressures. As these pressures are composed of the incident and reflected waves, the transfer function can be written in terms of the reflection coefficient using the waves' exponential form

$$H_{12} = \frac{e^{jkx_2} - re^{-jkx_2}}{e^{jkx_1} - re^{-jkx_1}} \tag{3.1}$$

where x_1 is the spacing between N_1 and the sample location, x_2 is the spacing between N_2 and the sample location, and r is the reflection coefficient. It is possible to rewrite Eq. (3.1) to give the reflection coefficient in terms of the transfer function

$$r = \frac{H_{12}e^{jkx_1} - e^{jkx_2}}{e^{-jkx_2} - H_{12}e^{-jkx_1}} \tag{3.2}$$

In normal incidence testing, the component of the wave that is not reflected must be absorbed by the material. The absorption coefficient is therefore determined by

$$\alpha = 1 - abs\,(r)^2 \tag{3.3}$$

where α is the absorption coefficient. Similarly, the normal surface impedance, Z, of the material may be expressed in terms of the reflection coefficient:

$$Z = \frac{1+r}{1-r} \tag{3.4}$$

3.1.2 Transmission Loss

The transmission coefficient τ of a material is the ratio of the incident sound pressure to the transmitted sound pressure on the opposite end of the acoustic sample. This requires four measurement points to be used, two upstream of the sample and two downstream. Additionally, as outlined in ASTM E2611-09 [160], the wave must be measured with two termination conditions; anechoic and non-anechoic.

Four acoustic waves are recorded to determine the transmission coefficient: (A) the incident wave, (B) the reflected wave, (C) the transmitted wave and (D) the reflected transmitted wave. These four waves can be seen in Fig. 3.3. As the measurement is performed twice, there is two sets of each of these four waves. The waves measured in the anechoic configuration are denoted with the subscript o and for the non-anechoic configuration are denoted with the subscript h. The transmission coefficient is given by

$$\tau = \frac{A_o D_h - A_h D_o}{C_o D_h - C_h D_o} \tag{3.5}$$

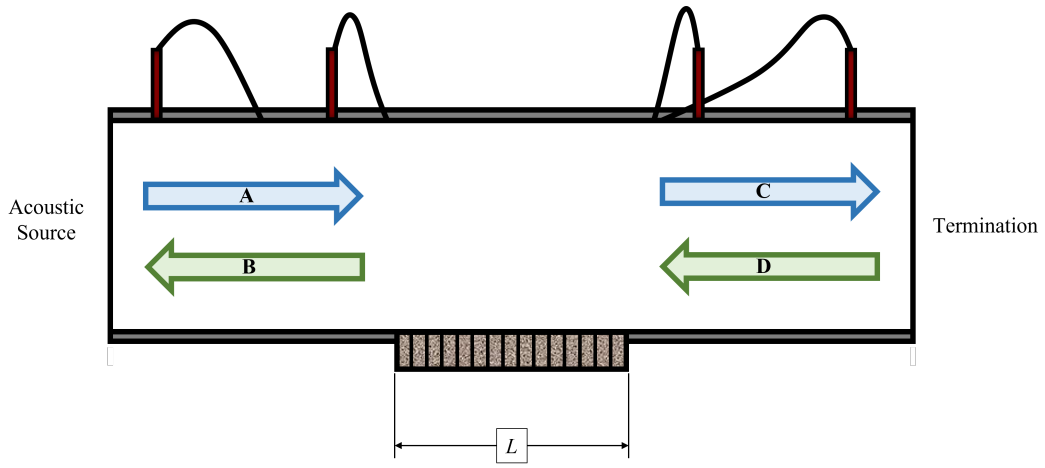

Figure 3.3: The transmission coefficient is determined using the four waves superimposed upstream and downstream of the acoustic sample as shown.

where each of A, C, and D refer to the transfer function for each wave of the same label. Using the transmission coefficient, it is possible to determine the transmission loss

$$TL = -20log_{10}\left(\frac{1}{\tau}\right) \tag{3.6}$$

in which TL is the transmission loss, given in decibels.

3.2 Optical Duct - LAUM

In the course of the characterisation of the liner design, testing was performed by LAUM. This test campaign includes high SPL testing and testing at Mach speeds of M = 0, M = 0.1 and M = 0.25. The test samples for LAUM were manufactured in TCD and sent to LAUM where the tests were conducted by Thomas Humbert.

The Optical Duct (OD) located in LAUM is a grazing incidence impedance tube with grazing flow capabilities. It is capable of computing the absorption coefficient and transmission loss using the scattering matrix approach. Impedance eduction can additionally be performed using a direct, Prony-like method obtained using an over-the-liner microphone array [162, 163].

The test section can accommodate a sample of length 0.02 m which is flush mounted on the wall of a waveguide which has a rectangular cross-section with a tube height of 0.04 m and width of 0.05 m. There is an anechoic termination at both ends of the tube to minimise internal reflections from propagating. Two Beyma CP850Nd compression drivers act as the

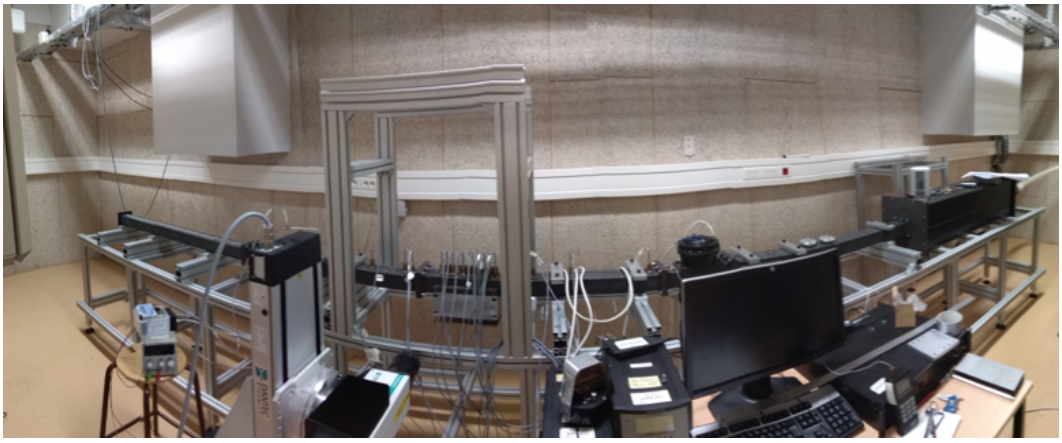

Figure 3.4: Photo of the Optical Duct located in LAUM [164]. The acoustic source is located upstream of the test section, on the right-hand side of the image.

acoustic source in the OD which can be placed upstream or downstream of the sample section. Acoustic excitation occurs between 100 to 4000 Hz by a sinusoidal wave in 5 Hz steps, at SPL up to 140 dB. The drivers are mounted opposite each other and can be mounted upstream or downstream of the test section relative to the flow. This allows the performance of the material to be measured in with-flow and against-flow configurations. The OD is capable of flow velocities up to 85 ms^{-1}, enabling acoustic testing at a range of Mach speeds between M = 0 and M = 0.25 [163, 165]. A schematic of the OD can be seen in Fig. 3.5.

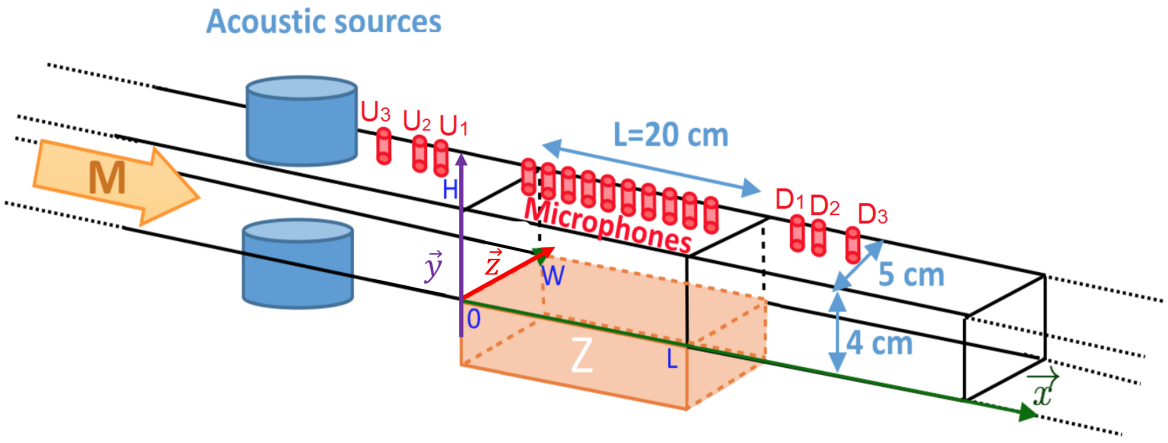

Figure 3.5: Schematic of the Optical Duct with the acoustic source in the upstream location. Adapted from D'Elia et al. [165]. The orientation of the schematic is the opposite of that seen in Fig. 3.4.

The OD has a test section 0.2 m in length, spanning the full 0.05 m width of the tube. The standard sample depth is 0.0495 m (49.5 mm) but can be increased by several centimetres if

necessary. The acoustic source locations are 0.0765 m from the test sample location in both the upstream and downstream source excitation[163, 165].

Acoustic pressures for the scattering matrix calculations are recorded by six microphones, three located upstream of the sample and three located downstream. The upstream microphones are located at a distance of U_1 = 112.3 mm, U_2 = 142.3 mm and U_3 = 287.3 mm from the sample. The downstream microphones are located at a distance of D_1 = 113.7 mm, D_2 = 143.7 mm and D_3 = 288.7 mm from the sample. The excitation signal in the OD is a swept sinus wave ranging from 100 Hz to 4000 Hz in 5 Hz steps. For each frequency step of the sine excitation, 300 cycles without flow, and 1000 cycles with flow are used to average the acoustic pressure. The absorption and transmission coefficients are directly obtained from the scattering matrix S:

$$\begin{pmatrix} p_2^+ \\ p_1^- \end{pmatrix} = S \begin{pmatrix} p_1^+ \\ p_2^- \end{pmatrix} = \begin{bmatrix} T^+ & R^- \\ R^+ & T^- \end{bmatrix} \begin{pmatrix} p_1^+ \\ p_2^- \end{pmatrix} \tag{3.7}$$

In the OD duct three microphones are used upstream and downstream to overestimate the incident and reflected waves. Measurements are carried out upstream and downstream and in order to obtain the elements of the scattering matrix in 3.7. The scattering matrix is computed using the microphone transfer function as outlined in Taktak et al. [166]. The scattering matrix obtained from measurements is also used in the inverse method. The impedance is obtained inversely by calculating this matrix using the multimodal method described by Aurégan et al. [167] where a numerical simulation of a two-dimensional lossless propagation model is carried out. The coefficients of the scattering matrix for plane wave propagation over a lined section depend solely on the energy flow through the system. The admittance can be found through an optimisation problem using the absolute value of the difference between computed and measured coefficients. In the case of this study, the input for the minimisation problem was the solution obtained through direct measurements from the 20 microphones obtained over the lined section, as the solution of the problem is not unique.

3.3 Advanced Noise Control Fan - UND

The Advanced Noise Control Fan (ANCF) was designed in the early 1990s, envisaged as a testbed for fan noise reduction technologies. It was designed to be a low-cost, low-technology

readiness level experimental rig. In addition to its role in aiding the development of fan noise reduction technologies, it has also served to further the understanding of aeroacoustic physics and code validation. In the over 20 years of its lifetime, the ANCF has been upgraded a number of times and most recently relocated from NASA Glenn Research Center to the Turbomachinary Laboratory at the University of Notre Dame [81].

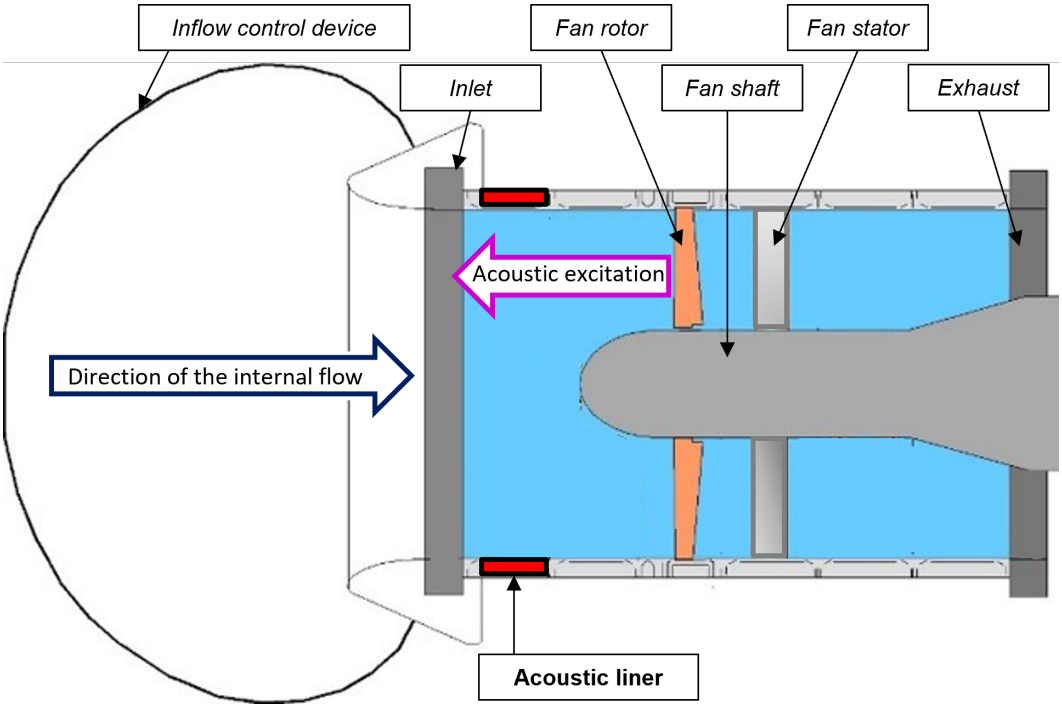

Figure 3.6: Schematic of the ANCF [81]

The ANCF is a duct fan which has a 1.22 metre (4 foot) internal diameter. The duct is highly configurable with ring sections which are capable of being moved to obtain the desired duct geometry or have hardwall sections replaced with liner sections for testing. These sections can be seen in Fig. 3.6. The fan speed is controlled by a 200 HP electric motor. The nominal operational speed is 1800 RPM, with a range of 100 RPM to 2400 RPM. At the nominal operating speed, the fan tip speed is approximately 115 ms^{-1}, the inlet Mach number is ∼0.15, and the fundamental blade passing frequency (BPF) is approximately 500 Hz. The ANCF rotor has 16 blades with a nominal pitch angle of 28°, though it can additionally be set to 18° or 38°. It is possible to run the ANCF in a rotor-only configuration, or with a stator stage attached downstream of the rotor. The stator count is variable and they are capable of being set to any angle. An Inflow Control Device (ICD) is installed at the front of the ANCF, which is used during static ground tests in order to condition the airflow into the duct.

The ICD conditions the airflow by breaking up ground vortices and reducing the turbulent flow which would otherwise become an additional noise source in the duct. The ICD is a layer of honeycomb sandwiched between two layers of fine mesh, installed in 22 longitudinal segments [81]. The ICD originally consisted of 11 longitudinal sections, however, this was found to generate cut-on modes within the operational frequency range of the rig, so the 22-segment design was built.

Since the transfer to the University of Notre Dame, ANCF testing has been conducted outdoors at the White Field (WF) Facility [82]. The data acquisition is performed by an array of ground-based microphones. This array typically consists of 30 microphones, split into a fore array and an aft array each containing 15 microphones. As the primary focus of this study is the ability of the inlet liner to reduce the upstream propagating fan noise so a single fore array of all 30 microphones was used. While a small aft reference array, consisting of 1 to 5 microphones, would ordinarily be used in addition to a large fore array, this was unintentionally omitted during this study. The reference array can be used to verify that the acoustic source remains unchanged in the aft, which would be expected in the case of an inlet liner. The microphones were set up at a radius of 20 feet from the ANCF. The microphones have a 3.2° spacing, spanning from the centre line of the ANCF at 0° to just past the inlet at 93.2°. The setup can be observed in Fig. 3.7.

Figure 3.7: ANCF setup at the White Field facility in the University of Notre Dame

The angle of separation between the microphones is the polar angle. As the outdoor test setup uses ground microphones for the data acquisition, the microphones are not in the same plane as the ANCF's central horizontal axis. To address this, the azimuthal angle is used for any calculations relating to the directivity of the noise and the power level calculations [82]. The azimuthal angle can be found using

$$\phi = cos^{-1}\left(\frac{R * cos(\theta)}{\sqrt{R^2 + H^2}}\right) \tag{3.8}$$

in which ϕ is the azimuthal angle, θ is the polar angle, R is the radial distance from the ANCF to the microphone and H is the height of the ANCF centre line from the ground.

The microphones used for the far-field array are PCB Piezotronics 130D20. The microphone is a 1/4" prepolarised, condenser microphone. It has a free-field frequency response characteristic with ± 1 dB frequency response between 100 to 4000 Hz, and ± 2 to 5 dB for 20 to 15,000 Hz. The microphones are mounted in the ground stands shown in Fig. 3.8 with the microphones pointing directly down at the metal ground plate. The ground plate is an acoustically hard surface with a reflection coefficient of ~ 1. As can be seen close-up in Fig. 3.8, there are two waves incident on the microphone; one directly from the acoustic source and one which is reflected off the metal ground plate. The magnitudes of the recorded microphone time signals are divided by two to address this. A sufficiently small distance between the plate and the microphone is used that allows constructive interference and improves the signal quality.

3.3.1 Far Field Array Performance at UND

Prior to its transfer to WF, the ANCF was housed in the Aero-Acoustic Propulsion Laboratory (AAPL) which also served as the primary test location for the rig. AAPL is a hemispherical test facility which is anechoic above 125 Hz. The far-field array used in AAPL was a fixed array with pole-mounted microphones at the same height as the horizontal centre-line plane of the ANCF. Anechoic wedges were placed on the floor between the ANCF and the microphone array to minimise reflections.

As described above, the far-field array used at the WF facility is a ground-based array, below the centre-line plane of the ANCF. The polar angles of the array do not correspond to the polar angles of the AAPL far-field array. To address this, the azimuthal angle of the microphones is used instead.

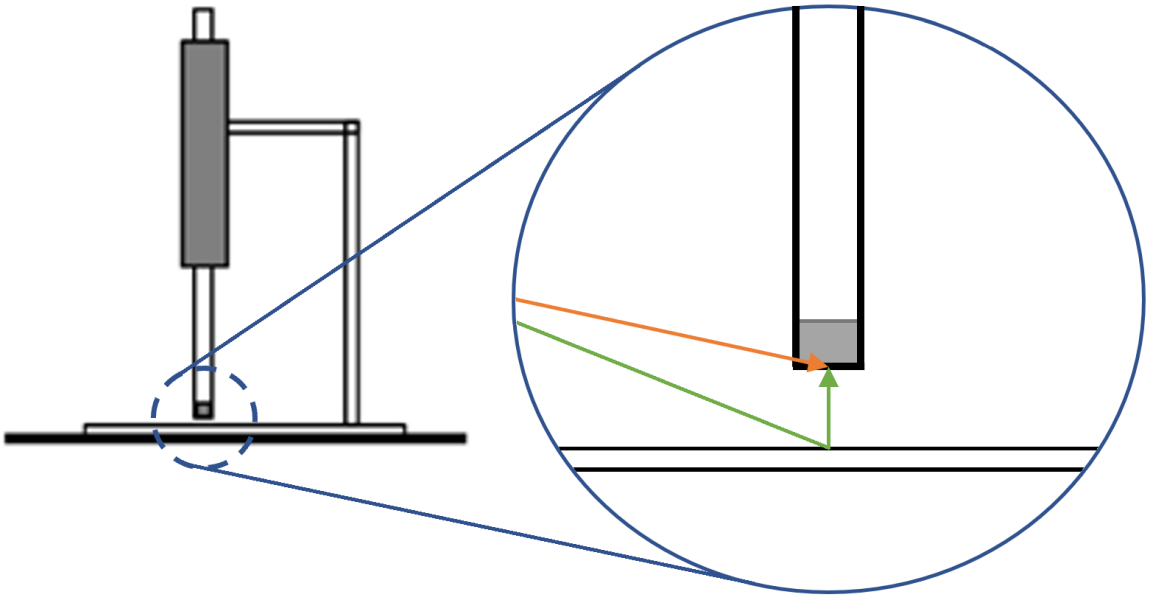

Figure 3.8: Schematic of the microphone in the ground-mic stand and a close-up of the incident wave.

Following the transfer of the ANCF to the WF facility, a comprehensive study of the far-field array was conducted by Figueroa-Ibrahim et al. [82]. In the study, both ground-based and pole-mounted arrays were used. The ground-based array was used at radii of r = 3.66 m (12 ft), 6.10 m (20 ft) and 7.62 m (25 ft). The pole-mounted array was placed at a 3.66 m (12 ft) radius from the ANCF and at a height of 3.05 m (10 ft) in the centre-line plane of the duct.

As a result of the study, Figueroa-Ibrahim et al. [82] concluded that the ground-based microphone array data resembled that of the pole-mounted array, meaning the ground-based array was a viable experimental set-up. The ground-based array was a simpler experimental setup, as the outdoor setup for the ANCF is a temporary setup which needs to be assembled and disassembled for each day of testing. Additionally, the tests yielded similar results to the data from tests conducted at AAPL a decade prior, validating the results obtained at WF facility and indicating the ANCF was still operating well following the transfer to UND.

3.3.2 Harmonic Bands and Acoustic Power Level Calculations

Data acquisition is performed using an HMB GEN2i Data Recorder which records the time series data from the 30-microphone array and the shaft rotation of the ANCF rig. The time histories are processed using ensemble averaging. An example of the time history can be seen in Fig. 3.9a. Shaft revolution-triggered ensemble averaging allows the tonal and broadband

components to be analysed separately by extracting the tones that are generated by the fan. The data is further analysed in terms of the frequency bands centred on the fan tones and harmonics. The 1^{st} harmonic band is defined as the integration about the 1^{st} fan tone, which occurs between 0.5B and 1.5B where B is the number of blades. As can be seen in Fig. 3.9b, the 1^{st} harmonic band is centred on 16 shaft orders and the integration is performed from 8 to 24 shaft orders. Similarly, the remaining harmonic bands are defined as the frequency range $B\,(N \pm 0.5)$, where N is the harmonic band number in question. This approach is used to analyse the overall (original), broadband and tonal data separately. With this approach, the fan harmonic data can be isolated from the overall time history spectra [168].

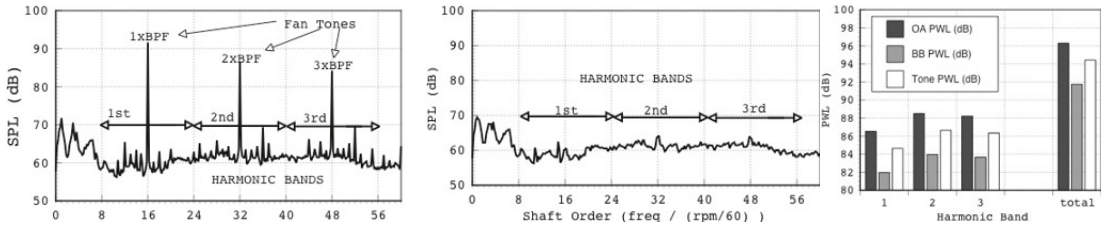

(a) Original spectra sample. (b) Broadband spectra sample. (c) Harmonic bands PWL.

Figure 3.9: Example of the far-field data reduction into broadband and harmonic bands [168].

The data can be converted into the acoustic Power Level (PWL) by squaring the pressure and multiplying by the appropriate area and then normalising by the specific acoustic impedance. The area is determined using the corrected azimuthal angle given in Eq. (3.8). This can be used to obtain the far-field acoustic data in terms of the overall, broadband and tonal power components [168].

Summary

The experimental methods and facilities that are used in the course of this project are outlined above. The GIIT in TCD is used in both normal and grazing incidence, without flow, in the design and initial characterisation of the acoustic liner. In normal incidence, the GIIT is used to measure the absorption coefficient and impedance of the liner as part of the optimisation in Chapter 5. Additionally, the GIIT is capable of transmission loss measurements in grazing acoustic incidence.

Further characterisation of the optimised liner design was conducted in the OD at LAUM, initially without flow and then at a range of Mach numbers and SPLs. The OD was used to

measure the absorption, transmission loss and impedance of the liner in the same direction as the mean flow and against the mean-flow direction.

Finally, the ANCF at UND test facilities are introduced. The ANCF is a TRL 3 test rig which is used for far-field measurements of the insertion loss measurement of the liner. The performance of the optimised liner design in both the OD and the ANCF rigs will be explored in Chapter 7.

Chapter 4

Design Concept and Numerical Simulation

In Chapter 2 approaches to developing noise-reducing technologies for aircraft engines were introduced. Acoustic metamaterials have been identified as an area of significant interest. Additionally, the use of additive manufacturing was identified as a method of removing design limitations that are encountered using traditional manufacturing methods. When the initial design of the liner presented in this work began, the design approach proposed by Tang et al. [23] was identified as having the most potential.

This chapter will further explore the design proposed by Tang et al. [23]. A numerical model of the design is introduced. A numerical study is performed using COMSOL Multiphysics to validate the results previously described by Tang et al. [23]. The validated model is then used to further study and optimise the design for use as a duct liner.

4.1 Design Concept

A number of approaches to developing novel acoustic treatments for aircraft engines were introduced and discussed in Section 2.2.2 and Section 2.3.1. Designs using variable depth liners have been shown to have significant promise at being able to target broadband noise. Other approaches, including those that use high transmission loss elements such as Helmholtz resonators, were also introduced. It was decided that a multi-degree-of-freedom liner would be pursued in this work. The benefits of additive manufacturing in the development of acoustic materials were further discussed in Section 2.4 which could be used to further expand the potential of these novel acoustic liners.

The design proposed by Tang et al. [23] was identified as holding significant potential and merited further investigation. In their initial paper, the concept of a "honeycomb core" structure with two perforated layers was introduced by the authors; the first perforated layer is a faceplate and the second perforated layer is a perforated septum which divides the core structure at various heights. The honeycomb core used has a square cross-section, and thus will be referred to as the core structure in this study. Using this approach, the acoustic reactance of the core structure is no longer determined simply by the depth of the liner as the core now has three different effective cavity depths. Additionally, the duct cells are divided by the perforated septum and can act as a pair of coupled Helmholtz resonators. A schematic of the design proposed by Tang et al. [23] can be seen in Fig. 1.2.

Tang et al. [25] used traditional manufacturing methods to manufacture their material. This required a multi-step process that starts with wire-cutting metal sheets and brazing

them together to form the square structure that would make up the “honeycomb core”. This was subsequently divided into trapezoidal sections by wire cutting. A separate metal sheet was folded in the same pattern as the trapezoidal sections and the two components along with a faceplate were then braised together. Finally, the perforations were added to the faceplate and septum using laser cutting.

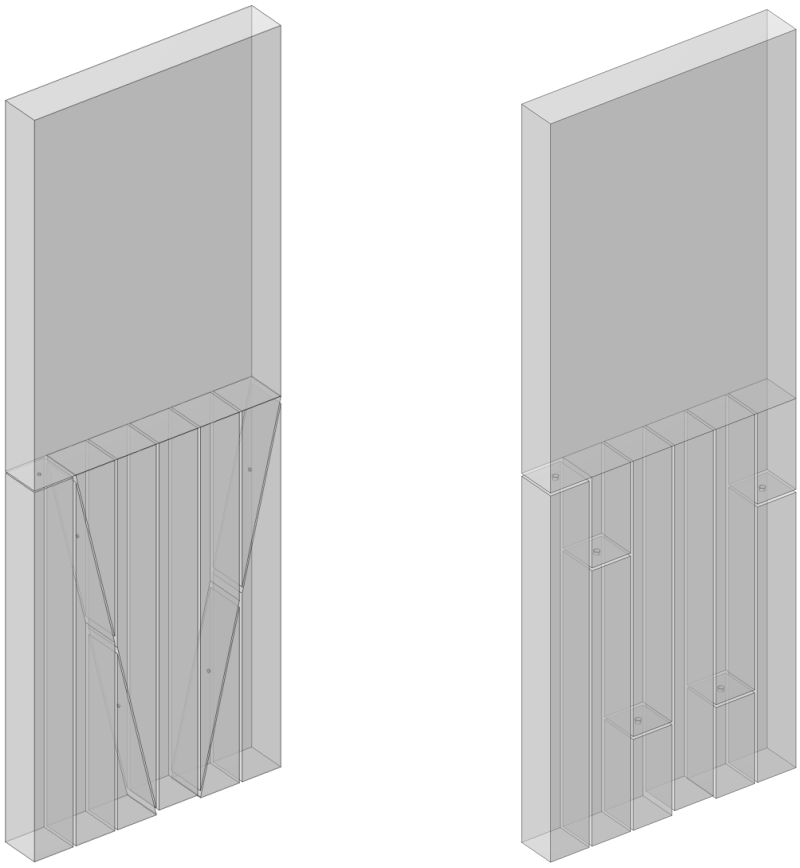

(a) Design featuring a diagonal septum. (b) Design featuring a horizontal septum.

Figure 4.1: Design concept for the AMM options investigated.

In this work, it is proposed to build upon this design premise, tailoring the technology to be used as an acoustic liner in the Advanced Noise Control Fan (ANCF) currently housed and operated by the Turbomachinery Research Group at the University of Notre Dame. It is advanced through acoustic optimisation and the manufacturing process. Design changes which were made to improve the acoustic performance were made possible by the manufacturing techniques used, which additionally allowed a more complex geometry to be used to utilise the space available in each of the test rigs. As the material being investigated in this work is produced using additive manufacturing, design limitations introduced by traditional

manufacturing methods do not apply. Two methods of incorporating the septum were investigated in this study, with both approaches having a periodic design which repeats every six cells. The first is a diagonal septum as seen in Fig. 4.1a. The second method has a horizontal septum as seen in Fig. 4.1b. In both models, the general structure is the same. The first cell has a perforated septum at the top of the cell, and the fourth cell has a non-perforated septum at the bottom of the cell. While the diagonal and horizontal septa divide the remaining cells differently, the height of the perforation in the septa is the same. In the second and sixth cells, the perforation is at 3/4 the height of the cell; in the third and fifth cells, the perforation is at 1/4 the height of the cell.

The final design of the liner is based on the results of a multi-stage optimisation process outlined in Chapter 5. This optimisation process incorporates both numerical and analytical solutions; with experimental results used as a means of validation and as an input in a semi-analytical solution. The first stage of this optimisation routine is a parametric study, which uses a numerical model of the material to determine the optimal septum geometry to maximise the absorption of the liner backing. This requires a reliable numerical model which is outlined in this chapter.

4.1.1 Analytical Solution

The acoustic impedance of the design described above in Section 4.1 can be analytically determined in a manner similar to the traditional SDOF liner. The liner backing and faceplate can still be modelled as separate components and combined to give the total impedance. In the SDOF model, there is only one cavity component and one faceplate. However, in the proposed liner design, there are multiple cavities and faceplate calculations. Additionally, coupling effects are present in the cells where there are multiple cavity sections. The impedance of the individual cavities is combined using an in-series relationship for the cavity impedances.

The liner design proposed by Tang et al. [169] has a diagonal corrugated septum similar to the model seen in Fig. 4.2a. However, in the analytical model, an equivalent model is used instead which has a horizontal septum instead similar to Fig. 4.2b. The impedance for an in-series connection MPP-cavity layer is given by

$$Z_n = Z_{Mn} + Z_{Cn} \tag{4.1}$$

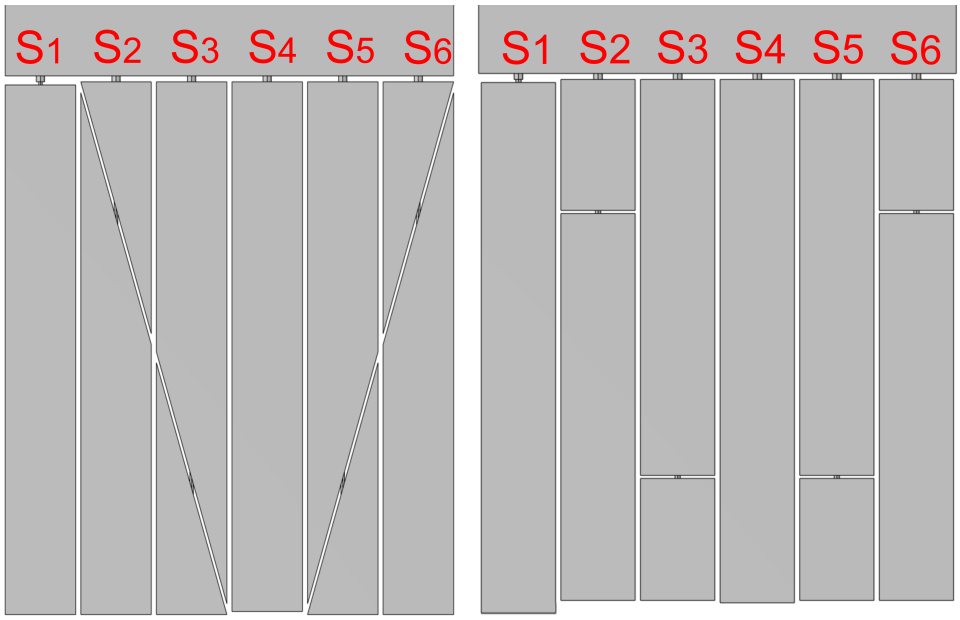

(a) Numerical Geometry (b) Equivalent Analytical Geometry

Figure 4.2: Geometry of the (a) numerical model and (b) the equivalent analytical model of the acoustic liner.

where n=1,2 refers to the layer, Z_{Mn} is the impedance of the MPP of the nth layer and Z_{Cn} is the impedance of the n^{th} cavity. For the bottom cavity, n=2, the impedance is given by

$$Z_{Cn} = -iZ_0 cot\left(kD_n\right) \tag{4.2}$$

where k is the acoustic wavenumber and D is the depth of the cavity. In cells where there are two cavities that have an in-series connection, the impedance of the top cavity, n=1, is given by

$$Z_{Cn} = Z_0 \frac{Z_{n+1} cos\left(kD_n\right) + jZ_0 sin\left(kD_n\right)}{Z_0 cos\left(kD_n\right) + jZ_{n+1} sin\left(kD_n\right)} \tag{4.3}$$

where $Z_0 = \rho_0 c_0$ is the characteristic impedance of air and Z_{n+1} is the total impedance of the bottom cavity and MPP.

The MPP impedance is the impedance of a small circular tube as described by Maa [170]

$$Z_{Mn} = \frac{i\omega\rho_0 t_n}{\phi_n}\left[1 - \frac{2J_1\left(y_n\sqrt{-i}\right)}{\left(y_n\sqrt{-i}\right)J_0(y_n\sqrt{-i})}\right]^{-1} + \frac{\sqrt{2}\eta y_n}{\phi_n d_n} + i\frac{0.85\omega\rho_0 d_n}{\phi_n} \tag{4.4}$$

where t_n, d_n, ϕ_n are the thickness, perforation diameter and porosity of the nth layer, $y_n = d_n\sqrt{\rho_0\omega/4\eta}$ is related to the ratio of the perforation diameter to the viscous boundary

layer thickness, and J_0, J_1 correspond to the 0th and 1st Bessel function of the first kind respectively. Additionally, ω is the angular frequency of sound and η is the dynamic viscosity of air [23].

The total acoustic impedance of the sample is given by

$$Z_T = \delta \left(\sum_{m=1}^{6} \frac{1}{Z_{Sm}} \right)^{-1} \tag{4.5}$$

where Z_{Sm} is the impedance of the cell with m = 1 - 6, relating to the cell number labelled S1 - S6 in Fig. 4.2, and $\delta = b_2^2/b_1^2$ with b_1 and b_2 referring to the internal and external length of the cells.

The absorption coefficient of the sample can be determined by

$$\alpha = 1 - \left| \frac{Z_T - Z_0}{Z_T + Z_0} \right|^2 \tag{4.6}$$

in which Z_0 is the characteristic acoustic impedance of air.

4.2 Numerical Simulation

A FEM numerical analysis of the experimental work conducted using the GIIT was implemented in the frequency domain. The simulations were performed using COMSOL Multiphysics® version 6.0 with the Acoustics module.

4.2.1 FEM Model

Due to the lack of axial symmetry in the material design, it was not possible to use a 2D axisymmetric representation of the model as can be seen in Fig. 4.1. Instead, a full 3D model was required which has higher computational costs but accurately replicates the experimental setup. Preliminary work and investigations in normal incidence were conducted using a single unit cell. The single-unit cell is a one-by-six array of ducts. The simulations to determine the transmission loss of the material in grazing incidence required complete modelling of the entire geometry and GIIT as the transmission loss measured is intrinsic to both the material and test rig.

Meshing

The meshing is performed with a user-controlled mesh. For acoustic meshing within COMSOL it is recommended to have at least 6 to 8 mesh elements per wavelength, so the maximum

element size is set at $1/8^{th}$ of the smallest acoustic wavelength of interest, λ_0. The minimum element size is set at $1/3^{rd}$ of the viscous boundary layer thickness, $d_{visc} = 220\mu m * \sqrt{\frac{100Hz}{f_0}}$. The model is meshed with a combination of swept mesh elements in duct sections, boundary layer meshing in the microperforated holes, and free tetrahedral mesh elements in the duct region directly above the sample. The swept mesh extrudes the surface mesh of a boundary through the domain. If a domain has different, complex geometries at either end of a domain or a non-planar boundary a swept mesh cannot be used.

When a swept mesh is required for a domain with incompatible end boundaries, a domain partition is used to create a transition zone. An example of this can be seen in Fig. 4.3. By partitioning the domain, the larger section can be meshed using a swept mesh first. A free tetrahedral mesh can then be used in the smaller domain which has two different end boundaries.

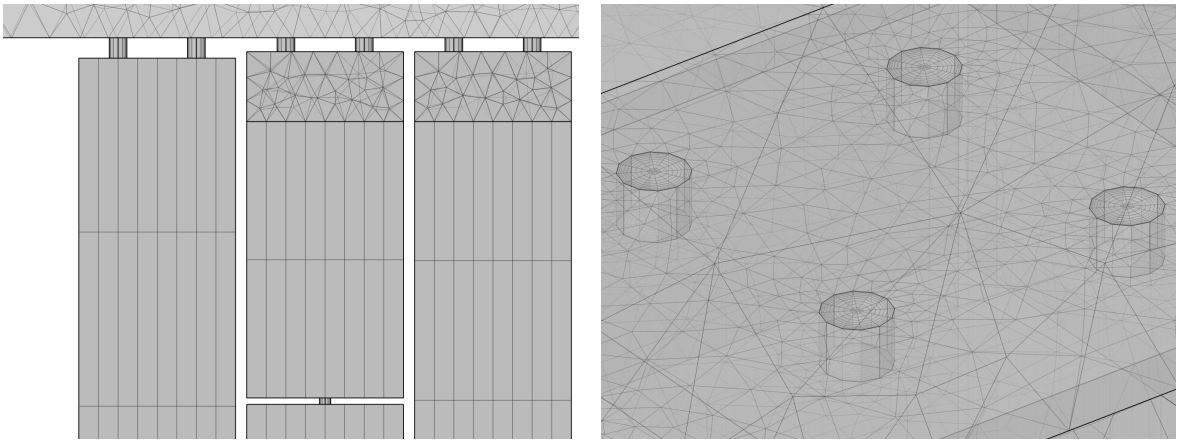

(a) Side-view of grazing incidence mesh (b) Isometric-view of grazing incidence mesh

Figure 4.3: Different mesh element types are used to mesh the different domains of the acoustic sample. In (a) the side view shows the different types of mesh elements that are used in the different geometric features, while (b) shows the boundary layers used to model the thermoviscous losses within the micro-perforation.

In the normal incidence model, at each aperture of the micro-perforated hole a hemisphere is modelled. This is achieved by adding a hemispherical domain at the top and bottom aperture of the perforation as part of the geometry. This hemisphere has a radius equal to twice the radius of the hole. This area is meshed separately from the duct. This allows for a more gradual transition for the boundary layer modelled along the walls in the perforations and captures the effect at the interface between the faceplate and the micro-perforated hole more accurately.

In the grazing incidence model, the micro-perforations are meshed using a swept mesh with boundary layers. The cell ducts are meshed with a combination of a swept mesh and free tetrahedral mesh to act as a transition between boundaries that are incompatible with the swept mesh. This can be seen in Fig. 4.3. The waveguide section directly above the sample is meshed using free tetrahedral meshing. A swept mesh is used in the waveguide regions upstream and downstream of the sample section.

4.2.2 Governing Equations

The numerical simulations were performed using the pressure acoustic module and the thermoviscous acoustics module to simulate boundary layer loss in the small micro-perforated holes. The pressure acoustics physics and thermoviscous physics are coupled using the acoustic-thermoviscous boundary interface.

The pressure acoustics module makes the assumption that the system is lossless and isentropic. These assumptions are valid in a number of applications, including the propagation of the wave in a duct or in large volumes. The governing equation in the pressure acoustics interface is formulated using the inhomogeneous Helmholtz equation:

$$\nabla \cdot \left(-\frac{1}{\rho_c} \left(\nabla p_t - \mathbf{q}_d \right) \right) - \frac{k_{eq}^2 p_t}{\rho_c} = Q_m \tag{4.7}$$

where p_t is the total pressure field and is the sum of the background pressure and the scattered pressure fields; k_{eq} is the wavenumber containing the ordinary wavenumber and the out-of-plane contributions; $\mathbf{q}_d$ is the dipole domain source and Q_m is the monopole domain source.

While the pressure acoustics assumptions that the system is lossless and isentropic hold valid for the impedance tube in which the acoustic wave propagates, the same assumption is not valid in the smaller ducts of the material. This is due to the much smaller volume relative to the surface area of these ducts. The cell ducts are much larger than the boundary layer and to model them entirely using thermoviscous acoustics is computationally expensive. This is particularly of concern during parameterisation studies, where many iterations of the model must be computed. Instead, the Narrow Region Acoustics feature in the Pressure Acoustics Module is used in these regions. The Narrow Region Acoustics adds the losses that are associated with the boundary layer effects in a homogenised way. These losses are solved analytically and applied to the bulk behaviour of the fluid. To perform this accurately, a number of assumptions are applied. The geometry of the cross-section of the duct must be

defined. Additionally, the acoustic wavelength must be much larger than the cross-section and the boundary layer thickness. These assumptions hold true for this duct which has a cross-section of 5.6 mm x 5.6 mm and a boundary layer thickness of 0.22 mm at 100 Hz. The acoustic wavelength is 3.43 m at 100 Hz and decreases to 0.172 m at 2000 Hz.

In the small regions of the micro-perforations in the faceplate and the duct septum, the pressure acoustics assumptions are not accurate. The thermoviscous physics module is used to model the losses in these regions. Thermoviscous modelling assumes small harmonic oscillations in the steady background properties. To study the behaviour of these small oscillations, the variables of interest are;

$$p = p_0 + p'e^{i\omega t}, \boldsymbol{u} = \boldsymbol{u}_0 + \boldsymbol{u}'e^{i\omega t}, T = T_0 + T'e^{i\omega t} \tag{4.8}$$

in which p is the pressure, $\boldsymbol{u}$ is the velocity, T is the temperature, and ω is the angular frequency. In each instance, the background mean flow of the variable is represented by the subscript 0, and the acoustic variable is represented by the primed variable. Thermoviscous acoustics assumes that the background fluid is quiescent, meaning $\boldsymbol{u}_0 = 0$. The background values of the pressure and the temperature have to be specified, either by definition in the module set-up or as functions of the model.

The governing equations used in the thermoviscous module in the frequency domain are the linearised Navier-Stokes equations:

$$i\omega\rho = -\rho_0 \left(\nabla \cdot \boldsymbol{u}\right) \tag{4.9}$$

$$i\omega\rho_0\boldsymbol{u} = \nabla \cdot \left(-p\boldsymbol{I} + \mu\left(\nabla\boldsymbol{u} + (\nabla\boldsymbol{u})^T\right) + \left(\mu_B - \frac{2}{3}\mu\right)\left(\nabla \cdot \boldsymbol{u}\right)\boldsymbol{I}\right) \tag{4.10}$$

$$i\omega\left(\rho_0 C_p T - T_0\alpha_0 p\right) = -\nabla \cdot \left(-k\nabla T\right) + Q \tag{4.11}$$

$$\rho = \rho_0\left(\beta_T p - \alpha_0 T\right) \tag{4.12}$$

These equations are; Eq. (4.9) the continuity equation, Eq. (4.10) the momentum equation, Eq. (4.11) the energy conservation equation, and Eq. (4.12) equation of state. In each of these equations, the left-hand term is the conserved quantity and the right-hand side corresponds to the quantity that locally changes the corresponding conserved quantity. The

diffusive loss terms present are due to the viscous shear and thermal conductivity of the fluid. The viscous shear losses are caused by velocity gradients and the thermal losses are caused by temperature gradients in the fluid. For the small features typically modelled using thermoviscous acoustics, these losses are significant to the acoustic behaviour of the model [171].

To properly capture the effects of these losses, the boundary layer relating to the viscous and thermal properties of the fluid must be accounted for. The depth of the boundary layers are given by:

$$\delta_{visc} = \sqrt{\frac{2\mu}{\omega\rho_0}}, \delta_{therm} = \sqrt{\frac{2k}{\omega\rho_0 C_p}} \tag{4.13}$$

where μ is the dynamic viscosity of the fluid, k is the thermal conductivity and C_p is the heat capacity at constant pressure. As the boundary layer thickness is inversely proportional to the angular frequency, the thickness of the layer decreases as the frequency increases. At 100 Hz, 20°C and 1 atm, the viscous boundary layer thickness of air is 0.22 mm. The Prandtl number, the ratio of the squared boundary layer thickness $\mathrm{Pr} = \mathrm{d}^2_{visc}/\ \mathrm{d}^2_{therm}$ is 0.7, indicating that the thermal and viscous effects are almost the same for air.

4.2.3 Estimation of the Absorption Coefficient

To calculate the reflection and absorption coefficients in COMSOL, a frequency domain study is applied to the model. The frequency range used in the study was between 200 Hz and 2 kHz to match the frequency range of the GIIT, and a step size of 5 Hz was used for the study. The incident acoustic impedance can be given as:

$$Z_{in} = \frac{\langle p_t \rangle}{\langle -v_z \rangle} \tag{4.14}$$

where $\langle p_t \rangle$ is the averaged total pressure at the radiation plane and $\langle v_z \rangle$ is the averaged velocity in the vertical direction. The total impedance of the system can thus be obtained using the impedance translation theorem [172] using:

$$Z_{trans} = z_0 \left(\frac{Z_{in} - iz_0 tan\left(k_0 x_1\right)}{-iZ_{in} tan\left(k_0 x_1\right)} \right) \tag{4.15}$$

where k_0 is the wavenumber, x_1 is the height of the material, and $z_0 = \rho_0 c_0$ is the specific acoustic impedance of air. From the transfer impedance of the material, it is possible to calculate the reflection coefficient

$$r = \left(\frac{Z_{trans} - z_0}{Z_{trans} + z_0} \right) \tag{4.16}$$

and with the reflection coefficient, it is possible to calculate the absorption coefficient using Eq. (3.3)

4.2.4 Estimation of the Transmission Loss

The transmission coefficient is determined numerically as the ratio of the total pressure measured at the termination to the incident pressure given by

$$\tau = \frac{p_{in}}{p_t} \tag{4.17}$$

where p_{in} is the initial pressure, p_t is the total pressure at the termination and τ is the transmission coefficient. The transmission loss can be determined using Eq. (3.6).

4.3 Physics Study

As discussed in Section 4.2.2 small features in acoustic structures are generally best modelled using thermoviscous acoustics while larger structures can be modelled using pressure acoustics. In small features, the effects of the viscosity and thermal properties of the fluid on the acoustic wave are necessary to properly model the acoustic behaviour of the system. However, as indicated previously, these models can be computationally costly when there is a large area which requires modelling. A physics study was conducted to determine the physics settings required to accurately model the behaviour of the device while also being computationally efficient.

For the single 1 x 6 unit cell shown in Fig. 4.1 this would not be an issue as the total size of the model is still reasonably small. However, the numerical model is used to investigate two parameters of the backing geometry; the septum thickness, t, and the micro-perforated hole diameter, d. The effect these two variables have on the overall performance of the geometry described in Section 4.1 is investigated as a part of an optimisation procedure which is outlined in Chapter 5. For a study that uses a range of values for both variables, it is important that the physics is efficiently modelled. In grazing incidence, the full-scale model is an array of 6 x 8 unit cells, totalling 288 individual cells. It is therefore preferable to assess the capabilities of models which incorporate narrow-region acoustics in order to minimise the computational costs for the larger models.

Two investigations into the effect of the physics selection are examined here. The first is a test of the 1 x 6 unit cell in normal incidence. The absorption coefficient of the array is determined numerically and compared to an analytical solution calculated using the method described in Section 4.1.1. An equivalent study is conducted in grazing incidence using the same test matrix. While the main grazing incidence simulation will be performed for the full-liner model, a simplified array consisting of 2 unit cells in a 1 x 12 cell array is used for this test.

4.3.1 Absorption Coefficient

In this study, the backing geometry used features of the diagonal septum configuration which can be seen in Fig. 4.1a. This is the equivalent model to the analytical model proposed by Tang et al. [23], which included a length correction for the size of the ducts to address the differences between the diagonal and horizontal set-up. In all studies, plane wave radiation in the pressure acoustics module is used to model the incident acoustic wave in the waveguide section above the sample.

The physics setup for each of the studies is summarised in Table 4.1. The primary focus of the study is to determine where in the model Narrow Region Acoustics (NRA) can replace Thermoviscous Acoustics (TV) to reduce the complexity of the model and allow faster computation times without reducing the quality of the simulation. The locations where boundary layer meshing is used are included in the description. Boundary layers are not required when using narrow region acoustics as the thermal and viscous losses are applied analytically instead of modelled numerically which is the case in thermoviscous acoustics. Hemispherical inclusions are additionally included in several of the studies. These inclusions are a thermoviscous domain that is modelled around the aperture of the perforations. An example of this can be seen in Fig. 4.4. The hemispherical domains have a radius equal to the diameter of the perforation. In certain applications, the inclusion of these regions can improve the accuracy of the model, as it helps capture the behaviour of the wave at the corner and can improve the transition from the large domain to the small domain.

There is a high degree of agreement between the different studies, excluding study 1. Study 1 only used narrow region acoustics in the liner structure with no thermoviscous acoustics included. The comparison between study 1 and study 2, seen in Fig. 4.5, shows that when only narrow region acoustics are used, the losses are significantly overestimated in the higher frequencies while also failing to capture the appropriate absorption coefficient at

	Cell Physics	Perf. Physics	Additional inclusions	Boundary Layers	Degrees of Freedom	Computation Time
Study 1	NRA	NRA	-	-	47800	4mins 24s
Study 2	NRA	TV	-	Perforations	101397	26mins 22s
Study 3	NRA	TV	Hemispheres	Perforations	180938	52mins 23s
Study 4	NRA	TV	Hemispheres	All TV regions	461118	6hrs 1min
Study 5	TV	TV	-	Perforations	176721	41mins 26s
Study 6	TV	TV	Hemispheres	All TV regions	589477	6hrs 39min

Table 4.1: Test matrix used to study the effect of the physics selection on the acoustic performance of the model in normal incidence.

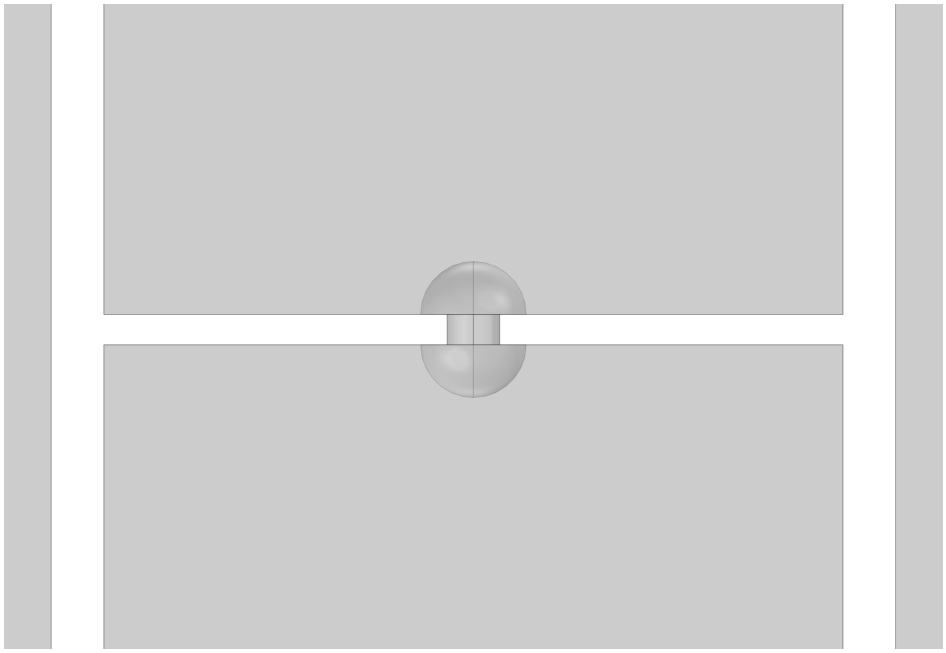

Figure 4.4: Hemispherical domains included to study the behaviour of the acoustics at the aperture of the septum perforations.

the peak frequency. For this reason, the use of narrow region acoustics in the perforations is ruled out.

The absorption coefficient of the studies was compared to the absorption coefficient predicted by Tang et al. [23] and the test with the highest degree of accuracy, study 2, can be seen in Fig. 4.6. It can be seen that the numerical model has a near complete agreement with the analytical absorption coefficient reported previously. The analytical coefficient determined in this work is generally in agreement with the numerical results and the analytical results reported by Tang et al. [23]. There is disagreement in the 400 Hz to 600 Hz range, and at the local peak observed in the 1200 Hz to 1300 Hz range. Due to the high agreement between the

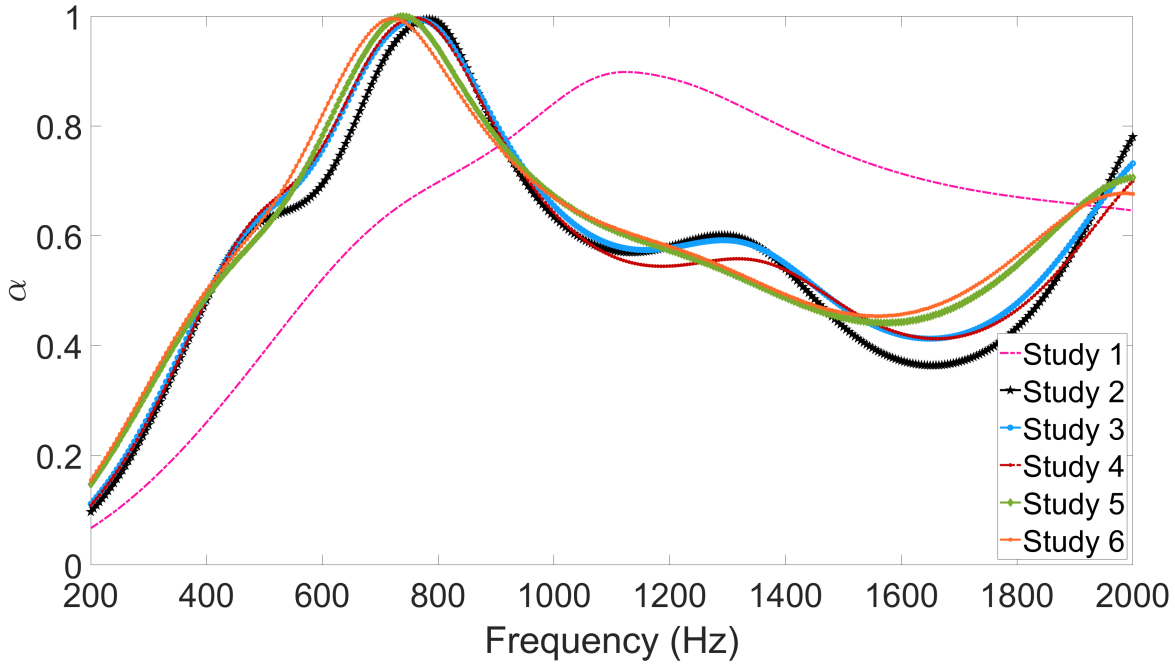

Figure 4.5: Comparison of the absorption coefficient determined using the different physics studies.

numerical study and the analytical prediction performed by Tang et al. [23], it was decided to primarily focus on the numerical predictions when optimising the liner backing.

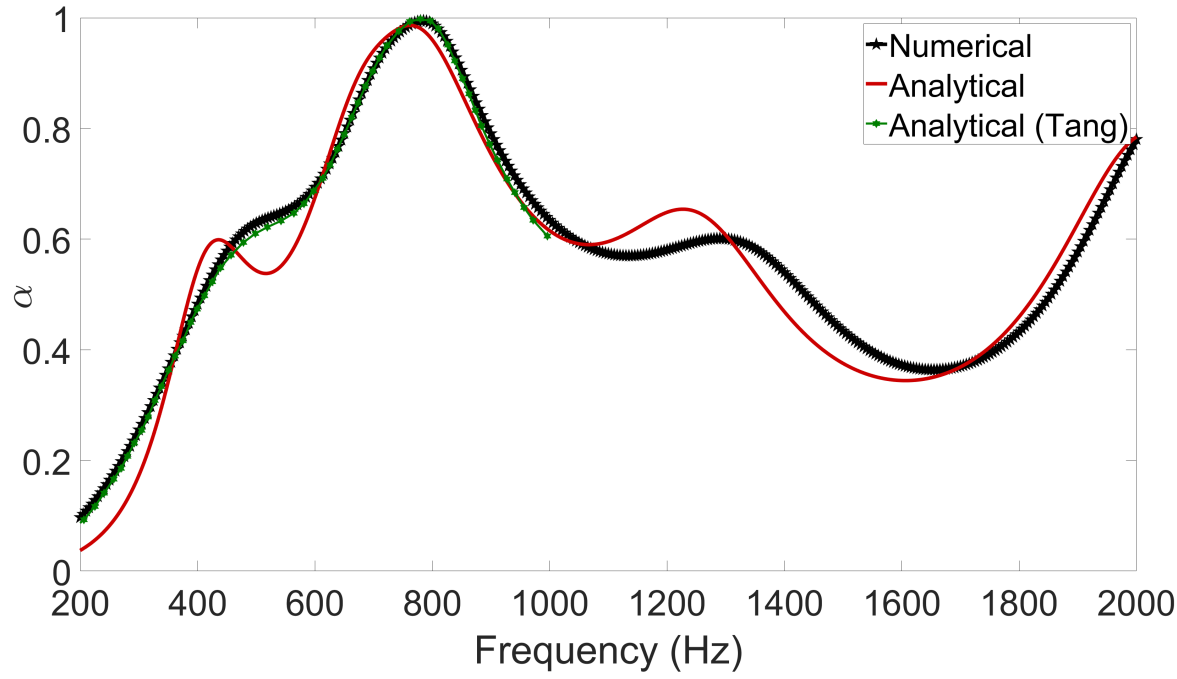

Figure 4.6: Comparison of the absorption coefficient determined by the analytical and numerical approaches outlined in this chapter. The absorption curve obtained analytically using Section 4.1.1 by Tang et al. [23] is also included as a reference.

4.3.2 Transmission Loss

The study was repeated in grazing incidence to examine the impact that the physics selection has on the transmission loss of the model. The same test matrix was used for the normal incidence absorption coefficient test, excluding Study 1 due to the poor performance of the full narrow region acoustics study. The full summary of the transmission loss study can be seen in Table 4.2. The geometry of the model used in this test, which can be seen in Fig. 4.7, consisted of a 1 x 12 cell array. This represents a 2 unit cell configuration. The waveguide is modelled using the pressure acoustics module. The port boundary condition is used to simulate the incident wave.

	Cell Physics	Perf. Physics	Additional inclusions	Boundary Layers	Degrees of Freedom	Computation Time
Study 2	NRA	TV	-	Perforations	129394	16min 14s
Study 3	NRA	TV	Hemispheres	Perforations	169548	24 mins 34 s
Study 4	NRA	TV	Hemispheres	All TV regions	211033	28 mins 50 s
Study 5	TV	TV	-	Perforations	559097	2hr 45 mins
Study 6	TV	TV	Hemispheres	All TV regions	713509	3hr 8 min

Table 4.2: Test matrix used to study the effect of the physics selection on the acoustic performance of the model in grazing incidence.

The results of the five physics tests can be seen in Fig. 4.8. Below 1200 Hz, there is a high level of agreement between the five results. There is a small difference in the magnitude of the transmission loss at 630 Hz, 910 Hz and 1010 Hz. The difference is within 1.6 dB at each of these frequencies. However, above 1200 Hz there is less agreement between the different studies. As can be seen, in both study 5 and study 6 where the duct is modelled using thermoviscous acoustics instead of narrow region acoustics, there is a sharp peak in the transmission loss. This occurs at 1330 Hz in study 5 and 1560 Hz in study 6. A minor increase in the transmission loss is also observed at approximately 1560 Hz for studies 2 - 4, however, there is an order of magnitude in the difference between the peaks.

When using the thermoviscous module it is important to use sufficiently fine meshes in order to accurately measure the losses due to the fluid-boundary integration. In very small features such as the perforations, the size of the boundary layers is on the same order of magnitude as the feature. However, in the body of the cell duct, the boundary layer is significantly smaller than the feature size. Even using a fine mesh appears to have resulted in an overestimation of the losses in the system due to the thermoviscous losses. In study 6,

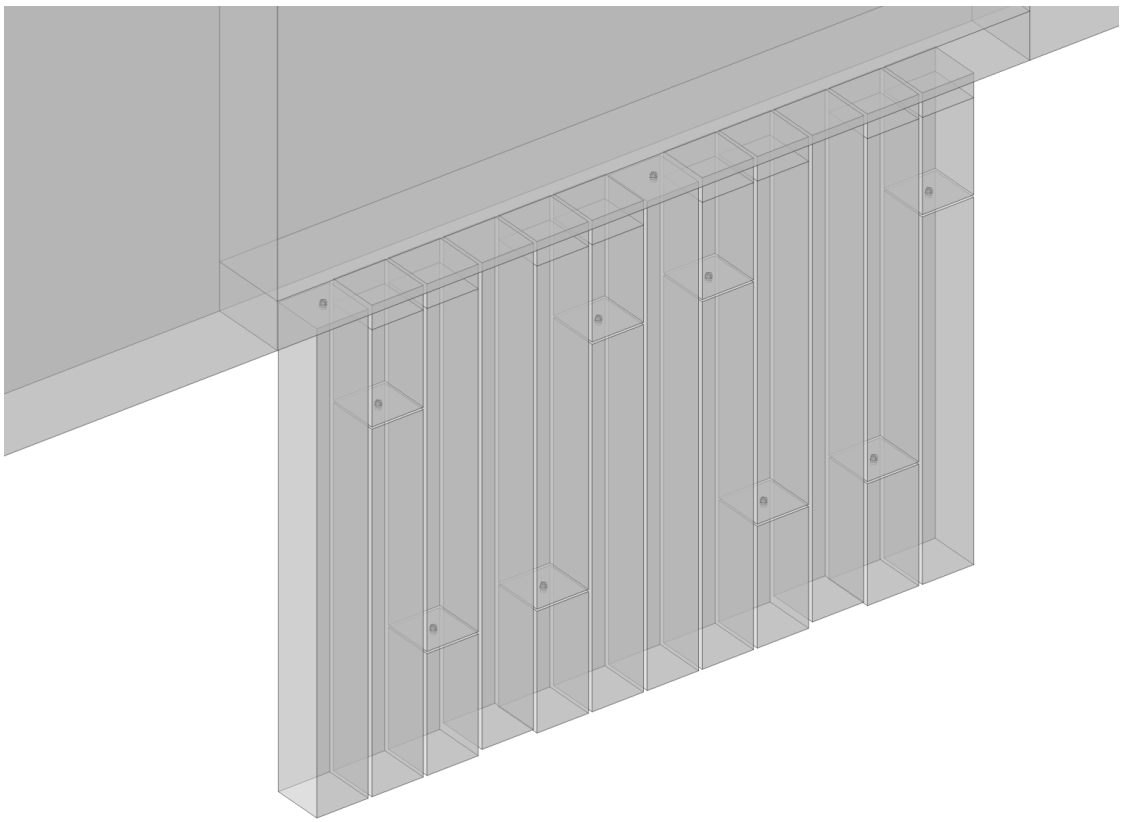

Figure 4.7: Geometry of the 2 unit cell array used for the transmission loss physics study.

where boundary layers were included in all thermoviscous regions, a significant transmission loss peak is observed. Similarly, in study 5 this is seen to a smaller degree at a slightly lower frequency, However, the narrow region acoustics has a much smaller equivalent peak. As the narrow region acoustics module computes the losses analytically and applies the losses to the estimation, as opposed to directly determining the losses in the model, it is not subject to the same issues with the mesh. While a finer mesh may be able to reduce the overestimation of the losses in the higher frequency range, this would come at a significant increase in computational time for the model. Even with a fine mesh on a small model, studies 5 and 6 take approximately 10 times longer to compute.

There is a very high level of agreement between studies 2, 3 and 4. These are the three models using the narrow region acoustics. Due to this high agreement, it was determined that it is possible to simulate the model with the narrow region acoustics in the ducts and thermoviscous acoustics in the perforations with boundary layers in the thermoviscous regions. The inclusion of the hemispheres at the apertures of the perforations is not necessary to obtain accurate results. This significantly reduces the computation costs of performing the grazing

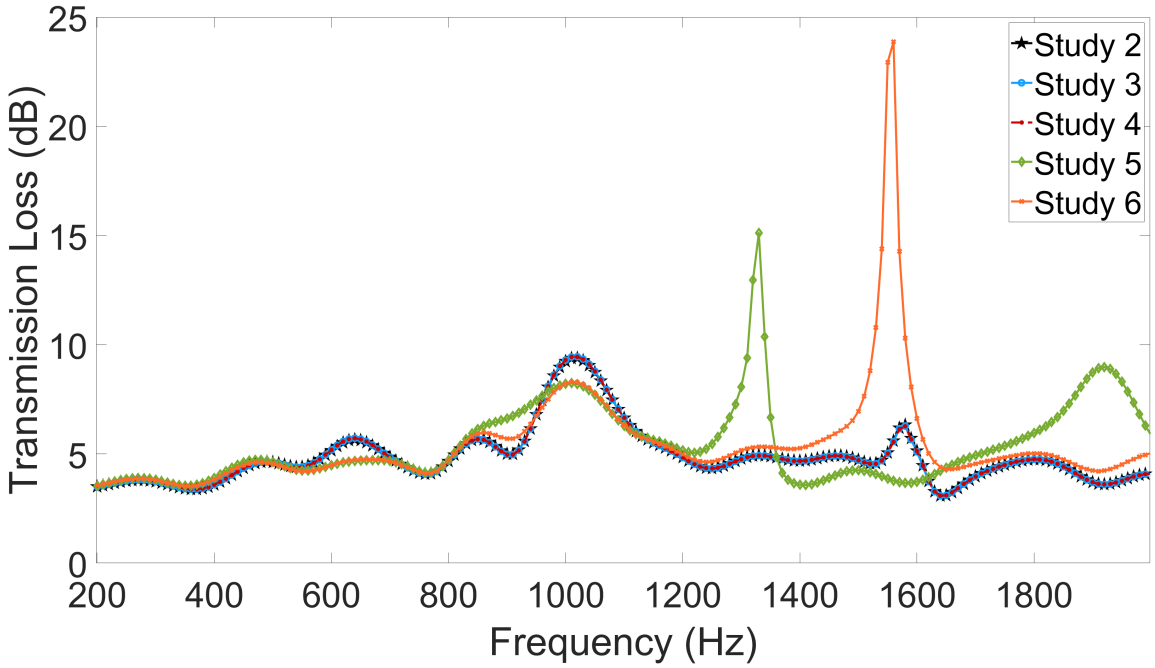

Figure 4.8: Comparison of the transmission loss determined using the different approaches to modelling the physics in the liner geometry as outlined in Table 4.2.

incidence model as in the full test there are over 288 individual cells. The inclusion of these small features on both ends of all perforations in the full model would result in a significant increase in the number of degrees of freedom in the model. It was therefore decided to use the physics approach outlined in study 2 for the numerical simulation of the grazing incidence liner.

Summary

This chapter introduced the design concept that will be used as the basis for the liner in this work. The concept proposed is a multi-degree-of-freedom liner which uses subdivisions within a honeycomb core to increase the frequency range of the liner. The method of numerical simulation used to predict the performance of the liner was introduced. Two investigations were performed to determine the physics selection required to accurately and efficiently model the liner.

The first investigation was performed in normal incidence. Similar behaviour was observed in the majority of studies, except when the liner is modelled entirely using narrow region acoustics. Based on a comparison between the numerical results, analytical results performed in this work and the analytical result reported by Tang et al. [23], it was determined that the

optimal method to model the liner in normal incidence was with narrow region acoustics in the cell ducts and thermoviscous acoustics with boundary layer in the perforations.

In grazing transmission, the same approaches to modelling the physics were investigated. There was a high degree of agreement between the different physics studies below 1200 Hz. Above 1200 Hz, the fully thermoviscous models demonstrated sharp transmission loss. While a finer mesh may be able to more accurately model the thermoviscous losses directly in the higher frequency ranges, the computational cost would be significant. As the studies using narrow region acoustics in the cell duct performed similarly to the fully thermoviscous acoustics models at low frequencies and were seen to be reliable in the normal incidence model, it was decided for transmission loss studies in grazing incidence, the modelling approach in study 2 would be used.

Chapter 5

Optimisation and Development

Two noise reduction technologies were optimised and tested in the course of this study; a standard SDOF liner comprising a microperforated panel over a honeycomb core and a hybrid acoustic metamaterial, the T-Liner. Both technologies were optimised for testing in the grazing incidence impedance tube at TCD, using the multi-stage optimisation procedure shown in Fig. 5.1.

The SDOF liner functions as a baseline comparison in the study which has undergone the same optimisation procedure to ensure a fair comparison. In the case of the SDOF liner, numerical parameterisation is not required as the reactance of the honeycomb structure is dependent on the depth of the liner. The depth of the sample was chosen to be 50 mm as this is a reasonable approximation of a typical liner and is facilitated by the experimental rig. A standard honeycomb core was manufactured, and the impedance and absorption coefficient were experimentally measured. The experimentally measured impedance was used as an input into the semi-analytical optimisation outlined in Section 5.1 in order to determine the optimal characteristics of an accompanying faceplate.

The T-Liner design concept of the acoustic liner design has previously been introduced in Section 4.1. The first stage of the multi-stage optimisation procedure of the T-Liner is a numerical parameterisation study. Based on the physics studies outlined in Section 4.3, the numerical simulation was performed to optimise the core section of the material. The core was manufactured, and the impedance and absorption coefficient were experimentally measured. From here the semi-analytical optimisation routine was used to determine the faceplate geometry as indicated in Fig. 5.1. The same semi-analytical optimisation routine was used for the SDOF and T-Liner configurations. The optimised liner was then produced and tested to validate the predictions. Upon validation, a larger sample is created which has the same unit cell geometry identified in normal incidence. This is done by increasing the size of the array of unit cells to take advantage of the space available in grazing incidence. The design is subsequently modified to fit into the curved test section of the ANCF.

This chapter will first introduce the semi-analytical solution that is used to optimise the faceplate of both liners. Next, the process of optimising both the SDOF liner and the T-Liner will be detailed. For the T-Liner, this will include the adaptation of the design to be used in the ANCF. Finally, the additive manufacturing methods used in this project will be outlined at the end of the chapter.

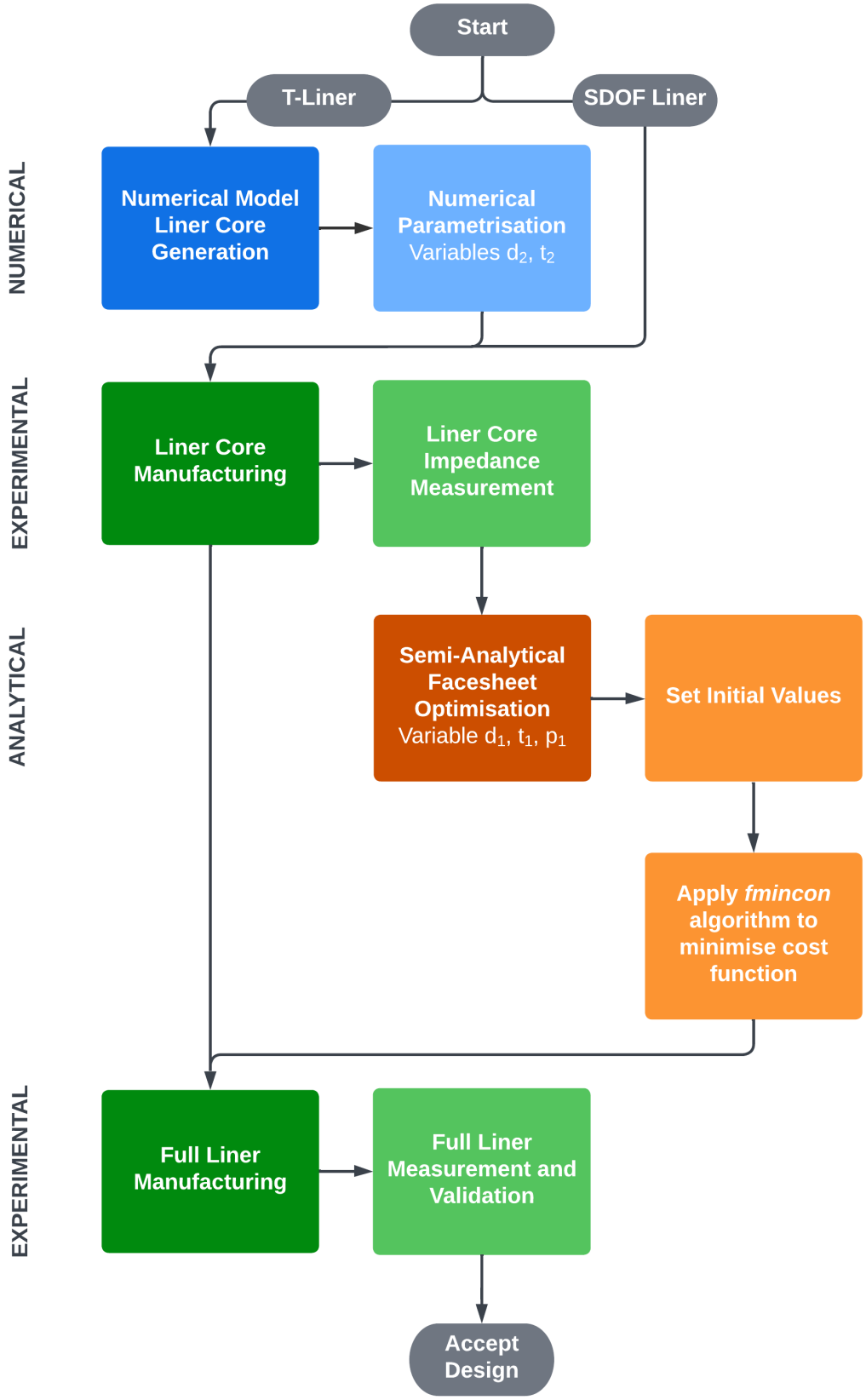

Figure 5.1: Design optimisation process for the liner geometry.

5.1 Semi-Analytical Solution

The perforated panel over honeycomb liner is very commonly used as an acoustic liner. When the perforations are of a sub-millimetre size the faceplate is typically called a micro-perforated panel (MPP). Building on the theory of the propagation of waves in a narrow tube of Rayleigh [173] and Crandall [174], the MPP was proposed by Maa [170, 175, 176]. By reducing the size of the perforations to sub-millimetre diameters, Maa [170] explains that the holes provide sufficient acoustic resistance, while also exhibiting a low acoustic mass reactance, to have a wide band absorber. Combining the MPP with a cavity creates an acoustic absorber which is capable of low-frequency attenuation. The performance at low frequencies is dependent on the depth of the cavity, D, which is a dominant parameter in the reactance of the absorber.

As discussed in Section 4.1.1, the acoustic impedance of the system can be written in terms of the faceplate, in this case, a microperforated panel, and the cavity core.

$$\begin{aligned} Z &= Z_{MPP} + Z_C \\ &= Z_{MPP} - iZ_0 cot\left(\frac{\omega D}{c_0}\right) \end{aligned} \tag{5.1}$$

where Z_{MPP} is the acoustic impedance of the microperforated plate, Z_C is the acoustic impedance of the cavity core, Z_0 is the characteristic acoustic impedance of air ω_0 is the angular frequency and c_0 is the speed of sound in air.

The acoustic impedance of a microperforated plate is given by:

$$Z_{MPP} = -Z_0 \left(\frac{i\omega_0}{c_0 \phi} \frac{J_0\left(\frac{d}{2}\sqrt{\frac{-i\omega_0}{\nu_0}}\right)}{J_2\left(\frac{d}{2}\sqrt{\frac{-i\omega_0}{\nu_0}}\right)} \left[t + 0.85d \cdot \Psi\left(\phi\right)\right] \right) \tag{5.2}$$

where ϕ is the porosity of the microperforated plate, J_0 and J_1 are the 0^{th} and 1^{st} order Bessel functions, ν_0 is the kinematic viscosity of air. The values t and d are the plate thickness and perforation diameter respectively [89]. Finally, $\Psi\left(\Phi\right)$ is the Fok function which is used to determine the hole-to-hole interactions [177] and is given by

$$\Psi\left(\Phi\right) = \sum_{n=0}^{a} a_n \left(\sqrt{\phi}\right)^n \tag{5.3}$$

where the first nine coefficient a_n that are used in this study are given in Table 5.1.

a_0	a_1	a_2	a_3	a_4	a_5	a_6	a_7	a_8
1	-1.4092	0	0.33818	0	0.06793	-0.02287	0.063015	-0.01614

Table 5.1: Fok function coefficients [89].

In the semi-analytical optimisation, an analytical value for the impedance from the core, either from the T-Liner or the SDOF Honeycomb, is not required. Instead, an experimentally measured value of the acoustic impedance of the core can be used as an input in the optimisation. The optimisation routine will then determine the faceplate geometry, i.e. hole diameter, plate thickness and porosity, to maximise the total absorption of the device. This allows an optimised faceplate to be generated for cores that have previously been optimised or do not have accurate analytical solutions. Using this, the specific acoustic impedance of the core and faceplate is

$$z = A\left(Z_{MPP} + Z_{exp}\right) \tag{5.4}$$

where A is the surface area of the device and Z_{exp} is the experimentally measured acoustic impedance. Using the specific acoustic impedance of the device, the absorption coefficient is

$$\alpha = 1 - |R|^2 = 1 - \left|\frac{z - z_0}{z + z_0}\right|^2 \tag{5.5}$$

where R is the reflection coefficient and z_0 is the characteristic specific acoustic impedance of air.

To maximise the absorption coefficient of the device, a cost function is defined to find the average absorption in the frequency range of interest

$$-\overline{\alpha} = -\frac{1}{f_2 - f_1}\int_{f_1}^{f_2} \alpha df \tag{5.6}$$

The optimisation is performed in Matlab using the *fmincon* algorithm which is used. The negative value of the mean absorption is used in the cost function as the algorithm aims to minimise the cost function, but the aim of the optimisation is to maximise the absorption coefficient. It is possible to apply a frequency weighting in the cost function if there is a particular frequency or frequency range that is to be targeted. In this study, frequency weighting was not used as the device was being optimised for general use in the sub 2 kHz range. The limits of f_1 and f_2 were set to 200 Hz and 2150 Hz, the operational range of the GIIT in TCD.

Two acoustic liner designs were optimised in this study using the above method; an SDOF liner and the T-Liner. In the standard SDOF design, it is possible to use the analytical solution for the cavity core given in Eq. (5.1). However, to keep the approach consistent for both liners, the semi-analytical approach using an experimental value for the cavity is used for the SDOF liner and the T-Liner.

Accuracy of Semi-analytical Solution

To verify the semi-analytical approach to optimising the faceplate for a specified experimental impedance, a test case of a standard 50 mm honeycomb core was performed. The honeycomb used had a cell wall thickness of 1 mm and the hexagonal cell had an inscribed cell with a radius of 2.5 mm. The impedance of the honeycomb was experimentally measured and used as an input in the semi-analytical optimisation. A numerical simulation of the honeycomb and the optimised faceplate was additionally performed for comparison.

The equations used for the semi-analytical optimisation were then used to predict the absorption coefficient of the faceplate with a cavity core instead of the honeycomb input. This was achieved by replacing the impedance input with -i$Z_0 cot\left(\frac{\omega D}{c_0}\right)$ in Eq. (5.1). An equivalent numerical simulation was performed, once again using the output from the semi-analytical optimisation.

The results of the two semi-analytical optimisations and the corresponding numerical simulations can be seen in Fig. 5.2. It can be seen that there is a very high agreement between the semi-analytical solution and the honeycomb numerical simulation, and the analytical solution and the cavity numerical simulation. Between the honeycomb models and the cavity models, there is a difference of approximately 150 Hz for the location of the absorption peak, though both approaches have almost complete absorption at these peaks.

Due to the agreement in both of the honeycomb-backed models and both of the cavity-backed models, it is evident that the honeycomb was responsible for the frequency shift. The wall thickness of the honeycomb was relatively large compared to the size of an individual honeycomb cell. This would effectively reduce the volume of the air in the core, which could affect the performance of the device. Additionally, the thickness of the walls would block a number of the perforations in the faceplate, reducing the effective porosity of the faceplate. Despite this frequency shift caused by the geometry of the honeycomb used, it was determined that the approach used in the semi-analytical optimisation routine was an acceptable method for optimising the T-Liner faceplate.

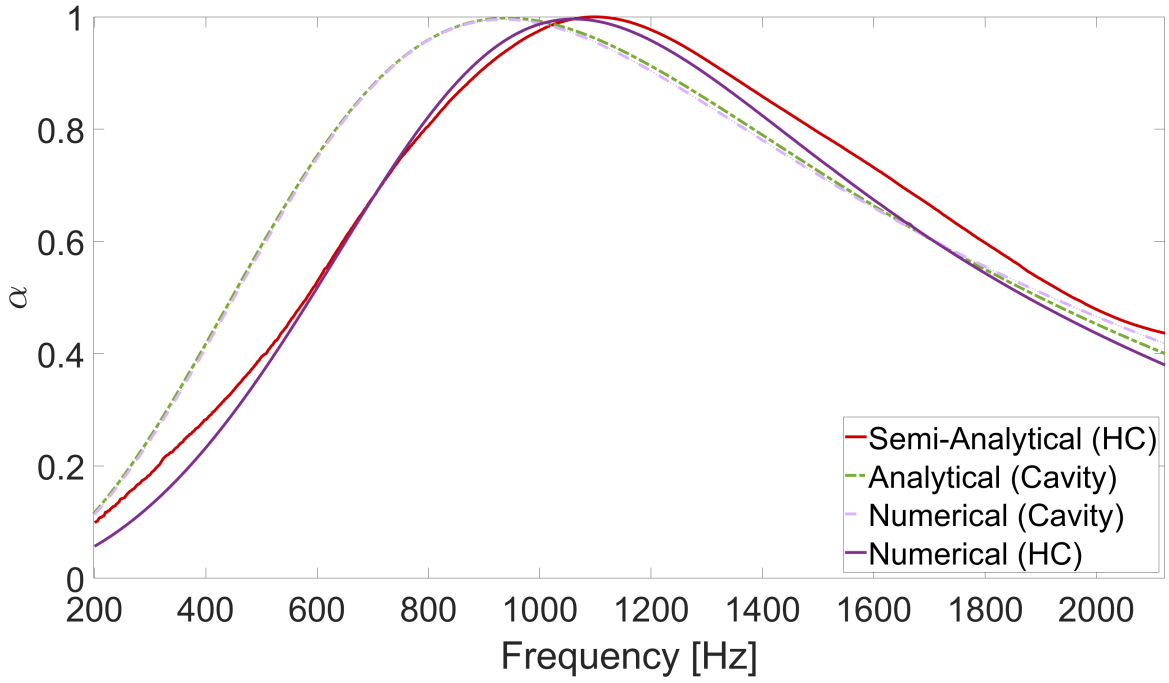

Figure 5.2: Comparison of the absorption coefficient prediction by the semi-analytical solution with a honeycomb core, the analytical solution with a cavity core and numerical simulation for both a honeycomb and cavity core.

5.2 Honeycomb Optimisation

The SDOF liner used in this work has a microperforated plate optimised using the approach described in Section 5.1 and a standard honeycomb core. The honeycomb core has a depth of 50 mm, a width of 50 mm and a length of 80 mm. The sample has a cell wall thickness of 1 mm and the hexagonal cell has an inscribed circle with a radius of 2.5 mm. The honeycomb core was made using a Creality Ender 3 FDM printer.

The Creality Ender 3 had a 0.4 mm nozzle installed. While the thickness of extruded filament would expand as a result of the extrusion process, it would be expected that the thickness of a feature would be a multiple of the nozzle thickness. The expected thickness of a feature that was intended to be 1 mm thick, would be closer to either 0.8 mm or 1.2 mm. Despite this, the measured wall thickness of the printed honeycomb core was 0.96 mm ($\pm 0.01mm$).

To measure the acoustic impedance of the honeycomb, it was tested in normal incidence using the Grazing Incidence Impedance Tube (GIIT). The acoustic impedance was determined using the method described in Section 3.1.1 for a frequency range of 200 Hz to 2100 Hz. The

acoustic impedance of the honeycomb is shown in terms of the real and imaginary components in Fig. 5.3.

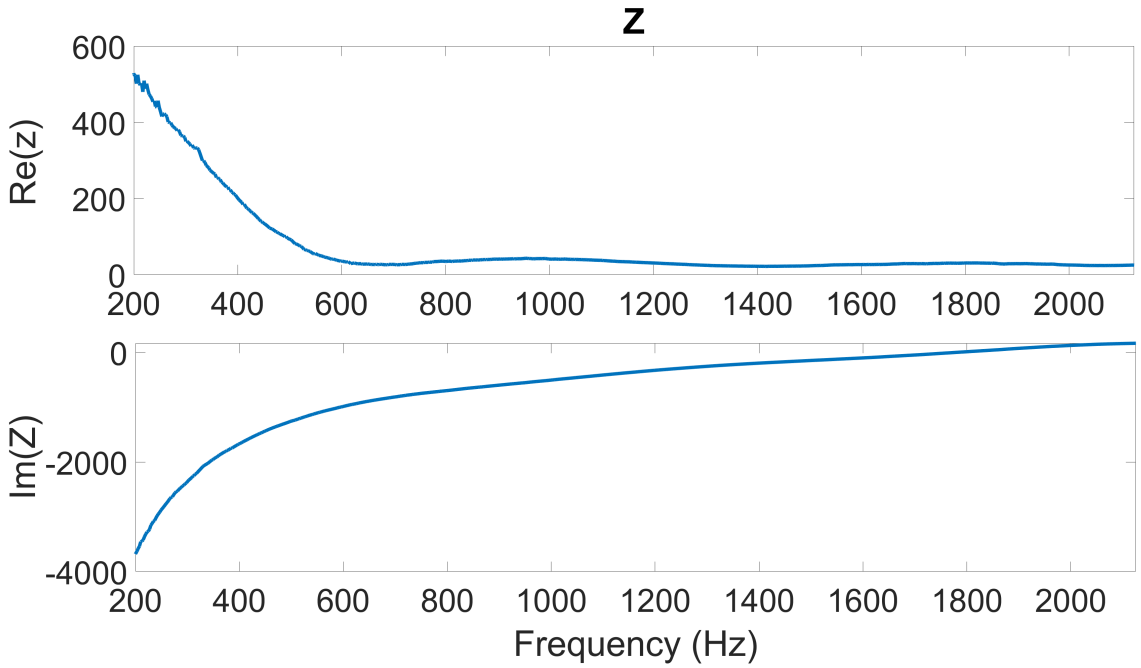

Figure 5.3: Impedance of the honeycomb core used for the SDOF liner.

This value for the acoustic impedance was used as an input in the semi-analytical optimisation to determine the faceplate geometry that would produce the highest mean absorption for the honeycomb core for a frequency range of 200 Hz to 2100 Hz. The faceplate design is a microperforated plate, in which the diameter of the perforations is below 1 mm, resulting in greater thermoviscous losses.

In the optimisation, the plate thickness (T), the perforation diameter (D) and the number of perforations (#P) are variables that are used by the algorithm to maximise the absorption coefficient. In the calculations, the number of perforations is used to determine the porosity of the plate, which is directly used in the calculations. After the optimisation is performed, the porosity is converted back to the number of perforations and is corrected to the nearest whole number. The ranges used by the optimisation routine are given in Table 5.2.

The optimisation routine found that the optimal faceplate for the input impedance had a plate thickness T = 0.899 mm, perforation diameter D = 0.3 mm and a perforation count of 1300. The resulting acoustic liner would have a mean absorption of $\overline{\alpha} = 0.58868$ for the frequency range. Although one of the objectives of this work is to produce an acoustic liner using additive manufacturing, it was initially intended to use traditional manufacturing

	Plate thickness (mm) T	Hole Diameter (mm) D	Number of Perf. #P
Minimum	0.2	0.200	100
Maximum	0.9	1.000	3000

Table 5.2: Upper and lower limits used in the microperforated plate optimisation for the SDOF liner.

methods for faceplate production and use additive manufacturing for the core structure of the liners. It was therefore necessary to limit the potential plates that could be used to produce the faceplate to those that are readily available or "off-the-shelf".

Two such pates that could be used had a thickness of 0.787 mm and 0.9 mm. The subsequent optimisation routine constrained the faceplate thickness to use these two faceplate values. The constrained optimisation routine found that the optimal faceplate for the measured input impedance had a plate thickness T = 0.787 mm, perforation diameter D = 0.5 mm and a perforation count of 357. The resulting acoustic liner, comprising the core and optimised faceplate, would have a mean absorption of $\overline{\alpha} = 0.4432$ for the frequency range. For ease of modelling, it was decided to increase the number of perforations to 364, which had a mean absorption of $\overline{\alpha} = 0.4431$. The comparison between the unconstrained and the constrained results can be seen in Fig. 5.4

Optimisation 1 is the unconstrained absorption coefficient, shown in black; optimisation 2 is the constrained absorption coefficient, shown in red. At frequencies below 900 Hz, the absorption coefficient of both models is similar. However, the constrained configuration peaks at 900 Hz with a maximum absorption coefficient of $\alpha = 0.92$. It reduces across the rest of the frequency range. The unconstrained configuration peaks at 1100 Hz with a $\alpha = 1$. It decreases across the rest of the frequency range. As a result, while both configurations have similar performance at sub-1 kHz frequencies, the unconstrained configuration is a better performer at higher frequencies.

The absorption coefficient of the optimised SDOF liner was experimentally measured as described in Section 3.1.1. The semi-analytical prediction of the absorption coefficient is shown in red and the experimentally measured absorption coefficient is shown in blue. There is good agreement between the predicted and measured absorption coefficients. The experimental results peak slightly lower at 880 Hz, compared to the predicted peak at 950 Hz, however, both peaks have approximately the same value $\alpha = 0.9152$ and $\alpha = 0.9262$

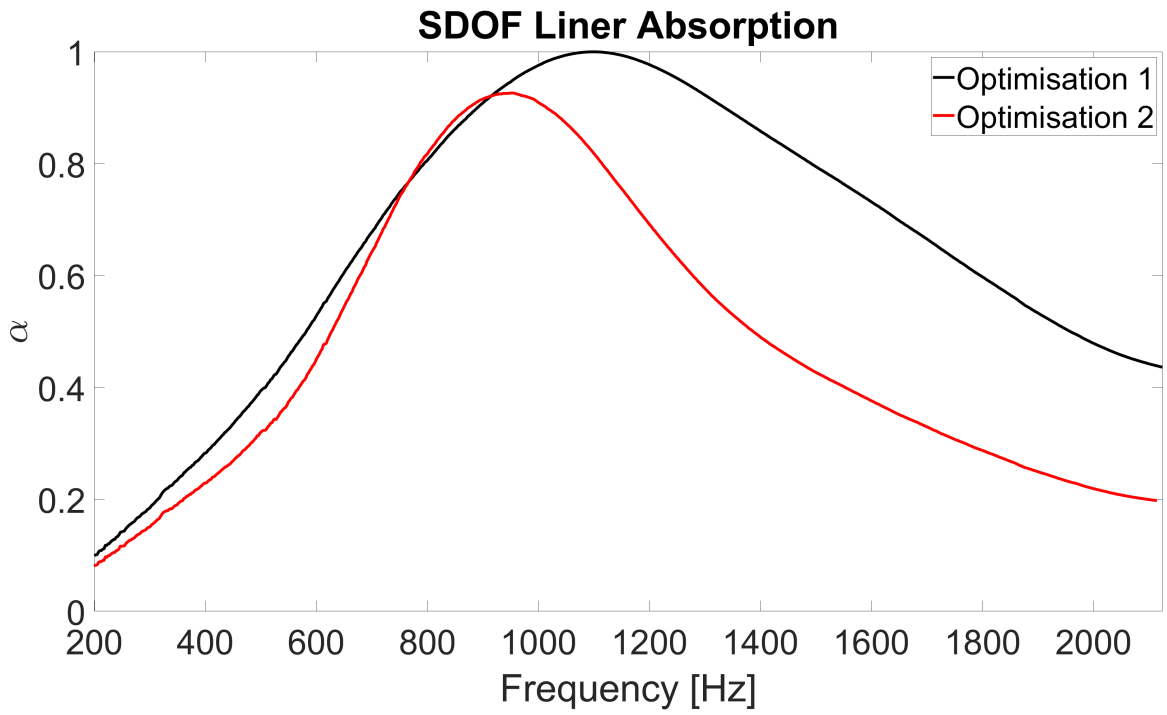

Figure 5.4: Optimised absorption coefficient for the SDOF liner for the unconstrained optimisation (Optimisation 1) and the constrained optimisation (Optimisation 2).

respectively. The spike in the absorption curve of the experimental results in Fig. Fig. 5.5 at 1550Hz is caused by structural vibrations of the micro-perforated plate [178]. The structural vibrations can be identified by the sharper, narrow band absorption peak than is seen in acoustic modes of the geometry. The mean absorption measured experimentally is $\overline{\alpha} = 0.5066$, higher than the predicted value of $\overline{\alpha} = 0.4431$.

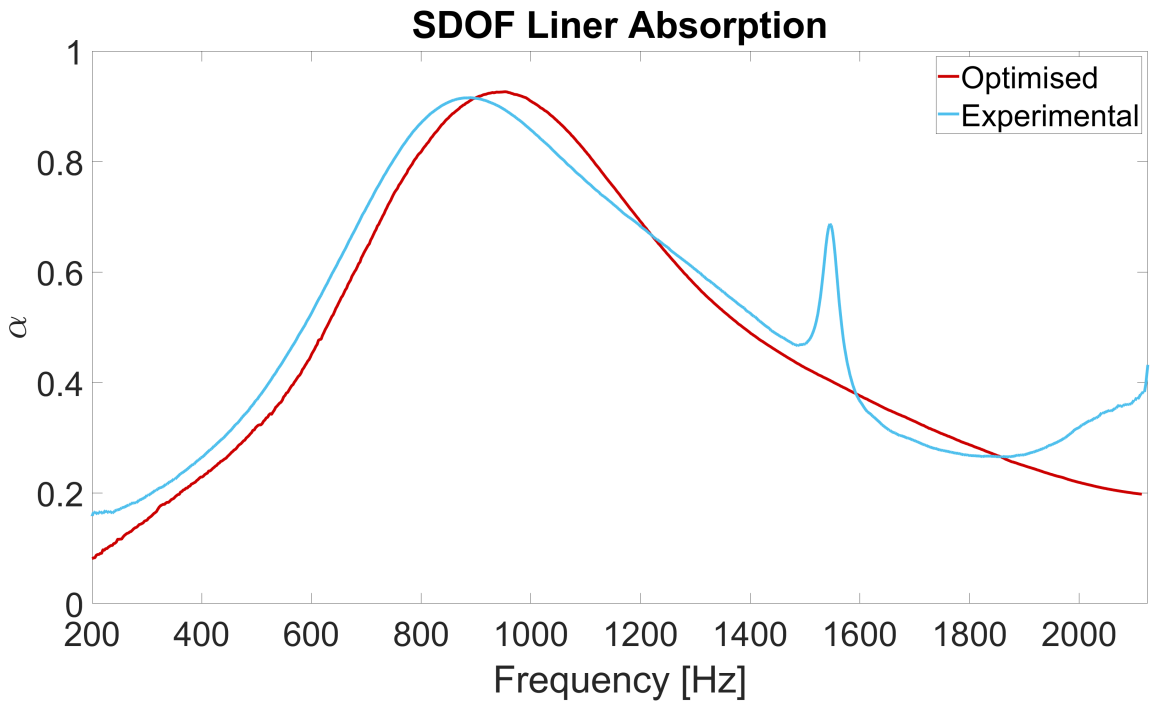

Figure 5.5: Comparison of the predicted and experimentally measured absorption coefficients of the SDOF liner.

5.3 T-Liner Parameterisation and Optimisation

The material studied in this investigation, the T-Liner, is based on the early work of Tang et al. [23] as discussed in Section 4.1. An initial numerical study was conducted in Section 4.3 which examined the most effective way to model the physics of the liner. The numerical simulation in normal incidence was verified against the work previously conducted by Tang et al. [23].

The T-Liner, intended for application as a nacelle acoustic liner, is optimised in this work using the routine outlined in Fig. 5.1. The optimisation is performed in normal incidence. Following the optimisation, the performance of the T-Liner is assessed in grazing incidence before adaptation for the ANCF.

The T-Liner design is an example of an acoustic metamaterial and can also be described as an MDOF liner. Many MDOF liners can also be described as acoustic metamaterials, as the complex geometries created exhibit behaviours not seen in naturally occurring materials as described in Section 2.3.1. The convention to refer to these materials using either term tends to be related to the background of the author, where those with a liners or applications

background refer to the materials as MDOF liners, while those with a more physics-based background would use acoustic metamaterial.

5.3.1 Core Parameterisation

The T-Liner design has a core structure that has multiple features that affect its acoustic impedance, as opposed to the SDOF liner where the core acoustic impedance only depends on the depth of the honeycomb core. In the core of the T-Liner, a septum that divides the individual cells is significant in determining the acoustic impedance of the core. The septum thickness, the diameter of the perforations in the septum and the heights at which it divides the cells all contribute to the frequency response and overall acoustic behaviour. In the course of this study, the same geometry will be used for the septum in each cell although its height will vary. Two configurations for the septum location will be used; a diagonal septum configuration and a horizontal septum configuration. As described in Section 1.1, in the diagonal septum configuration the septum divides cells of the core in pairs. This results in the height of the septum occurring at three-quarters the cell height in the first cell and one-quarter of the height in the second cell. This is mirrored in the final two cells of the structure as can be seen in Fig. 5.6a. In the horizontal configuration, the septum height is set to correspond with the septum perforations height in the diagonal configuration. This can be seen in Fig. 5.6b.

To determine the optimal septum geometry, a numerical simulation of both septum configurations was used in a parametric study. The geometry of both configurations can be seen in Fig. 5.6, and the corresponding values for the geometry can be found in Table 5.3.

Parameter		Value (mm)
Total cell height	h	50
Upper duct height	$h_{1,R2}$	12.35
Lower duct height	$h_{2,R2}$	37.25
Duct internal width	b_1	5.6
Duct total width	b_2	6
Septum perforation diameter	d	-
Septum thickness	t	-

Table 5.3: Initial geometry for parametric study

The same limits and frequency step size were used for both parametric studies. The values for these settings are given in Table 5.4. The lower limit of both the septum thickness and the perforation diameter is based on the print capabilities of the 3D printers that are

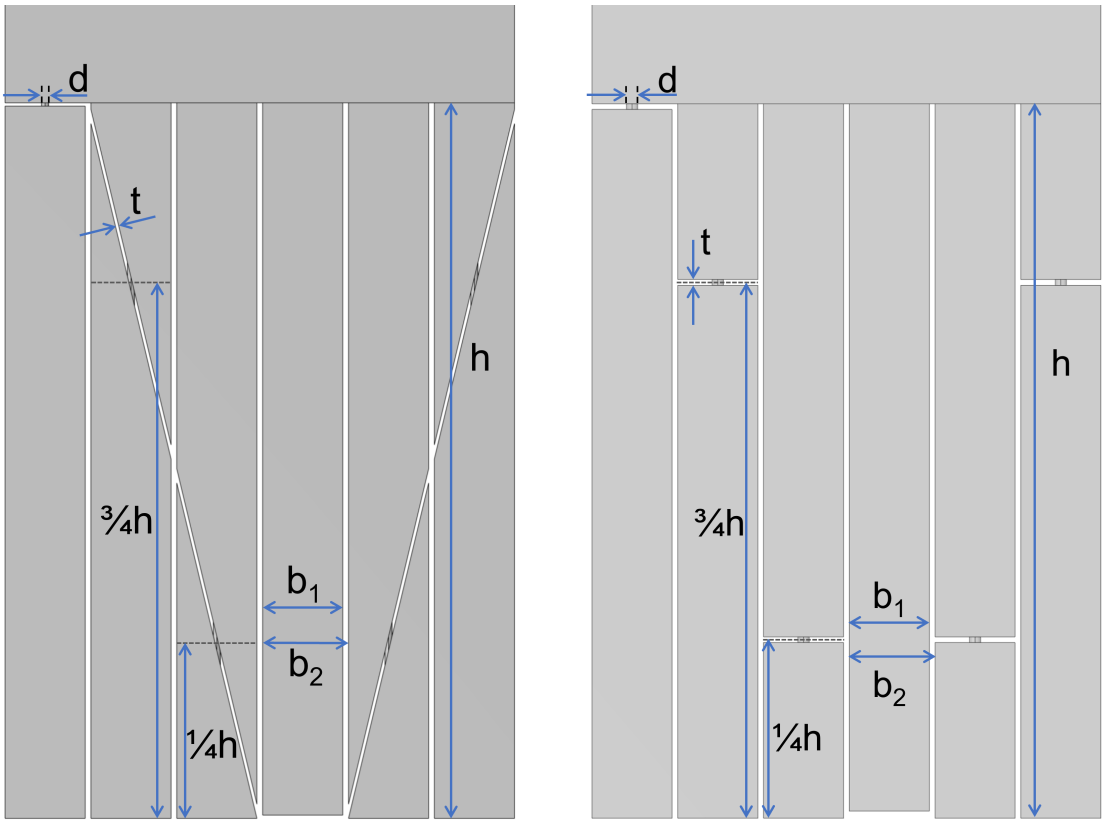

(a) Diagonal Configuration (b) Horizontal Configuration

Figure 5.6: Schematic of the core geometry used in the numerical parametric study.

used in this study. The physics settings used in both studies were based on the results of the preliminary tests described in Section 4.3. From this test, study 2 was identified as the most efficient approach to accurately model the system. The waveguide was modelled using Pressure Acoustics and the cell duct of the core was modelled using Narrow Region Acoustics. Both of these settings are part of the Pressure Acoustics Interface. The perforations were modelled using Thermoviscous Acoustics which is part of the Thermoviscous Acoustics Interface. Boundary layer meshing was used in the perforations to accurately model the losses experienced due to the fluid-boundary interactions. This is summarised in Fig. 5.7.

In total, 153 combinations of septum thickness and perforation diameter were examined in each of the two combinations. The diagonal configuration took 144 hrs and 2 mins to compute. The horizontal configuration took 102 hrs and 44 mins to compute. The mean absorption coefficient of each configuration was calculated, and the highest of each configuration was found and are given in Table 5.5. The mean absorption coefficient of the horizontal

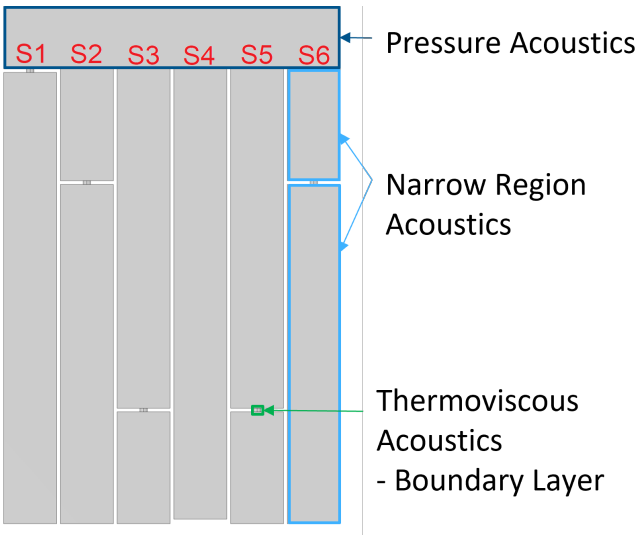

Figure 5.7: Schematic of the core geometry used in the parametric studies with the physics settings used in each region highlighted. This physics setting is Study 2 as presented in Table 4.1.

	Septum Thickness (mm) t	Perforation Diameter (mm) d
Minimum	0.2	0.2
Maximum	0.4	0.8
Step size	0.025	0.025

Table 5.4: The ranges used for the parametric sweep to determine the septum geometry that would have the highest mean absorption.

configuration was almost 25% higher than for the diagonal configuration so it was selected for manufacturing and further optimisation.

	Septum Thickness (mm) t	Perforation Diameter (mm) d	$\overline{\alpha}$
Diagonal	0.4	0.3	0.4072
Horizontal	0.2	0.4	0.5154

Table 5.5: Results of the parametric sweep for both the diagonal and horizontal septum configurations. The configuration with the highest mean absorption is presented for each configuration.

The absorption coefficient of the two configurations can be seen in Fig. 5.8. The two configurations have similar behaviours, however, the horizontal configuration has a consistently higher absorption coefficient with the exception of the first absorption peak observed at approximately 800 Hz. In the diagonal configuration, this peak occurs at 770 Hz and

has a value of $\alpha = 0.9931$. In the horizontal configuration, it occurs at 810 Hz and has a maximum value of $\alpha = 0.9252$. While developing a liner that has a high absorption at sub-2 kHz frequencies is one of the main objectives of this work, the slightly higher performance of the diagonal configuration at this narrow frequency range does not offset the benefits of the better performance by the horizontal configuration across the rest of the frequency range.

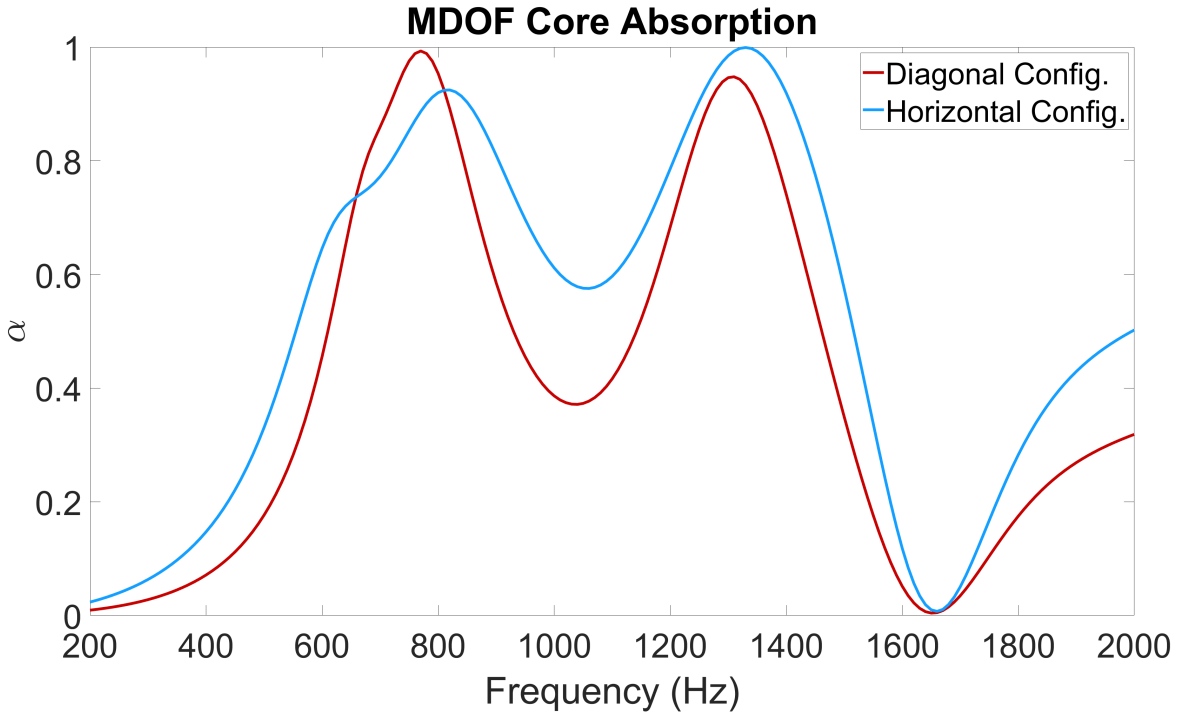

Figure 5.8: Comparison of the highest mean absorption of the diagonal and horizontal configurations.

5.3.2 Liner Faceplate Optimisation

A prototype of the core was produced using the design parameters identified in the parametric study. A Prusa SL1 was used to produce the sample. The acoustic impedance of this MDOF core was experimentally measured using the GIIT. Using the same approach that was used for the SDOF core, the experimentally measured acoustic impedance was used as an input for the cavity core instead of an analytically determined value. The acoustic impedance of the MDOF core is shown in terms of the real and imaginary components in Fig. 5.9.

In the optimisation, the plate thickness (T), the perforation diameter (D) and the number of perforations (#P) are variables that are used by the algorithm to maximise the absorption coefficient. The ranges used by the optimisation routine are given in Table 5.6. These are the same ranges that were used for the optimisation of the SDOF liner.

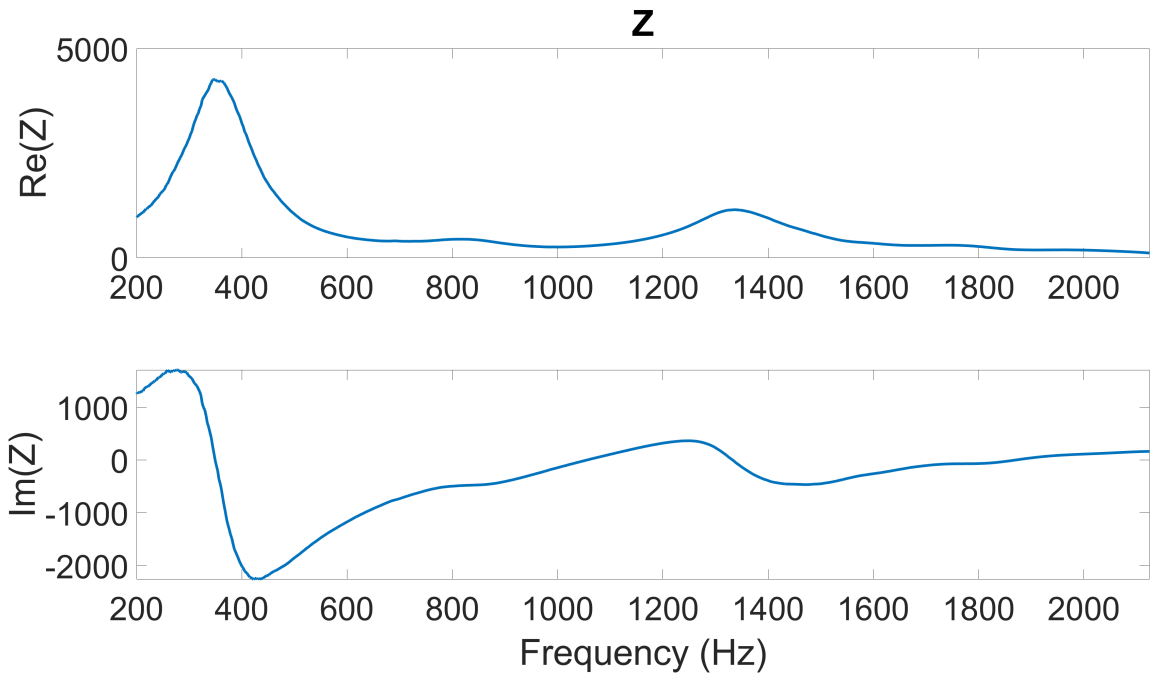

Figure 5.9: Impedance of the MDOF core used for the T-Liner.

	faceplate Thickness (mm) T	Perforation Diameter (mm) D	Number of Perf. #P
Minimum	0.2	0.3	100
Maximum	0.9	1.0	3000

Table 5.6: Upper and lower limits used in the microperforated plate optimisation for the T-Liner.

The optimal configuration identified was a microperforated plate with a thickness T = 0.74392 mm, a perforation diameter D = 0.3 mm and a perforation count of 2500. The resulting acoustic liner would have a mean absorption of $\overline{\alpha} = 0.6922$ for the frequency range. As was seen in the SDOF liner design, a limited number of stock plate thicknesses were available for manufacturing. As the value of the optimal configuration was close to the plate thickness used for the SDOF liner, T = 0787 mm, this was thickness was chosen as a constraint for the optimisation. Additionally, due to the design of the core, a fixed number of holes per duct was used as opposed to a range of values as was seen in Section 5.2. Three values for the number of perforations were used; 104, 416, and 936. These values for the number of perforations correspond to 1 perforation per cell, 4 perforations per cell and 9 perforations per cell respectively. The optimisation was repeated with these limitations.

With these limits applied, the new configuration for the microperforated plate was a thickness T = 0.787 mm, a perforation diameter D = 1.0 mm and a perforation count of 416. This is the perforation count for 4 perforations per cell. The resulting acoustic liner would have a mean absorption of $\overline{\alpha} = 0.6603$ for the frequency range. The comparison between the two designs can be seen in Fig. 5.10.

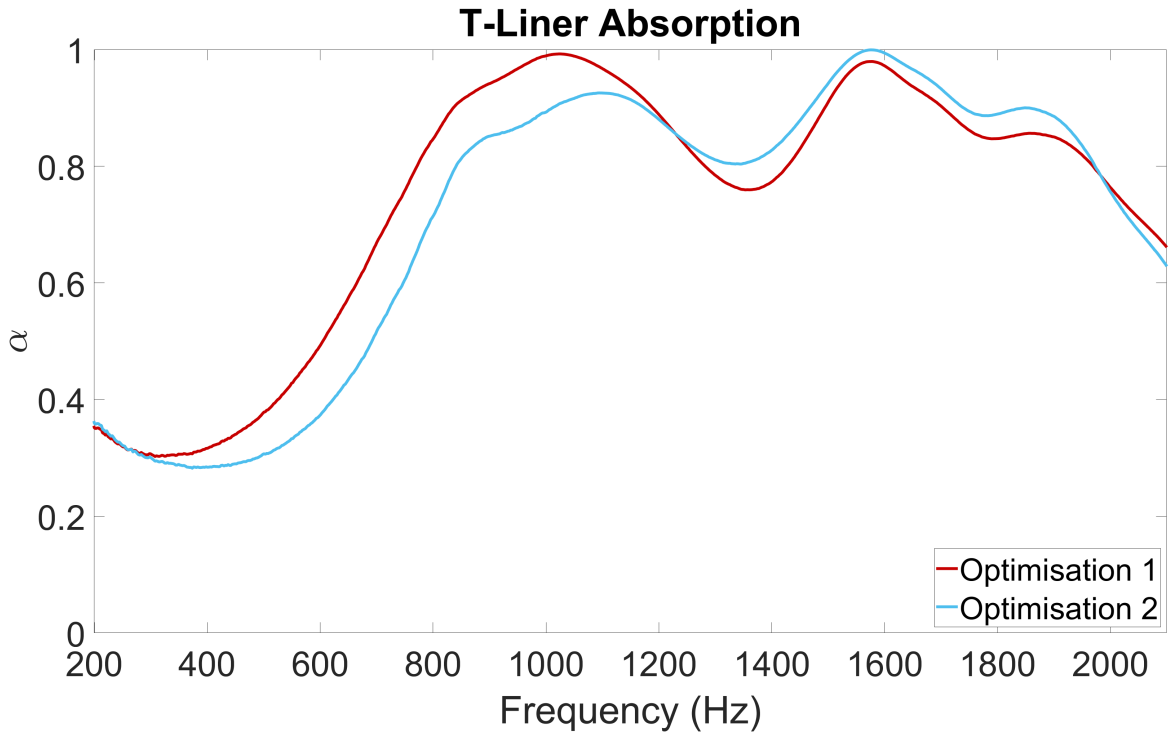

Figure 5.10: Optimised absorption coefficient for the T-Liner for the unconstrained optimisation (Optimisation1) and the constrained optimisation (Optimisation 2)

The unconstrained optimisation configuration (Optimisation 1) is shown in red and the constrained optimisation configuration (Optimisation 2) is shown in blue. Both configurations have similar behaviours across the frequency range. Below 1200 Hz, Optimisation 1 has a higher absorption coefficient with an absorption peak of $\alpha = 0.9925$ at 1020 Hz. The equivalent absorption peak for Optimisation 2 is at 1095 Hz, with an absorption peak of $\alpha = 0.9256$. Above 1200 Hz, Optimisation 2 performs better though the difference in performance is lower than it was in the lower frequency range. The Optimisation 2 configuration has an absorption peak of $\alpha = 0.9995$ at 1575 Hz, while the equivalent absorption peak for Optimisation 1 is $\alpha = 0.9796$ at the same frequency.

The microperforated plate was manufactured to the specification identified by the optimisation and tests in the GIIT. The experimental and predicted absorption coefficient can

be seen in Fig. 5.11. The experimentally measured mean absorption coefficient of the device was $\overline{\alpha} = 0.6603$ which is higher than the predicted value of $\overline{\alpha} = 0.6050$. Both the experimental and predicted results have an absorption coefficient greater than $\alpha = 0.8$ for frequencies above 800 Hz and have two absorption peaks, however, the locations of these peaks differ. Both peaks of the experimental results occur at higher frequencies than predicted by the optimisation. In the optimisation, the predicted absorption peaks were $\alpha = 0.9256$ at 1095 Hz and $\alpha = 0.9995$ at 1575 Hz. The measured absorption peaks were $\alpha = 0.9737$ at 1310 Hz and $\alpha = 0.9477$ at 2000 Hz.

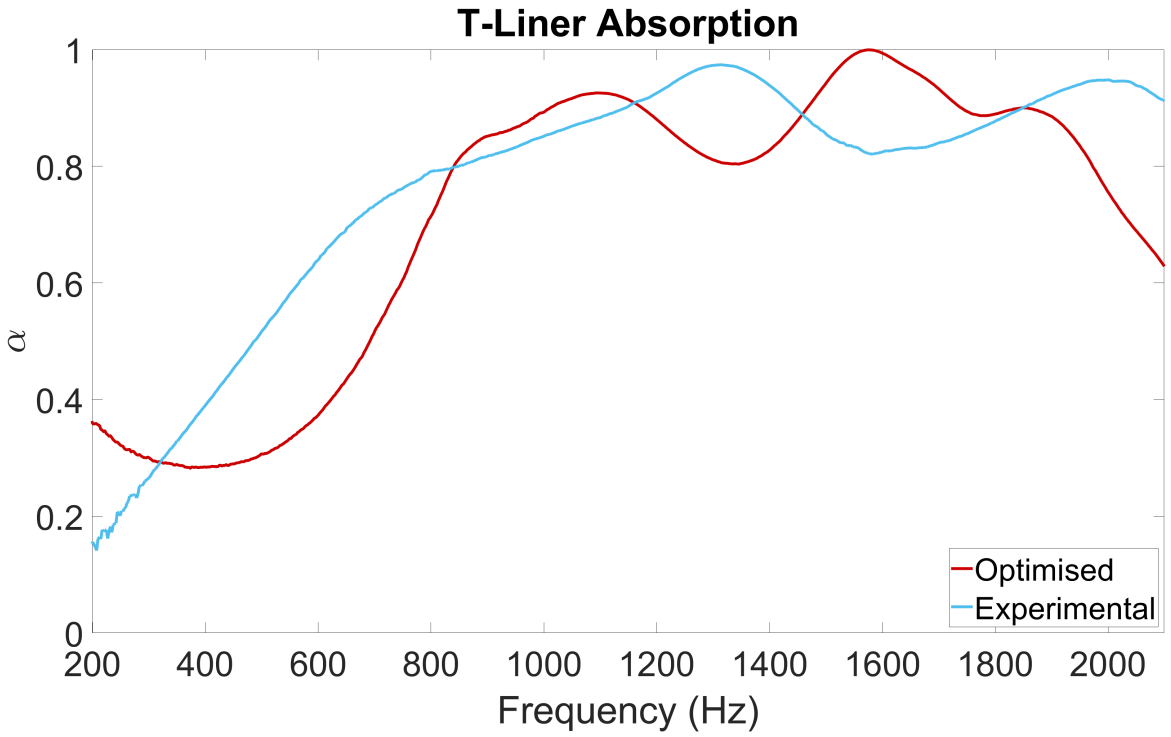

Figure 5.11: Comparison of the predicted and experimentally measured absorption coefficients of the T-Liner.

Integrated Faceplate

Over the course of the study, the quality of the T-Liner that was produced was improved. Small defects in the early prints such as small tears in the septum impacted the results obtained. After the quality of the prints was improved, a new sample of the T-Liner core was produced and the acoustic impedance measurement was repeated. Additionally, at this point, it was determined that the best approach moving forward was to produce the T-Liner samples with an integrated faceplate as opposed to the initial plan of only producing the

core structure with additive manufacturing and using traditional methods to produce the faceplate.

The measurement of the acoustic impedance of the T-Liner core was repeated with a new sample. The result of this acoustic impedance measurement can be seen in Fig. 5.12. This new measurement was again used in the semi-analytical optimisation. As the faceplate was to be printed in addition to the core structure, the original range for the plate thickness seen in Table 5.6 was used. The number of perforations per cell was fixed to only used #P = 104, 416, 936. For this input, the optimal configuration was a plate that had a thickness T = 0.5 mm, a perforation diameter D = 0.63 mm and 416 perforations. This configuration had a mean absorption $\overline{\alpha} = 0.7195$.

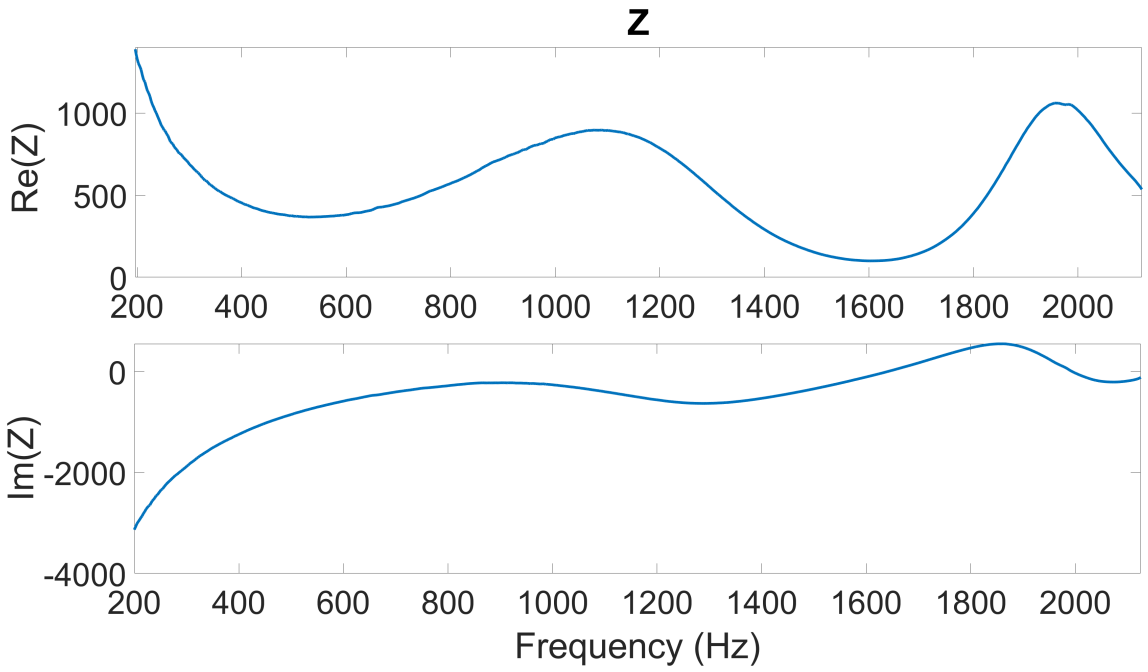

Figure 5.12: Impedance of the higher quality MDOF core used for the integrated T-Liner.

The new version of the T-Liner was produced, this time with the faceplate and core created as one single component. The absorption coefficient was measured and can be seen in Fig. 5.13. The experimental mean absorption coefficient was found to be $\overline{\alpha} = 0.7297$, which is slightly higher than the predicted value of $\overline{\alpha} = 0.7195$. The predicted absorption coefficient is shown in red and the experimental absorption coefficient is shown in blue.

While the mean absorption coefficient is similar for the experimental and predicted results, there is a difference between the performance. The experimental T-Liner has a flatter absorption peak than was predicted in the optimisation routine. Between 930 Hz and 1765

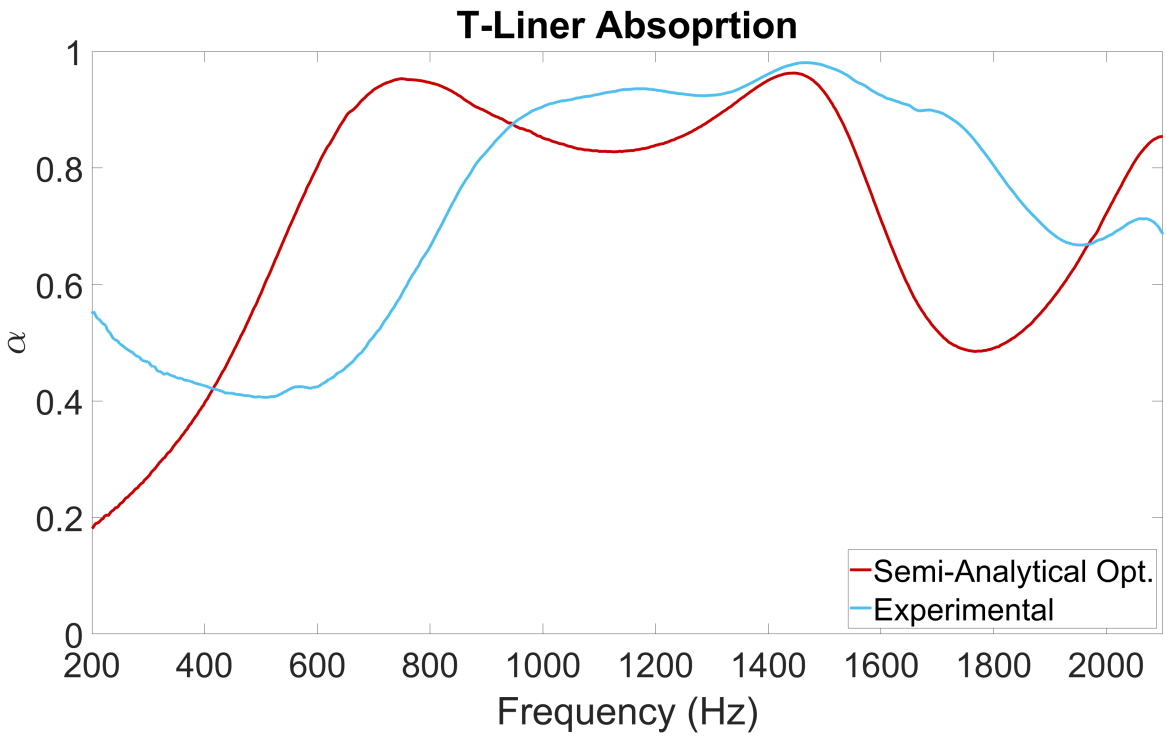

Figure 5.13: Comparison of the predicted and experimentally measured absorption coefficients of the T-Liner with an integrated faceplate.

Hz the absorption coefficient is greater than $\alpha = 0.85$, with a maximum value of $\alpha = 0.98$ at 1460 Hz. Above 690 Hz, the T-Liner consistently has an absorption coefficient greater than $\alpha = 0.5$ and above 780 Hz it remains greater than $\alpha = 0.65$. However, while the experimental result is more constant than the predicted performance, it does not perform as well as expected at lower frequencies. Between 410 Hz and 940 Hz, the T-Liner was predicted to perform better. Despite this, the high level of absorption seen across the frequency range was determined to be worthy of further testing in grazing incidence. The transmission loss of the liner is explored in detail in Section 7.2.

A full description of the geometry used in each test facility is presented in Section 5.4. This description includes a summary of the final design parameters of the unit cell, the number of unit cells in each sample and the external dimensions of the samples.

5.3.3 ANCF Adaptation

The ANCF is a large duct fan that has an internal diameter of 1219.2 mm (4 ft). The liner casing that is used to install test articles on the ANCF inlet has the same curvature as the

body of the duct. The test section within this casing is 228.6 mm in length in the axial direction and has a depth of 57.15 mm. The casing can be seen in Fig. 5.14 in two sections.

The casing is split into two sections allowing it to be installed in an aft configuration where the support structure for the ANCF centre-body would prevent the casing from being installed in a single piece. Additionally, having the casing can aid in the installation of test articles as there is easier access when it is in two components. The carpet padding and foam which can be seen in the liner casing can be used to pad the casing if a test article is not the same depth as the test section.

(a) Cross-section View (b) Isometric View

Figure 5.14: Liner casing that is used to attach test articles to the ANCF for testing.

The impedance tubes that were used to design and perform initial tests on the T-Liner had flat test sections and the test articles which were installed did not feature any curvature. Without modification to the design, the difficulty of installing the T-Liner in the casing would be increased as the design would not allow individual components to sit flush with each other. This could also cause potential issues with samples shifting during installation and testing. Therefore, modification to the design was required. Three methods of modifying the design to accommodate the curvature of the ANCF were considered:

1. Keep the design of the T-Liner the same and add wedge supports to the sides to fill the gaps.

2. Keep the internal design of the T-liner ducts the same and increase the thickness of the duct walls in the radial direction.

3. Adapt the T-Liner to have the same curvature as the casing by increasing the internal volume of the ducts.

The third option was selected for the design modification. While the acoustic performance of the T-Liner would be affected by changing the internal volume of the liner ducts, the change in volume was minor and the optimal use of space was considered worthwhile. The majority of the geometric parameters of the T-Liner were kept unchanged. The only modification was to the width of the internal ducts of the liner and by extension the overall width of the liner, in the spanwise direction. To achieve this, the geometry of the active surface of the liner was fixed with the optimised parameters from Section 5.3.2, and the body of the core structure was increased using an angular extrusion method. This is shown in Fig. 5.15 where the width of the component at the active surface, the top, is 50 mm and the width at the bottom is 50 + 8δ mm. Here, δ is the additional width of each cell due to the angular extrusion. It has an approximate value of $\delta = 0.3125$ mm.

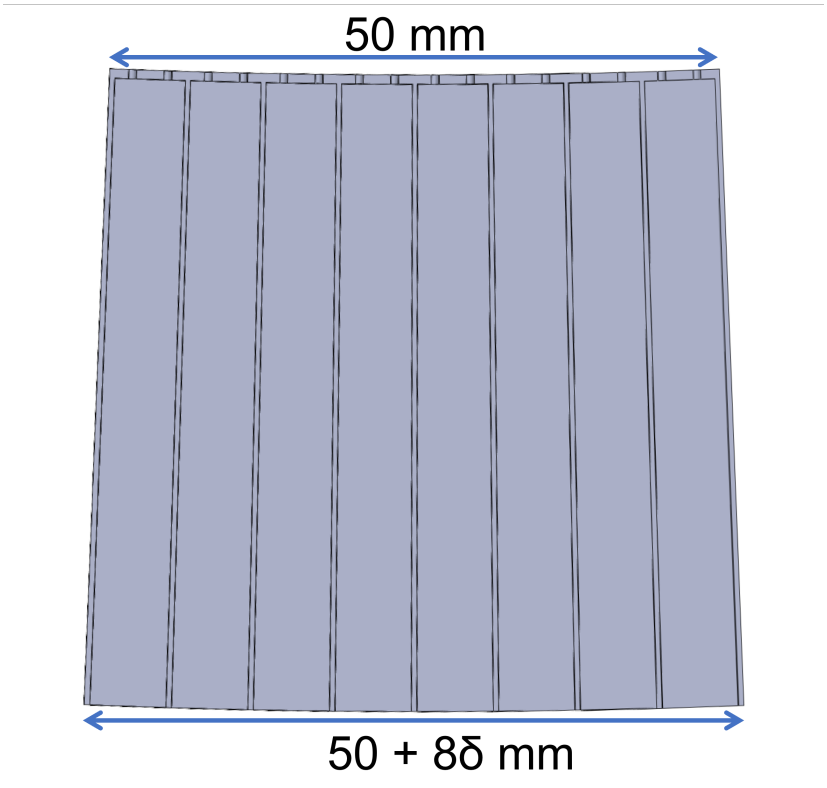

Figure 5.15: End view of the T-Liner design for the ANCF showing the difference in width at the top and bottom of the structure.

The value of δ was not directly determined as part of the adaptation of the design for the ANCF's curvature. Instead, the angular width of the sample was used. The calculations that were used to determine the ideal angular width of a single component can be seen in Appendix B. The ideal angular width, or arc width, of an individual component, was identified as $\beta = \sim 4.56°$. With this angular width, a total of 79 components were required circumferentially to produce the liner.

5.4 Final Design

In total three variations of the T-Liner design were required for testing. These were: a TCD GIIT test article, a LAUM test article and an ANCF test article. All three test articles consist of three components, two identical components labelled A and one component labelled B.

There are two variants of the unit cell used in this investigation. The unit cell of the TCD and LAUM test articles are the same, and the devices only differ in the total length of the device. The unit cell of the ANCF test article is modified in the spanwise direction to account for the curvature of the rig.

The unit cell for all three test articles is the same in the axial direction which is shown in Fig. 5.16. The schematic in Fig. 5.16a is to scale from the CAD model of the T-Liner. Figure 5.16b is not to scale and is intended for illustrative purposes. The value for each of the parameters seen in Fig. 5.16b are given in Table 5.7. The geometry of the cells R2 and R3 are the inverse of each other, meaning the upper cavity of R2 has the same volume as the lower volume of R3, and the lower cavity of R2 has the same volume as the upper volume of R3. Additionally, cells R2 and R6 are the same, as are cells R3 and R5. By adding an additional row of R1, the sample becomes symmetric through the midplane of R4. This is used in the design of the full liners to reduce the number of unique parts required.

A schematic of the faceplate geometry of the T-Liner can be seen in Fig. 5.17, with the corresponding dimensions given in Table 5.8. There are two values used to describe the peroration spacing in the faceplate, the separation within a single cell (intra-cell spacing) and the separation of perforations between neighbouring cells (inter-cell spacing). The external wall thickness of the T-Liner is labelled c in the drawing.

In the spanwise direction, there are two variants of the unit cell. The TCD and LAUM test articles have a rectangular cross-section while the ANCF test article has a circular cross-section.

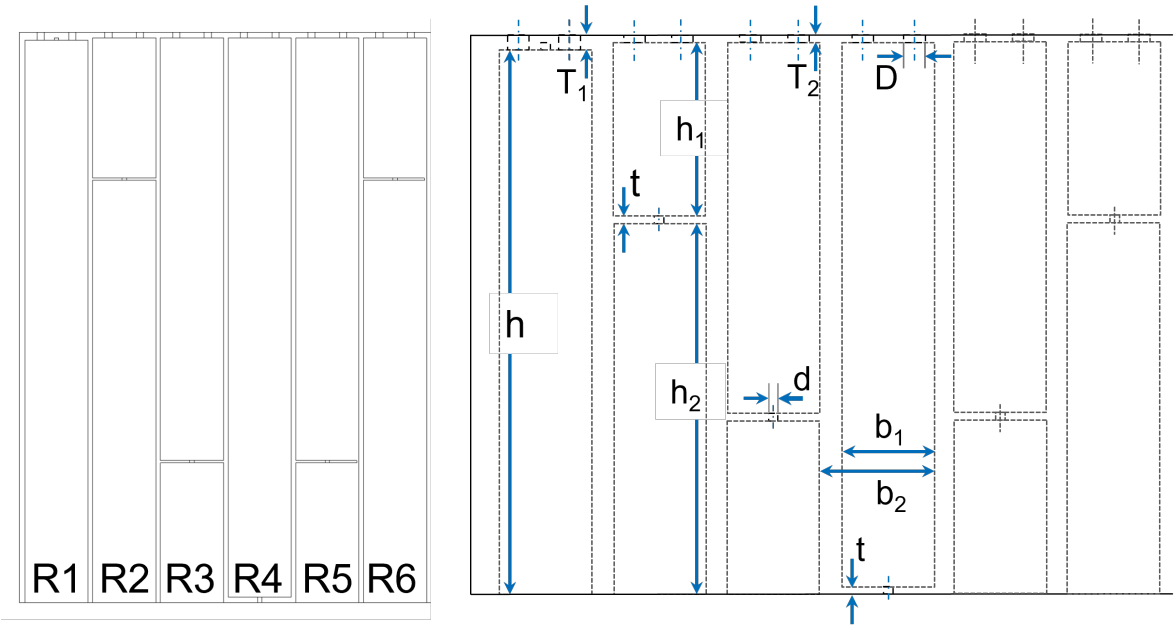

(a) Unit cell row labels

(b) Unit cell geometric parameters

Figure 5.16: Side view of a single unit cell of the final design.

Parameter			Value
Total liner height	(mm)	H	50.5
Total cell height	(mm)	h	50
Upper duct height	(mm)	$h_{1,R2}$	12.35
Lower duct height	(mm)	$h_{2,R2}$	37.25
Upper duct height		$h_{1,R3}$	$h_{2,R2}$
Lower duct height		$h_{2,R3}$	$h_{1,R2}$
Duct internal width	(mm)	b_1	5.6
Duct total width	(mm)	b_2	6
Septum perforation diameter	(mm)	d	0.4
Septum thickness	(mm)	t	0.2
Faceplate thickness	(mm)	T	0.5
Faceplate perforation diameter	(mm)	D	0.63
Faceplate perforation count		#P	416

Table 5.7: Final parameters for the T-Liner unit cell seen in Fig. 5.16.

TCD Configuration

In the TCD test campaign, two configurations were tested; the first configuration is used for normal incidence testing and the second configuration is used for grazing incidence testing. The second configuration is the "full" T-Liner design, with the same length that is necessary for testing in the ANCF rig. The full design is assembled with three components; two Part A

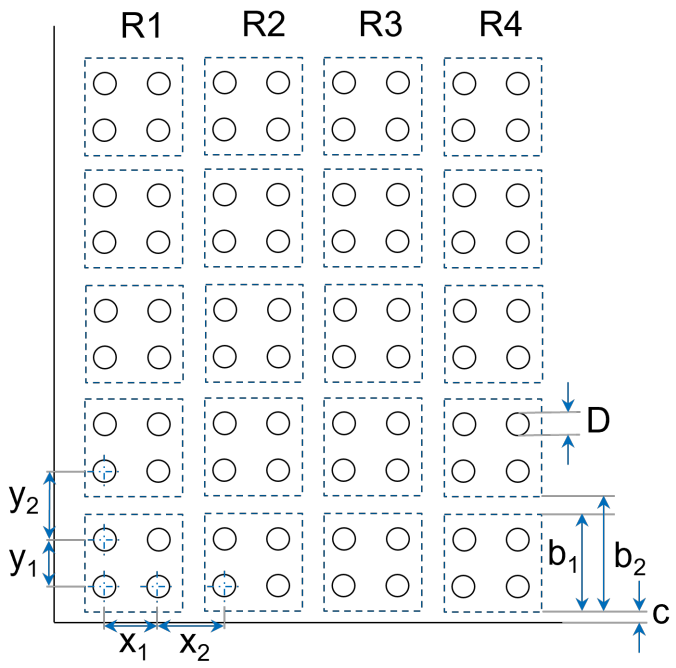

Figure 5.17: Geometry of the T-Liner faceplate.

Parameter			Value
Duct internal width	(mm)	b_1	5.6
Duct total width	(mm)	b_2	6
External wall thickness	(mm)	c	1.2
Faceplate perforation diameter	(mm)	D	0.63
Intra-cell perforation spacing (length)	(mm)	x_1	2.8
Inter-cell perforation spacing (length)	(mm)	x_2	3.2
Intra-cell perforation spacing (width)		y_1	x_1
Inter-cell perforation spacing (width)		y_2	x_2

Table 5.8: Final parameters for the T-Liner faceplate in Fig. 5.17.

components and one Part B component. The normal incidence configuration is a single Part B component.

The full test article has a length of 228.6 mm, a spanwise width of 50 mm and a depth of 50.5 mm. The normal incidence test article has a height of 78.4 mm, a width of 50 mm and a depth of 50.5 mm. The test section for the normal incidence testing has a height of 80 mm, so the holder for the T-Liner sample has a 0.8 mm spacer to centre the sample along the midplane of the rig.

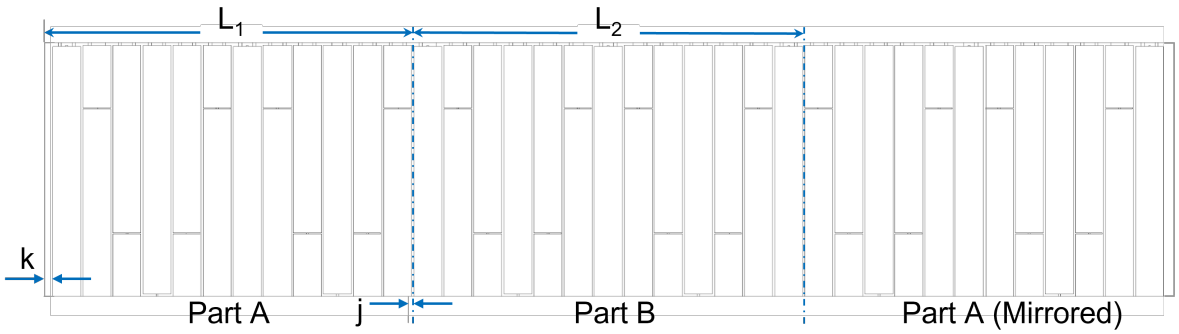

Figure 5.18: Side view of the test article that was tested in TCD.

Part A		Part B	
Parameter	Value	Parameter	Value
Unit Cells	2	Unit Cells	2 + R1
L_1	75.1 mm	L_2	78.4 mm
j	0.4 mm	j	0.4 mm
k	3.1 mm		

Table 5.9: Values of parameters in Fig. 5.18

The full test article can be seen in Fig. 5.18. The length of each of the parts used to assemble the full test article, as well as the number of unit cells required to make the length of the liner are given in Table 5.9.

As was mentioned previously, there are two variants of the T-Liner unit cell which have a different design in the span-wise direction. The TCD and LAUM test articles have the same unit cell which has a rectangular cross-section in the span-wise direction. In this variant of the unit cell, seen in Fig. 5.19, the cells have the same widths b_1 and b_2 in the spanwise direction as in the axial direction. The T-Liner has 8 unit cells across its width. The thickness of the external wall is labelled c and has a value of c = 1.2 mm. The value of c was chosen to give the component a total width of 50 mm which is the width of the test facilities in TCD and LAUM.

In total, the TCD configuration of the full test article consists of 8 x (6 + R1) unit cells.

LAUM Configuration

The test section of the Optical Duct in LAUM has a length of 200 mm, span-wise width of 50 mm and a standard depth of 49.5 mm, which can be increased by several centimetres to accommodate deeper test articles. The depth of the test section had to be increased slightly

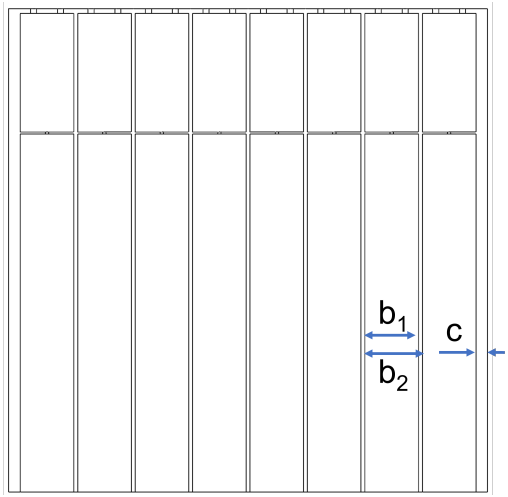

Figure 5.19: End view of the TCD T-Liner design with a section view cut through the second row of the unit cell, R2.

to test the T-Liner as the test article has a depth of 50.5 mm. The same unit cell geometry was used to produce the test articles for LAUM, and the test article was 8 unit cells wide in the spanwise direction. The total length of the test article had to be reduced. It was decided to reduce the length of the test article by one unit cell, which is 36 mm long. This reduced the total length of the T-Liner to 186.4 mm. To increase the length of the test article to 200 mm, a solid 6.8 mm block was added to each end of the sample.

The complete test article was produced in three parts. This can be seen in Fig. 5.20, and the value of the parameters shown in the figure are defined in Table 5.10. The third part is a mirror image of the first part, both labelled Part A in Fig. 5.20. Part A comprises two complete unit cells and the solid block at the outer end of the sample. The inner end of the part is 0.4 mm, the standard wall thickness of a cell. The middle part, labelled Part B, comprises one full unit cell and an additional row of R1 cells seen in Fig. 5.16a. As cells R2 and R6, and R3 and R5 are geometrically the same this allows the cell pattern to repeat across the block when Part A is mirrored at the end of Part B. The wall thickness at both ends of Part B are 0.4 mm thick, which means the gap between cells at the interface between Part A and Part B is 0.8 mm thick.

The LAUM test article has the same spanwise unit cell as the TCD configuration, seen in Fig. 5.19. The rectangular cross-section is 8 unit cells wide and the external walls are 1.2 mm thick.

In total, the LAUM configuration of the full test article consists of 8 x (5 + R1) unit cells.

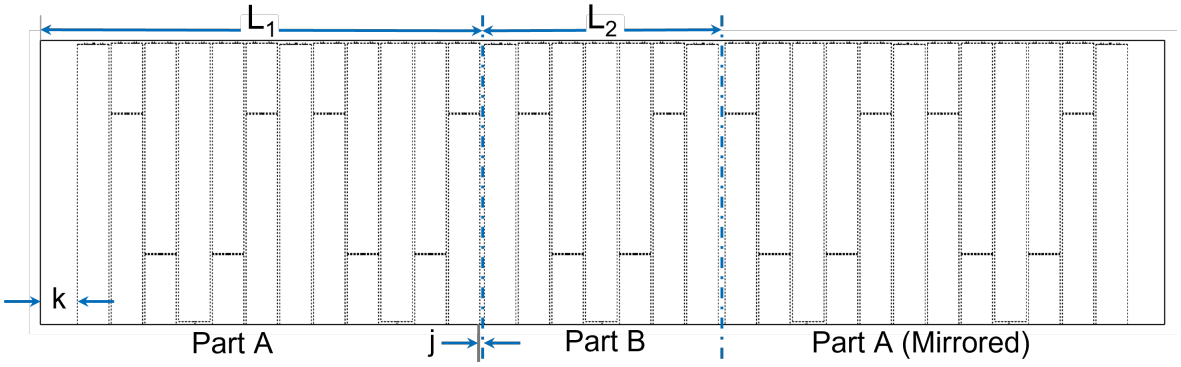

Figure 5.20: Side view of the test article that was tested in LAUM.

Part A		Part B	
Parameter	Value	Parameter	Value
Unit Cells	2	Unit Cells	1 + R1
L_1	78.7 mm	L_2	42.6 mm
j	0.4 mm	j	0.4 mm
k	6.8 mm		

Table 5.10: Values of parameters

ANCF Configuration

The geometry of the ANCF variant in the axial direction is the same as the TCD variant in the axial direction. The side view schematic and corresponding parameters can be found in Fig. 5.18 and Table 5.9. An isometric view of the curved T-Liner design can be seen in Fig. 5.21 which has an axial section view.

As was discussed in Section 5.3.3, the component design for the ANCF has a curved cross-section in the spanwise direction to match the curvature of the rig. This can be seen in the end-view in Fig. 5.22, which has a section view through the second row of the unit cell. The width of the component is an angular width $\beta = 4.56°$. At the top surface of the faceplate, the component has an absolute width of 50 mm, and at the bottom of the core, it has an absolute width of 52.5 mm. When designing the component, only the cavity volume was created using the angular extrusion. The wall thickness was kept at the same value as in the rectangular component, (b_2 - b_1) = 0.4 mm.

The ANCF T-Liner design has an external wall thickness of c = 0.415 mm. This is only slightly thicker than the internal wall thickness. The value was chosen to minimise the spacing between components when installed in the ANCF. 79 parts are needed to fill the

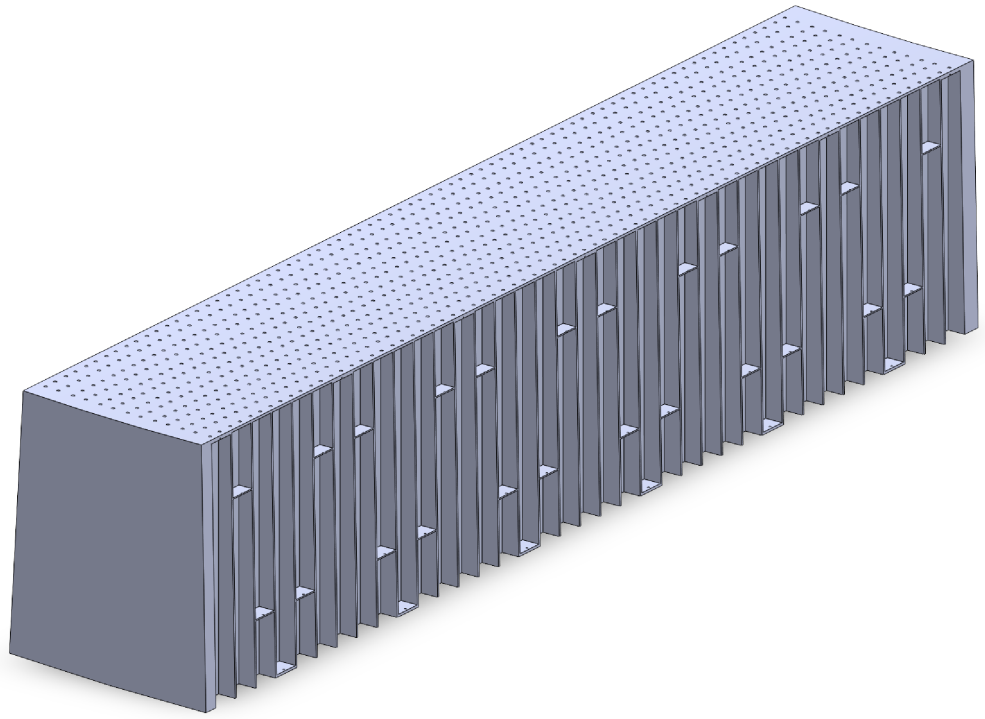

Figure 5.21: Isometric section view of the curved T-Liner design.

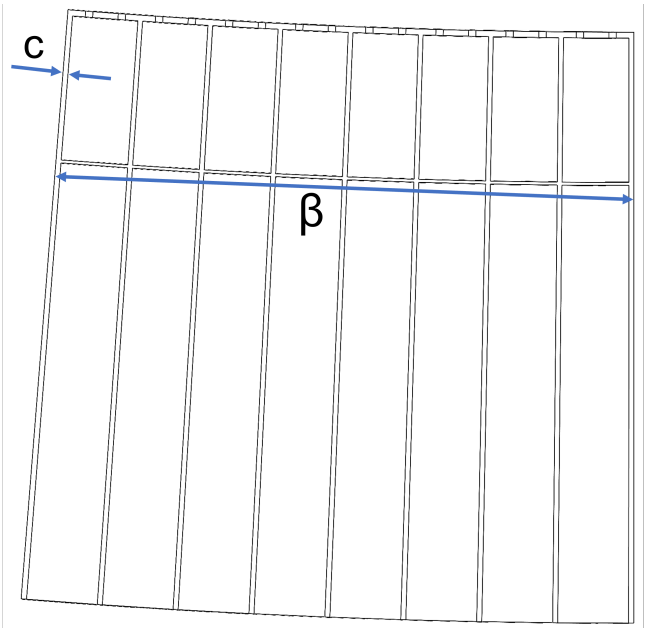

Figure 5.22: End view of the ANCF T-Liner design with a section view cut through the second row of the unit cell, R2.

ANCF circumferentially, and the liner is three parts in length. In total 237 parts are required to fill the test section of the ANCF; 158 of Part A and 79 of Part B.

Chapter 6

Additive Manufacturing and Liner Production

The T-liner was optimised using the multi-stage optimisation routine which included numerical parameterisation, semi-analytical optimisation and experimentally measured inputs. The final designs summarised at the end of Chapter 5 were achievable using additive manufacturing, which was used throughout the optimisation routine.

In the following chapter, the process by which the T-Liner was manufactured is explored. The constraints and limitations encountered through the process, as well as the different additive manufacturing approaches investigated, are discussed. Additionally, the quality of the test samples that were manufactured for testing in the ANCF is assessed.

6.1 Additive Manufacturing Technologies

While there are many different methods of additive manufacturing, they can be summarised into three main categories based on the raw material used at the start of the process. These are; solid-based systems, liquid-based systems, and powder-based systems. These categories remain quite broad, and as a result, the technologies involved can vary quite significantly. One element of the process which is commonly seen in the majority of techniques is a phase change to facilitate the formation of the final design [144, 150]. Figure 6.1 shows these three broad categories and further breaks these categories into some of each class' most common technology.

Three of the main methods of additive manufacturing used in TCD include Fused Deposition Modelling (FDM), Stereolithography (SLA) and Selective Laser Melting (SLM). Each of these technologies belongs to a different class of printer; FDM is a solid-based system, SLA is a liquid-based system, and SLM is a powder-based system.

Fused Deposition Modelling

Fused Deposition Modelling (FDM) is a method of melt additive manufacturing. The FDM printer feeds a material filament into an extrusion head and nozzle which heats the material to its melting point and deposits the material layer by layer. The path that the printer follows is a series of spatial coordinates that are generated from a CAD model. The use of different nozzle sizes can improve the resolution of the prints at the cost of increased print times [179, 180].

Numerous different materials can be used in FDM printing, including thermoplastic polymers, ceramics and composites. Each of the materials has different applications and benefits,

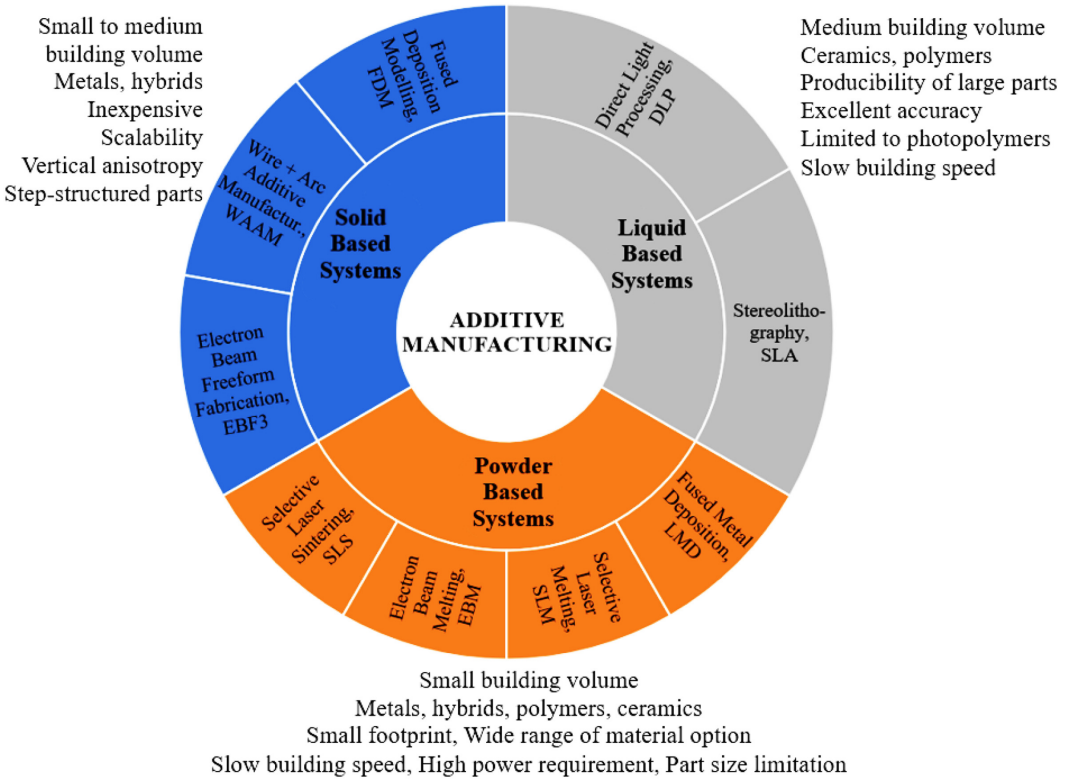

Figure 6.1: Classifications of additive manufacturing processes [143]

with Polylactic Acid (PLA) being the most commonly used thermoplastic filament followed closely by Acrylonitrile Butadiene Styrene (ABS) and Polyvinyl Alcohol (PVA). PLA is a bioplastic which has a low cost of production and is easy to work with as it has a lower melting point than other thermoplastics and is not prone to warping. ABS is often used in situations where the material needs to be more durable as it is less brittle than PLA and is capable of withstanding higher temperatures. PVA is a water-soluble thermoplastic that is largely used to produce support structures for complex geometries or to produce inserts that can later be dissolved.

Stereolithography

Stereolithography (SLA) is a fast prototyping form of additive manufacturing. This method uses a liquid resin photopolymer that can be cured when exposed to the appropriate form of light. The cured resin forms very thin solid layers which stack to form the object. generally between 25μm and 100μm. To cure the resin, SLA uses a directed laser beam as the light source. This is done by reflecting the laser beam off of a pair of mirror galvanometers and

then a series of mirrors that trace out each layer. SLA is often used in prototyping as it is able to achieve high levels of precision and accuracy [181–183].

Masked stereolithography (M-SLA) uses a LED and LCD photomask to produce the pattern for each layer. The LED array is located below the LCD photomask digital display. The entire LED array illuminates for every layer but the LCD photomask deactivates individual pixels to produce the pattern for each layer which allows the LED light to pass through [182]. As a result of the technology used to produce and direct the light, a single point produced by an SLA printer will have a circular footprint while an M-SLA printer will have a square footprint. The square point produced by the LCD photomask of the M-SLA printer is known as a voxel. The size of the voxel can be a limiting factor in the print quality of a model [184].

Selective Laser Melting

Selective Laser Melting (SLM) uses a high-powered laser to form the parts, similar to the SLA. However, instead of curing a resin, the SLM uses metallic powders as a raw material. A thin layer of the metal powder is deposited on the build plate and the high-powered laser traces the path of the CAD model. The laser beam melts and fuses the powder particles to form the layer. Once the layer is completed, the build plate lowers by the height of a single layer and a new layer of powder is added. Once the model is complete, the excess powder is manually removed. Unlike most other methods which require support structures to be generated for overhanging features, the unused powder in SLM printing can act as a supporting layer for overhangs removing the need for support structures [185].

6.1.1 Impact of Print Technology

With a wide range of additive manufacturing techniques available, multiple factors can impact the decision to use a particular method. Initial considerations such as cost and the intended function of the printed components are significant factors. For components intended to be used where high levels of durability and heat resistance are required, systems which can produce metal components would be necessary. However, for fast prototyping and visualisation of design concepts, quicker and cheaper options would be better suited [144, 186].

Kennedy et al. [187] explore how the technology used to produce an object can affect the overall quality and performance of the material. In the study, a periodic structure was produced using different additive manufacturing methods and the performance of the materials investigated. Figure 6.2 shows the print quality of the samples produced using FDM, SLA

and SLM printing techniques. The holes in the surface of the samples are supposed to have a radius of 1 mm. In all cases defects were introduced to the print based on the technology used. Most notably, in Fig. 6.2a it is clear that physical defects are present, with the holes being elliptical, filament separation between successive passes and threads of filament crossing the hole. Kennedy et al. [187] also reported that in the case of the SLA prints, difficulties arose with the removal of excess resin at the end of the print for deeper samples. This limited the number of cells of the periodic structure which could be printed as a single sample.

In terms of the acoustic performance of the samples, it was seen that both the SLA and SLM samples were in close agreement with the numerical models. The SLA printer used in the study was a FormLabs Form 2 costing €5,000. The SLM printer used in the study was a 3D Systems Prox DMP 200 costing €450,000. The difference in cost associated with the printers, while achieving similar results experimentally shows significant potential for the SLA printers when the benefits of metal components are not required.

While printing defects such as geometric distortion and filament separation which [187] observed in the FDM prints can negatively impact the performance of the liner, artefacts created by different printing processes can also be an advantage. Kennedy and Ciochon [188] study the surface quality of FDM prints using a number of non-destructive measurements, namely CT scanning, digital microscope imaging and confocal microscope imaging. These techniques allowed the surface roughness of FDM samples to be studied and quantified which were then used as geometric features on subsequent designs which were manufactured using SLA printing. The surface roughness was applied in a number of ways, from all over the internal surface of the samples, to only specific elements of the geometry. By adding the surface roughness, the volume of air cavities within the samples was reduced while simultaneously increasing the surface area. This resulted in an increase in the overall performance of all designs when compared to the smooth samples though the greatest increase was seen for the samples in which the surface roughness was applied to all internal surfaces.

This study showed the significance that surface roughness can have on the performance of a design but also the benefit of using these non-destructive imaging techniques to better assess the quality of materials produced. By taking advantage of these approaches during design processes, it is possible to enhance the performance of a device and determine the quality of internal features of final samples before testing.

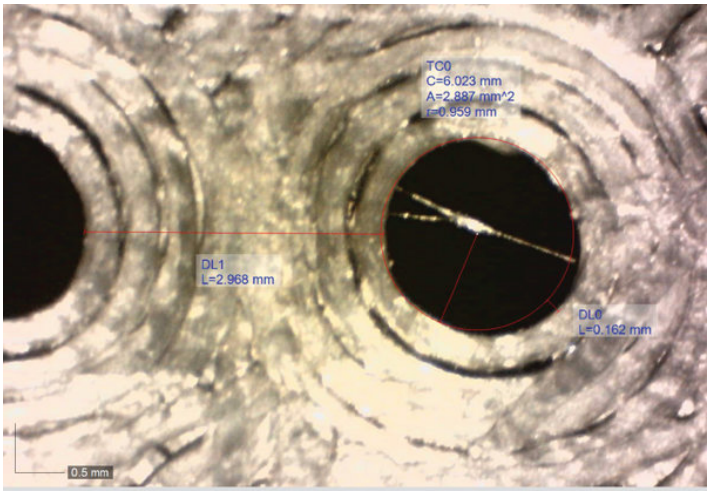

(a) FDM

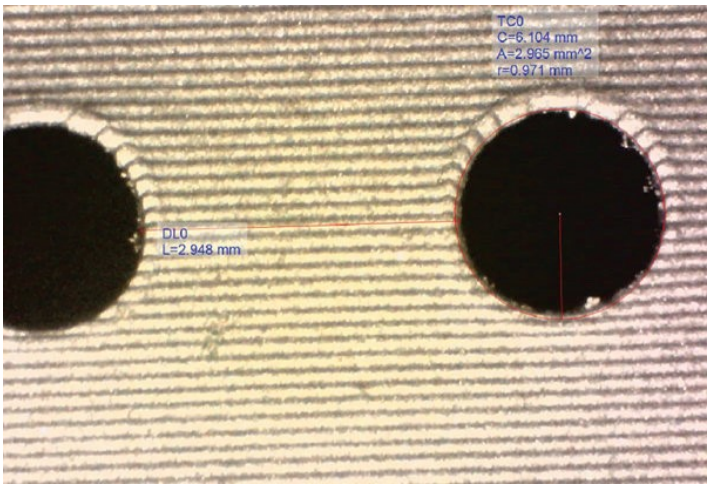

(b) SLA

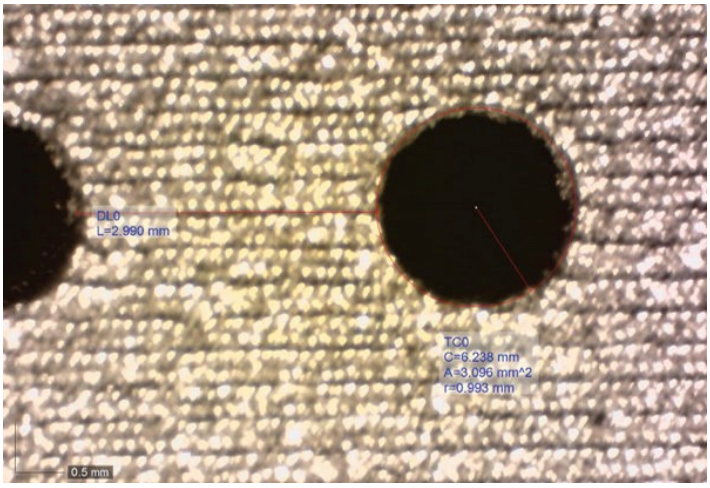

(c) SLM

Figure 6.2: Microscope imaging of the sample quality using different printing technologies: (a) FDM, (b) SLA and (c) SLM [187].

6.2 Liner Production

Of the methods introduced in Section 6.1, FDM and SLA were the only methods used in this work. SLM printers are capable of producing high-quality parts which have already seen implementation in the aviation sector, such as those used by GE for the LM9000 engine [151]. However, the production of parts using SLM printers has a higher associated cost compared with FDM and SLA printing. These costs are beneficial in situations where components are being reliably mass-produced and are able to reduce the number of parts being manufactured using traditional approaches. For the purposes of this study, the scale of production would not be sufficient to see cost benefits. Additionally, the liner is designed for testing in the ANCF rig which does not require the same material properties and durability that a full aero-engine would.

FDM and SLA printing are both commonly used methods of 3D printing. Due to the relatively low cost, both methods have seen wide-scale adoption in industry settings for proof of concept fabrication and among hobbyist communities.

6.2.1 Additive Manufacturing using FDM

The FDM printer used in this work was a Creality Ender 3. The Ender 3 is a low-cost tabletop FDM printer. Is very commonly used by amateur and hobbyist printers due to the low cost and reliable, consistent print quality. It has a build volume of 200 mm x 200 mm x 250 mm and a print precision of ± 0.1 mm. The standard nozzle width used on the Ender 3 is a 0.4 mm nozzle, with the option to replace the stock nozzle with different sizes. The stock extruder hot end, the component that heats the filament in an FDM printer, is able to print with nozzles ranging in size from 0.2 mm to 0.8 mm. Larger nozzle sizes are useful for prints that do not require a large amount of detail and enable faster printing speeds, while smaller nozzles can allow a greater level of detail to be achieved.

As is the case for nearly all methods of additive manufacturing, FDM requires a change of state of the input material to work. The filament used in the process is heated to a semi-molten state by the extruder hot end before being forced through the printer nozzle. The nozzle lightly compresses the semi-molten filament as it is extruded, which is how the printer produces a layer. As the layers printed are very thin, the filament cools in the air quickly, forming the structure. Additional cooling can be added with fans that are mounted on the extruder, however, in most applications, these are primarily used to keep the hot end at the

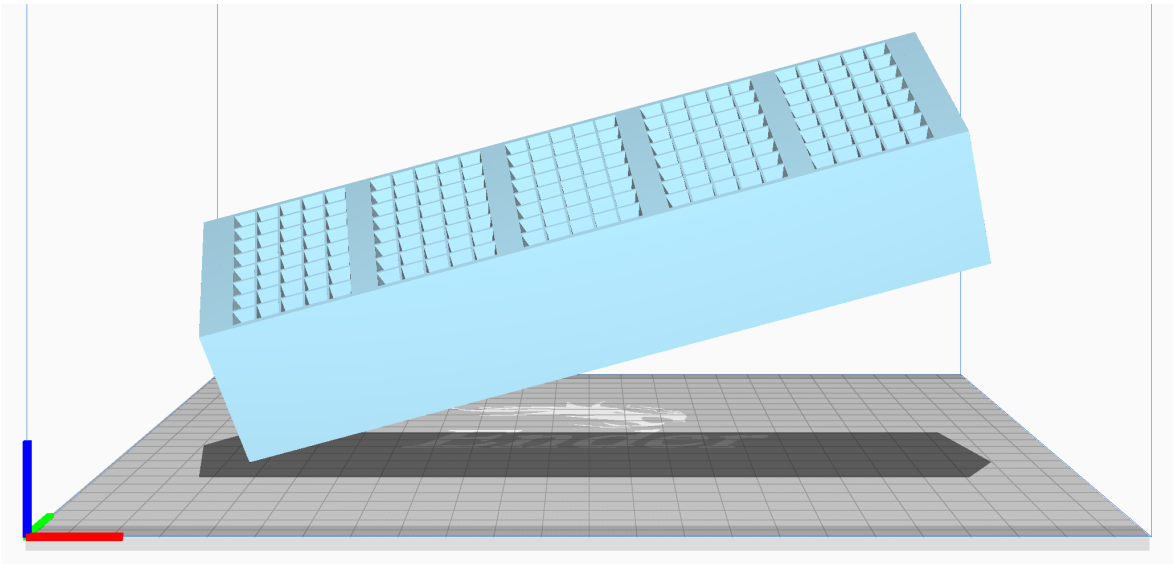

Figure 6.3: Example of the angle used in T-Liner prints using FDM

correct temperature. As the change of state in FDM printing is from a solid to a semi-molten state and back to a solid, there is very little post-processing required. For the majority of cases, the removal of support structures and potentially sanding the surface that the supports were attached to are all that is required.

The SDOF honeycomb backing used in this study was printed in PLA using FDM. The honeycomb did not have a high degree of detail required and was printed using a stock 0.4 mm nozzle size.

The first attempt to print the T-Liner backing was also performed using FDM. However, a number of issues became apparent from the initial stages. The cell walls of the T-Liner are 0.4 mm wide, the same as the size of the nozzle. As the stock nozzle was the same size as the width of the feature to be printed, it was not able to correctly print the walls as the nozzle could not compress the semi-molten filament, which is required to fuse the layers of the print together. To counter this, the model was printed at angles such that none of the walls or septa were vertical. An example of this can be seen in Fig. 6.3. The supports and additional features required for successful prints are not included in this image as they would make the model and relevant angles difficult to see. By printing at an angle, the effective width of the feature is slightly greater. The increase in the width of the feature depends on the angle used. Unfortunately, it was still not possible to print the structure. Prints would only successfully produce cell divisions in one direction and a large amount of layer separation was observed.

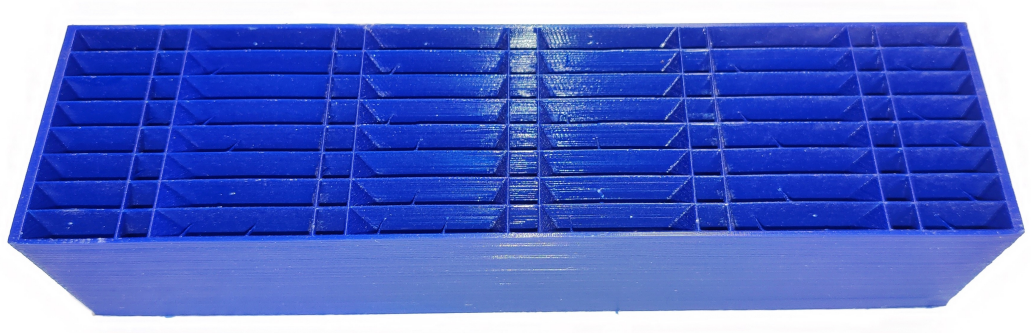

Figure 6.4: Best print of the T-Liner achieved using FDM.

The stock nozzle was replaced by both 0.3 mm and 0.2 mm nozzles. While the Ender 3 is supposed to be able to use a 0.2 mm nozzle, calibration prints were not successful when using the 0.2 mm nozzle. The 0.3 mm nozzle did successfully print calibration prints so it was used for additional attempts to print the T-Liner. As was the case with the 0.4 mm nozzle, the 0.3 mm nozzle required printing at angles. While the print quality of the 0.3 mm nozzle was higher than that of the 0.4 mm nozzle, the prints were still ultimately failures. No configuration was able to successfully print all cell divisions required. The best print produced using FDM can be seen in Fig. 6.4. The overall quality of the print was greater than was seen in many of the other attempts, with no obvious layer separation or other common quality issues. However, the span-wise walls were not printed, with only occasional threads indicating where the divisions were supposed to occur.

It was additionally seen that the FDM printer was not able to print the small septum perforations. The depth at which the perforations were supposed to occur within such narrow ducts meant traditional methods to produce the features would not be feasible on the scale required for this project. It would additionally have negated the benefit of using additive manufacturing as the range of sizes the perforations could be created would have been limited. It was therefore decided that FDM printing was not a suitable method of additive manufacturing for this work.

6.2.2 Additive Manufacturing using SLA

In the course of this work, four different models of SLA printers were used. During the design optimisation phase, prototype manufacturing was completed using a Prusa SL1S. The final

manufacturing was completed using 6 printers: one Prusa SL1S, two Prusa SL1s, one Elegoo Mars 3 and two Elegoo Saturn Ss. All four models are mSLA printers.

The Prusa SL1S is the newer, speed variant of the Prusa SL1. The SL1S has a 5.96" LCD screen which has a 49 μm xy resolution. The SL1 has a 5.5" LCD screen which has a 47 μm xy resolution. Both printers can print layers with a height of 0.025 mm up to a layer height of 0.1 mm. The Elegoo Saturn S has a 9.1" LCD screen with a 48 μm xy resolution. It can print at layer heights from 0.01 mm up to 0.15 mm and has a z-axis resolution of 1.25 μm. The Elegoo Mars 3 has a 6.6" LCD screen with a 35 μm xy resolution. It can print at layer heights from 0.01 mm up to 0.2 mm and has a z-axis resolution of 1.25 μ m.

The process of finding a method to accurately and reliably print a model using SLA printing can involve a significant amount of trial and error, particularly for complex models or models which have very fine details. While the design of the T-Liner is not geometrically as complex as many other models which are printed using SLA, the very thin walls, and small perforations were initially difficult to print without structural failures. The earliest attempts to print the liner were performed in parallel with the parametric studies to develop the method and skills required to print the liner once the optimal backing parameters were identified.

Generally, when using SLA, it is not possible to print a feature which overhangs empty space without supports. It is possible to a small degree, which is how layers can gradually increase along the length of a print, however, it can only be achieved up to a length scale of 1 mm while retaining decent print quality. When a feature must have an overhang, supports must be printed which can anchor the feature to the build plate. The test prints of the liner were performed with the bottom of the device flat against the build plate. The walls of the ducts were able to print reliably, however, the septum needed supports to be printed. These supports could not be easily removed without damaging the septum.

To counter this, the liner was placed on its side and rotated by 45 degrees, as shown in Fig. 6.5. As a result of this, none of the features was perpendicular to the build plate and could be gradually built up layer by layer. The first full sample of the liner backing was produced using this print orientation. However, during the cleaning and curing procedure, it was commonly seen that the septum would tear through the middle. These tears would originate at the perforations printed in the septum. It was realised that having layers print corner-to-corner, with a hole in the middle was introducing a point of failure to the septum.

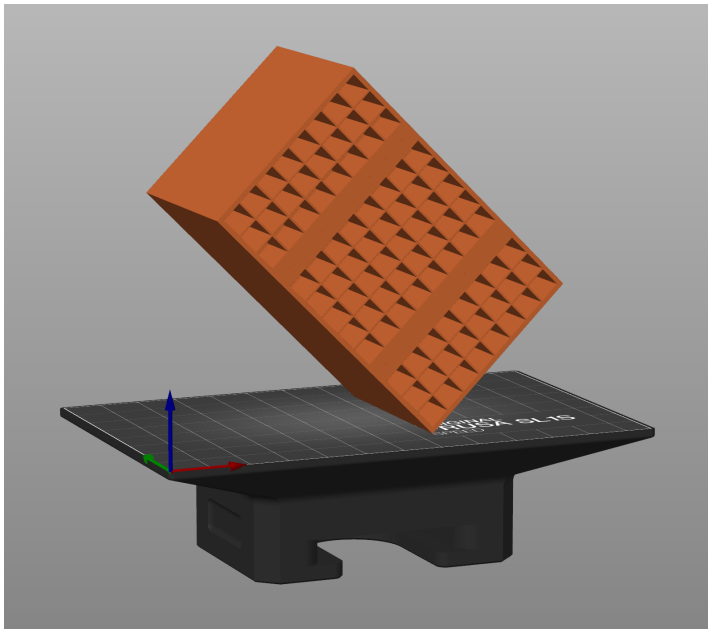

Figure 6.5: Print orientation used to avoid supports on the septum.

A test print that was intended to determine the minimum hole size the printer could produce had tears in almost all of the septums. This test print can be seen in Fig. 6.6a. The angle of the liner was reduced from 45 degrees to 30 degrees, which meant there was no longer a layer that connected corner-to-corner across a cell and passed through a perforation. The perforation size test was repeated at the lower angle, which can be seen in Fig. 6.6b. As can be seen, at the lower angle the septum did not split as was seen previously. Using the improved test print, it was determined that the smallest perforation size that could be printed without sealing or having significant deformation was a diameter d = 0.3 mm. While this was smaller than the minimum perforation size being used in the parametric study which was running in parallel, neither the diagonal nor horizontal septum configurations performed optimally with a smaller diameter than 0.3 mm.

While changing the angle of the liner relative to the build plate prevented the septum from splitting, the printed samples were not completely free of defects. Often, very small cracks formed in the walls and near the corner of the septum and walls which were not easily seen by the naked eye. These defects were not ideal, however, while investigations into improving the performance of the print quality were being performed, which looked at the exposure times and the post-processing procedure, a number of test articles were produced which were used for the initial faceplate optimisation discussed in Section 5.3.2.

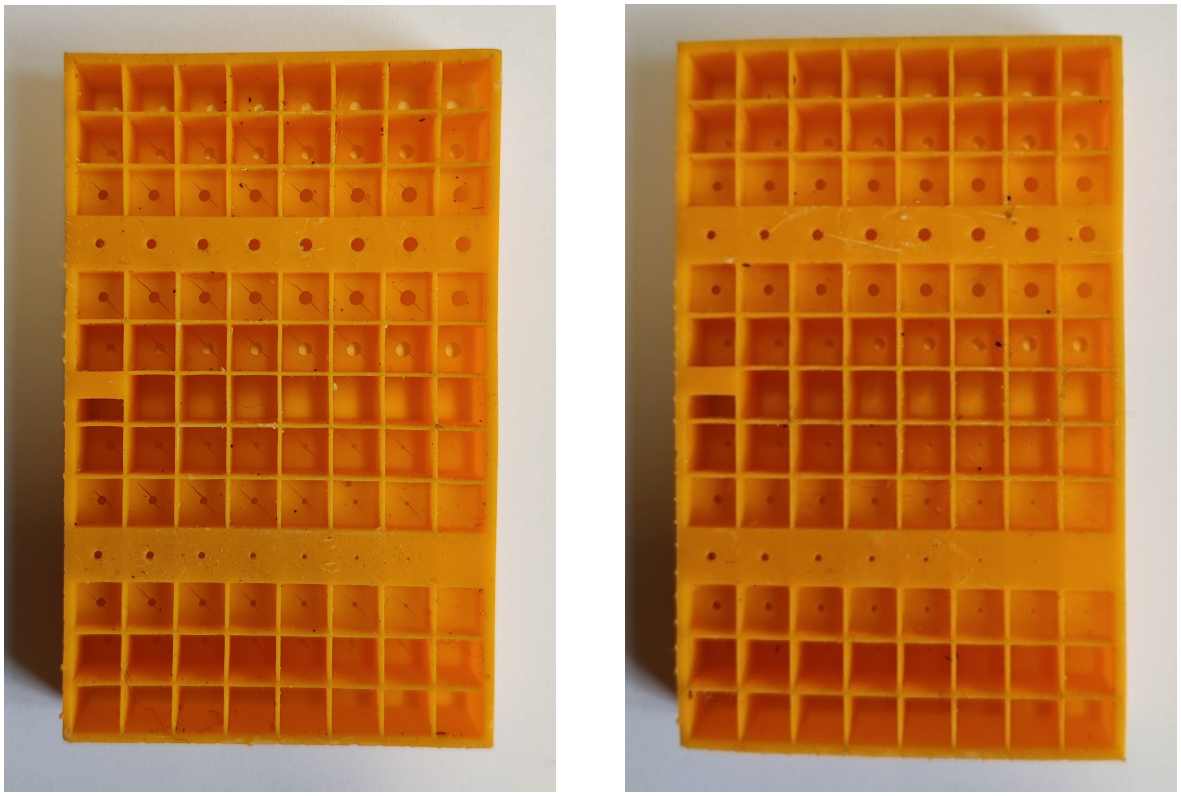

(a) Print angle = 45° (b) Print angle = 30°

Figure 6.6: Comparison of the print quality for different print angles.

During this time, a new photo-polymer resin was introduced by Prusa which was intended to replace the original Tough Resin that had been used so far in this investigation. The new resin, Prusament, was developed to be tougher than the previous resin while also achieving higher print quality and faster speeds. Test prints with the Prusament resin were able to print perforations down to a diameter d = 0.25 mm with good quality. While it had already been determined that perforations of this size would not be used in the liner design, it showed that the quality of prints with the new resin was higher. A comparison between an old test print using the Original Tough resin and the Prusament Tough resin can be seen in Fig. 6.7. With the higher-quality Prusament resin, the minor defects that had been encountered previously were significantly reduced. Using the higher quality backing that could be produced with the Prusament resin, the optimisation of the T-Liner faceplate was repeated as discussed in Section 5.3.2.

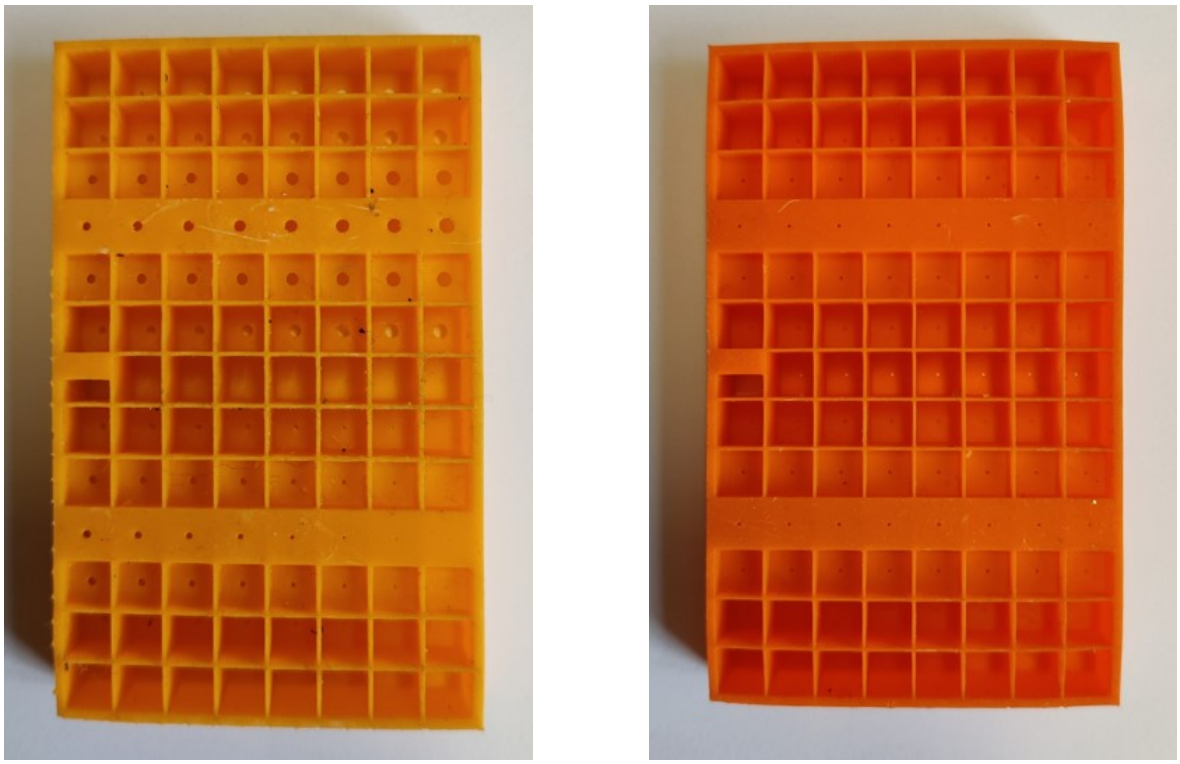

(a) Prusa Original Tough Resin

(b) Prusament Tough Resin

Figure 6.7: Comparison of print quality with the Original Prusa Tough resin and the Prusament Tough resin.

Print Tank Volume

The test section of the ANCF rig is 228.6 mm in length. The Prusa SL1S, which was the only printer being used during the design and prototyping phase of this investigation, has a maximum build volume of 127 mm x 80 mm x150 mm. It was not possible to orient the T-Liner design in such a way as to fit within the printer's build volume. The design was split into two components.

The footprint and volume of the T-Liner design was relatively large for the size of the printer being used to produce it, however, the majority of the model was empty space. The estimate for the amount of resin required for a single component was approximately 115 ml. The resin tank on the SL1S is capable of holding 200 ml of resin. Despite the tank having a volume almost double the estimated resin requirement, due to resin becoming trapped in the cavities of the T-Liner during printing the printer would run out of resin before completing the print.

It is possible to add more resin during the printing process. However, when this was attempted it would introduce additional errors to the print. Most commonly, when the print was paused to allow the protective casing to be opened, the next layer printed would not properly bond to the previous layer. The degree to which this occurred varied from small holes a couple of centimetres in size, to entire segments of the liner warping as new layers adhered to the resin tank film better than the previous layer. In the rare case that the resin tank was successfully refilled, and the resumed print did not have layer separation at the level at the tank was refilled, the weight of the print became so great before the print was completed that it was pulled off the build plate, either partially or completely.

It was therefore decided to print the T-Liner in three components.

Build Plate Adhesion

As the build plate in SLA prints is inverted and prints by raising after the completion of each layer, it is vitally important that the model is firmly attached to the build plate. In particular, the design of the T-Liner has a large number of cavities that can trap resin. This trapped resin significantly increases the weight of the print sample which increases the chance of the sample either partially or completely detaching from the build plate during the print. The quality of build plate adhesion was improved by increasing the surface roughness of the build plate, increasing the burn time of the bottom layers and using a build plate adhesive.

The build plate surface roughness is increased by sanding the build plate with low-grit sandpaper. The build plate is sanded in a single direction to add shallow groves to the surface of the build plate. It is important to ensure that the surface is sanded evenly across the surface, as an uneven surface can affect the levelling of the build plate. The groves provide a better surface for the resin to adhere to than the smooth aluminium build plate.

The bottom layers of the print, sometimes referred to as burn layers, are given longer exposure times than the standard layer exposure time to improve the bond between the print and the build plate. During SLA printing, the exposure time solidifies the resin layer by layer in set patterns to build the model. However, during the printing process, the resin is not completely cured which is why post-print curing is required after the sample is cleaned. This is done to prevent excess resin curing outside of the desired layer pattern. In the burn layers, a longer exposure is used which cures the resin more to improve the adhesion to the build plate. The burn layers are typically 8 - 10 times longer than the standard exposure and it is performed for the first 5 - 10 layers. During the T-Liner printing, the bottom 15 layers were

used as burn layers with an exposure of 60 seconds on the Prusa printers and 75 seconds on the Elegoo printers. All of the burn layers were part of the support structure base and did not affect the quality of the T-Liner prints. In addition to the burn layers, a build plate adhesive was used to improve the initial bond between the build plate and the bottom layers.

Cleaning

Unlike printing techniques such as FDM where there is little to no post-processing, other than removing support structures, SLA printing requires additional cleaning and curing after a print is completed. After an SLA print is completed, the printed sample will remain covered in a layer of uncured resin and the printed component itself will still require additional curing to completely set the structure. The first stage of the post-process procedure is to clean the excess resin using a solvent. For most SLA photo-polymers, IPA is used as the solvent. Tissue and IPA wipes are commonly used to remove the majority of the surface resin, before submerging the printed component in an IPA bath. IPA baths generally have either a magnetic stirrer or use ultrasonic waves to disrupt the IPA to clean the component. It is advised to only clean the samples for 2-5 minutes in the IPA bath, as the print is still not completely cured and excess time spent in the IPA can affect the quality of the final component.

After the component is cleaned in the IPA bath, it must be dried and cured. As IPA has a high volatility, it does not require high temperatures to evaporate the IPA on the surface of the component. However, it is still advisable to remove as much as possible with tissue. The component is then placed in a curer which contains a strong UV light source. Curers will occasionally contain a heating element in addition to the UV source to allow drying and curing. Depending on the size and complexity of the sample, curing times can vary, but ranges from 8 - 14 minutes are typically advised. Most printed components will have support structures which have to be removed during the post-processing. While the exact point that these get removed can depend heavily on the design of the sample, they are typically removed after the sample is cleaned and before it is cured.

The design of the T-Liner has a large number of cavities that are mostly enclosed, with only small submillimeter holes preventing them from being completely sealed. Due to this design, a large amount of resin is prone to be trapped in the cavities during the printing process. If this resin was left in the component when placed in the IPA bath, a large amount of resin would be wasted. It would also increase the amount of IPA used as the bath would

become contaminated by resin very quickly, requiring more frequent replacement. To avoid the higher level of waste, a slightly modified post-process procedure was followed. The cleaning station used for this process can be seen in Fig. 6.8. The cleaning station was out of the way of direct sunlight to reduce the amount of UV the samples were exposed to, and the windows near the cleaning station were covered to reduce the amount of scattered light coming in the windows.

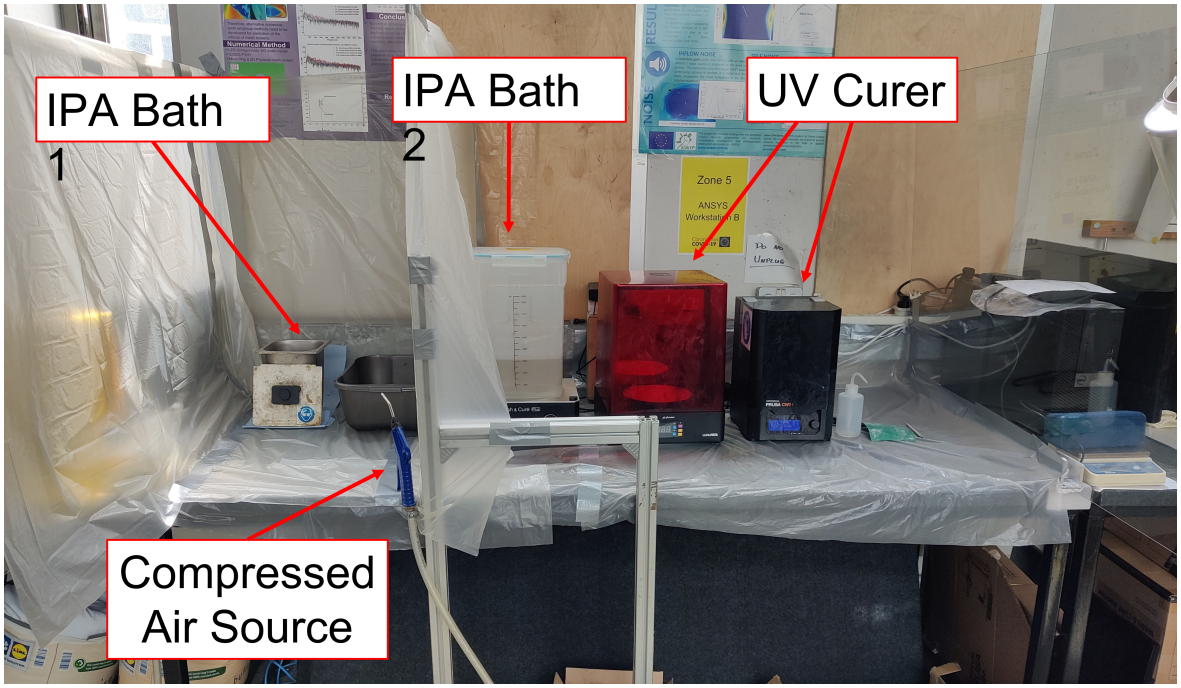

Figure 6.8: Cleaning station used in TCD for the post-processing procedure of the T-Liner samples.

The following steps were completed as the post-processing procedure:

1. The print was removed from the build plate and placed in a basin at a slight angle with the faceplate facing down. The basin was placed in a dark location without sunlight or other UV sources.

2. The component was left for 20 - 30 minutes to allow the resin to drain naturally under the influence of gravity. Most of the trapped resin would drain during this time and could be recovered for subsequent prints.

3. The compressed air source seen in Fig. 6.8 was used to remove additional resin from the cavities by blasting them individually.

4. The samples were submerged in IPA Bath 1 for 20 - 30 seconds and were then sprayed with the compressed air a second time. The short IPA bath helped the compressed air dislodge most of the remaining resin.

5. The supports were carefully removed from the prints. A dense support structure was used which was easiest to remove before curing. It was removed before the main IPA bath to minimise the amount of resin contaminating the IPA.

6. The component was washed in IPA Bath 2 for 6 minutes. This was slightly longer than is typically advised, but earlier prints would occasionally still have small amounts of resin on the surface after the 5-minute bath.

7. The compressed air was used to remove as much IPA from the cavities as possible. The design of the T-Liner has a lot of very thin surfaces which were prone to warping and cracking when heated for long periods of time to evaporate all the IPA.

8. The component was placed in the UV curer and dried at 32° for 40 seconds. If no evidence of IPA was seen around the faceplate perforations after heating, the component was cured for 12 minutes. If IPA was seen, the component was sprayed with the compressed air and heated a second time before curing.

Once the component was cured, the post-process procedure was completed and the component was ready for testing or to be packaged for shipment. The printing was completed using 6 printers: one Prusa SL1S, two Prusa SL1s, one Elegoo Mars 3 and two Elegoo Saturn S. Each part was printed at a rate of approximately 80 cm^3hr^{-1} and took 480 hours to manufacture the total amount. Taking into account the post-processing which was performed at the same time as the printing, the manufacturing process took a total of 550 hours.

6.3 Manufacturing Performance

During the design and optimisation parts of the investigation, the parameters of the material were chosen to provide the theoretical best performance. The parametric study was performed using a step size of 20 μm to 25 μm, while the semi-analytical study corrected values to 10 μm. The quality and accuracy of the printed test articles have a significant impact on the overall performance of the device, so an assessment of the print quality was conducted. This was done by measuring the size of the printed features using a digital microscope.

The digital microscope used in this study is a Dinolite AD7013MTL. The Dinolite has a 5 Megapixel CMOS sensor and is capable of 20 - 90 x magnification. It has 8 white LED lights which illuminate the object being studied. The software for the Dinolite allows for calibration of the microscope to allow direct measurements to be performed.

A magnification of 39.8 x was used in this study. The microscope was calibrated at the beginning and was verified at the end of the measurements using the calibration card to ensure that the calibration was accurate for all measurements. In total, measurements were performed on 26 samples of the test articles that were to be tested on the ANCF liner. This is ∼11% of the components that were printed for the rig. The number of samples measured for each part type, Part A or Part B, and the printer used to print the part is summarised in Table 6.1. The ratio of Part A to Part B measured and the ratio of Prusa to Elegoo parts measured is proportional to the number of components of each type used in the ANCF.

	Prusa Part A	Prusa Part B	Elegoo Part A	Elegoo Part B
#Samples	10	4	8	4

Table 6.1: Number of samples of each part type and printer measured using the digital microscope.

Measurements were performed on six parameters; three faceplate parameters and three backing parameters. The faceplate parameters measured were the faceplate perforation diameter D, the intra-cell perforation spacing x_1 and the inter-cell perforation spacing x_2. The backing parameters measured were the septum perforation diameter d, the internal cell width b_1 and the external cell width b_2. Two perforations on both the faceplate and septum were measured for every sample. Measurements of the perforation spacing and the widths were all performed in the axial direction as the measurements were performed on the ANCF T-Liner components which are curved in the spanwise direction. While the span-wise width of the components can be calculated or measured from the CAD used in the printing process, it was not used as a direct input in the design of the device. Two examples of the measurements performed on the faceplate of Part A can be seen in Fig. 6.9. Additional images of the measurements for the backing parameters and for Part B can be seen in Appendix A, along with the full set of results of the measurements.

It was not possible to measure the thickness of the faceplate or the septum, or the septum heights in the cells during the assessment of the print quality. These values could only have been obtained by cutting the samples being measured open. As the measurements were

performed on samples that were going to be tested in the ANCF, it was not possible to cut them open for these measurements. While the use of a non-destructive scanning technique like CT scanning may have provided a greater understanding of the overall quality of the prints without damaging the test articles, limited time and resources during this phase of the study prevented such measurements from being performed.

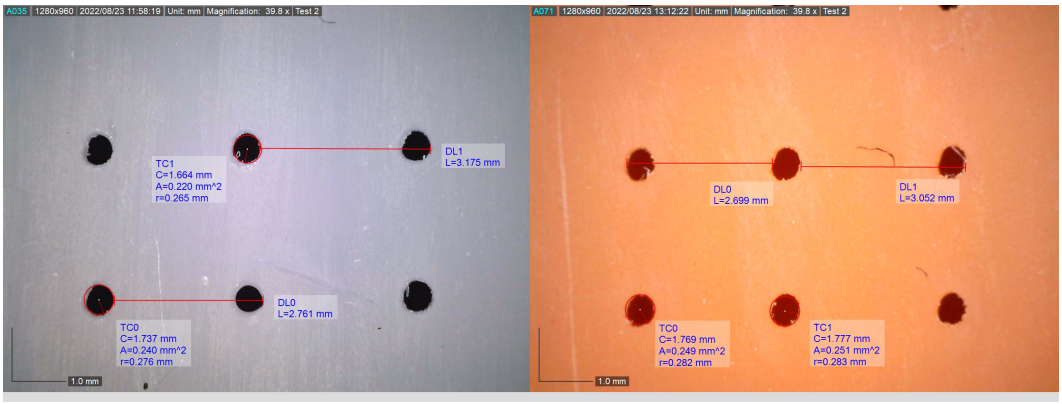

(a) Elegoo (b) Prusa

Figure 6.9: Print quality of the top surface of Part A from an (a) Elegoo printer and (b) Prusa printer.

Sample		Front			Back		
		D	x_1	x_2	d	b_1	b_2
Mean (mm)	A Elegoo	0.585	2.726	3.138	0.370	5.480	5.936
	A Prusa	0.587	2.686	3.102	0.364	5.453	5.859
	B Elegoo	0.586	2.823	3.219	0.382	5.545	6.013
	B Prusa	0.593	2.778	3.164	0.372	5.491	5.931
Target (mm)		0.63	2.8	3.2	0.4	5.6	6.0
%Error	A Elegoo	7.103	2.638	1.926	7.500	2.152	1.075
	A Prusa	6.857	4.082	3.069	8.950	2.632	2.347
	B Elegoo	7.024	0.821	0.586	4.625	0.982	0.217
	B Prusa	5.833	0.804	1.117	7.000	1.951	1.146

Table 6.2: Mean value and percentage error on the measured geometric parameters. The errors are summarised by part and printer.

The summary of measurements can be found in Table 6.2. The summary gives the mean value and percentage error for each of the measured parameters. The measurements are separated into Part A and Part B, and by printer type. The quality of the prints of the Part B samples is higher than the Part A samples in all measurements. The samples were selected after the manufacturing and post-processing were completed, with samples chosen

from across the manufacturing period. However, while Part A and Part B components were printed in parallel, the early stages of the printing were primarily spent printing Part A components while the majority of the Part B components were printed towards the end. The higher quality of the Part B samples is potentially a result of the additional experience with handling the geometry and the post-processing procedure. However, without additional examination with a larger sample size, the exact cause of the higher quality can not be definitively determined.

Using the measurements performed, the parameter values that were printed for the ANCF liner were computed and are summarised in Table 6.3, where "Value (Actual)" is the mean value determined. All measurements are calculated proportionally to the ratio of Part A to Part B components, and the ratio of Elegoo to Prusa components that were in the final liner. The standard deviation of each of the values was determined. While the size of the perforations in both the faceplate and the septa have a higher error than the wall thicknesses, they have a much smaller standard deviation meaning while the perforation size is less accurate compared to the intended value, they are still quite precise.

	Value (Design)	Value (Actual)	% Error	σ	min	max
H	50 mm	-	-	-	-	-
x_1	2.8 mm	2.74 mm	2.54	0.0511	2.67	2.80
x_2	3.2 mm	3.14 mm	1.99	0.0462	3.04	3.18
b_1	5.6 mm	5.48 mm	2.11	0.0366	5.41	5.53
b_2	6 mm	5.92 mm	1.41	0.0457	5.85	5.99
T_1	0.7 mm	-	-	-	-	-
T_2	0.5 mm	-	-	-	-	-
t	0.2 mm	-	-	-	-	-
D	0.63 mm	0.59 mm	6.80	0.0085	0.54	0.62
d	0.4 mm	0.37 mm	7.50	0.0087	0.34	0.39

Table 6.3: Value of the geometric parameters of parts printed for testing in the ANCF rig, corrected for the measured error. Corrections are weight to account for each test article containing two Part A components and one Part B component, and the ratio of Prusa to Elegoo printed components.

The corrected values of the parameters were also determined for the parts printed on only the Prusa printers. This can be found in Table 6.4. This is used for the error estimate on the print quality for the test articles that were tested in the impedance tubes at TCD and LAUM. Although the measurements were performed on samples that were produced for the ANCF

which have a curved spanwise cross-section, the measurements were only of dimensions in the axial direction which should be the same for both variants of the T-Liner unit cell.

	Value (Design)	Value (Actual)	% Error	σ	min	max
H	50.5 mm	50.94 mm	1.88	0.2342	50.54	51.27
x_1	2.8 mm	2.72 mm	2.98	0.0465	2.67	2.80
x_2	3.2 mm	3.12 mm	2.42	0.0450	3.04	3.18
b_1	5.6 mm	5.47 mm	2.40	0.0324	5.40	5.51
b_2	6.0 mm	5.88 mm	1.95	0.0459	5.80	5.95
T_1	0.7 mm	0.72 mm	-	-	-	-
T_2	0.5 mm	0.49 mm	2.4	0.0223	0.446	0.518
t	0.23 mm	0.23 mm	1.13	0.0127	0.214	0.232
D	0.63 mm	0.59 mm	6.56	0.0074	0.54	0.62
d	0.4 mm	0.37 mm	8.33	0.0090	0.34	0.39

Table 6.4: Value of the geometric parameters of parts printed using the Prusa printers, corrected for the measured error. Corrections are weight to account for each test article containing two Part A components and one Part B component.

Chapter 7

Characterisation and Performance

A novel acoustic liner was designed following an optimisation procedure which included numerical parameterisation and semi-analytical optimisation. Geometric considerations and constraints, as well as the limitations of the additive manufacturing process used, were taken into account and the optimised design was modified for installation in the ANCF rig. Additive manufacturing was used throughout the process to produce test samples. The additive manufacturing techniques used in liner production, and the overall print quality and accuracy were discussed.

In this chapter, the acoustic performance of the test samples is presented. The testing was conducted in two grazing impedance tubes of TRL 2 located in TCD and LAUM, and the final test was conducted on the ANCF which has a TRL 3 which is located in UND.

7.1 Normal Incidence

Three acoustic liner designs were developed in the course of this study using the Optimisation Procedure outlined in Chapter 5. The first liner was an SDOF liner, which comprises a microperforated panel over a honeycomb backing. A metal plate was used to manufacture the microperforated plate and is a separate component to the honeycomb backing. The other two designs are two generations of an MDOF liner. The first generation is a microperforated panel over a variable geometry, honeycomb backing in which perforated septa divide the cells of the honeycomb at different heights creating multiple cavity configurations. In this generation, the microperforated plate is made of the same metal plate as the SDOF liner. The second generation of the MDOF liner, referred to as the T-Liner, has the same backing geometry but features an integrated faceplate. The geometry of the integrated faceplate is different to the metal plate as there was a greater degree of freedom with the additive manufacturing process used for the second generation. All three samples had a surface area of 50 mm x 80 mm. The SDOF and T-Liner v1 both had a total height of 50.787 mm and the T-Liner v2 had a total height of 50.5 mm. The difference in height is due to the difference in the thickness of the faceplate used in the different configurations.

The predicted and experimental performance of the SDOF liner can be seen in Fig. 7.1. The semi-analytical prediction of the optimised absorption coefficient is shown in red, the numerical prediction is shown by the broken green line and the experimentally measured absorption coefficient is shown in blue. The absorption coefficient, α is on the vertical axis and the frequency in Hertz, Hz, is on the horizontal axis. The mean absorption measured

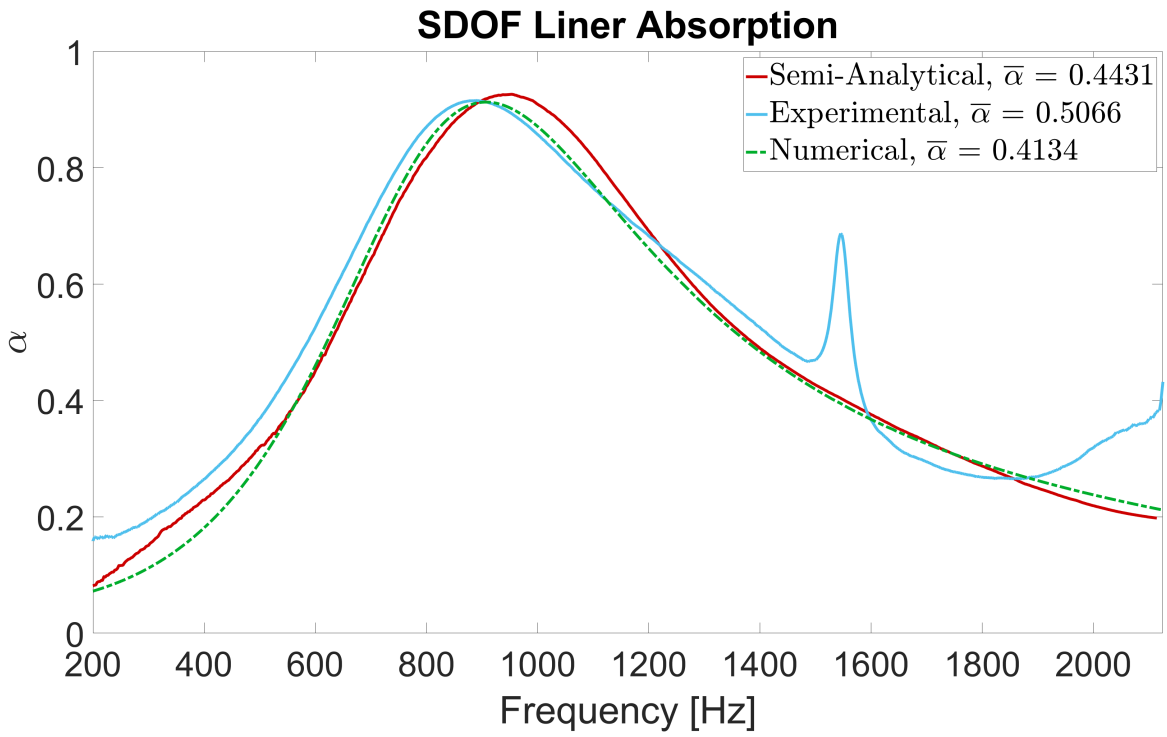

Figure 7.1: Comparison of the absorption coefficient of the final geometry for the SDOF liner, measured in normal incidence in the GIIT at TCD.

experimentally is $\overline{\alpha} = 0.5066$, higher than the semi-analytical predicted value of $\overline{\alpha} = 0.4431$ and the numerically predicted value of $\overline{\alpha} = 0.4134$. Despite the higher mean absorption in the experimental result, there is good agreement between the overall behaviour of the three absorption coefficients. The frequency of the absorption coefficient peak is higher in semi-analytical prediction at 950 Hz than the experimental results and the numerical simulation which are at 880 Hz and 890 Hz respectively. However, all three peaks have approximately the same value $\alpha = 0.92$. As discussed previously, the spike in the absorption curve of the experimental results at 1550 Hz is caused by structural vibrations of the micro-perforated plate. This is not seen in the analytical or numerical results as both of the predictive models only modelled the volume of the air and did not include the structural behaviours.

The performance of the final T-Liner design is presented in Fig. 7.2, which shows the absorption coefficient of the semi-analytical, experimental, and numerical data. The semi-analytical results are shown as the solid red line; the experimental results are shown as the solid light blue line; and the numerical results are shown in the broken (dot-dash) green line. The absorption coefficient, α is on the vertical axis and the frequency in Hertz, Hz, is on the horizontal axis. Across the frequency range, the mean absorption coefficient of the

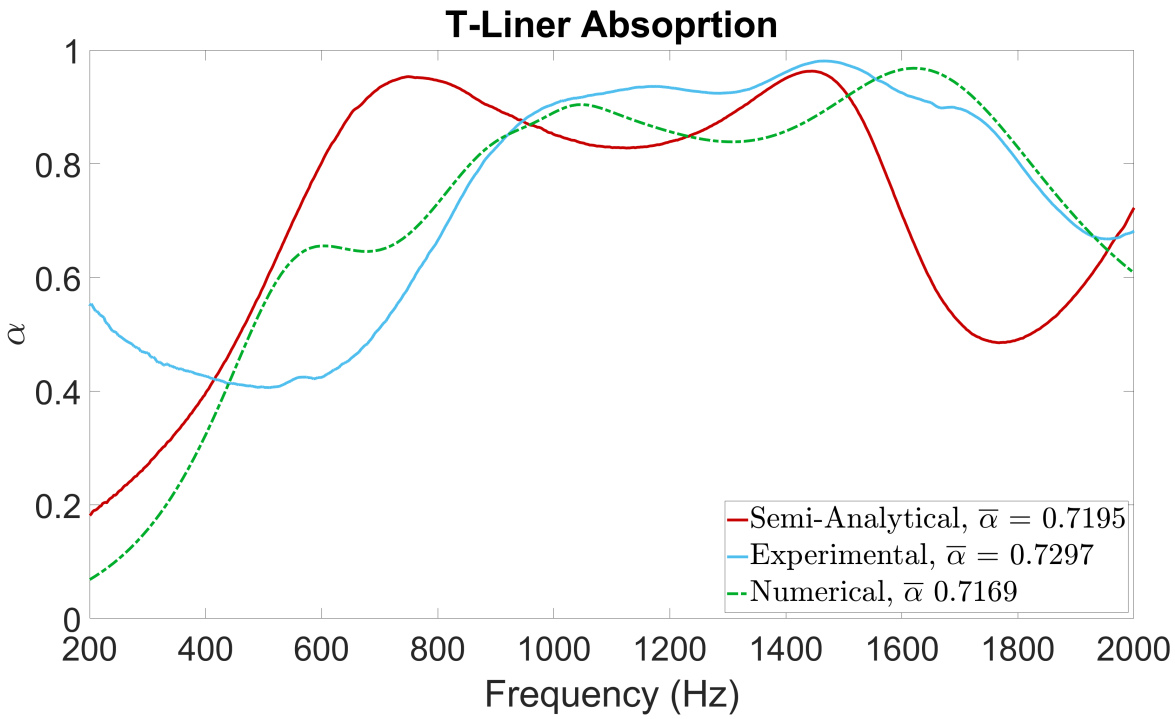

Figure 7.2: Comparison of the absorption coefficient of the final geometry for the T-Liner, measured in normal incidence in the GIIT at TCD.

semi-analytical results is $\overline{\alpha} = 0.7159$; the mean absorption coefficient of the experimental results is $\overline{\alpha} = 0.7375$; and the mean absorption coefficient of the numerical results is $\overline{\alpha} = 0.7169$. For all three sets of results, the absorption coefficient is greater than 0.8 between 800 Hz and 1.8 Hz. There is a good agreement for all three results between 800 Hz and 1200 Hz, and again around the 1600 Hz peak. The semi-analytical and experimental results show more similarities in their behaviour below 800 Hz than with the numerical results, however, it is the numerical and semi-analytical results which are in closer agreement between 1200 Hz and 1600 Hz. In this frequency range, the numerical and semi-analytical show a drop in the absorption coefficient to 0.8 and 0.84 respectively. Meanwhile, the experimental absorption coefficient remains above 0.92 in this range with a peak absorption coefficient of 0.98 at 1465 Hz.

In Fig. 7.2, the decrease in the experimental absorption coefficient between 200 Hz and 600 Hz is irregular. Similar behaviour is often indicative of poor measurement quality in the frequency range, which is closer to the lower limit of the speakers used in the GIIT. However, the measurements were repeated five times over a number of days. The samples were remounted in the GIIT, and new microphone calibrations were taken each day. The

behaviour was consistent throughout each of these tests and was not observed in the SDOF measurements that were performed during the same test campaigns. This indicates that the behaviour is a result of the test sample.

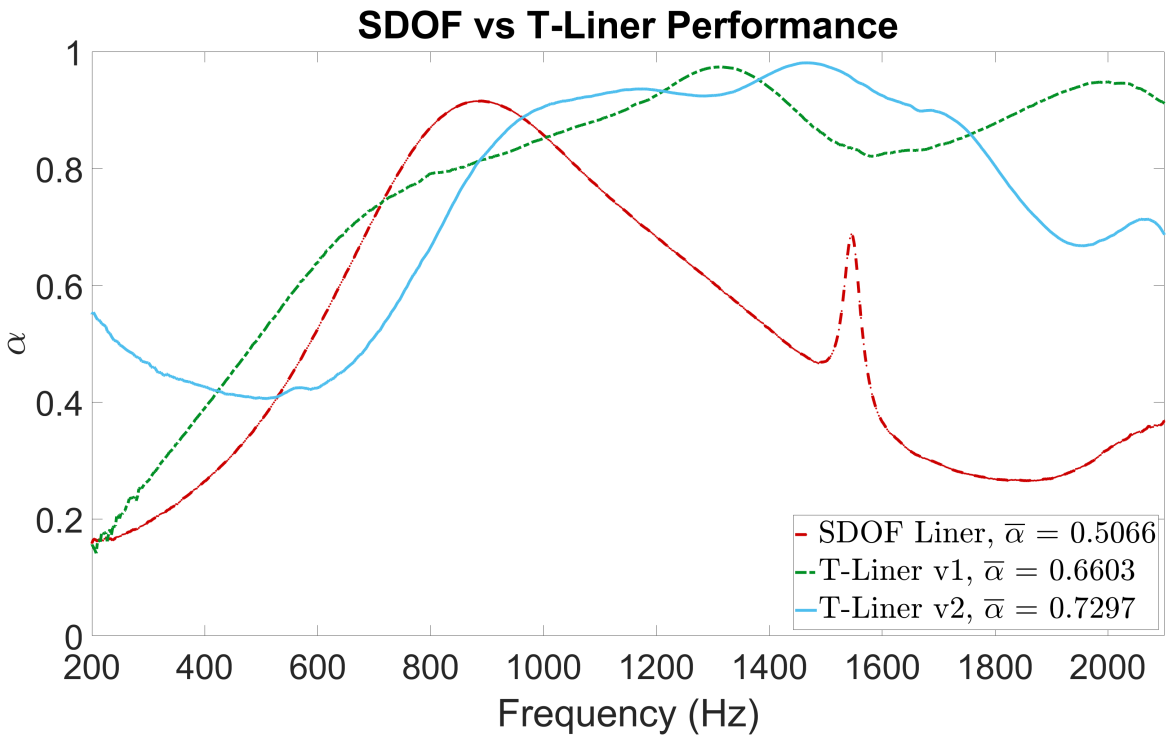

Figure 7.3: Comparison of the experimental absorption coefficient of the SDOF liner, the T-Liner with a metal faceplate (T-Liner v1) and the T-liner with an integrated faceplate (T-Liner v2) as measured in normal incidence in the GIIT at TCD.

The experimental performance of the three designs, the SDOF liner and both generations of the T-Liner, are presented in Fig. 7.3. The absorption coefficient, α is on the vertical axis and the frequency in Hertz, Hz, is on the horizontal axis. The SDOF liner shown by the broken red line has a mean absorption coefficient of $\overline{\alpha} = 0.5066$; the T-Liner with a metal faceplate shown by the broken green line has a mean absorption coefficient of $\overline{\alpha} = 0.6603$; the T-Liner with the integrated faceplate shown by the solid blue line has a mean absorption coefficient of $\overline{\alpha} = 0.7297$. Both versions of the T-Liner display an improvement in the absorption coefficient compared to the SDOF liner. The higher mean absorption of the integrated faceplate liner made it the preferred design for the development of an acoustic liner for the ANCF. This design had the added benefit of being made entirely by additive manufacturing, which gave greater control over the geometry and would not have the same

limitations that conventional manufacturing approaches would have when adapting the design for the curvature of the ANCF.

7.2 Grazing Incidence

Grazing incidence experiments were performed on the T-Liner in the GIIT at TCD and in the OD at LAUM. The experiments in TCD only measured the transmission loss of the test article with no flow. The experiments in LAUM measured the impedance and transmission loss of the T-Liner. Measurements were performed at a number of SPL with no flow, and with-flow at a single SPL.

7.2.1 TCD

Figure 7.4 shows the comparison of the transmission loss of the SDOF liner and the T-Liner in grazing incidence. Both numerical and experimental results are presented. The experimental results are shown with a solid line; the experimental SDOF liner is shown in red and the T-Liner is shown in blue. The numerical results of both liners are shown by a broken line; the SDOF liner is shown in black and the T-Liner is shown in green. The transmission loss in decibels, dB, is on the vertical axis and the frequency in Hertz, Hz, is given on the horizontal axis.

The SDOF liner experimental measurement has a transmission loss peak of 6.5 dB at 640 Hz while the numerical simulation predicts a transmission loss peak of 7.9 dB at 865 Hz. The T-Liner experimental measurement has a transmission loss peak of 15.2 dB at 810 Hz, while the numerical simulation has a transmission loss peak of 38.0 dB at 985 Hz. While there is a significant difference in the magnitude of the transmission loss between the numerical and experimental results, the shift in performance between the experimental and numerical is similar for both liners. The numerical simulation of the T-Liner is a full-geometric model using the physics settings defined by study 2 in Section 4.3.2. Study 2 uses pressure acoustics in the waveguide simulating the GIIT, NRA pressure acoustics to model the ducts and thermoviscous acoustics with boundary layers in all of the perforations. The full geometry model is an array of 37 x 8 cell arrays; 8 unit cells in the spanwise direction and 6 unit cells in the axial direction with one additional row of cells at the end for symmetry. Despite using the least computationally expensive physics setting, the simulation took approximately 230 hrs on a high-performance workstation. The numerical simulation of the SDOF liner used the

interior perforated panel (IPP) to model the faceplate of the liner as opposed to the direct perforation modelling that was used for the T-Liner. The IPP uses the analytical solution of a microperforated panel to determine the losses in the panel in a similar manner to the narrow region acoustics. The predictive capabilities of the IPP, as opposed to the direct perforation modelling used for the T-Liner, show that further refinement of the perforation modelling used in the T-Liner numerical simulations may yield more accurate predictions.

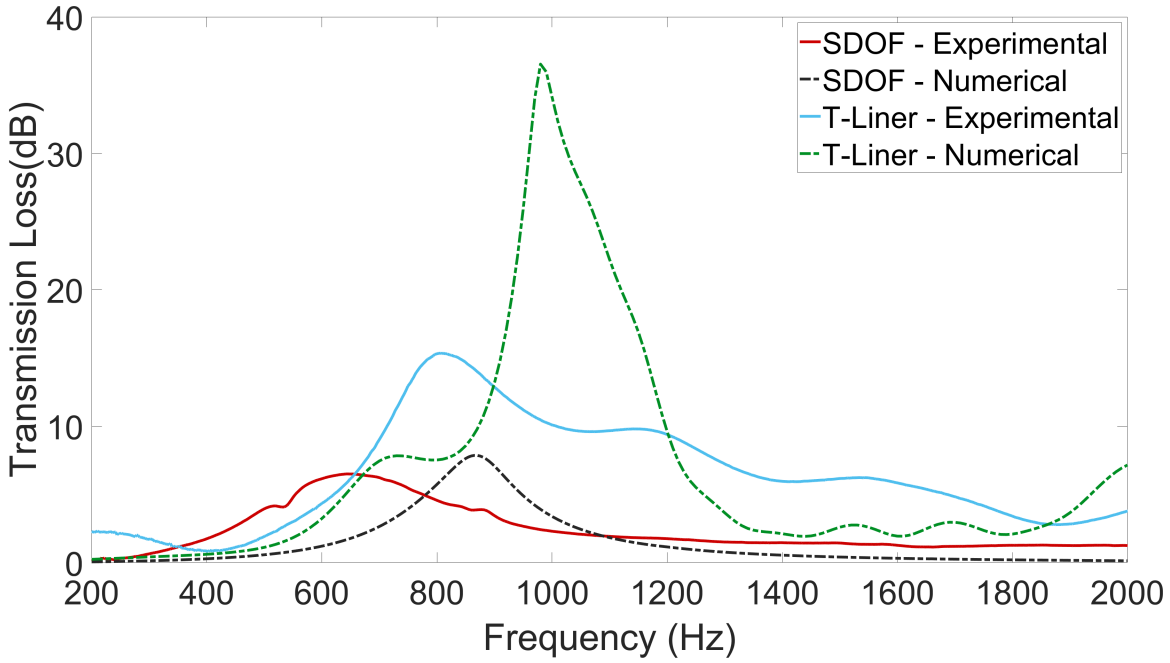

Figure 7.4: Comparison of the numerical and experimental transmission loss of the T-Liner in grazing incidence, measured in the GIIT at TCD. A hardwall baseline measurement is included for reference.

Comparing the experimental and the numerical performance of the T-Liner, both sets of results show that between 700 Hz and 1.2 kHz the transmission loss is greater than 8 dB. Within this range, the numerical results have a higher transmission loss. Above 1.2 kHz the experimental data shows a more gradual reduction in amplitude from approximately 10.0 dB at 1.2kHz to 5.0 dB at 1.7 kHz. However, it is within this frequency range that the liner will be expected to perform the best when installed in the ANCF.

7.2.2 LAUM

The test articles used in this section of the investigation were manufactured in TCD. The experimental measurements presented were performed by Thomas Humbert in LAUM.

The test articles used for the testing in LAUM were manufactured using the Prusa SL1 and SL1s. The test section in LAUM is 200 mm in length so a short test article was used. The full geometry of the T-Liner configuration tested in LAUM can be found in Section 5.4. The T-Liner was tested at a range of SPL and Mach speeds. The first set of tests was performed with no background flow in the tube, at four SPL; 100 dB, 120 dB, 130 dB and 140 dB. The second set of tests was performed at an SPL of 140 dB to ensure a high signal-to-noise ratio for three Mach speeds; M = 0, M = 0.1, and M = 0.25. For the Mach speed tests, both with-flow acoustic excitation and counter-flow acoustic excitation measurements were performed. The flow condition in the with-flow acoustic excitation is the same as those experienced by an exhaust liner in the ANCF, while the counter-flow acoustic excitation is the same as those experienced by an inlet liner. The standard test speeds of the ANCF are between M = 0.1 and M = 0.2.

The transmission loss of the liner at each of the tested SPL can be seen in Fig. 7.5. The transmission loss in decibels, dB, is on the vertical axis and the frequency in Hertz, Hz, is given on the horizontal axis. The 100 dB SPL is shown in blue, the 120 dB SPL is shown in red, the 130 dB SPL is shown in green and the 140 dB SPL is shown in black. The greatest transmission loss measured is in the 100 dB with a transmission loss peak of 27.7 dB at 1055 Hz, with a secondary transmission loss peak of 9.8 dB at 2890 Hz. Similar behaviour is seen in the 120 dB test which has a transmission loss peak of 26.9 dB at 1075 Hz and 9.0 dB at 2910 Hz. Non-linear behaviour is seen at the higher SPL. The peak transmission loss in the 130 dB test is 23.5 dB at 1090 Hz, and in the 140 dB test, this drops further to 16.2 dB at 1185 Hz. However, it is also seen that as the transmission loss peak is reduced as the SPL increase, there is a small increase in the broadband transmission loss of 1.5 dB to 2 dB. At 140 dB, a transmission loss greater than 5.5 dB is observed over a frequency range of nearly 2300 Hz, between 750 Hz and 3045 Hz. The non-linearity seen in the transmission loss as the SPL increases most likely arises from the small POA of the faceplate of the T-Liner which is approximately 3.1% and the very small POA of the septa which is approximately 0.04%. This is to be expected due to the large increase in the acoustic particle velocity which is compressed into the minuscule apertures.

The effect of flow on the transmission loss of the T-Liner can be seen in Fig. 7.6. The transmission loss in decibels, dB, is on the vertical axis and the frequency in Hertz, Hz, is given on the horizontal axis. The performance of the T-Liner was tested at 140 dB for three

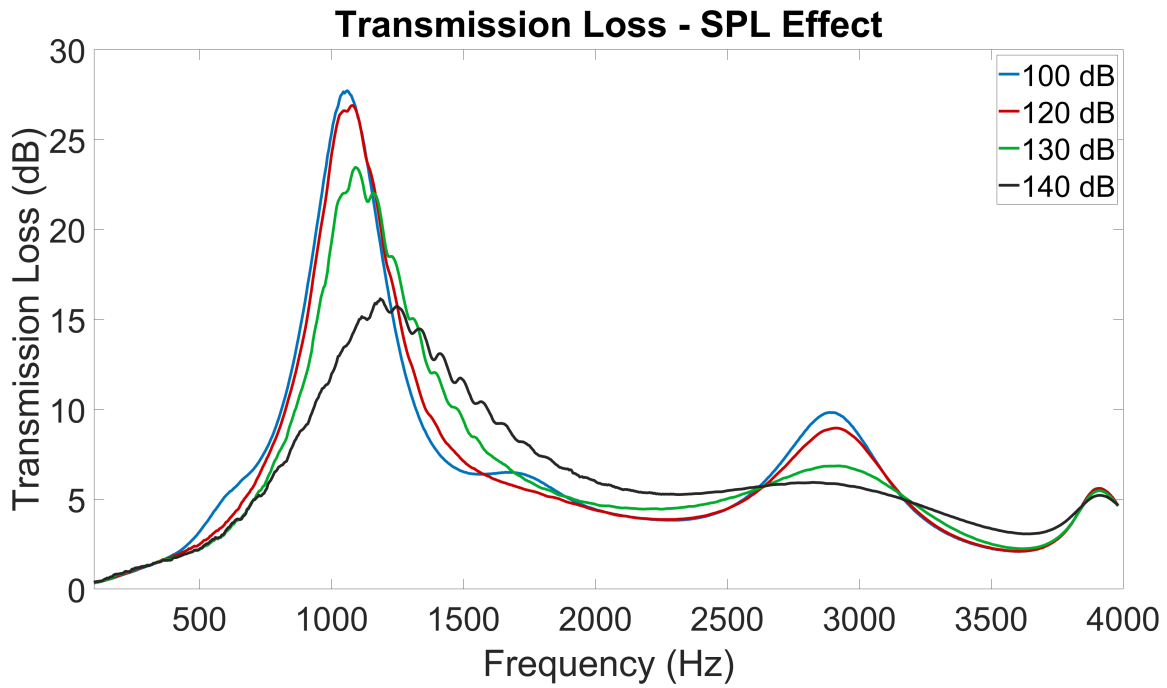

Figure 7.5: Transmission loss performance of the T-Liner for different excitation SPL measured experimentally in LAUM.

Mach speeds, for with-flow and counter-flow acoustic excitation. The Mach 0 results are shown in blue, the Mach 0.1 results are shown in red and the Mach 0.25 results are shown in green. For Mach 0.1 and Mach 0.25, the solid line represents the with-flow acoustic excitation and the broken line represents the counter-flow acoustic excitation. Classic convention effects are seen, with the counter-flow configuration increasing the broadband transmission loss, but reducing the transmission loss. At Mach 0.25, the counter-flow test has a transmission loss of at least 6.5 dB for the entire frequency range above 530 Hz, while the counter-flow Mach 0.1 transmission loss is greater than 0.5 dB above 580 Hz. However, this improved broadband performance came with the cost of reducing the peak from 16.2 dB at Mach 0, to 10.8 dB at Mach 0.25.

A numerical simulation of the T-Liner tested in LAUM was also conducted. The comparison of the numerical and experimental results at 100 dB can be seen in Fig. 7.7. The transmission loss in decibels, dB, is on the vertical axis and the frequency in Hertz, Hz, is given on the horizontal axis. The experimental results are the solid blue line and the numerical results are the broken red line. The numerical simulation was performed for an acoustic excitation of 94 dB, however, the non-linear effects of the liner seen in Fig. 7.5 would not be noticeable at this level. The numerical simulation predicted a peak transmission loss of 38.1

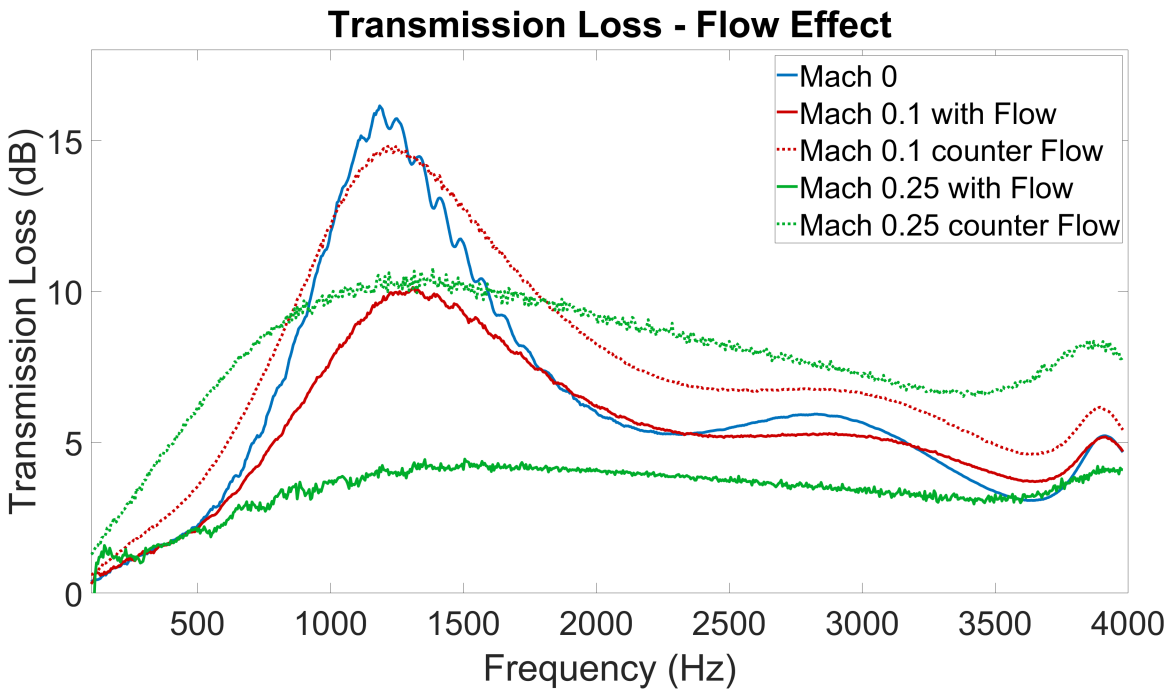

Figure 7.6: Transmission loss performance of the T-Liner as a result of flow conditions at 140 dB measured experimentally in LAUM. With-flow acoustic excitation is shown by a solid line and counter-flow acoustic excitation is shown by a broken line.

dB at 1080 Hz, with a secondary peak of 20.7 dB at 3070 Hz. Between the two peaks, there were a number of artefacts in the data, most likely arising from the modelling of the thermo-viscous acoustics in the perforations of the T-Liner. As was seen in Section 4.3, the grazing incidence numerical modelling was more susceptible to the excess losses being measured due to the physics and meshing selection in features.

The experimental data, seen previously in Fig. 7.5, has a transmission loss peak of 27.7 dB at 1055 Hz, with a secondary transmission loss peak of 9.8 dB at 2890 Hz. There is a reduction in the magnitude and frequency of the transmission loss between the numerical and experimental data. The numerical and experimental results both indicate high transmission loss between 1 kHz and 1.1 kHz, with a secondary peak around 3 kHz. These regions are shown in the figure by the green box. As was reported in Section 6.3, the perforations in the faceplate and septum of the T-Liner printed smaller than the design specification which was used in the numerical modelling. As can be seen in Table 6.4, the faceplate perforations were approximately 6.6% smaller in diameter than in the design, and the septa perforations were 8.3% smaller. As a result, while the numerical simulation shows the performance of the idealised liner that matches the design from Chapter 5, the liner experimentally tested

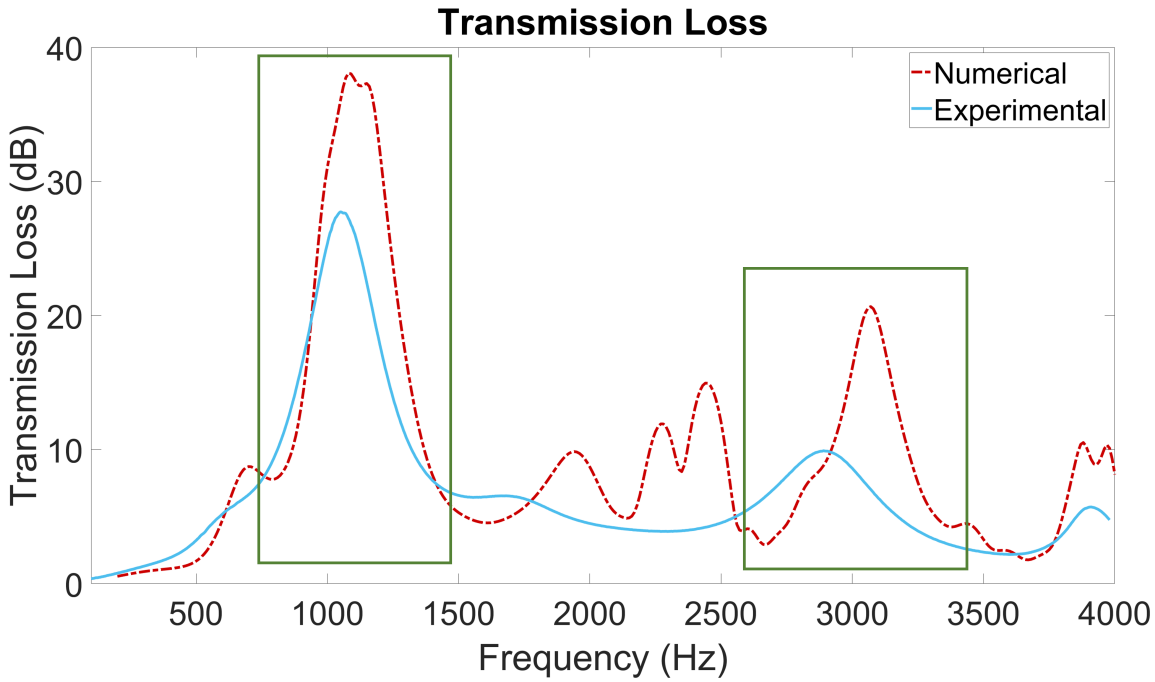

Figure 7.7: Comparison of the transmission loss measured experimentally in LAUM and predicted by the numerical simulation in TCD.

has a slightly different internal geometry. It is also possible that not all the perforations and channels may not be completely clear. A similar flattening of the experimental results compared to numerical data was noted in Kennedy et al. [187] when the cross-section of cavities was not completely vacated and when the surfaces are not perfectly smooth. It was noted to the authors that during the preparation of the liner for testing, it was difficult to mount without any leakage due to the test article comprising three separate components, and the quality of the interfacing surfaces of the components.

The acoustic impedance of the T-Liner was also measured experimentally in LAUM using the inverse method described in 3.2 as it provides a cleaner result compared to direct eduction over the lined section. The effect of the incident SPL and the background mean flow in the duct were examined, using the same test points that were seen in the Transmission Loss measurements. Figure 7.8 shows the effect of the incident SPL. The real component of the impedance is given in Fig. 7.8a and the imaginary component of the impedance is given in Fig. 7.8b. The impedance is on the vertical axis and the frequency in Hertz, Hz, is given on the horizontal axis. The 100 dB SPL is shown in blue, the 120 dB SPL is shown in red, the 130 dB SPL is shown in green and the 140 dB SPL is shown in black. The T-liner proposed shows strong resistive behaviour which exhibits non-linear effects as the incident SPL is increased.

At higher SPL there is an induced flattening around 2 $\rho_0 c_0$. This flattening is also observed in the reactance, though to a lesser extent. Additionally, it can be seen that for all incident SPL, the reactance is 0 at frequencies corresponding to the spikes in transmission loss seen in Fig. 7.7.

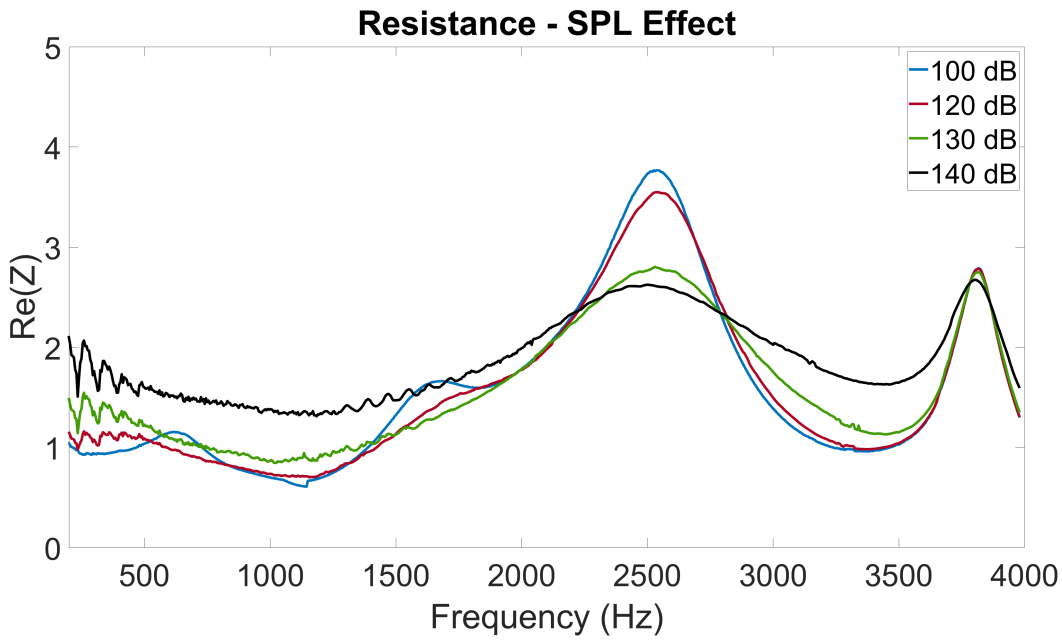

(a) Real component of the acoustic impedance.

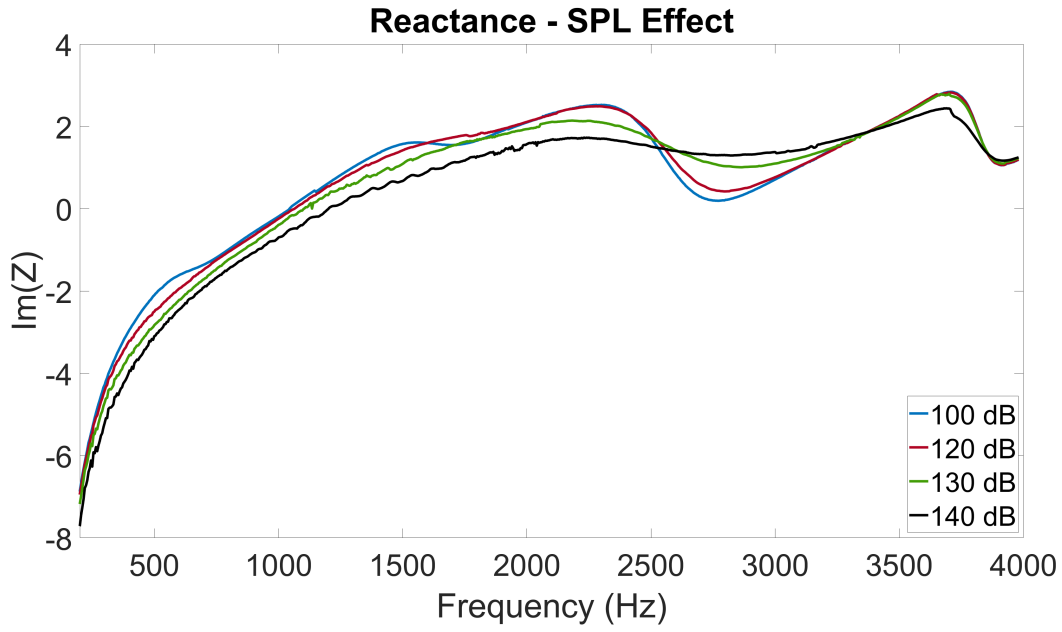

(b) Imaginary component of the acoustic impedance.

Figure 7.8: Comparison of the Fig. 7.8a resistance and Fig. 7.8b reactance measured experimentally in LAUM.

Figure 7.9 shows the effect of the flow on the impedance of the T-Liner. The real component of the impedance is given in Fig. 7.9a and the imaginary component of the impedance is given in Fig. 7.9b. The impedance is on the vertical axis and the frequency in Hertz, Hz, is given on the horizontal axis. The performance of the T-Liner was tested at 140 dB for three Mach speeds, for with-flow and counter-flow acoustic excitation. The Mach 0 results are shown in blue, the Mach 0.1 results are shown in red and the Mach 0.25 results are shown in green. For Mach 0.1 and Mach 0.25, the solid line represents the with-flow acoustic excitation and the broken line represents the counter-flow acoustic excitation. It is seen that there is a significant increase in the resistance with the introduction of the background mean flow. In particular, the counter-flow test shows the greatest overall increase to the resistance. The reactance is flattened by the introduction of the flow, however, the impact on the reactance is less pronounced than is seen in the resistance. There is also very little difference between the counter-flow and with-flow tests for the reactance.

As was seen in the experimental results from the GIIT at TCD in Section 7.2.1, the first peak of the transmission loss of the T-Liner is expected to be in the 800 Hz to 1200 Hz range, which is in agreement with the results obtained in LAUM. Additionally, the flow tests performed in LAUM reveal that the T-Liner performs well in a counter-flow configuration at M = 0.1 to M = 0.25, with the transmission loss peak flattening into higher broadband transmission loss as the Mach speed increases. The counter-flow configuration corresponds to the flow conditions experienced by an inlet acoustic liner in the ANCF. The ANCF has a range of test speeds which have an inlet flow speed between M = 0.1 and M = 0.2 with a nominal operational speed of M = 0.15. The T-liner examined is a highly resistive treatment with an acoustic behaviour that is quite sensitive to the flow direction and shows non-linear effects.

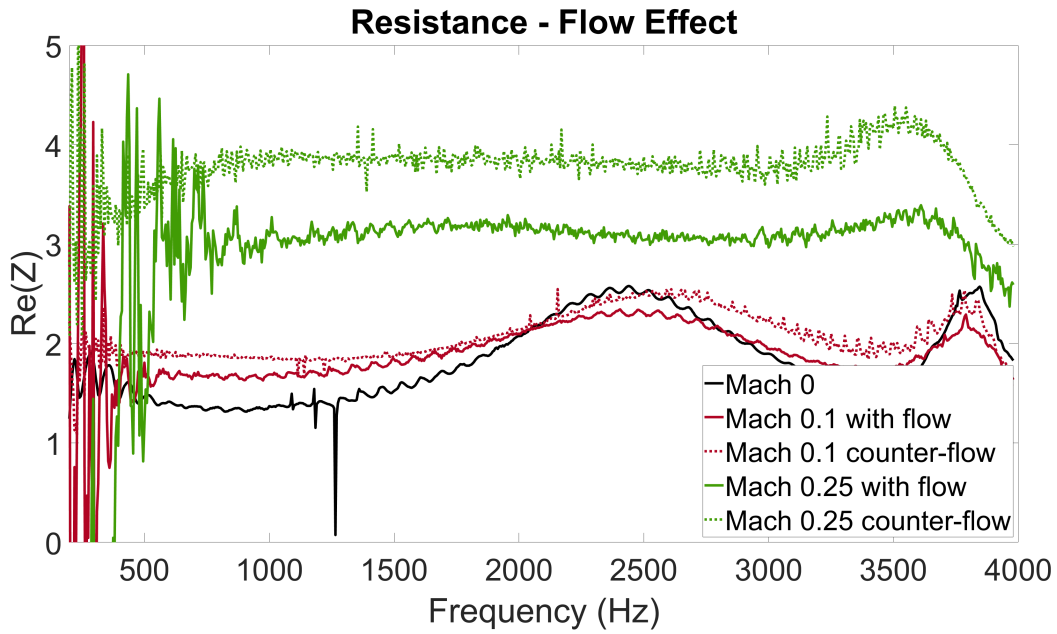

(a) Real component of the acoustic impedance.

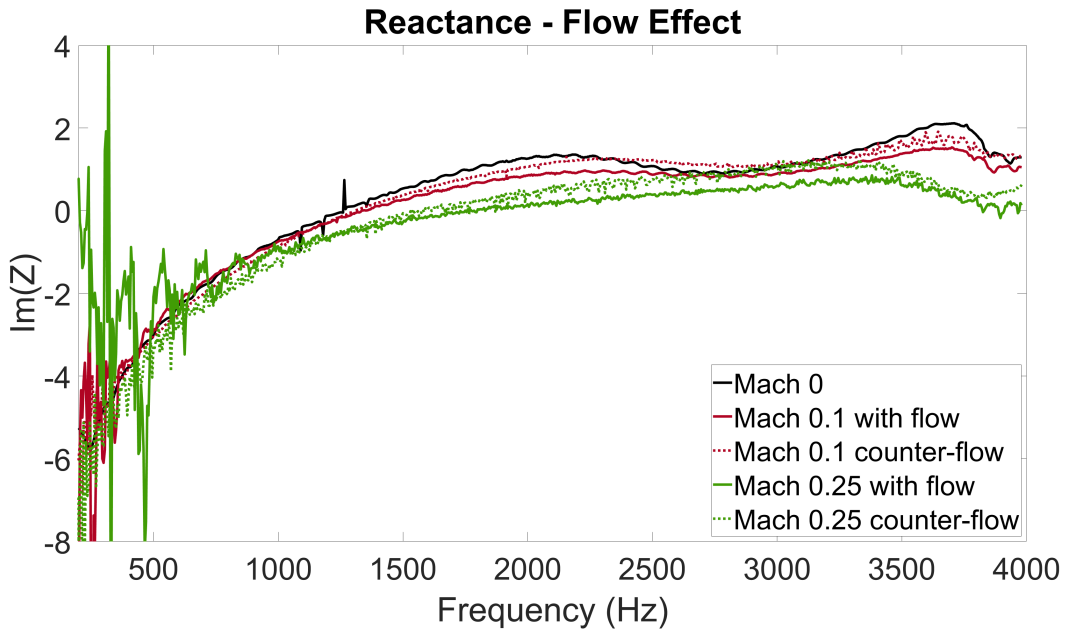

(b) Imaginary component of the acoustic impedance.

Figure 7.9: Comparison of the Fig. 7.9a resistance and Fig. 7.9b reactance measured experimentally in LAUM.

7.3 ANCF

All test articles which were installed in the ANCF in this work were designed and manufactured in TCD. In order to completely fill the test section of the ANCF, 237 components are required which are described in Section 5.4 and an additional 13 samples were produced in

case any components were damaged during the shipping or installation. Of the 250 components that were manufactured, 166 were Part A components and 84 were Part B components.

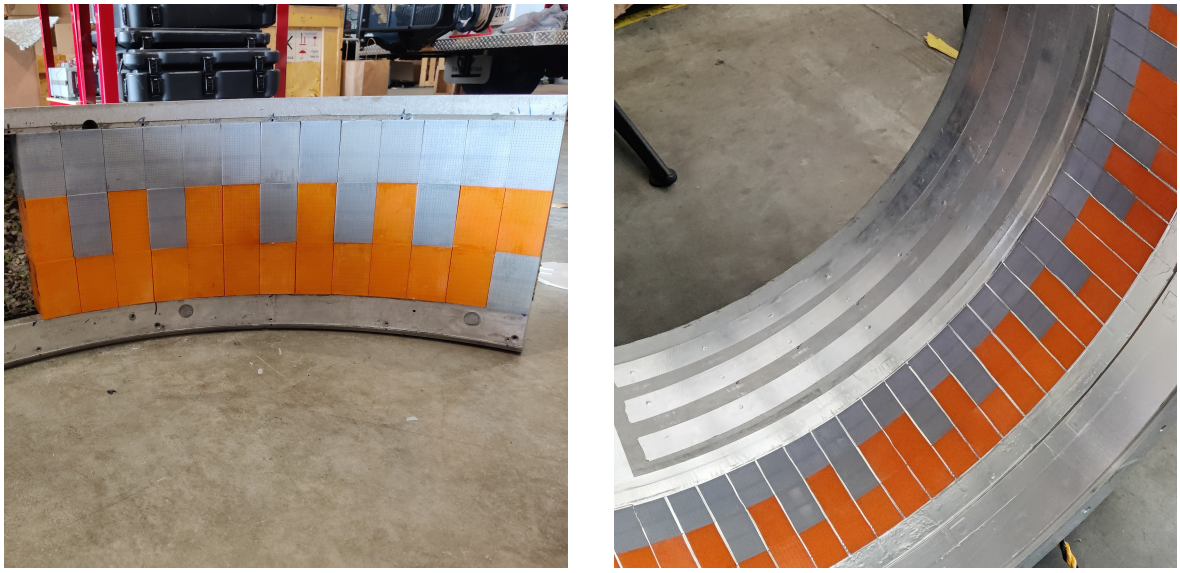

(a) T-Liner installation test

(b) T-Liner final installation

Figure 7.10: Installation of the T-Liner in the ANCF casing.

The installation of the T-Liner was achieved without the use of a coarse metal facesheet. A metal facesheet is often used to help hold a test article in place in the liner casing, however, as the T-Liner was designed with a specific POA which the metal facesheet would adversely affect it was not used. The T-Liner was primarily held in place in the casing by the wedged nature of the design and the very tight fit of the components. An adhesive was additionally used between components in the axial and spanwise directions, but not between the liner and the casing. While installing the T-Liner casing, the position of each component was carefully laid out. Due to the very tight fit of the T-liner within the casing, and very small variations along the inner surface of the casing, the ends of Part A components that were in contact with the casing often had to be sanded down to fit without damaging the liner. Figure 7.10a shows a close-up of the liner during the process of setting the position of the components in the casing. The grey components seen were produced using the Elegoo printers and the orange components were produced using the Prusa printers; the pattern of the components in the casing was specifically chosen to minimise the risk of the different components behaving differently and impacting the overall performance of the liner. The components were set in a systematic pattern to create a liner that would behave uniformly.

Figure 7.11: Completed liner installation in the casing prior to being attached to the ANCF.

After the liner was completely installed in the casing, aluminium tape was applied along the interface of all of the components in the axial direction. This ensured there were no gaps present between the segments of the liner. This can be seen in Fig. 7.10b. The aluminium tape was not applied along the interface of the components in the circumferential direction as a tighter seal was possible in between the components due to the compression of the components in this direction during the installation process. Aluminium tape was additionally added to the fore and aft of the liner test to ensure a smooth transition from the casing to the liner section. The full T-Liner installation in the ANCF casing can be seen in Fig. 7.11. The completed liner was attached to the ANCF prior to moving the rig to the outdoors test

facility located at the White Field Research Facility where acoustic testing is performed as described in Section 3.3.

The acoustic measurements were performed as described in Section 3.3, with a far-field microphone array. The microphones were set at a radius of 6.1 m (20 ft) from the ANCF. All 30 microphones were placed in the fore location, in front of the ANCF inlet with a microphone spacing of 3.2°, spanning from the centre line of the ANCF at 0° to just past the inlet at 93.2°. The rotor was configured with 16 blades at a pitch angle of 28°, and the stator configuration of 14 vanes. Acoustic measurements were performed at 6 fan speeds between 1500 RPM and 2000 RPM, in 100 RPM increments. An additional static test was performed at 0 RPM at the beginning and end of the testing which provides an ambient SPL reading for the tests.

The acoustic testing was performed for the T-Liner and for a hardwall treatment. The hardwall is the baseline measurement which is used to assess the performance of the T-Liner. For the hardwall test, the T-Liner was covered using aluminium tape. An example of the ANCF spectra can be seen in **??**; the spectra for the baseline configuration is shown in black in Fig. 7.12a and the spectra of the liner configuration is shown in green in Fig. 7.12b.

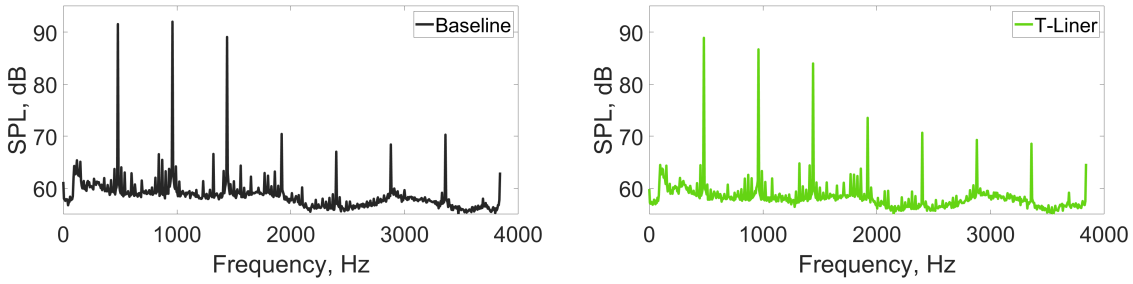

(a) Baseline spectra at 1800 RPM

(b) T-Liner spectra at 1800 RPM

Figure 7.12: Example of the (a) baseline and (b) liner spectra of the ANCF at a test speed of 1800 RPM.

The fan tones can be seen by the periodic sharp increases in the SPL. These tones are a function of the number of blades in the fan, B, and occur at shaft orders which are integer multiples of B. The shaft order can be converted to frequency by multiplying by the test RPM and dividing by 60, $RPM/60$. As a result of this, the frequency at which the fan tones occur increases with increasing fan speed.

While the T-Liner is designed to attenuate broadband noise, there is a frequency at which its performance is highest as indicated by the transmission loss peak. In Section 7.2.2 it was shown that the frequency at which the T-liner performs best is dependent on the incident

SPL and flow conditions. The preliminary testing in the GIIT, the greatest transmission loss occurred at 810 Hz while testing in the OD indicated the peak could occur as high as 1.2 kHz for an incident SPL of 140 dB with a counter-flow mean flow of M = 0.25. The T-liner will perform best at a test RPM where the frequency of a fan tone corresponds to the frequency of the transmission loss peak. In the ANCF testing, the highest inlet flow speed was approximately M = 0.2. To determine the fan speed at which the frequency response of the T-liner and the fan tone match, a direct comparison of each test point was necessary.

For each of the test points, the 2BFP occurred within the 810 Hz to 1.2 kHz frequency range. The spectra centred on the 2BFP were isolated for each test speed between 1500 RPM and 1800 RPM which is seen in Fig. 7.13. 2A comparison of the full spectra of the T-Liner at each of the tested RPMs can be seen in Fig. C.1. The recorded SPL in decibels, dB, is on the vertical axis and the frequency in hertz, Hz, is on the horizontal axis. The baseline for each test speed is shown in the solid black line for each speed. The corresponding liner is shown: in solid green for 1500 RPM; in solid blue for 1600 RPM; in solid cyan for 1700 RPM; in solid pink for 1800 RPM; in solid orange for 1900 RPM; in solid red for 2000 RPM. The most significant reduction is seen in the 1800 RPM test point, which is the nominal operating speed of the ANCF. This speed is the primary focus of the in-depth analysis of the liner's performance, for the entire microphone array.

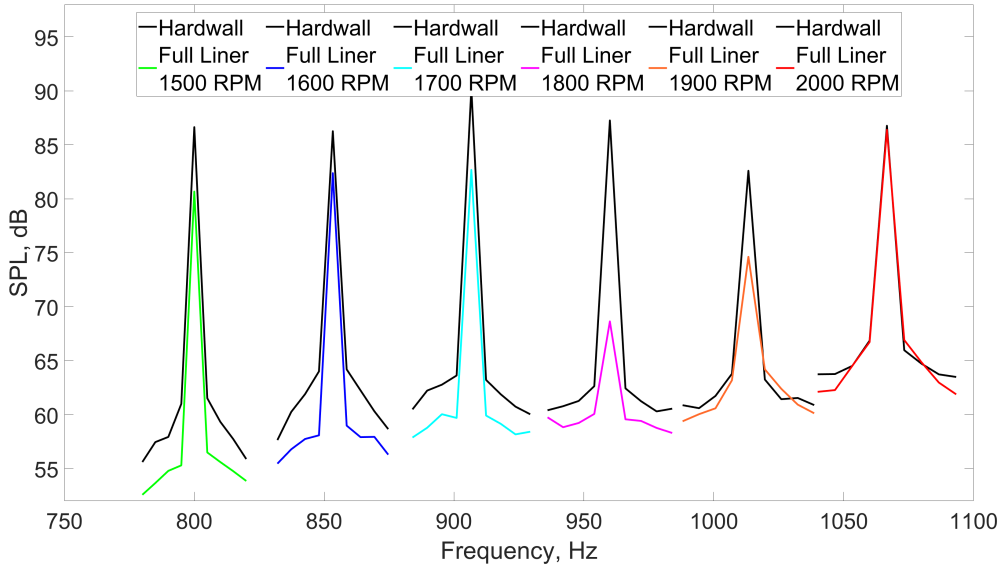

Figure 7.13: Comparison of the Hardwall and Liner SPL in decibels at the 2BFP for each RPM test point.

At all fan speeds, significant broadband noise reduction is observed in the frequency range between the first and third BPF. This corresponds to the frequency range that the T-Liner displayed the first peak in the transmission loss which was seen in Fig. 7.6. At most RPM the subharmonic tones of the 2^{nd} BPF are reduced significantly, in some instances resulting in the amplitude of the subharmonics only being 2-3 dB greater than the broadband level.

The most significant reductions are observed for the fan speeds which have a BPF close to 1000 Hz. These are fan speeds of 1700 RPM, 1800 RPM and 1900 RPM. The grazing incidence results from both TCD and LAUM both identified the frequency range of 800 Hz to 1200 Hz as the range where the T-Liner performance is greatest. Of these three speeds, the RPM with the greatest tonal reduction is the 1800 RPM in which the 2^{nd} BPF is almost completely eliminated. This result is in line with the predictions from the preliminary grazing incidence testing that was performed in TCD and LAUM.

The experimental results from TCD, seen in Fig. 7.4 experienced a transmission loss peak at 810 Hz for an incident acoustic field of 90 dB. The LAUM data seen in Fig. 7.5 shows that as the amplitude of the incidence acoustic field increases, the frequency of transmission loss peak also increases. With the T-Liner installed so close to the fan in the ANCF, the acoustic field present at the surface of the liner would be greater than is measured by the far field array. The frequency of the peak is further increased to a degree in the presence of flow. While the frequency of the peak transmission loss seen in LAUM is slightly above 1 kHz, the version of the T-Liner examined in that test was shorter in length than the configurations tested in TCD and the ANCF.

7.3.1 Directivity

To examine the T-Liner's ability to reduce the radiated fan noise generated by the ANCF, the directivity of the insertion loss was measured. The insertion loss is the difference in SPL between the T-Liner measurement and the baseline measurement, which is obtained by subtracting the T-Liner data from the hardwall data at each microphone location. The resulting data set is used to generate the directivity plots seen in Figs. 7.14 to 7.19. The frequency in Hertz is shown on the vertical axis; the azimuthal angle of the microphone location is shown on the horizontal axis, and the colour axis gives the SPL difference in decibels. A positive value for the SPL difference indicates where the liner reduced the noise and a negative value indicates an increase in SPL. During testing, two of the microphone inputs were faulty. These locations are at azimuthal angles 67.6° and 73.5°, and are marked

by a broken white line in Fig. 7.14. In all images, these microphones can be seen as bands of a constant colour measuring 0 dB in the SPL reduction as the SPL difference in these microphone locations is set to zero for the full frequency range.

The scale of the colour bar is fixed between -1 dB and 5 dB. Across the full range of frequencies and microphone locations, SPL reductions greater than 5 dB are present, particularly at the BPFs. However, in order to display the broadband behaviours of the T-Liner the range is set to the same order of magnitude as the broadband reduction. The "hot patches" observed in the data indicate areas where the SPL reduction is clipped at 5 dB. The narrow hot patches indicate a particular frequency that is being significantly reduced, which is mostly seen at the BPF. Broader hot patches indicate there is a broader level of noise reduction, where tones near the BPF are also significantly reduced. This is seen more in the lower RPM tests.

The directivity of the SPL reduction shows a similar pattern at all test RPM. At all RPM, except 2000 RPM, there is a significant reduction to the 2^{nd} BPF across the full range of angles. In general, the broadband performance is greatest when moving away from the centre-line axis of the ANCF. Figure 7.17, the directivity of the 1800 RPM test, displays the most broadband noise reduction along both the frequency range and the location range. This is the fan speed that displayed the greatest broadband and tonal reduction in Fig. C.1. At 1800 RPM, the 2^{nd} BPF occurs in the frequency range previously identified as the optimal frequency range for transmission loss by the T-Liner. Additionally, the inlet flow speed at 1800 RPM is approximately Mach 0.15. In Section 7.2.2 it was noted that as the Mach speed of the flow increased from M0.1 to M0.25, the transmission loss of the T-Liner flattened, reducing the peak performance but increasing the broadband performance. The inlet flow speed of Mach 0.15 is on the lower end of the speeds that were tested, indicating that there would still be a small peak to the overall performance of the liner.

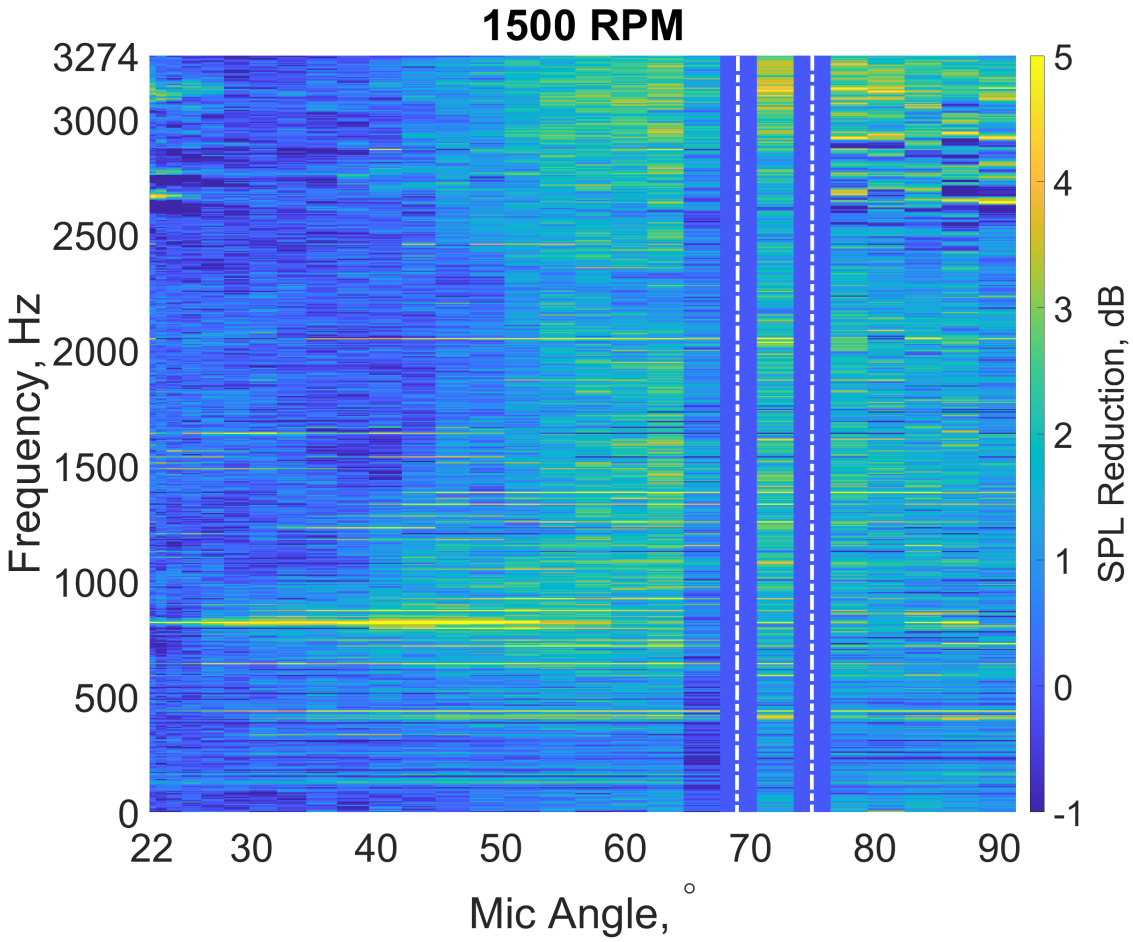

Figure 7.14: Directivity plot of the difference in SPL between the baseline measurement and full liner measurement measured at 1500 RPM. Angles for microphone measurements are corrected to the azimuthal angle.

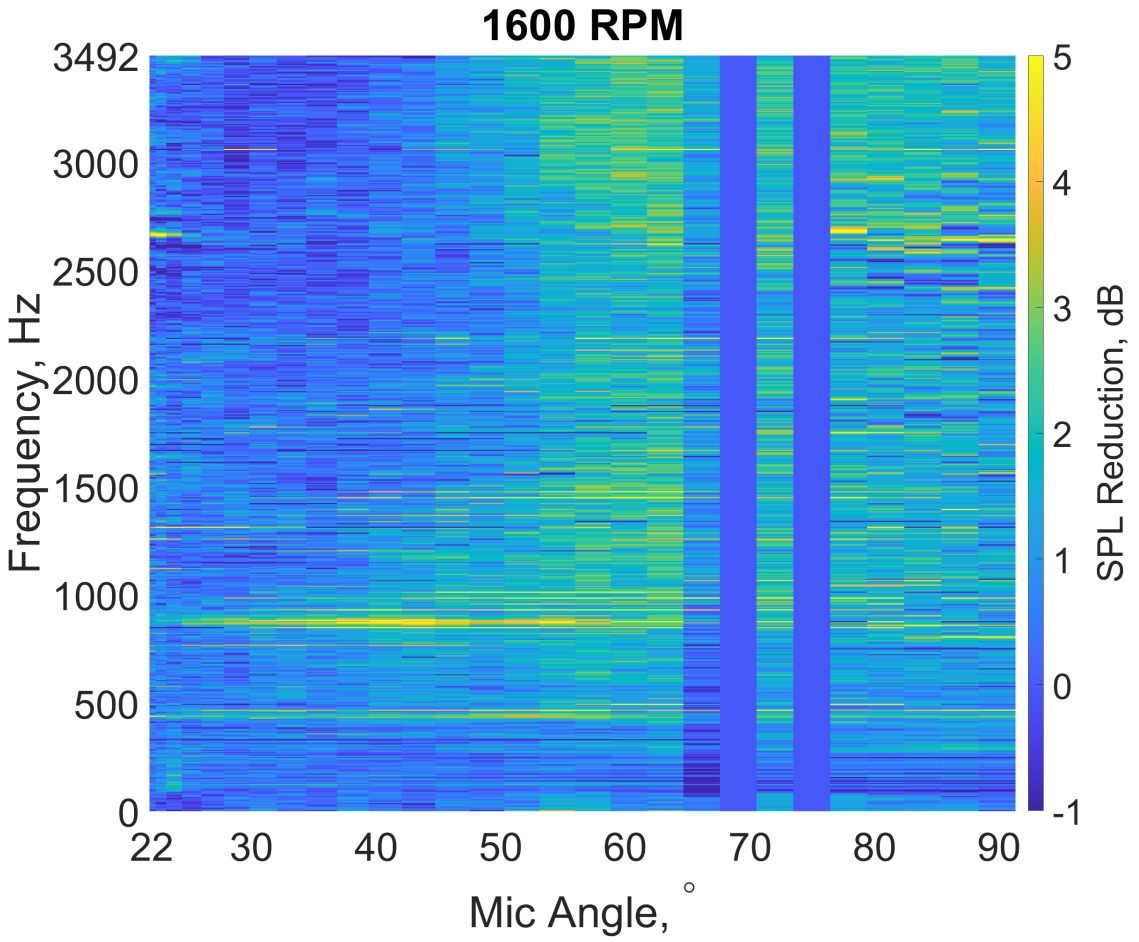

Figure 7.15: Directivity plot of the difference in SPL between the baseline measurement and full liner measurement measured at 1600 RPM. Angles for microphone measurements are corrected to the azimuthal angle.

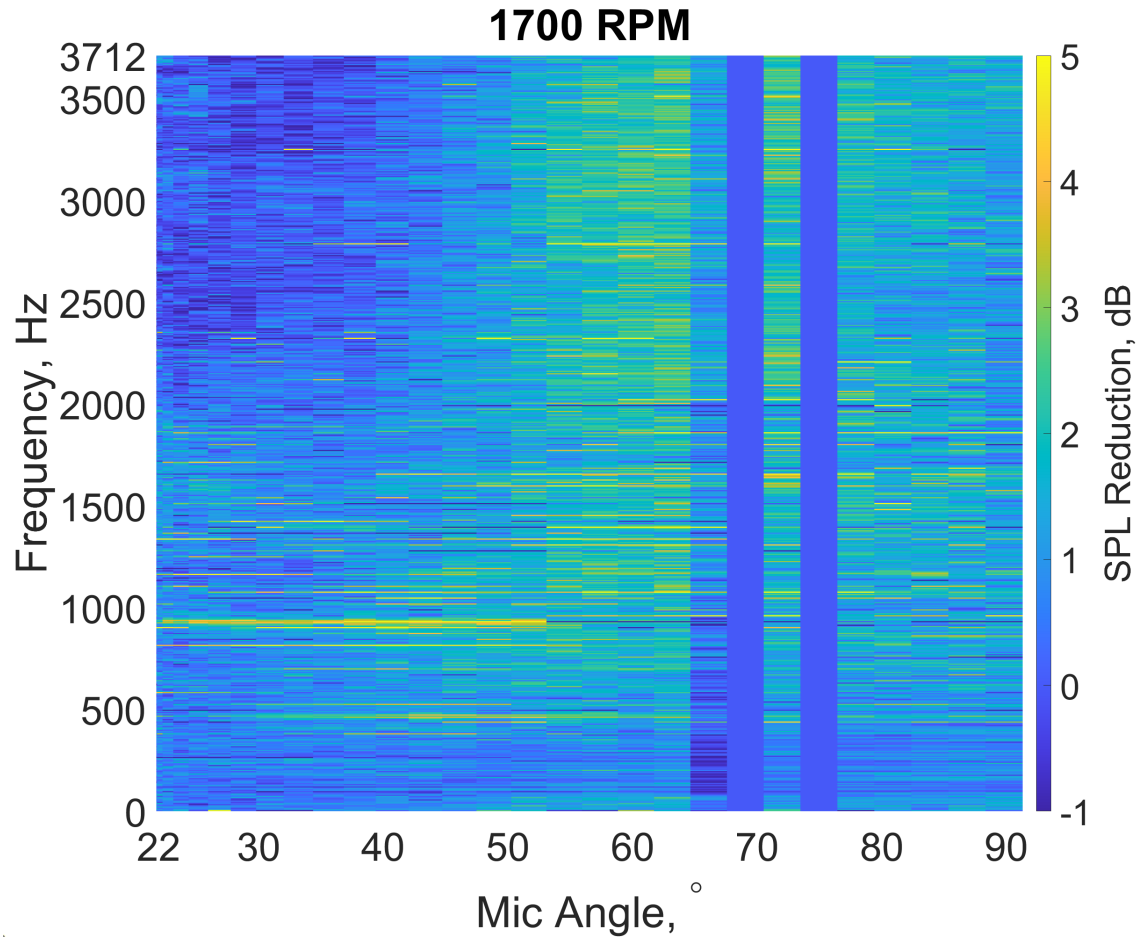

Figure 7.16: Directivity plot of the difference in SPL between the baseline measurement and full liner measurement measured at 1700 RPM. Angles for microphone measurements are corrected to the azimuthal angle.

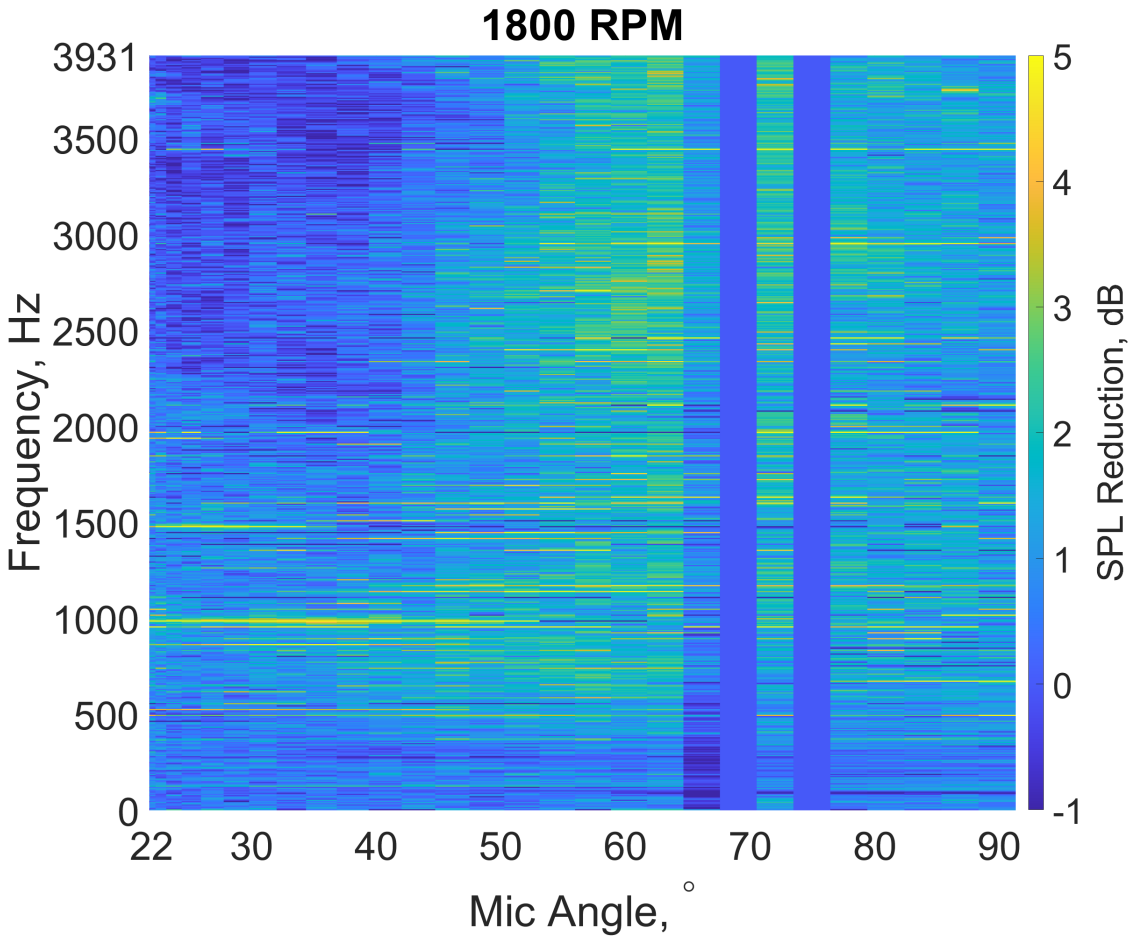

Figure 7.17: Directivity plot of the difference in SPL between the baseline measurement and full liner measurement measured at 1800 RPM. Angles for microphone measurements are corrected to the azimuthal angle.

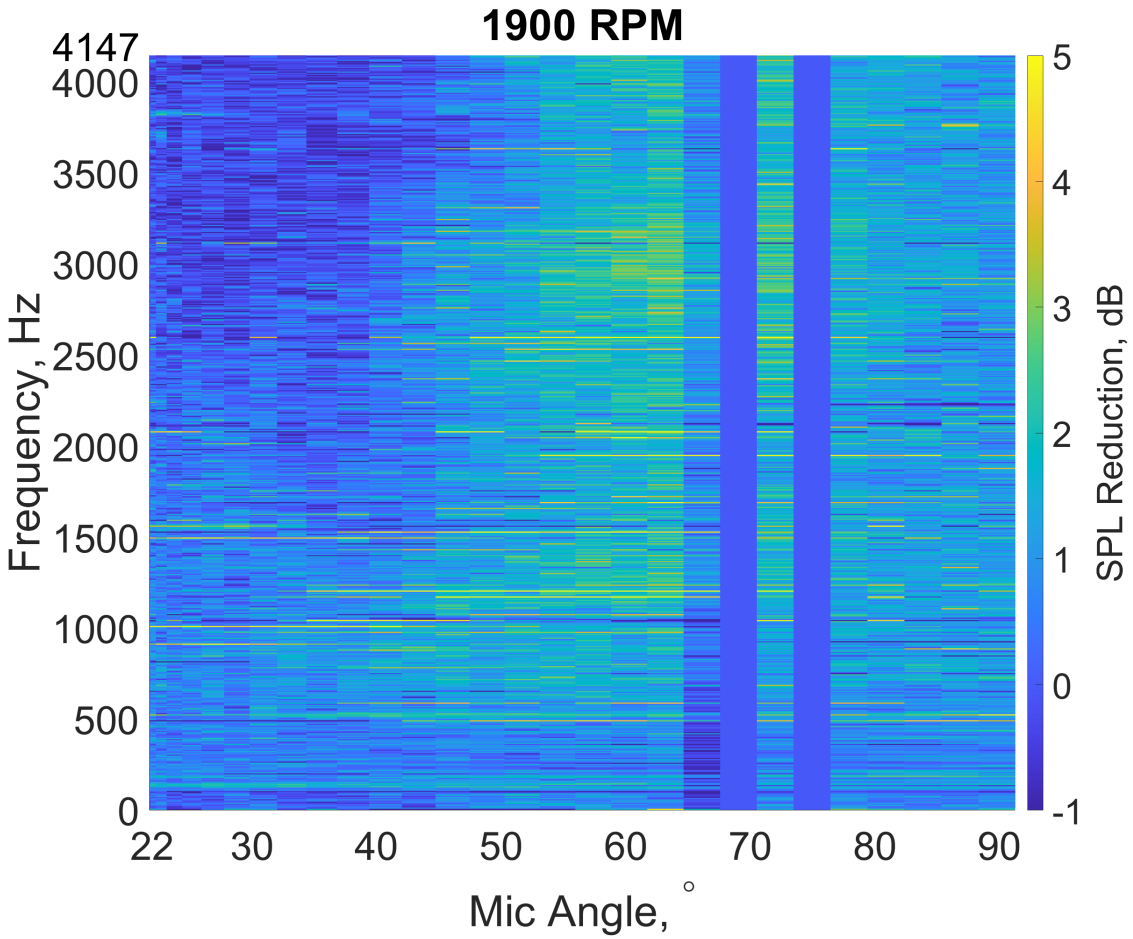

Figure 7.18: Directivity plot of the difference in SPL between the baseline measurement and full liner measurement measured at 1900 RPM. Angles for microphone measurements are corrected to the azimuthal angle.

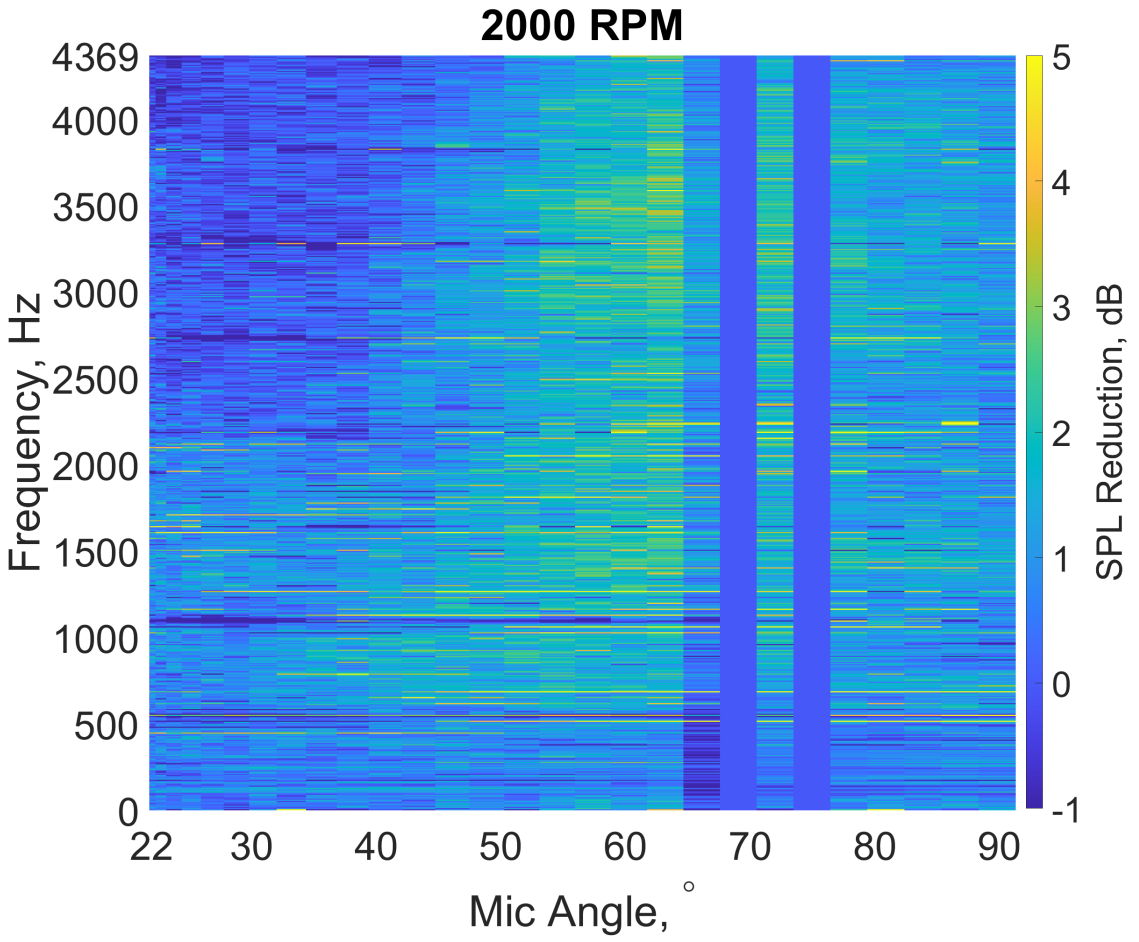

Figure 7.19: Directivity plot of the difference in SPL between the baseline measurement and full liner measurement measured at 2000 RPM. Angles for microphone measurements are corrected to the azimuthal angle.

7.3.2 Performance at 1800 RPM

The performance of the T-Liner at a fan speed of 1800 RPM is capable of both high tonal noise reduction and broadband noise reduction across a wide range of angles relative to the ANCF. In Fig. 7.20, the spectra of the T-Liner and the baseline measurements can be seen which allow both the tonal and broadband performance of the liner to be assessed. Figure 7.20a presents the spectra recorded at microphone location 13, which is at an angle of 43.5°. Figure 7.20b presents the spectra recorded at microphone location 16, which is at an angle of 52°. The SPL in decibels, dB, is on the vertical axis and the frequency in Hertz, Hz, is on the horizontal axis.

In Fig. 7.20, the baseline data is shown by the broken blue line. The T-Liner data is shown by the solid red line. The annotations in blue show reductions in the SPL recorded at tones, while the annotations in green show the reduction in the OASPL reduction.

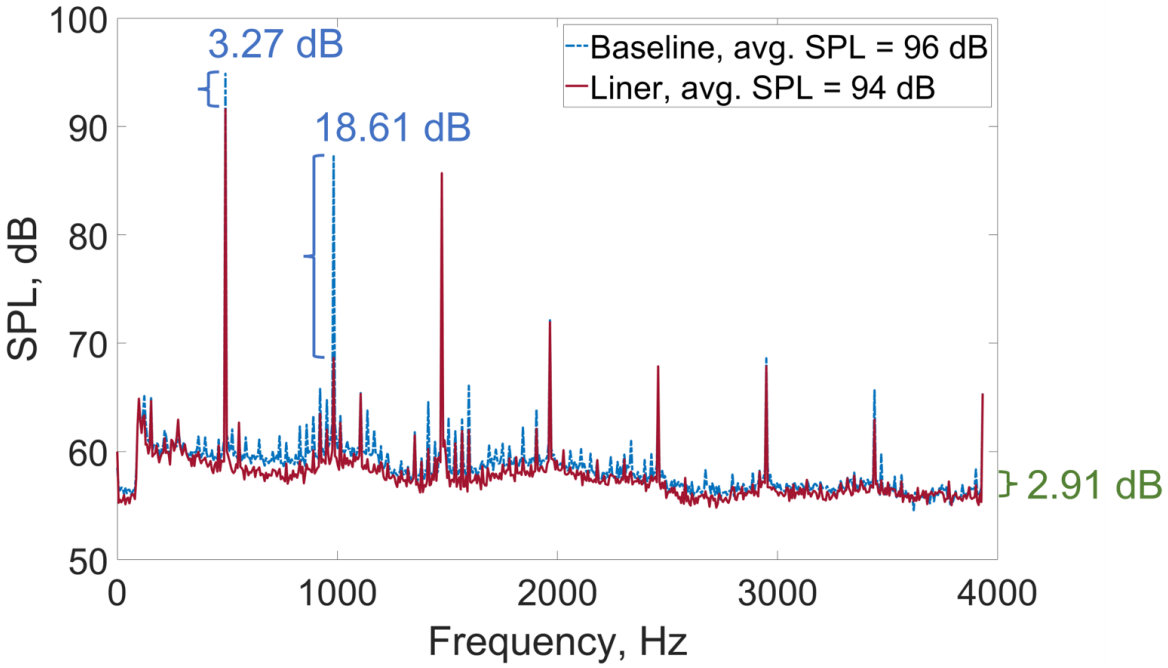

(a) Spectra at microphone location 13

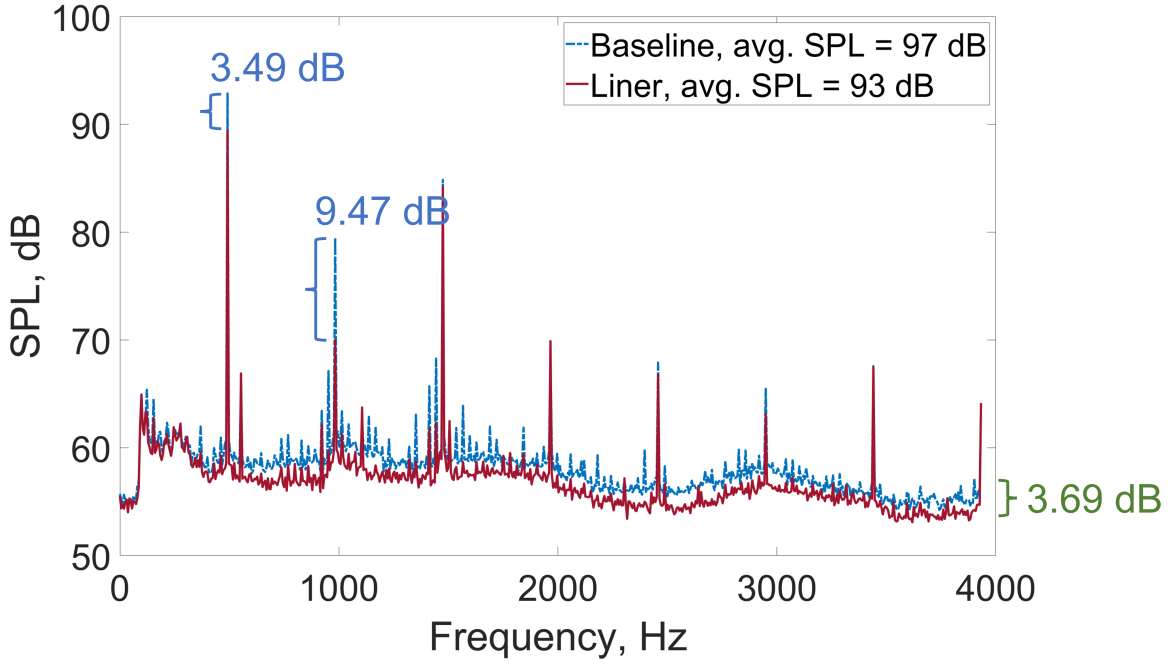

(b) Spectra at microphone location 16

Figure 7.20: Spectra for the individual microphone measurements at locations 13 and 16, at 1800 RPM. The baseline measurement is shown in the broken blue line and the liner measurement is shown in red.

The average SPL across the full frequency range and overall microphone locations is 94.0 dB for the baseline configuration. The average SPL reduction for the full-liner configuration is 91.4 dB. The resulting average SPL reduction by the liner is 2.6 dB. While the highest broadband noise reduction is observed at higher azimuthal angles, the liner reduces the tones generated by the first and second blade passing frequency significantly at lower azimuthal angles.

The greatest tonal reductions were observed at microphone location 13 (mic13), corresponding to an azimuthal angle of 43.5°. The greatest overall broadband reduction was observed at microphone location 16 (mic16), corresponding to an azimuthal angle of 52°. The individual spectra at both of these locations, for both the baseline and liner configurations, are shown in Fig. 7.20. The spectra for mic13 are seen in Fig. 7.20a and the spectra for mic16 are seen Fig. 7.20b. In Fig. 7.20a, the fundamental tone of the ANCF, located at 480 Hz, is reduced by 3.3 dB and the 2^{st} BPF, located at 960 Hz, is reduced by 18.6 dB. The average SPL across the entire frequency range is reduced by 2.9 dB. In Fig. 7.20b, the fundamental tone is reduced by 3.5 dB and the 1^{st} harmonic is reduced by approximately 9.5 dB. The average SPL across the entire frequency range is reduced by 3.0 dB. The overall noise reduction across the frequency range, and all microphone locations, is 3.7 dB. The significant reduction of the 2^{nd} BPF is expected as the tone occurs at approximately the same frequency as the peak of the transmission loss predicted in Fig. 7.5.

By removing the tonal contributions as described in Section 3.3.2, it is possible to directly compare the broadband behaviour of the liner in comparison to the hardwall. In Fig. 7.21 the broadband noise contributions can be seen for the spectra seen in Fig. 7.20. By directly comparing the broadband noise for the hardwall and liner cases, it is easier to better examine the use of the T-Liner as a broadband liner, or whether the performance is limited to the tonal noise. The SPL in decibels, dB, is on the vertical axis and the frequency in Hertz, Hz, is on the horizontal axis. In Fig. 7.20, the baseline data is shown by the broken blue line and the T-Liner data is shown by the solid red line.

For mic13, seen in Fig. 7.21a, the average SPL across the full frequency range for the baseline configuration is 58.6 dB and the average SPL for the T-Liner configuration is 57.4 dB. This is an average 1.2 dB reduction across the frequency range. It can be seen that at higher frequencies, the broadband performance of the liner is not as significant as it was at lower frequencies. For mic16, seen in Fig. 7.21b, the average SPL across the full frequency range

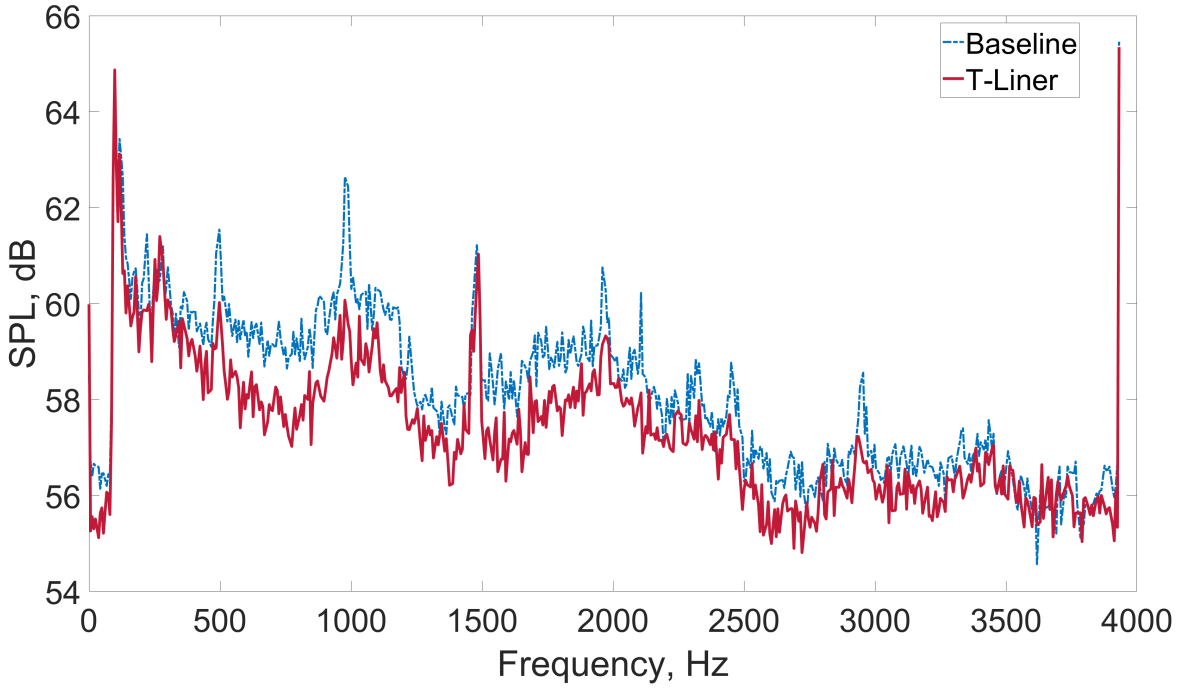

(a) Broadband spectra at microphone location 13

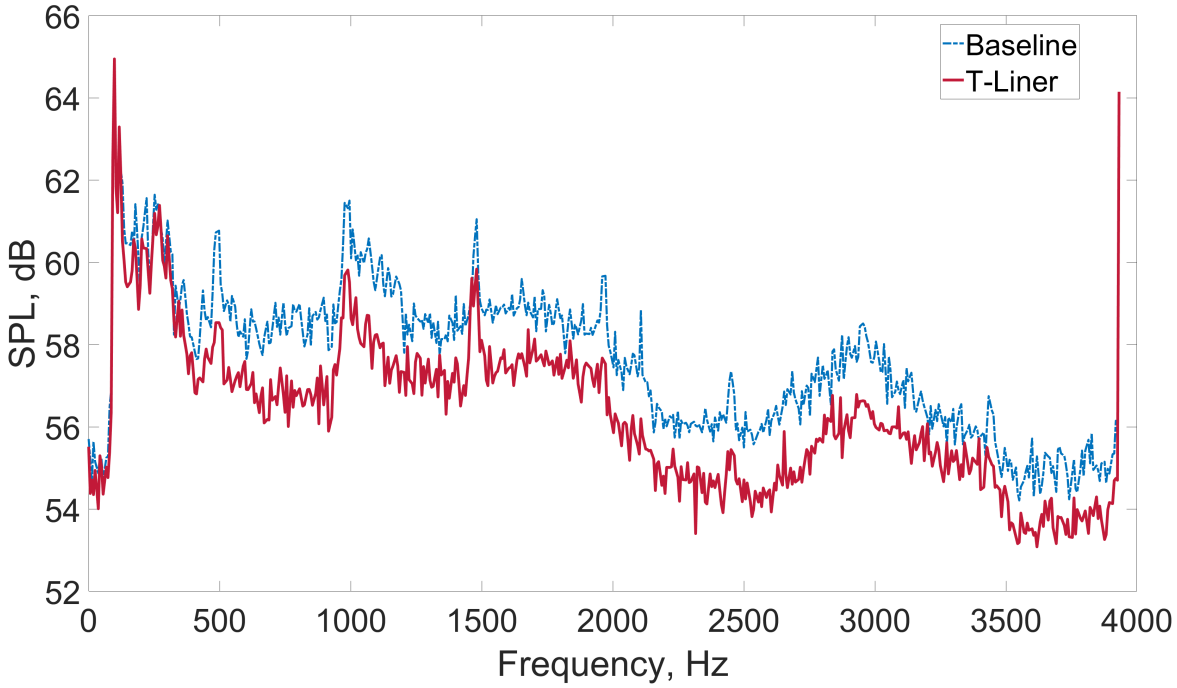

(b) Broadband spectra at microphone location 16

Figure 7.21: Broadband spectra for the individual microphone measurements at locations 13 and 16, at 1800 RPM. The baseline measurement is shown in the broken blue line and the liner measurement is shown in red.

for the baseline configuration is 58.1 dB and the average SPL for the T-Liner configuration is 56.7 dB. This is an average 1.4 dB reduction across the frequency range. In comparison

to the performance measured at mic13, the performance of the T-Liner at mic16 is more consistent, achieving similar levels of broadband noise reduction across the frequency range.

The ANCF measurements typically record an uncertainty of ±1 dB. The recorded SPL reductions by the T-Liner in comparison to the baseline configuration are small, particularly when taking into account the uncertainty in the measurements. The repeatability of the measurements performed on the ANCF to further assess the performance of the T-Liner, in particular the broadband behaviour.

7.3.2.1 Repeatability of ANCF Results

To determine the repeatability of the measurement performed on the ANCF the standard deviation across the measurements was determined. The standard deviation was determined using 4 data sets for the T-Liner measurements and 8 data sets for the baseline measurements for each of the individual microphone locations.

Figure 7.22 shows the standard deviation on the measurements at mic13. Figure 7.23 shows the standard deviation on the measurements at mic16. The sound pressure level in decibels, dB, is shown on the vertical axis and the frequency in hertz is on the horizontal axis. The standard deviation of the full spectra for the entire frequency range for mic13 is seen in Fig. 7.22a, and the performance of the liner at the tones corresponding to 1BPF and 2BPF can be seen in Figs. 7.22b and 7.22c respectively. Similarly, the standard deviation of the full spectra for mic16 is seen in Fig. 7.23a, and the performance of the liner at the tones corresponding to 1BPF and 2BPF can be seen in Figs. 7.23b and 7.23c respectively.

The low standard deviation observed, particularly on the T-Liner data shows a high degree of repeatability in the liner performance. In general, there is a gap between the upper limit of the Liner standard deviation and the lower limit of the baseline standard deviation. This is not the case in the 2BPF tone observed at mic16, seen in Fig. 7.23c, however, this is specifically seen at the tone and in the broadband behaviour seen in Fig. 7.23a there is a gap in the standard deviations of the liner and the baseline measurements.

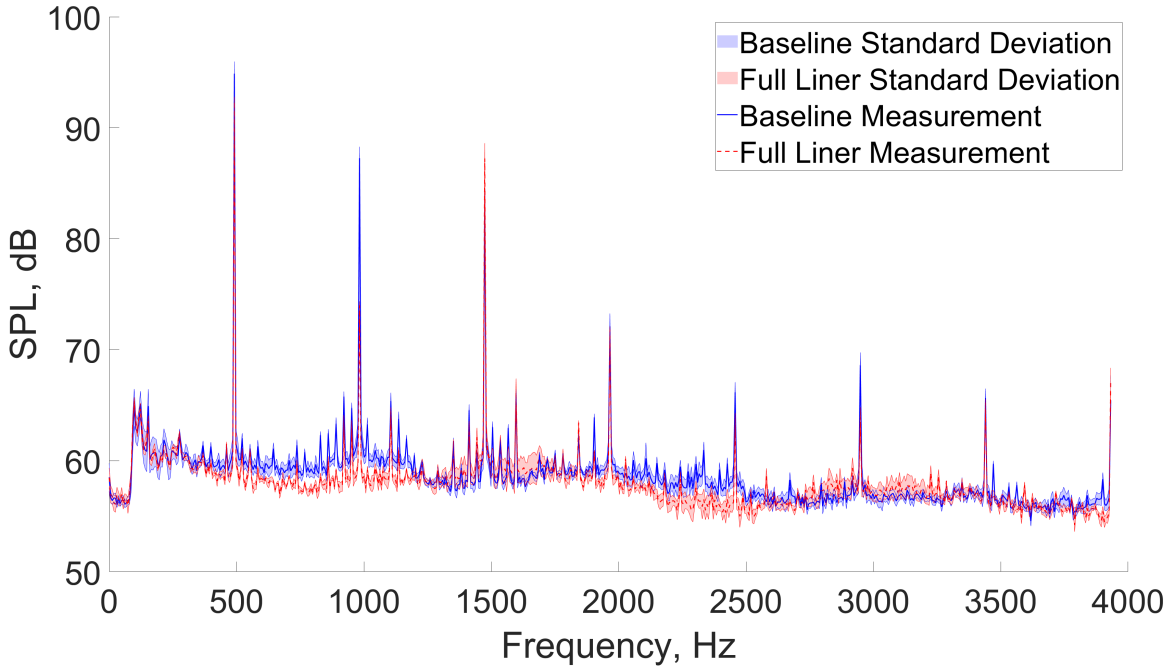

(a) Standard deviation of the full spectra

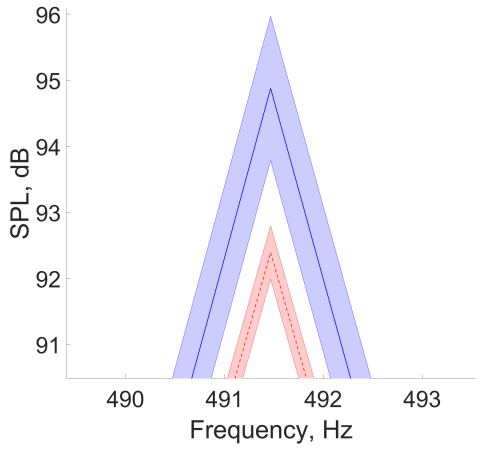

(b) Standard deviation of the 1BPF

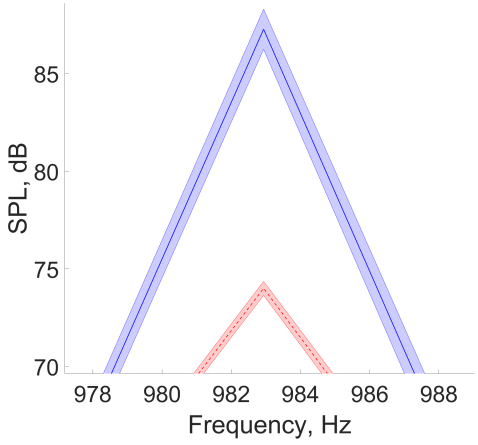

(c) Standard deviation of the 2BPF

Figure 7.22: Standard deviation of the baseline and liner measurements measured by mic13.

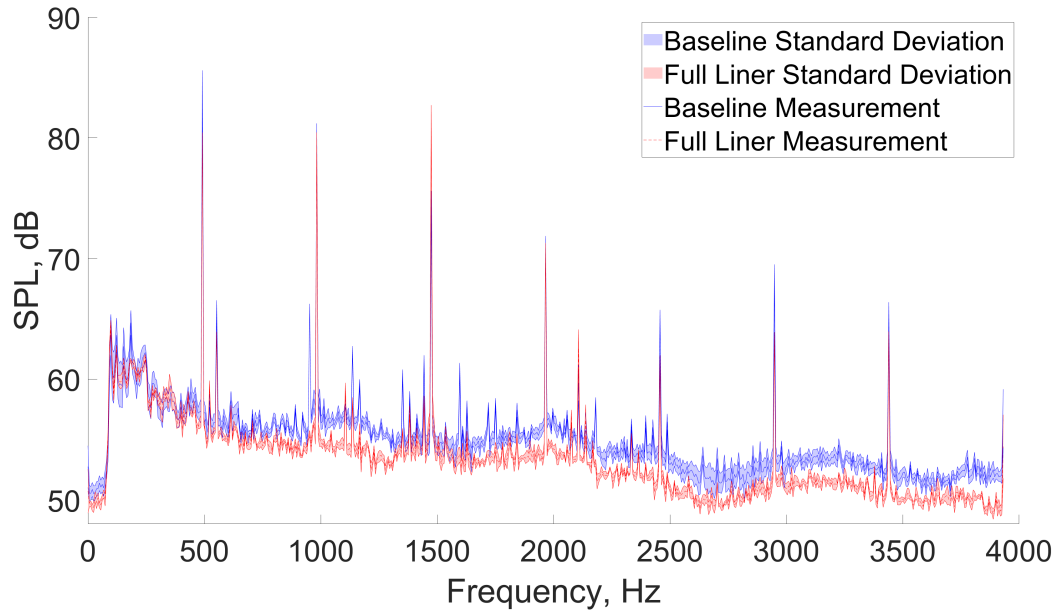

(a) Standard deviation of the full spectra

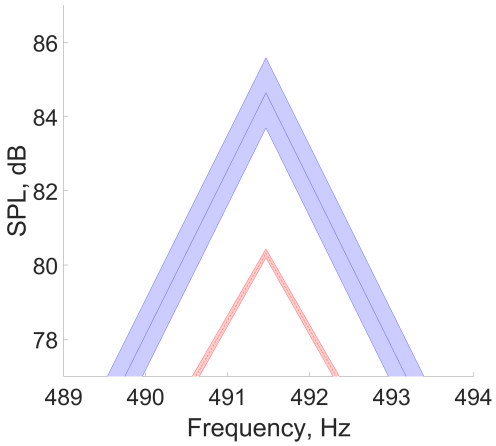

(b) Standard deviation of the 1BPF

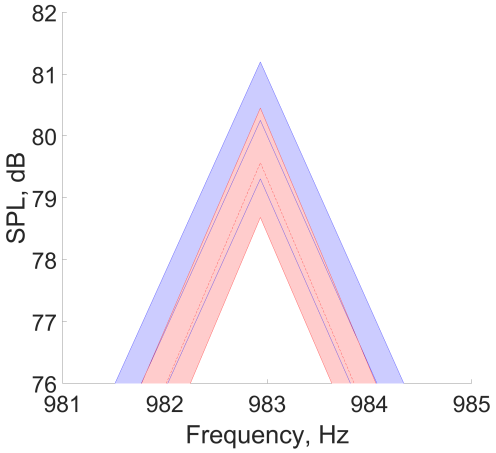

(c) Standard deviation of the 2BPF

Figure 7.23: Standard deviation of the baseline and liner measurements measured by mic16.

7.3.2.2 Sound Power Level Measurements

The overall performance of the liner is best seen in terms of the sound power level, PWL, across each of the harmonic bands described in Section 3.3.2. The PWL for each harmonic band is determined by integrating the individual microphone spectra over each of the harmonic bands and multiplying by the area. The PWL calculation had to be corrected for the microphone array used, accounting for the change in the area caused by using a fore-only microphone array. The overall PWL for each of the harmonic bands are given in Fig. 7.24, along with the sum. The tonal and broadband harmonic bands are given by Fig. 7.25 and Fig. 7.26 respectively, which separates the overall PWL into the tonal and broadband contributions. In Fig. 7.24 it can be seen the greatest reductions to the Overall PWL occur in the first and second harmonic bands. However, this is largely due to the significantly higher tonal PWL reductions that are achieved in these harmonic bands. In Fig. 7.26 it can be seen that the T-Liner has quite a consistent reduction in the broadband PWL. The greatest contribution to the overall reduction in the PWL is by the tonal PWL reduction in the 2^{nd} harmonic band where there is a reduction of 5.3 dB, as seen in Fig. 7.25. As a result of this, the overall PWL reduction for the 2^{nd} harmonic band is 4.7 dB. Across all harmonic bands, there was a 2.7 dB reduction in the overall PWL which is indicated by the Sum data set in Fig. 7.24. The sum reduction in the tonal PWL across all harmonic bands is 3.0 dB, and the sum reduction in the broadband PWL is 1.1 dB.

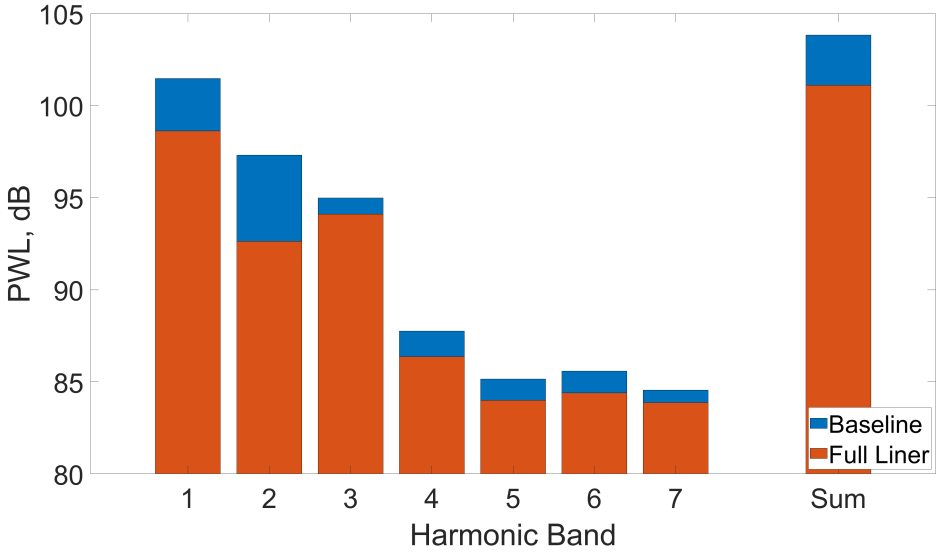

Figure 7.24: Overall PWL of each of the harmonic bands for the T-Liner compared with the baseline measurements measured at 1800 RPM.

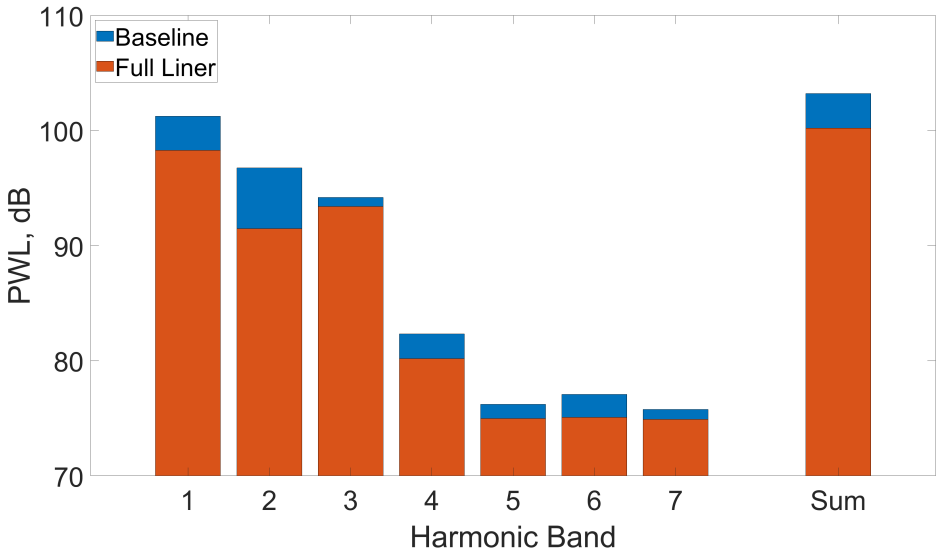

Figure 7.25: Tonal PWL of each of the harmonic bands for the T-Liner compared with the baseline measurements measured at 1800 RPM.

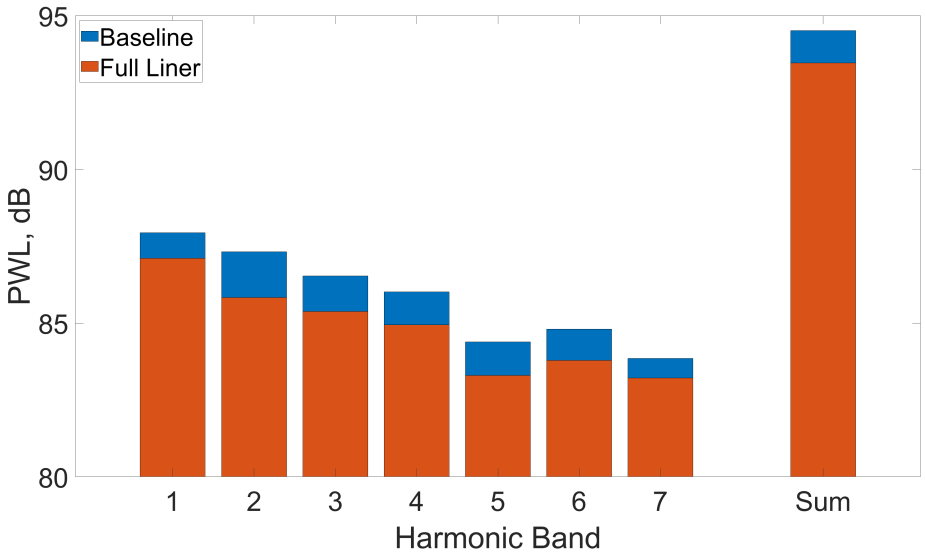

Figure 7.26: Broadband PWL of each of the harmonic bands for the T-Liner compared with the baseline measurements measured at 1800 RPM.

Summary

The T-liner design was tested in normal incidence as part of the multi-stage optimisation routine. During this testing, the absorption coefficient of the final T-Liner design with an integrated faceplate was found to have a maximum values of up to $\alpha = 0.97$ experimentally. It also has a very broadband response with a mean absorption coefficient value of $\overline{\alpha} = 0.73$ in

the 200 Hz to 2125 Hz range. In comparison, the optimised SDOF liner with the same liner depths only achieved a mean absorption coefficient $\overline{\alpha} = 0.51$ for the same frequency range.

The performance of the liner was subsequently assessed in two grazing acoustic incidence impedance tubes. The tests determined that the liner has a good broadband frequency response. In addition, the liner has a high bandlimited transmission loss centred around approximately 1 kHz, with values of 27.0 dB achieved at 100 dB incident sound levels at $M = 0$. The liner exhibited non-linear behaviours, as increasing sound levels resulted in an improved broadband response, albeit at the cost of some of the high performance at the peak. When tested with a grazing mean flow at 140 dB incident sound level, it was observed that an increasing flow velocity improved the broadband response of the liner, especially in the counter-flow direction. This would benefit the performance of an inlet liner attenuating fan noise. A transmission loss attenuation of at least 6 dB was measured in the 500 Hz to 4 kHz range was measured, with peak values of approximately 10 dB in the LAUM OD at Mach 0.25.

The T-Liner was tested in the ANCF and its performance was assessed at a range of fan speeds and radiation angles. The liner performed best at the nominal operating speed of the ANCF, at 1800 RPM. At 1800 RPM, the frequency of the 2BPF is the same as the peak transmission loss frequency determined during the testing in LAUM. At this speed, a tonal reduction of 18.6 dB at a radiation angle of 43.5° was measured. Both broadband and tonal noise PWL reductions of 1.1 dB and 3 dB respectively were achieved, with an overall PWL reduction of 2.7 dB across all harmonics achieved by the liner.

Chapter 8

Conclusions

8.1 Summary

In order to reduce the impact of the growing aviation sector, new methods of acoustic noise reduction are required for aircraft. In particular, the noise produced by the engines of aircraft is a growing concern and the current design trends for engine nacelles limit the space available to install acoustic treatments. This study assesses the performance of a novel acoustic metamaterial as a next-generation acoustic liner for aircraft engine nacelles. Furthermore, this study utilises additive manufacturing techniques in the design of acoustic metamaterials in order to explore designs that are not viable using conventional manufacturing techniques.

The overarching aim of this thesis was to design and develop an acoustic metamaterial liner to reduce aeroengine noise. In order to achieve this, a viable design was developed and optimised and its performance was measured on a realistic engine-simulator fan rig. In addition to this, the influence and benefits of using additive manufacturing to produce the material are assessed. The following objectives were achieved in the course of this study:

- An acoustic metamaterial taking the form of a multi-degree of freedom liner was designed and optimised to attenuate noise in the low-frequency range. This was achieved through a multi-step optimisation routine utilising numerical and analytical techniques with experimentally measured inputs to improve the performance of the liner.

- The final liner which was developed was achievable using SLA additive manufacturing. The design features narrow ducts divided at various heights by internal septa and sub-millimetre perforations which could not be manufactured using traditional manufacturing techniques.

- In addition, a micro-perforated faceplate is integrated into the 3D-printed design. The performance of the integrated faceplate device was shown to be higher than a similarly optimised design which was made using a combination of SLA printing and traditional manufacturing techniques. Due to the limitations posed on perforation size and plate thickness when using traditional manufacturing techniques, the performance of the fully 3D-printed device was notably higher.

- The absorption coefficient in normal acoustic incidence was found to perform well below 2 kHz, with maximum values of up to $\alpha = 0.97$ measured experimentally and a very broadband response. A mean absorption coefficient value of $\overline{\alpha} = 0.73$ in the 200 Hz to

2125 Hz range was achieved, compared to $\overline{\alpha} = 0.51$ for an optimised SDOF liner. This comparison can be seen in Fig. 7.3.

- The performance of the liner was additionally assessed in two grazing acoustic incidence impedance tubes. The tests determined that the liner has a good broadband frequency response. In addition, the liner has a high bandlimited transmission loss centred around approximately 1 kHz, with values of 27 dB achieved at 100 dB incident sound levels at $M = 0$, as seen in Fig. 7.5. Due to the non-linear nature of the liner, increasing sound levels result in an improved broadband response, albeit at the cost of some of the high performance at the peak.

- When tested with a grazing mean flow at 140 dB incident sound level, it was observed that an increasing flow velocity improved the broadband response of the liner. This is most prominent in the counter-flow direction which would benefit the performance of an inlet liner attenuating fan noise. A transmission loss attenuation of at least 6 dB and up to 10 dB in the 500 Hz to 4 kHz range was measured in the Le Mans OD at Mach 0.25, seen in Fig. 7.6.

- The grazing assessment conducted in the LAUM rig showed that the T-liner performs better at both high amplitude and high Mach number due to non-linearities in the nature of the design.

- The liner design was adapted for installation in the ANCF test rig which, as a duct fan, has a curved cross-section and a TRL of 3. In total, 237 individual liner blocks were 3D printed and installed in the ANCF liner casing for testing, seen in Fig. 7.11.

- The liner was tested in the ANCF and its performance was assessed at a range of fan speeds and radiation angles.

- The liner performed well, in particular at the most important and nominal speed of 1800 RPM where the first harmonic of the BPF of the rig aligned with the peak transmission loss frequency of the liner. This resulted in a tonal reduction of 18.6 dB at a radiation angle of 43.5°.

- Both broadband and tonal noise PWL reductions of 1.1 dB and 3 dB respectively were achieved, with an overall PWL reduction of 2.7 dB across all harmonics achieved by the liner.

8.2 Future Work

The work presented in this study shows the significant potential to use additively manufactured acoustic metamaterials as nacelle liners. There are a number of areas in which the work should be expanded upon in order to improve the performance of the concept and make it more viable for real-world applications;

- The T-Liner was only tested under normal incidence and grazing incidence in the impedance tubes in TCD and LAUM. As a result, the potential effect of the angle on incidence on the device is unknown. In duct rigs, such as the ANCF, the modal content of the noise source will result in incident angles other than standard grazing incidence. An investigation of the impact of the angle of incidence would improve the understanding on the T-Liner and how to improve the acoustic performance.

- In the design of the T-Liner presented, the variable geometry of the cells was highly repetitive. A more complex optimisation for that would allow for the device to be developed in which each duct of the unit cell is individually optimised in order to improve the frequency response of the device. As the device is additively manufactured, a more complex device with unique ducts would not have a significant impact on the production of the device once the CAD geometry is generated.

- This work was conducted using relatively cheap SLA printers which were printed using a plastic-based resin with similar properties to ABS. The performance of the liner is affected by the quality of the print, so a more rigorous assessment of the printing capabilities of a device would allow a final design to be printed with features such as perforation diameters closer to the intended size.

- Were a similar device to be implemented in an aircraft engine nacelle, the performance of the device would have to be assessed at a range of temperatures that are present in aircraft nacelles. The ABS-like materials would not be suitable in these cases. Therefore, as further advances are made, metal 3D printed liners which can withstand the high temperatures of aeroengines would need to be investigated.

Bibliography

[1] Toru Hasegawa. Effects of Novel Coronavirus (COVID-19) on Civil Aviation: Economic Impact Analysis, December 2022. URL https://www.icao.int/sustainability/Documents/Covid-19/ICAO_coronavirus_Econ_Impact.pdf.

[2] IATA. Air Passenger Numbers to Recover in 2024, January 2022. URL https://www.iata.org/en/pressroom/2022-releases/2022-03-01-01/.

[3] Deborah A. Black, John A. Black, Tharit Issarayangyun, and Stephen E. Samuels. Aircraft noise exposure and resident's stress and hypertension: A public health perspective for airport environmental management. *Journal of Air Transport Management*, 13(5): 264–276, September 2007. ISSN 0969-6997. doi: 10.1016/j.jairtraman.2007.04.003. URL http://www.sciencedirect.com/science/article/pii/S0969699707000403.

[4] Lars Jarup, Marie-Louise Dudley, Wolfgang Babisch, Danny Houthuijs, Wim Swart, Goran Pershagen, Gosta Bluhm, Klea Katsouyanni, Manolis Velonakis, Ennio Cadum, and Federica Vigna-Taglianti. Hypertension and Exposure to Noise near Airports (HYENA): Study Design and Noise Exposure Assessment. *Environmental Health Perspectives*, 113(11):1473–1478, July 2005. ISSN 0091-6765. doi: 10.1289/ehp.8037. URL http://www.ncbi.nlm.nih.gov/pmc/articles/PMC1310905/.

[5] Frank Theakston, editor. *Burden of disease from environmental noise: quantification of healthy life years lost in Europe.* World Health Organization, Regional Office for Europe, Copenhagen, 2011. ISBN 978-92-890-0229-5. OCLC: 779684347.

[6] M. Sørensen. Road traffic noise and risk for non-Hodgkin lymphoma among adults. *EuroNoise*, 43:99–104, 2015.

[7] Europäische Kommission and Europäische Kommission, editors. *Flightpath 2050: Europe's vision for aviation ; maintaining global leadership and serving society's needs ;*

report of the High-Level Group on Aviation Research. Policy / European Commission. Publ. Off. of the Europ. Union, Luxembourg, 2011. ISBN 978-92-79-19724-6. OCLC: 930887434.

[8] Donald Bartlett. The effects of using noise reduction turbofan engine nozzle designs on a turbojet engine. *Journal of Applied Sciences and Arts*, 1(2):2, 2016.

[9] Ann P. Dowling and Yasser Mahmoudi. Combustion noise. *Proceedings of the Combustion Institute*, 35(1):65–100, 2015. ISSN 15407489. doi: 10.1016/j.proci.2014.08.016. URL https://linkinghub.elsevier.com/retrieve/pii/S1540748914004003.

[10] Michael G. Jones, Douglas M. Nark, Earl Ayle, and Fumitaka Ichihashi. Acoustic panel liner for an engine nacelle, May 2016. URL https://patents.google.com/patent/US9334059B1/en?q=(nasa)&inventor=Michael+G.+Jones&oq=Michael+G.+Jones+nasa.

[11] Michael G. Jones, Joseph E. Grady, James D. Kiser, Christopher Miller, and James D. Heidmann. Acoustic liners for turbine engines, Oct 2018. URL https://patents.google.com/patent/US10107139B1/en?q=(nasa)&inventor=Michael+G.+Jones&oq=Michael+G.+Jones+nasa.

[12] Jeremy Astley Rie Sugimoto and Paul Murray. Low frequency liners for turbofan engines. In *Proceedings of 20th International Congress on Acoustics, ICA 2010*, Sydney, Australia, August 2010.

[13] Giorgio Palma, Huina Mao, Lorenzo Burghignoli, Peter Göransson, and Umberto Iemma. Acoustic Metamaterials in Aeronautics. *Applied Sciences*, May 2018. doi: 10.20944/preprints201805.0096.v1. URL http://www.preprints.org/manuscript/201805.0096/v1.

[14] Guangxin Liao, Congcong Luan, Zhenwei Wang, Jiapeng Liu, Xinhua Yao, and Jianzhong Fu. Acoustic Metamaterials: A Review of Theories, Structures, Fabrication Approaches, and Applications. *Advanced Materials Technologies*, 6(5):2000787, May 2021. ISSN 2365-709X, 2365-709X. doi: 10.1002/admt.202000787. URL https://onlinelibrary.wiley.com/doi/10.1002/admt.202000787.

[15] Nansha Gao, Zhicheng Zhang, Jie Deng, Xinyu Guo, Baozhu Cheng, and Hong Hou. Acoustic Metamaterials for Noise Reduction: A Review. *Advanced Materials Technologies*, 7(6):2100698, June 2022. ISSN 2365-709X, 2365-709X. doi: 10.1002/admt.202100698. URL https://onlinelibrary.wiley.com/doi/10.1002/admt.202100698.

[16] Guancong Ma and Ping Sheng. Acoustic metamaterials: From local resonances to broad horizons. *Science Advances*, 2(2):e1501595, February 2016. ISSN 2375-2548. doi: 10.1126/sciadv.1501595. URL http://advances.sciencemag.org/lookup/doi/10.1126/sciadv.1501595.

[17] Shuang Chen, Yuancheng Fan, Quanhong Fu, Hongjing Wu, Yabin Jin, Jianbang Zheng, and Fuli Zhang. A Review of Tunable Acoustic Metamaterials. *Applied Sciences*, 8(9):1480, August 2018. ISSN 2076-3417. doi: 10.3390/app8091480. URL http://www.mdpi.com/2076-3417/8/9/1480.

[18] Michael G. Jones, Douglas M. Nark, and Brian M. Howerton. Overview of Liner Activities in Support of the International Forum for Aviation Research. In *25th AIAA/CEAS Aeroacoustics Conference*, Delft, The Netherlands, May 2019. American Institute of Aeronautics and Astronautics. ISBN 978-1-62410-588-3. doi: 10.2514/6.2019-2599. URL https://arc.aiaa.org/doi/10.2514/6.2019-2599.

[19] Hans Boden, Stefan Sack, and Stefan Jacob. Impedance measurements for 3-D printed liners. In *25th AIAA/CEAS Aeroacoustics Conference*, Delft, The Netherlands, May 2019. American Institute of Aeronautics and Astronautics. ISBN 978-1-62410-588-3. doi: 10.2514/6.2019-2600. URL https://arc.aiaa.org/doi/10.2514/6.2019-2600.

[20] Friedrich Bake, Ralf Burgmayer, Anita Schulz, Karsten Knobloch, Lars Enghardt, and Michael G Jones. IFAR liner benchmark challenge #1 – DLR impedance eduction of uniform and axially segmented liners and comparison with NASA results. *International Journal of Aeroacoustics*, page 1475472X2110238, June 2021. ISSN 1475-472X, 2048-4003. doi: 10.1177/1475472X211023844. URL http://journals.sagepub.com/doi/10.1177/1475472X211023844.

[21] Tatsuya Ishii, Kenichiro Nagai, Hideshi Oinuma, and Shunji Enomoto. Experimental Study of Acoustic Liner Panels Shared in IFAR Program. In *25th AIAA/CEAS*

Aeroacoustics Conference, Delft, The Netherlands, May 2019. American Institute of Aeronautics and Astronautics. ISBN 978-1-62410-588-3. doi: 10.2514/6.2019-2602. URL https://arc.aiaa.org/doi/10.2514/6.2019-2602.

[22] Yufan Tang, Shuwei Ren, Han Meng, Fengxian Xin, Lixi Huang, Tianning Chen, Chuanzeng Zhang, and Tian Jian Lu. Hybrid acoustic metamaterial as super absorber for broadband low-frequency sound. *Scientific Reports*, 7(1), Dec 2017. ISSN 2045-2322. doi: 10.1038/srep43340. URL http://www.nature.com/articles/srep43340.

[23] Yufan Tang, Feihao Li, Fengxian Xin, and Tian Jian Lu. Heterogeneously perforated honeycomb-corrugation hybrid sandwich panel as sound absorber. *Materials & Design*, 134:502–512, Nov 2017. ISSN 02641275. doi: 10.1016/j.matdes.2017.09.006.

[24] Yufan Tang, Fengxian Xin, and Tian Jian Lu. Sound absorption of micro-perforated sandwich panel with honeycomb-corrugation hybrid core at high temperatures. *Composite Structures*, 226:111285, Oct 2019. ISSN 02638223. doi: 10.1016/j.compstruct.2019.111285.

[25] Yufan Tang, Wei He, Fengxian Xin, and Tian Jian Lu. Nonlinear sound absorption of ultralight hybrid-cored sandwich panels. *Mechanical Systems and Signal Processing*, 135:106428, Jan 2020. ISSN 08883270. doi: 10.1016/j.ymssp.2019.106428.

[26] Suresh Palani, Paul Murray, Alan McAlpine, Daisuke Sasaki, and Christoph Richter. Slanted septum and multiple folded cavity liners for broadband sound absorption. *International Journal of Aeroacoustics*, 20(5-7):633–661, September 2021. ISSN 1475-472X, 2048-4003. doi: 10.1177/1475472X211023835. URL http://journals.sagepub.com/doi/10.1177/1475472X211023835.

[27] Bundesverband der Deutschen Luftverkehrswirtschaft. Aviation invests billions in active and passive noise control, Apr 2017. URL https://www.bdl.aero/en/topics-and-positions/sustainability/aircraft-noise/.

[28] Lawrence K. Loftin. *Quest for Performance: the Evolution of Modern Aircraft*, volume 1. NASA, US, 1 edition, January 1985. ISBN 19850023776.

[29] The European Parliament and The Council of the European Union. Regulation (EU) No 598/2014 of the European Parliament and of the Council of 16 April 2014 on the

establishment of rules and procedures with regard to the introduction of noise-related operating restrictions at Union airports within a Balanced Approach and repealing Directive 2002/30/EC. Regulation (EU) No 598/2014, Official Journal of the European Union, 2014.

[30] Christian Kurrer. *Air and noise pollution — Fact Sheets on the European Union — European Parliament*. European Parliament, Oct 2022. URL `https://www.europarl.europa.eu/factsheets/en/sheet/75/air-and-noise-pollution`.

[31] Marta Rojek, Marek W. Rajzer, Wiktoria Wojciechowska, Tomasz Drozdz, Pawel Skalski, Tomasz Pizon, Andrzej Januszewicz, and Danuta Czarnecka. Relationship among long-term aircraft noise exposure, blood pressure profile, and arterial stiffness. 37:1350, Jul 2019. ISSN 0263-6352. doi: 10.1097/HJH.0000000000002060.

[32] Wiktoria Wojciechowska, Andrzej Januszewicz, Tomasz Drozdz, Marta Rojek, Justyna Baczalska, Michal Terlecki, Karol Kurasz, Agnieszka Olszanecka, Mikolaj Smolski, Aleksander Prejbisz, Piotr Dobrowolski, Tomasz Hryniewiecki, Reinhold Kreutz, and Marek Rajzer. Impact of reduction in aircraft noise exposure on blood pressure and arterial stiffness during covid-19 pandemic: Cross-sectional and longitudinal study. *Journal of Hypertension*, 39:e204, Apr 2021. ISSN 0263-6352. doi: 10.1097/01.hjh.0000746744.08145.f6.

[33] Fingal County Council. *Noise Action Plan for Dublin Airport*. Dingal County Council, Dublin, Ireland, Sep 2018. URL `https://www.dublinairport.com/docs/default-source/airport-noise/dublin-airport-noise-action-plan.pdf`.

[34] European Aviation Safety Agency. and EEA. *European aviation environmental: report 2016*. Publications Office, LU, 2016. URL `https://data.europa.eu/doi/10.2822/385503`.

[35] L. Bertsch, M. Snellen, L. Enghardt, and C. Hillenherms. Aircraft noise generation and assessment: executive summary. *CEAS Aeronautical Journal*, 10(1):3–9, Mar 2019. ISSN 1869-5582, 1869-5590. doi: 10.1007/s13272-019-00384-3.

[36] Fernando Nobre. Aircraft noise, Dec 2003. URL `https://www.slideshare.net/FernandoNobre1/aircraft-noise-27755949`.

[37] Herve Batard. Aircraft noise reduction : AIRBUS industrial needs in terms of new materials for nacelle liners, January 2003.

[38] Eleonora Neri. *Characterisation and Reduction of Aircraft Landing Gear Noise*. PhD thesis, Trinity College Dublin, 2017.

[39] DG Crighton. Basic principles of aerodynamic noise generation. *Progress in Aerospace Sciences*, 16(1):31–96, 1975. ISSN 0376-0421.

[40] Yong Li, Xunnian Wang, and Dejiu Zhang. Control strategies for aircraft airframe noise reduction. *Chinese Journal of Aeronautics*, 26(2):249–260, 4. ISSN 1000-9361. doi: 10.1016/j.cja.2013.02.001.

[41] Katsumi Takeda, Hideo Nishiwaki, and Shouichi Fujii. *The reduction of cavity noise at subsonic speeds*. Sep 1990. URL `https://ui.adsabs.harvard.edu/abs/1990rcns.rept.....T`. ADS Bibcode: 1990rcns.rept.....T.

[42] Gareth J. Bennett, Eleonora Neri, and John Kennedy. Noise Characterization of a Full-Scale Nose Landing Gear. *Journal of Aircraft*, 55(6):2476 – 2490, August 2018. ISSN 0021-8669, 1533-3868. doi: 10.2514/1.C034750. URL `https://arc.aiaa.org/doi/10.2514/1.C034750`.

[43] Roberto Merino-Martínez, Eleonora Neri, Mirjam Snellen, John Kennedy, Dick G. Simons, and Gareth J. Bennett. Multi-Approach Study of Nose Landing Gear Noise. *Journal of Aircraft*, 57(3):517–533, May 2020. ISSN 1533-3868. doi: 10.2514/1.C035655. URL `https://arc.aiaa.org/doi/10.2514/1.C035655`.

[44] Roberto Merino-Martínez, John Kennedy, and Gareth J. Bennett. Experimental study of realistic low–noise technologies applied to a full–scale nose landing gear. *Aerospace Science and Technology*, 113:106705, June 2021. ISSN 12709638. doi: 10.1016/j.ast.2021.106705. URL `https://linkinghub.elsevier.com/retrieve/pii/S1270963821002157`.

[45] Yong Li, Malcolm G. Smith, Xin Zhang, and N. Molin. Noise Sources Control of an Aircraft Landing Gear. In *13th AIAA/CEAS Aeroacoustics Conference (28th AIAA Aeroacoustics Conference)*, Rome, Italy, May 2007. American Institute of Aeronautics and Astronautics. ISBN 978-1-62410-003-1. doi: 10.2514/6.2007-3465. URL `https://arc.aiaa.org/doi/10.2514/6.2007-3465`.

[46] Eleonora Neri, John Kennedy, and Gareth J. Bennett. Bay cavity noise for full-scale nose landing gear: A comparison between experimental and numerical results. *Aerospace Science and Technology*, 72:278–291, January 2018. ISSN 12709638. doi: 10.1016/j.ast.2017.11.016. URL http://linkinghub.elsevier.com/retrieve/pii/S1270963817314736.

[47] Gareth J. Bennett, Patrick N. Okolo, Kun Zhao, John Philo, Yaoyi Guan, and Scott C. Morris. Cavity Resonance Suppression Using Fluidic Spoilers. *AIAA Journal*, 57(2): 706–719, November 2018. ISSN 0001-1452, 1533-385X. doi: 10.2514/1.J057407. URL https://arc.aiaa.org/doi/10.2514/1.J057407.

[48] Kun Zhao, Patrick Okolo, Eleonora Neri, Peng Chen, John Kennedy, and Gareth J. Bennett. Noise reduction technologies for aircraft landing gear-A bibliographic review. *Progress in Aerospace Sciences*, 112:100589, November 2019. ISSN 03760421. doi: 10.1016/j.paerosci.2019.100589. URL https://linkinghub.elsevier.com/retrieve/pii/S0376042119300338.

[49] Katsumi Takeda, Hideo Nishiwaki, and Shouichi Fujii. The reduction of cavity noise at subsonic speeds. *Unknown*, 1990.

[50] Gareth J Bennett, Kun Zhao, John Philo, Yaoyi Guan, and Scott C Morris. Cavity Noise Suppression Using Fluidic Spoilers (AIAA2016-2756). In *22nd AIAA/CEAS Aeroacoustics Conference*, Lyon, France, May 2016. AIAA. ISBN 978-1-62410-386-5. doi: 10.2514/6.2016-2756. URL http://arc.aiaa.org/doi/10.2514/6.2016-2756.

[51] Wing Commander Maurice A. Smith. *Flight Magazine*, 1947.

[52] Henry B. Moore and J. Michael Clinch. Measurement of Jet Noise Suppression Using a Small Turbojet Engine. In *SAE International*, page 670157, February 1967. doi: 10.4271/670157. URL https://www.sae.org/content/670157/.

[53] Jeff Dahl. Jet engine, Dec 2007. URL https://en.wikipedia.org/wiki/Jet_engine.

[54] K Aainsqatsi. Jet engine, Jul 2008. URL https://en.wikipedia.org/wiki/Jet_engine.

[55] Alan H. Marsh and A. L. McPike. Noise Levels of Turbojet- and Turbofan-Powered Aircraft. *The Journal of the Acoustical Society of America*, 34(12):1993–1993, Decem-

ber 1962. ISSN 0001-4966. doi: 10.1121/1.1937078. URL http://asa.scitation.org/doi/10.1121/1.1937078.

[56] Pratt and Whitney. PW1500G Product Card. *Pratt and Whitney UTC*, 2018. URL http://newsroom.pw.utc.com/download/PW1500G.pdf.

[57] Laurent Leylekian, Maxime Lebrun, and Pierre Lempereur. An overview of aircraft noise reduction technologies. *AerospaceLab Journal*, Issue 7:15 pages, 2014. doi: 10.12762/2014.AL07-01.

[58] Dennis L Huff. Noise Reduction Technologies for Turbofan Engines. In *INTER-Noise 2006*, Honolulu, September 2006. doi: NASA/TM2007-214495.

[59] Trevor M. Young. Noise and Emissions. In *Performance of the Jet Transport Airplane: Analysis Methods, Flight Operations and Regulations*, pages 523–542. John Wiley & Sons, Ltd, Chichester, UK, November 2017. ISBN 978-1-118-53478-6 978-1-118-38486-2. doi: 10.1002/9781118534786.ch21. URL https://onlinelibrary.wiley.com/doi/10.1002/9781118534786.ch21.

[60] Joe Walsh. Progress in engine noise reduction and future challenges, Oct 2016.

[61] M. Gorj Bandpy and M. Azimi. Passive Techniques for Fan Noise Reduction in New Turbofan Engines: Review. *Journal of Engineering Science and Technology Review*, 6 (1):59–61, February 2013. ISSN 17919320, 17912377. doi: 10.25103/jestr.061.11. URL http://jestr.org/downloads/Volume6Issue1/fulltext116113.pdf.

[62] Daniel L Sutliff. *Rotating Rake Turbofan Duct Mode Measurement System.* Number NASA/TM-2005-213828. NASA Glenn Research Center, Oct 2005.

[63] D. Casalino, F. Diozzi, R. Sannino, and A. Paonessa. Aircraft Noise Reduction Technologies: A Bibliographic Review. *Aerospace Science and Technology*, 12(1):1–17, 2008. ISSN 1270-9638. doi: 10.1016/j.ast.2007.10.004.

[64] A. S Ginevsky, Ye. V Vlasov, and R. K Karavosov. *Acoustic Control of Turbulent Jets.* Springer Berlin, Heidelberg, 2004. ISBN 978-3-540-39914-8. URL https://doi.org/10.1007/978-3-540-39914-8. OCLC: 1050922124.

[65] J. F. Groeneweg and E. J. Rice. Aircraft turbofan noise. 109:130–141, Jan 1987. ISSN 0889-504X, 1528-8900. doi: 10.1115/1.3262058.

[66] J. M. Tyler and T. G. Sofrin. Axial Flow Compressor Noise Studies. January 1962. doi: 10.4271/620532. URL https://www.sae.org/content/620532/.

[67] Richard P. Woodward and Frederick W. Glaser. Wind tunnel measurements of blade/vane ratio and spacing effects on fan noise. *Journal of Aircraft*, 20(1):58–65, January 1983. ISSN 0021-8669, 1533-3868. doi: 10.2514/3.44828. URL https://arc.aiaa.org/doi/10.2514/3.44828.

[68] Richard Woodward, David Elliot, Christopher Hughes, and Jeffrey Berton. Benefits of swept and leaned stators for fan noise reduction. In *37th Aerospace Sciences Meeting and Exhibit*, Reno,NV,U.S.A., January 1999. American Institute of Aeronautics and Astronautics. doi: 10.2514/6.1999-479. URL https://arc.aiaa.org/doi/10.2514/6.1999-479.

[69] R. Wagner. Aeroacoustics of the bifurcated 2d supersonic inlet. M.s.thesis, Virginia Polytechnic Institute and State University, 1995.

[70] K.C. Miller. Comparison of the aeroacoustics of two small-scale supersonic inlets. M.s.thesis, Virginia Polytechnic Institute and State University, 1996.

[71] C.A. Hanuska. Aeroacoustic effect of choking at inlet guide vanes in subsonic and supersonic inlets. M.s.thesis, Virginia Polytechnic Institute and State University, 1998.

[72] S.-M. Li, C.A. Hanuska, and W.F. Ng. AN EXPERIMENTAL INVESTIGATION OF THE AEROACOUSTICS OF A TWO-DIMENSIONAL BIFURCATED SUPERSONIC INLET. *Journal of Sound and Vibration*, 248(1):105–121, November 2001. ISSN 0022460X. doi: 10.1006/jsvi.2001.3731. URL https://linkinghub.elsevier.com/retrieve/pii/S0022460X01937319.

[73] Tamer Elnady. *Modelling and Characterization of Perforates in Lined Ducts and Mufflers*. Phd, KTH, Stockholm, Sweden, 2004.

[74] Batard Hervé and France Airbus. The Zero splice engine intake liner: an efficient way of reducing Aircraft Noise without any weight or aerodynamic penalty. Technical report, Airbus France, 2004.

[75] Fabrice Gantie, Herve Batard, Nicholas Baker, and Peter Schwaller. Zero Splice Technology and Acoustic Benefits. In *12th AIAA/CEAS Aeroacoustics Confer-*

ence (27th AIAA Aeroacoustics Conference), Cambridge, Massachusetts, May 2006. American Institute of Aeronautics and Astronautics. ISBN 978-1-62410-021-5. doi: 10.2514/6.2006-2455. URL http://arc.aiaa.org/doi/10.2514/6.2006-2455.

[76] Andrew Kempton. Acoustic liners for modern aero-engines. In *15th CEAS-ASC Workshop and 1st Scientific Workshop of X-Noise EV Acoustic Liners and Associated Propagation Techniques*, Lausanne, Switzerland, October 2011. URL https://www.win.tue.nl/ceas-asc/Workshop15/CEAS-ASC_XNoise-EV_K1_Kempton.pdf.

[77] Bombardier produces 'one-piece' nacelle for Clean Sky programme, February 2015. URL https://www.aero-mag.com/bombardier-produces-one-piece-nacelle-for-clean-sky-programme/. Library Catalog: www.aero-mag.com Section: News.

[78] Andrew Kempton. Acoustic liners for modern aero-engines. In *15th CEAS-ASC Workshop and 1st Scientific Workshop of X-Noise EV Acoustic Liners and Associated Propagation Techniques*, Lausanne, Switzerland, Oct 2011. URL https://www.win.tue.nl/ceas-asc/Workshop15/CEAS-ASC_XNoise-EV_K1_Kempton.pdf.

[79] XuQiang Ma and ZhengTao Su. Development of acoustic liner in aero engine: a review. *Science China Technological Sciences*, 63(12):2491–2504, Dec 2020. ISSN 1674-7321, 1869-1900. doi: 10.1007/s11431-019-1501-3.

[80] Daniel L Sutliff, Douglas M Nark, and Michael G Jones. Multi-degree-of-freedom liner development: Concept to flight test. *International Journal of Aeroacoustics*, 20(5–7): 792–825, Sep 2021. ISSN 1475-472X. doi: 10.1177/1475472X211023860.

[81] Daniel L. Sutliff. A 20 Year Retrospective of The Advanced Noise Control Fan – Contributions to Turbofan Noise Research. In *AIAA Propulsion and Energy 2019 Forum*, Indianapolis, IN, August 2019. American Institute of Aeronautics and Astronautics. ISBN 978-1-62410-590-6. doi: 10.2514/6.2019-3824. URL https://arc.aiaa.org/doi/10.2514/6.2019-3824.

[82] Kelvin M. Figueroa-Ibrahim, Scott Morris, Mark Ross, and Daniel L. Sutliff. Evaluation of Radiated Sound from the Advanced Noise Control Fan facility in an Outdoor Environment Using Ground Microphones. In *AIAA Propulsion and Energy 2019 Forum*, Indianapolis, IN, August 2019. American Institute of Aeronautics and

Astronautics. ISBN 978-1-62410-590-6. doi: 10.2514/6.2019-3825. URL https://arc.aiaa.org/doi/10.2514/6.2019-3825.

[83] Matthew Gazella, Tamuto Takakura, Daniel L. Sutliff, Richard Bozak, and Brian J. Tester. Evaluating the acoustic benefits of over-the-rotor acoustic treatments installed on the advanced noise control fan. In *23rd AIAA/CEAS Aeroacoustics Conference*, Denver, Colorado, Jun 2017. American Institute of Aeronautics and Astronautics. ISBN 978-1-62410-504-3. doi: 10.2514/6.2017-3872. URL https://arc.aiaa.org/doi/10.2514/6.2017-3872.

[84] Daniel L Sutliff, Richard F Bozak, Michael G Jones, and Douglas M Nark. Investigations of three over-the-rotor liner concepts at various technology readiness levels. *International Journal of Aeroacoustics*, 20(5–7):826–866, Sep 2021. ISSN 1475-472X, 2048-4003. doi: 10.1177/1475472X211025803.

[85] Daniel L Sutliff and Michael G Jones. Low-speed fan noise attenuation from a foam-metal liner. *Journal of aircraft*, 46(4):1381–1394, 2009.

[86] Michael G. Jones and Brian M. Howerton. Evaluation of novel liner concepts for fan and airframe noise reduction. In *22nd AIAA/CEAS Aeroacoustics Conference*, Lyon, France, May 2016. American Institute of Aeronautics and Astronautics. ISBN 978-1-62410-386-5. doi: 10.2514/6.2016-2787. URL https://arc.aiaa.org/doi/10.2514/6.2016-2787.

[87] Ricardo A. Burdisso, Wing F. Ng, and Andrew Provenza. *Fan Noise Control Using Herschel-quincke Resonators*. Number NASA/CR-2003-212097. Jan 2003.

[88] Daniel L. Sutliff, Michael G. Jones, and Douglas M. Nark. In-duct and farfield experimental measurements from the ancf for the purpose of improved broadband liner optimization. American Institute of Aeronautics and Astronautics, Jun 2014. ISBN 978-1-62410-285-1. doi: 10.2514/6.2014-3231. URL http://arc.aiaa.org/doi/10.2514/6.2014-3231.

[89] Andrew McKay, Ian Davis, Jack Killeen, and Gareth J Bennett. Semsa: a compact super absorber optimised for broadband, low-frequency noise attenuation. *Scientific Reports*, 10(1):17967, 2020.

[90] Martha C Brown, Douglas M Nark, and Michael G Jones. Preliminary design of a distributed facesheet acoustic liner for broadband acoustic attenuation. In *AIAA AVIATION 2023 Forum*, page 3638, 2023.

[91] J. Merhaut. *Theory of Electroacoustics*. Advanced Book Program. McGraw-Hill International Book Company, 1981. ISBN 978-0-07-041478-5. URL `https://books.google.ie/books?id=ZxOfAQAAIAAJ`.

[92] Ian Davis, Andrew McKay, and Gareth J. Bennett. A graph-theory approach to optimisation of an acoustic absorber targeting a specific noise spectrum that approaches the causal optimum minimum depth. *Journal of Sound and Vibration*, 505:116135, 2021. ISSN 0022-460X. doi: 10.1016/j.jsv.2021.116135.

[93] R.J. Astley, R. Sugimoto, and P. Mustafi. Computational aero-acoustics for fan duct propagation and radiation. current status and application to turbofan liner optimisation. *Journal of Sound and Vibration*, 330(16):3832–3845, Aug 2011. ISSN 0022460X. doi: 10.1016/j.jsv.2011.03.022.

[94] Kaisa Miettinen. *Nonlinear Multiobjective Optimization*. Springer Science And Business Media, 1999. ISBN 978-0-7923-8278-2. Google-Books-ID: ha_zLdNtXSMC.

[95] R. S. Kshetrimayum. A brief intro to metamaterials. *IEEE Potentials*, 23(5):44–46, December 2005. ISSN 0278-6648. doi: 10.1109/MP.2005.1368916.

[96] Tie Jun Cui, David Smith, and Ruopeng Liu, editors. *Metamaterials*. Springer US, Boston, MA, 2010. ISBN 978-1-4419-0572-7 978-1-4419-0573-4. doi: 10.1007/978-1-4419-0573-4. URL `http://link.springer.com/10.1007/978-1-4419-0573-4`.

[97] Viktor G. Veselago. The electrodynamics of substances with simultaneously negative values of ϵ and μ. *Physics-Uspekhi*, 10(4):509–514, April 1968. ISSN 1063-7869. URL `https://ufn.ru/en/articles/1968/4/d/`.

[98] D. R. Smith, Willie J. Padilla, D. C. Vier, S. C. Nemat-Nasser, and S. Schultz. Composite medium with simultaneously negative permeability and permittivity. *Physical Review Letters*, 84(18):4184–4187, May 2000. ISSN 0031-9007, 1079-7114. doi: 10.1103/PhysRevLett.84.4184.

[99] J. B. Pendry, A. J. Holden, W. J. Stewart, and I. Youngs. Extremely low frequency plasmons in metallic mesostructures. *Physical Review Letters*, 76(25):4773–4776, Jun 1996. ISSN 0031-9007, 1079-7114. doi: 10.1103/PhysRevLett.76.4773.

[100] J.B. Pendry, A.J. Holden, D.J. Robbins, and W.J. Stewart. Magnetism from conductors and enhanced nonlinear phenomena. *IEEE Transactions on Microwave Theory and Techniques*, 47(11):2075–2084, Nov 1999. ISSN 00189480. doi: 10.1109/22.798002.

[101] J. B. Pendry. Negative Refraction Makes a Perfect Lens. *Physical Review Letters*, 85 (18):3966–3969, October 2000. ISSN 0031-9007, 1079-7114. doi: 10.1103/PhysRevLett. 85.3966. URL `https://link.aps.org/doi/10.1103/PhysRevLett.85.3966`.

[102] Jensen Li and C. T. Chan. Double-negative acoustic metamaterial. *Physical Review E*, 70(5), November 2004. ISSN 1539-3755, 1550-2376. doi: 10.1103/PhysRevE.70.055602. URL `https://link.aps.org/doi/10.1103/PhysRevE.70.055602`.

[103] S. Laureti, D. A. Hutchins, L. A. J. Davis, S. J. Leigh, and M. Ricci. High-resolution acoustic imaging at low frequencies using 3D-printed metamaterials. *AIP Advances*, 6 (12):121701, December 2016. ISSN 2158-3226. doi: 10.1063/1.4968606. URL `http://aip.scitation.org/doi/10.1063/1.4968606`.

[104] Nadege Kaina, Fabrice Lemoult, Mathias Fink, and Geoffroy Lerosey. Negative refractive index and acoustic superlens from multiple scattering in single negative metamaterials. *Nature*, 525(7567):77–81, Sep 2015. ISSN 0028-0836, 1476-4687. doi: 10.1038/nature14678. URL `http://www.nature.com/doifinder/10.1038/nature14678`.

[105] Michael R. Haberman and Matthew D. Guild. Acoustic metamaterials. *Physics Today*, 69(6):42–48, June 2016. ISSN 0031-9228, 1945-0699. doi: 10.1063/PT.3.3198. URL `http://physicstoday.scitation.org/doi/10.1063/PT.3.3198`.

[106] Nicholas Fang, Dongjuan Xi, Jianyi Xu, Muralidhar Ambati, Werayut Srituravanich, Cheng Sun, and Xiang Zhang. Ultrasonic metamaterials with negative modulus. *Nature Materials*, 5(6):452–456, June 2006. ISSN 1476-1122. doi: 10.1038/nmat1644. URL `https://www.nature.com/nmat/journal/v5/n6/full/nmat1644.html`.

[107] Ming Gao, Zhiqiang Wu, and Zhijie Wen. Effective negative mass nonlinear acoustic metamaterial with pure cubic oscillator. *Advances in Civil Engineering*, 2018:1–15, 09 2018. doi: 10.1155/2018/3081783.

[108] Graeme W. Milton and John R. Willis. On modifications of Newton's second law and linear continuum elastodynamics. *Proceedings of the Royal Society A: Mathematical, Physical and Engineering Sciences*, 463(2079):855–880, March 2007. ISSN 1364-5021, 1471-2946. doi: 10.1098/rspa.2006.1795. URL `http://rspa.royalsocietypublishing.org/cgi/doi/10.1098/rspa.2006.1795`.

[109] Qi Wei, Ying Cheng, and Xiao-jun Liu. Acoustic total transmission and total reflection in zero-index metamaterials with defects. *Applied Physics Letters*, 102(17):174104, April 2013. ISSN 0003-6951, 1077-3118. doi: 10.1063/1.4803919. URL `http://aip.scitation.org/doi/10.1063/1.4803919`.

[110] T. Zandbergen. Do locally reacting acoustic liners always behave as they should? *AIAA Journal*, 18(4):396–397, 1980. ISSN 0001-1452. doi: 10.2514/3.50771.

[111] Benjamin S. Beck, Noah H. Schiller, and Michael G. Jones. Impedance assessment of a dual-resonance acoustic liner. *Applied Acoustics*, 93:15–22, Jun 2015. ISSN 0003682X. doi: 10.1016/j.apacoust.2015.01.011.

[112] Stefan Busse-Gerstengarbe, Steffen Nitsch, Friedrich Bake, and Lars Enghardt. A comprehensive study on non-locally reacting liners, part1: Experimental investigation. In *19th AIAA/CEAS Aeroacoustics Conference*, Berlin, Germany, May 2013. American Institute of Aeronautics and Astronautics. ISBN 978-1-62410-213-4. doi: 10.2514/6.2013-2073. URL `https://arc.aiaa.org/doi/10.2514/6.2013-2073`.

[113] Kemeng Gong, Xiaofan Wang, Huajiang Ouyang, and Jiliang Mo. Tuneable gradient Helmholtz-resonator-based acoustic metasurface for acoustic focusing. *Journal of Physics D: Applied Physics*, 52(38):385303, September 2019. ISSN 0022-3727, 1361-6463. doi: 10.1088/1361-6463/ab2b85. URL `https://iopscience.iop.org/article/10.1088/1361-6463/ab2b85`.

[114] Chenming Liu, Baizhan Xia, and Dejie Yu. The spiral-labyrinthine acoustic metamaterial by coiling up space. *Physics Letters A*, 381(36):3112–3118, Sep 2017. ISSN 03759601. doi: 10.1016/j.physleta.2017.07.041.

[115] Pan Li, Qiujiao Du, Meiyu Liu, and Pai Peng. Space-coiling Acoustic Metasurface with Independent Modulations of Phase and Amplitude, January 2019. URL `http://arxiv.org/abs/1901.02726`. arXiv:1901.02726 [physics].

[116] Zixian Liang and Jensen Li. Extreme Acoustic Metamaterial by Coiling Up Space. *Physical Review Letters*, 108(11):114301, March 2012. ISSN 0031-9007, 1079-7114. doi: 10.1103/PhysRevLett.108.114301. URL https://link.aps.org/doi/10.1103/PhysRevLett.108.114301.

[117] Zixian Liang, Tianhua Feng, Shukin Lok, Fu Liu, Kung Bo Ng, Chi Hou Chan, Jinjin Wang, Seunghoon Han, Sangyoon Lee, and Jensen Li. Space-coiling metamaterials with double negativity and conical dispersion. *Scientific Reports*, 3(1), Dec 2013. ISSN 2045-2322. doi: 10.1038/srep01614. URL http://www.nature.com/articles/srep01614.

[118] Yangbo Xie, Wenqi Wang, Huanyang Chen, Adam Konneker, Bogdan-Ioan Popa, and Steven A. Cummer. Wavefront modulation and subwavelength diffractive acoustics with an acoustic metasurface. *Nature Communications*, 5(1), Dec 2014. ISSN 2041-1723. doi: 10.1038/ncomms6553. URL http://www.nature.com/articles/ncomms6553.

[119] Reza Ghaffarivardavagh, Jacob Nikolajczyk, R. Glynn Holt, Stephan Anderson, and Xin Zhang. Horn-like space-coiling metamaterials toward simultaneous phase and amplitude modulation. *Nature Communications*, 9(1):1349, April 2018. ISSN 2041-1723. doi: 10.1038/s41467-018-03839-z. URL https://www.nature.com/articles/s41467-018-03839-z.

[120] Andrew T. Chambers, James M. Manimala, and Michael G. Jones. Design and optimization of 3d folded-core acoustic liners for enhanced low-frequency performance. *AIAA Journal*, 58(1):206–218, Jan 2020. ISSN 0001-1452, 1533-385X. doi: 10.2514/1.J058017.

[121] Jun Mei, Guancong Ma, Min Yang, Zhiyu Yang, Weijia Wen, and Ping Sheng. Dark acoustic metamaterials as super absorbers for low-frequency sound. *Nature Communications*, 3(1), January 2012. ISSN 2041-1723. doi: 10.1038/ncomms1758. URL http://www.nature.com/articles/ncomms1758.

[122] Z. Yang, Jun Mei, Min Yang, N. H. Chan, and Ping Sheng. Membrane-Type Acoustic Metamaterial with Negative Dynamic Mass. *Physical Review Letters*, 101(20):204301, November 2008. ISSN 0031-9007, 1079-7114. doi: 10.1103/PhysRevLett.101.204301. URL https://link.aps.org/doi/10.1103/PhysRevLett.101.204301.

[123] Christina J. Naify, Chia-Ming Chang, Geoffrey McKnight, Florian Scheulen, and Steven Nutt. Membrane-type metamaterials: Transmission loss of multi-celled arrays. *Journal of Applied Physics*, 109(10):104902, May 2011. ISSN 0021-8979, 1089-7550. doi: 10.1063/1.3583656. URL `http://aip.scitation.org/doi/10.1063/1.3583656`.

[124] Junjuan Zhao, Xianhui Li, Wenjiang Wang, Yueyue Wang, Liying Zhu, and Yunan Liu. Membrane-type acoustic metamaterials with tunable frequency by a compact magnet. *The Journal of the Acoustical Society of America*, 145(5):EL400–EL404, May 2019. ISSN 0001-4966. doi: 10.1121/1.5107431. URL `http://asa.scitation.org/doi/10.1121/1.5107431`.

[125] J. B. Pendry. Controlling electromagnetic fields. *Science*, 312(5781):1780–1782, Jun 2006. ISSN 0036-8075, 1095-9203. doi: 10.1126/science.1125907.

[126] Graeme W Milton, Marc Briane, and John R Willis. On cloaking for elasticity and physical equations with a transformation invariant form. *New Journal of Physics*, 8 (10):248–248, Oct 2006. ISSN 1367-2630. doi: 10.1088/1367-2630/8/10/248.

[127] Steven A Cummer and David Schurig. One path to acoustic cloaking. *New Journal of Physics*, 9(3):45–45, Mar 2007. ISSN 1367-2630. doi: 10.1088/1367-2630/9/3/045.

[128] A. N Norris. Acoustic cloaking theory. *Proceedings of the Royal Society A: Mathematical, Physical and Engineering Sciences*, 464(2097):2411–2434, Sep 2008. ISSN 1364-5021, 1471-2946. doi: 10.1098/rspa.2008.0076.

[129] Andrew N. Norris. Acoustic metafluids. *The Journal of the Acoustical Society of America*, 125(2):839–849, Feb 2009. ISSN 0001-4966. doi: 10.1121/1.3050288.

[130] Muamer Kadic, Tiemo Bückmann, Nicolas Stenger, Michael Thiel, and Martin Wegener. On the practicability of pentamode mechanical metamaterials. *Applied Physics Letters*, 100(19):191901, May 2012. ISSN 0003-6951. doi: 10.1063/1.4709436.

[131] Shuhao Wu, Zhen Luo, Zuyu Li, Shutian Liu, and Lai-Chang Zhang. Topological design of pentamode metamaterials with additive manufacturing. *Computer Methods in Applied Mechanics and Engineering*, 377:113708, Apr 2021. ISSN 00457825. doi: 10.1016/j.cma.2021.113708.

[132] Muamer Kadic, Tiemo Bückmann, Robert Schittny, Peter Gumbsch, and Martin Wegener. Pentamode metamaterials with independently tailored bulk modulus and mass density. *Physical Review Applied*, 2(5):054007, Nov 2014. ISSN 2331-7019. doi: 10.1103/PhysRevApplied.2.054007.

[133] Andrew N. Norris. Acoustic cloaking. *Acoustics Today*, 11(1):38–46, 2015.

[134] Bogdan-Ioan Popa, Lucian Zigoneanu, and Steven A. Cummer. Experimental acoustic ground cloak in air. *Physical Review Letters*, 106(25), Jun 2011. ISSN 0031-9007, 1079-7114. doi: 10.1103/PhysRevLett.106.253901. URL `https://link.aps.org/doi/10.1103/PhysRevLett.106.253901`.

[135] Weiwei Kan, Bin Liang, Xuefeng Zhu, Ruiqi Li, Xinye Zou, Haodong Wu, Jun Yang, and Jianchun Cheng. Acoustic illusion near boundaries of arbitrary curved geometry. *Scientific Reports*, 3(11):1427, Mar 2013. ISSN 2045-2322. doi: 10.1038/srep01427.

[136] Lucian Zigoneanu, Bogdan-Ioan Popa, and Steven A. Cummer. Three-dimensional broadband omnidirectional acoustic ground cloak. *Nature Materials*, 13(44):352–355, Apr 2014. ISSN 1476-4660. doi: 10.1038/nmat3901.

[137] Umberto Iemma, Michael Carley, and Riccardo Pellegrini. Tailoring acoustic metamaterials to aeroacoustic applications. page 1–8, Melbourne, Australia, 2014. URL `http://www.acoustics.asn.au/conference_proceedings/INTERNOISE2014/papers/p37.pdf`.

[138] Hyeonbin Ryoo and Wonju Jeon. Effect of compressibility and non-uniformity in flow on the scattering pattern of acoustic cloak. *Scientific Reports*, 7(1), Dec 2017. ISSN 2045-2322. doi: 10.1038/s41598-017-02143-y. URL `http://www.nature.com/articles/s41598-017-02143-y`.

[139] Yifan Zhu, Krupali Donda, Shiwang Fan, Liyun Cao, and Badreddine Assouar. Broadband ultra-thin acoustic metasurface absorber with coiled structure. *Applied Physics Express*, 12(11):114002, November 2019. ISSN 1882-0778, 1882-0786. doi: 10.7567/1882-0786/ab494a. URL `https://iopscience.iop.org/article/10.7567/1882-0786/ab494a`.

[140] Reza Ghaffarivardavagh, Jacob Nikolajczyk, Stephan Anderson, and Xin Zhang. Ultra-open acoustic metamaterial silencer based on Fano-like interference. *Physical Review B*,

99(2):024302, January 2019. doi: 10.1103/PhysRevB.99.024302. URL https://link.aps.org/doi/10.1103/PhysRevB.99.024302.

[141] Clare L. Pool, Kenneth F. Udall, Richard G. Stretton, and Julian M. Reed. Duct wall for a fan of a gas turbine engine, May 2013. URL https://patents.google.com/patent/US8434995B2/en.

[142] Paul Murray, Richard Astley, Rie Sugimoto, and Andrew Kempton. An acoustic liner, Jun 2012. URL https://patents.google.com/patent/EP2466095A2/en?oq=Patent-EP+2+466+095+A2+2012.

[143] Sadettin Cem Altıparmak and Bowen Xiao. A market assessment of additive manufacturing potential for the aerospace industry. *Journal of Manufacturing Processes*, 68: 728–738, Aug 2021. ISSN 15266125. doi: 10.1016/j.jmapro.2021.05.072.

[144] K. Satish Prakash, T. Nancharaih, and V.V. Subba Rao. Additive manufacturing techniques in manufacturing -an overview. *Materials Today: Proceedings*, 5(2):3873–3882, 2018. ISSN 22147853. doi: 10.1016/j.matpr.2017.11.642.

[145] Joel C. Najmon, Sajjad Raeisi, and Andres Tovar. *Review of additive manufacturing technologies and applications in the aerospace industry*, page 7–31. Elsevier, 2019. ISBN 978-0-12-814062-8. doi: 10.1016/B978-0-12-814062-8.00002-9. URL https://linkinghub.elsevier.com/retrieve/pii/B9780128140628000029.

[146] Babak Kianian. Wohlers report 2017: 3d printing and additive manufacturing state of the industry, annual worldwide progress report. *Wohlers Associates, Inc.*, 2017.

[147] Sejak Akre. *Aerospace Additive Manufacturing Market Size, Share, Analysis, Growth, Trend, Forecast 2030.* Market Research Future, Feb 2021. URL https://www.marketresearchfuture.com/reports/aerospace-additive-manufacturing-market-1551.

[148] 2014. URL https://www2.deloitte.com/us/en/insights/focus/3d-opportunity/additive-manufacturing-3d-opportunity-in-aerospace.html.

[149] GE Additive. Concept laser m2 series 5, n.d. URL https://www.ge.com/additive/additive-manufacturing/machines/m2series5?utm_medium=public+relations.

[150] Luke Dowling. *Development of localised process parameter control for repeatability in metal additive manufacturing*. PhD thesis, Trinity College Dublin, the University of Dublin, 2021. URL http://www.tara.tcd.ie/handle/2262/97088.

[151] GE Additive. Ge aviation and ge additive engineers have switched four existing parts from castings to metal 3d printing-and see potential for hundreds more: Ge additive, May 2021. URL https://www.ge.com/additive/blog/ge-aviation-and-ge-additive-engineers-have-switched-four-existing-parts-castings-

[152] Lucas Mearian. Boeing turns to 3d-printed parts to save millions on its 787 dreamliner, Apr 2017. URL https://www.computerworld.com/article/3188899/boeing-turns-to-3d-printed-parts-to-save-millions-on-its-787-dreamliner.html.

[153] Sebastian Soller, S Beyer, A Dahlhaus, A Konrad, J Kretschmer, N Rackemann, and W Zeiss. Development of liquid rocket engine injectors using additive manufacturing. In *European Conference for Aeronautics and Space Science*, Jul 2015.

[154] Tereza Pultarova published. Airbus sending 3d printer to space station next year to pave way for off-earth factories, Jun 2022. URL https://www.space.com/airbus-metal-3d-printer-orbital-satellite-factory.

[155] Michael Jones, T Parrott, Daniel Sutliff, and C Hughes. Assessment of soft vane and metal foam engine noise reduction concepts. May 2009. doi: 10.2514/6.2009-3142.

[156] Christopher Hughes and John Gazzaniga. *Effect of Two Advanced Noise Reduction Technologies on the Aerodynamic Performance of an Ultra High Bypass Ratio Fan*. Aeroacoustics Conferences. American Institute of Aeronautics and Astronautics, May 2009. doi: 10.2514/6.2009-3139. URL https://arc.aiaa.org/doi/10.2514/6.2009-3139.

[157] Michael Czech and Russell H. Thomas. *Open Rotor Installed Aeroacoustic Testing with Conventional and Unconventional Airframes*. Aeroacoustics Conferences. American Institute of Aeronautics and Astronautics, May 2013. doi: 10.2514/6.2013-2185. URL https://arc.aiaa.org/doi/10.2514/6.2013-2185.

[158] Russell H Thomas, Casey L Burley, Leonard V Lopes, Christopher J Bahr, Frank H Gern, and Dale E Van Zante. System noise assessment and the potential for low noise

hybrid wing body aircraft with open rotor propulsion. In *52nd Aerospace Sciences Meeting*, page 0258, 2014.

[159] Juliette Pierre, Filippo Iervolino, Rouhollah D. Farahani, Nicola Piccirelli, Martin Lévesque, and Daniel Therriault. Material extrusion additive manufacturing of multifunctional sandwich panels with load-bearing and acoustic capabilities for aerospace applications. *Additive Manufacturing*, 61:103344, Jan 2023. ISSN 2214-8604. doi: 10.1016/j.addma.2022.103344.

[160] ASTM E2611-09. Standard Test Method for Measurement of Normal Incidence Sound Transmission of Acoustical Materials Based on the Transfer Matrix Method. Technical Report ASTM E2611-09, ASTM International, 2009.

[161] BS EN ISO 15034-2:2001. Acoustics - Determination of sound absorption coefficient and impedance in impedance tubes - Part 2: Transfer-function method. Technical Standard BS EN ISO 15034-2:2001, British Standard, April 2002.

[162] Ygaäl Renou and Yves Aurégan. Failure of the ingard–myers boundary condition for a lined duct: An experimental investigation. *The Journal of the Acoustical Society of America*, 130(1):52–60, Jul 2011. ISSN 0001-4966. doi: 10.1121/1.3586789.

[163] Thomas Humbert, Ronan Delalande, Gwenael Gabard, Joachim Golliard, and Yves Auregan. Performance of the matrix pencil algorithm in direct impedance eduction of liners: some numerical experiments. In *25th AIAA/CEAS Aeroacoustics Conference*, Delft, The Netherlands, May 2019. American Institute of Aeronautics and Astronautics. ISBN 978-1-62410-588-3. doi: 10.2514/6.2019-2676. URL `https://arc.aiaa.org/doi/10.2514/6.2019-2676`.

[164] Massimo Emiliano D'Elia. *Flow-acoustic Interaction with Innovative Materials*. Phd thesis, Le Mans Université, 2021.

[165] Massimo Emiliano D'Elia, Thomas Humbert, and Yves Auregan. Direct impedance eduction of liners from laser doppler velocimetry measurements. In *25th AIAA/CEAS Aeroacoustics Conference*, Delft, The Netherlands, May 2019. American Institute of Aeronautics and Astronautics. ISBN 978-1-62410-588-3. doi: 10.2514/6.2019-2516. URL `https://arc.aiaa.org/doi/10.2514/6.2019-2516`.

[166] Mohamed Taktak, jean-michel Ville, Mohamed Haddar, Gwenael Gabard, and Félix Foucart. A 3d multiport scattering matrix based-method for educing wall impedance of cylindrical lined duct section: Simulation and error evaluation. *Advances in Acoustics and Vibration*, 2009, Jan 2009. doi: 10.1155/2009/928367.

[167] Yves Aurégan, Maud Leroux, and Vincent Pagneux. Measurement of liner impedance with flow by an inverse method. May 2004. doi: 10.2514/6.2004-2838.

[168] Joseph McAllister, Raymond Loew, Joel Lauer, and Daniel Sutliff. The advanced noise control fan baseline measurements. In *47th AIAA Aerospace Sciences Meeting including The New Horizons Forum and Aerospace Exposition*, Orlando, Florida, Jan 2009. American Institute of Aeronautics and Astronautics. ISBN 978-1-60086-973-0. doi: 10.2514/6.2009-624. URL https://arc.aiaa.org/doi/10.2514/6.2009-624.

[169] Yufan Tang, Fengxian Xin, Lixi Huang, and Tianjian Lu. Deep subwavelength acoustic metamaterial for low-frequency sound absorption. *EPL (Europhysics Letters)*, 118(4): 44002, May 2017. ISSN 0295-5075, 1286-4854. doi: 10.1209/0295-5075/118/44002.

[170] Dah-You Maa. Potential of microperforated panel absorber. *Journal of the Acoustical Society of America*, 1998. doi: doi.org/10.1121/1.423870.

[171] Mads Herring Jensen. Theory of thermoviscous acoustics: Thermal and viscous losses, Feb 2014. URL https://www.comsol.com/blogs/theory-of-thermoviscous-acoustics-thermal-and-viscous-losses/.

[172] Wenjiong Chen, Shutian Liu, Liyong Tong, and Sheng Li. Design of multi-layered porous fibrous metals for optimal sound absorption in the low frequency range. *Theoretical and Applied Mechanics Letters*, 6(1):42–48, January 2016. ISSN 20950349. doi: 10.1016/j.taml.2015.12.002. URL https://linkinghub.elsevier.com/retrieve/pii/S2095034916000027.

[173] J. W. S. Rayleigh. *The Theory of Sound, Volume One.* publisher not identified, Cambridge University Press, Place of publication not identified, Cambridge, 1877. ISBN 978-0-486-14043-8.

[174] I.B. Crandall. *Theory of vibrating systems and sound...* Creative Media Partners, LLC, 1926. ISBN 978-0-343-29006-1. URL https://books.google.ie/books?id=M_QIjwEACAAJ.

[175] Dah-You Maa. Theory and design of microperforated panel sound-absorbing constructions. *Scientia Sinica*, 18:55–71, 1975. ISSN 1. doi: 10.1360/ya1975-18-1-55.

[176] Dah-You Maa. Microperforated-panel wideband absorbers. *Noise Control Engineering Journal*, 29(3):77, 1987. ISSN 07362501. doi: 10.3397/1.2827694.

[177] VA Fok. Teoreticheskoe issledovanie provodimosti kruglogo otverstiya v peregorodke, postavlennoi poperek truby (theoretical study of the conductance of a circular hole in a partition across a tube). *Doklady Akademii Nauk SSSR (Soviet Physics Doklady)*, 31 (9):875–882, 1941.

[178] Muttalip Aşkın Temiz, Jonathan Tournadre, Ines Lopez Arteaga, and Avraham Hirschberg. Modelling vibro-acoustic coupling in flexible micro-perforated plates by a patch-impedance approach. *Applied Acoustics*, 125:80–90, October 2017. ISSN 0003682X. doi: 10.1016/j.apacoust.2017.04.012. URL `https://linkinghub.elsevier.com/retrieve/pii/S0003682X16304182`.

[179] Syed H. Masood. Intelligent rapid prototyping with fused deposition modelling. *Rapid Prototyping Journal*, 2(1):24–33, Mar 1996. ISSN 1355-2546. doi: 10.1108/13552549610109054.

[180] Sung-Hoon Ahn, Michael Montero, Dan Odell, Shad Roundy, and Paul K. Wright. Anisotropic material properties of fused deposition modeling abs. *Rapid Prototyping Journal*, 8(4):248–257, Oct 2002. ISSN 1355-2546. doi: 10.1108/13552540210441166.

[181] Malcolm N. Cooke, John P. Fisher, David Dean, Clare Rimnac, and Antonios G. Mikos. Use of stereolithography to manufacture critical-sized 3d biodegradable scaffolds for bone ingrowth. *Journal of Biomedical Materials Research. Part B, Applied Biomaterials*, 64(2):65–69, Feb 2003. ISSN 1552-4981. doi: 10.1002/jbm.b.10485.

[182] Gohki Oda, Takashi Miyoshi, Yasuhiro Takaya, Taeho Ha, and Keiichi Kimura. Microfabrication of overhanging shape using lcd microstereolithography. In Isamu Miyamoto, Henry Helvajian, Kazuyoshi Itoh, Kojiro F. Kobayashi, Andreas Ostendorf, and Koji Sugioka, editors, *Fifth International Symposium on Laser Precision Microfabrication*, page 649–654, Oct 2004. doi: 10.1117/12.596758. URL `http://proceedings.spiedigitallibrary.org/proceeding.aspx?articleid=857538`.

[183] R. Liska, M. Schuster, R. Inführ, C. Turecek, C. Fritscher, B. Seidl, V. Schmidt, L. Kuna, A. Haase, F. Varga, H. Lichtenegger, and J. Stampfl. Photopolymers for rapid prototyping. *Journal of Coatings Technology and Research*, 4(4):505–510, Nov 2007. ISSN 1547-0091, 1935-3804. doi: 10.1007/s11998-007-9059-3.

[184] Mary Kathryn Thompson and Michael Mischkot. Design of test parts to characterize micro additive manufacturing processes. *Procedia CIRP*, 34:223–228, 2015. ISSN 22128271. doi: 10.1016/j.procir.2015.07.065.

[185] C. Y. Yap, C. K. Chua, Z. L. Dong, Z. H. Liu, D. Q. Zhang, L. E. Loh, and S. L. Sing. Review of selective laser melting: Materials and applications. *Applied Physics Reviews*, 2(4):041101, Dec 2015. ISSN 1931-9401. doi: 10.1063/1.4935926.

[186] Mariano Jiménez, Luis Romero, Iris A. Domínguez, María del Mar Espinosa, and Manuel Domínguez. Additive manufacturing technologies: An overview about 3d printing methods and future prospects. *Complexity*, 2019:1–30, Feb 2019. ISSN 1076-2787, 1099-0526. doi: 10.1155/2019/9656938.

[187] John Kennedy, Lara Flanagan, Luke Dowling, G. J. Bennett, Henry Rice, and Daniel Trimble. The influence of additive manufacturing processes on the performance of a periodic acoustic metamaterial. *International Journal of Polymer Science*, 2019:1–11, Jul 2019. ISSN 1687-9422, 1687-9430. doi: 10.1155/2019/7029143.

[188] John Kennedy and Agnieszka Ciochon. Applying lessons learnt from additive manufacturing to the design of novel acoustic absorbers. *SSRN*, 2023. doi: doi.org/10.2139/ssrn.4398234.

[189] Jeremy Straub. In search of technology readiness level (trl) 10. *Aerospace Science and Technology*, 46:312–320, 2015. ISSN 1270-9638. doi: https://doi.org/10.1016/j.ast.2015.07.007. URL `https://www.sciencedirect.com/science/article/pii/S127096381500214X`.

[190] Stephen J Kapurch. *NASA systems engineering handbook*. Diane Publishing, 2010.

[191] ESA TEC-SHS. Technology readiness levels handbook. Technical report, TEC-SHS/5551/MG/ap Iss1 Rev6, 2008.

[192] NASA Earth Science and Technology Office. *Technology Readiness Levels (TRLs)*, Mar 2020. URL `https://esto.nasa.gov/trl/`.

Appendix A

Additional Print Quality

Additional information relating to the quality of the samples manufactured for testing at the ANCF facility. The print quality of the back of the Part A components are seen in Figs. A.1 and A.2. The print quality of part B can be seen in Figs. A.3 to A.5. The complete breakdown of all measurements summarised Section 6.3 can be found in Table A.1.

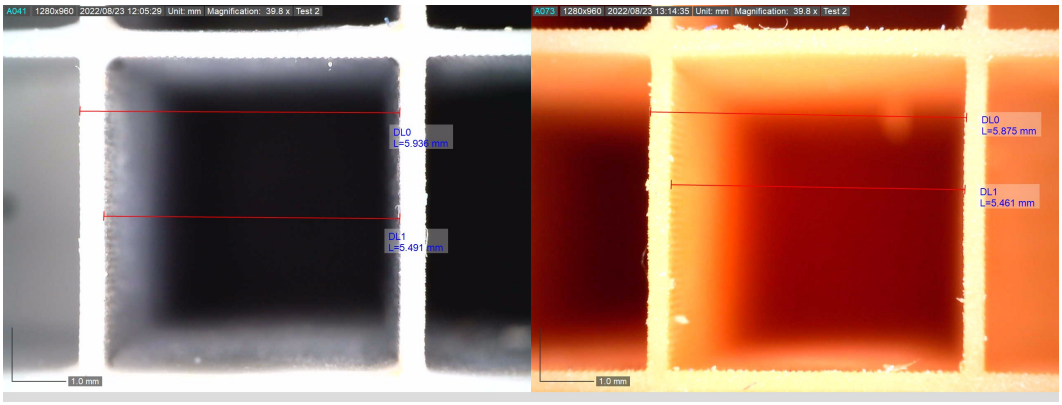

(a) Elegoo (b) Prusa

Figure A.1: Print quality of the bottom surface spacing of Part A from an (a) Elegoo printer and (b) Prusa printer.

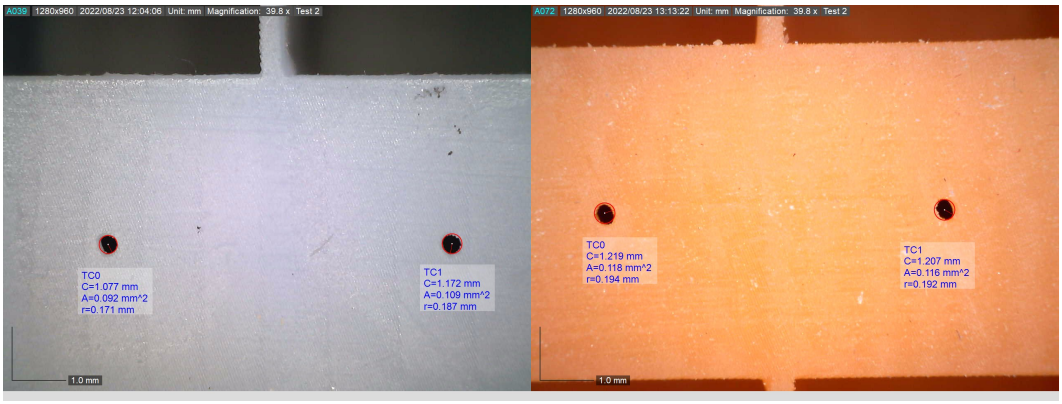

(a) Elegoo (b) Prusa

Figure A.2: Print quality of the bottom perforation diameter of Part A from an (a) Elegoo printer and (b) Prusa printer.

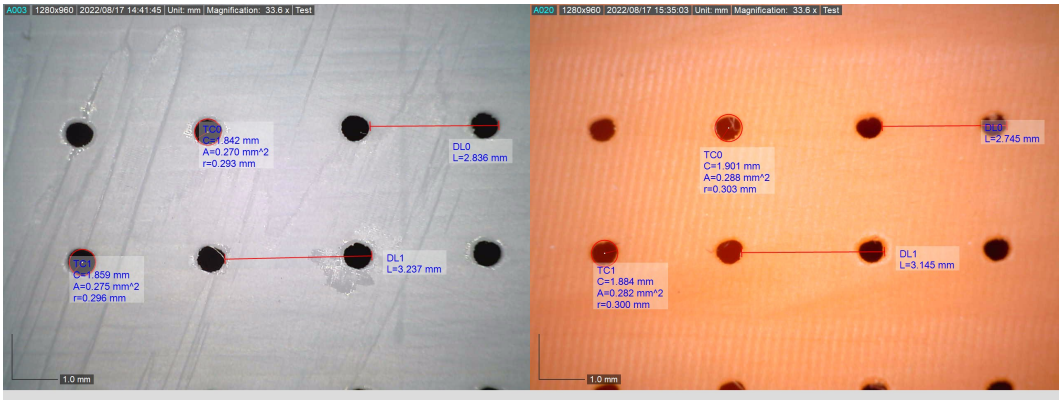

(a) Elegoo (b) Prusa

Figure A.3: Print quality of the top surface of sample B from an (a) Elegoo printer and (b) Prusa printer.

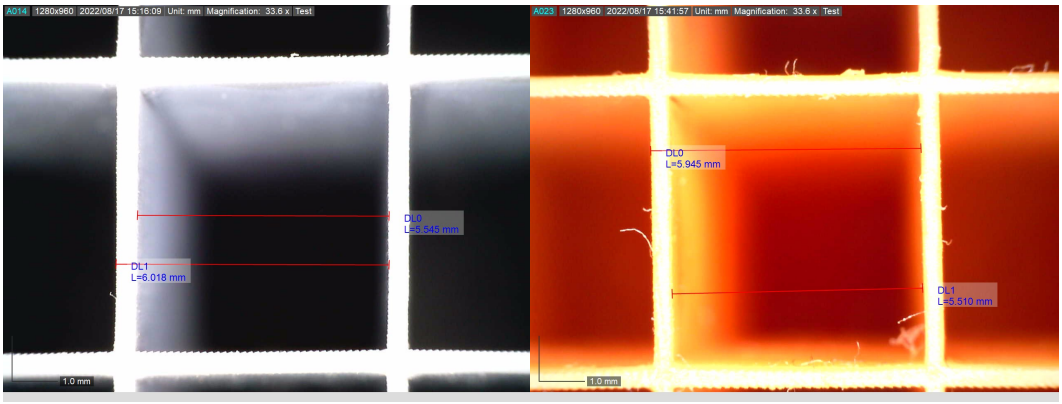

(a) Elegoo (b) Prusa

Figure A.4: Print quality of the bottom surface spacing of sample B from an (a) Elegoo printer and (b) Prusa printer.

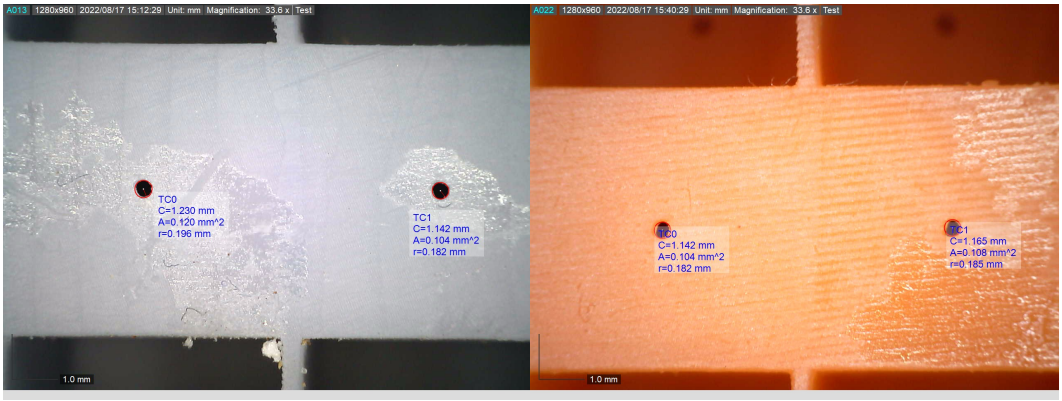

(a) Elegoo (b) Prusa

Figure A.5: Print quality of the bottom perforation diameter of sample B from an (a) Elegoo printer and (b) Prusa printer.

	Front				Back			
sample	D		x_1	x_2	d		b_1	b_2
A1 Elegoo	0.276	0.265	2.761	3.175	0.180	0.174	5.491	5.997
A2 Elegoo	0.291	0.301	2.745	3.113	0.171	0.187	5.491	5.936
A3 Elegoo	0.276	0.287	2.715	3.190	0.175	0.187	5.491	5.951
A4 Elegoo	0.306	0.306	2.699	3.144	0.196	0.194	5.506	5.936
A5 Elegoo	0.289	0.295	2.669	3.098	0.180	0.195	5.506	5.920
A6 Elegoo	0.296	0.295	2.745	3.129	0.175	0.187	5.476	5.921
A7 Elegoo	0.308	0.302	2.776	3.144	0.192	0.187	5.446	5.921
A8 Elegoo	0.293	0.296	2.699	3.114	0.196	0.184	5.429	5.902
mean		0.293	2.726	3.138		0.185	5.480	5.936
A9 Prusa	0.292	0.295	2.684	3.129	0.190	0.187	5.460	5.874
A10 Prusa	0.301	0.296	2.669	3.099	0.176	0.175	5.460	5.890
A11 Prusa	0.282	0.283	2.699	3.052	0.194	0.192	5.461	5.875
A12 Prusa	0.278	0.298	2.669	3.037	0.175	0.185	5.445	5.828
A13 Prusa	0.295	0.296	2.699	3.083	0.171	0.187	5.399	5.813
A14 Prusa	0.302	0.309	2.699	3.129	0.180	0.185	5.446	5.844
A15 Prusa	0.283	0.304	2.715	3.144	0.174	0.175	5.414	5.799
A16 Prusa	0.282	0.304	2.684	3.098	0.174	0.179	5.475	5.890
A17 Prusa	0.271	0.298	2.670	3.164	0.175	0.187	5.460	5.874
A18 Prusa	0.304	0.295	2.669	3.083	0.185	0.196	5.506	5.905
mean		0.293	2.686	3.102		0.182	5.453	5.859
B1 Elegoo	0.291	0.296	2.801	3.201	0.197	0.197	5.563	6.036
B2 Elegoo	0.293	0.296	2.836	3.237	0.196	0.182	5.545	6.018
B3 Elegoo	0.291	0.291	2.819	3.219	0.182	0.196	5.509	5.999
B4 Elegoo	0.294	0.291	2.836	3.218	0.193	0.183	5.563	5.999
mean		0.293	2.823	3.219		0.191	5.545	6.013
B5 Prusa	0.303	0.300	2.745	3.145	0.182	0.185	5.510	5.945
B6 Prusa	0.296	0.293	2.800	3.182	0.182	0.197	5.472	5.945
B7 Prusa	0.301	0.291	2.783	3.167	0.182	0.182	5.472	5.908
B8 Prusa	0.293	0.296	2.782	3.163	0.196	0.182	5.509	5.927
mean		0.297	2.778	3.164		0.186	5.491	5.931
target		0.315	2.800	3.200		0.200	5.400	6.000

Table A.1: Measurement of the hole size, hole separation and wall thickness of the printed samples, sorted by Part type and printer.

	Value (Design)	Value (Actual)	% Error	σ	min	max
H	50 mm	-	-	-	-	-
x_1	2.8 mm	2.76 mm	2.03	0.0565	2.67	2.80
x_2	3.2 mm	3.17 mm	1.48	0.0476	3.04	3.18
b_1	5.6 mm	5.50 mm	1.76	0.0414	5.43	5.56
b_2	6 mm	5.96 mm	0.79	0.0455	5.90	6.04
T_1	0.7 mm	-	-	-	-	-
T_2	0.5 mm	-	-	-	-	-
t	0.2 mm	-	-	-	-	-
D	0.63 mm	0.59 mm	7.08	0.0097	0.53	0.62
d	0.4 mm	0.37 mm	6.54	0.0083	0.34	0.39

Table A.2: Value of the geometric parameters of parts printed using the Elegoo printers, corrected for the measured error. Corrections are weight to account for each test article containing two Part A components and one Part B component.

Appendix B

Geometric Adaptation for ANCF

To determine the geometry needed to adapt the T-Liner into a circular configuration, a number of calculations were performed looking at the number of cells and the corresponding external wall thicknesses of the samples.

When choosing the configurations of the samples, the aim was to minimise the size of the width. The ranges explored in Table B.1 were selected as smaller samples would result in a significantly higher amount of printing. However, the printers were performing close to their limit so designing larger parts was not at this time possible. The selected design specifications are shown in blue.

The expansion included in the sample sizes in Tables B.1 and B.2 is based on previously observed printing performance. Typically expansion is seen on FDM-printed parts, due to the slight compression of the filament during extrusion, while shrinkage is observed in SLA-printed parts after the final curing. However, on the initial samples printed for testing in TCD, a small expansion is observed instead. This is potentially due to very narrow walls that make up the majority of the sample being spread by the square grid of the ducts.

$Width_{wall}$ (mm)	0.4	0.4	0.4	0.4	0.4
$Width_{cell}$ (mm)	6	6	6	6	6
No. of Cells	6	7	8	9	10
Angle	3.4212°	3.98512°	4.5491°	5.1130°	5.6769°
Expansion	3.4246°	3.9891°	4.5536°	5.1181°	5.6826°
Cells/Circ	105.1209	90.2453	79.0579	70.3382	63.3510
$Angle_{gap}$	0.4139°	0.9778°	0.2635°	1.7297°	1.9929°
$Width_{gap}$ (mm)	4.4034	10.4034	2.8034	18.4034	21.2034

Table B.1: Optimal Cells per Sample

$Width_{wall}$ (mm)	0.4	0.405	0.41	0.415	0.42
$Width_{cell}$ (mm)	6	6	6	6	6
No. of Cells	8	8	8	8	8
Angle	4.5491°	4.5500°	4.5510°	4.5519°	4.5528°
Expansion	4.5536°	4.5546°	4.5555°	4.5564°	4.5574°
Cells/Circ	79.0579	79.0416	79.0253	79.0089	78.9926
$Angle_{gap}$	0.2635°	0.1892°	0.1150°	0.0407°	4.5193°
$Width_{gap}$ (mm)	2.8034	2.0134	1.2234	0.4334	48.0834

Table B.2: Optimal Outer Walls Width

Part	No. of Cells	Wall Thickness 1 (mm)	Wall Thickness 2 (mm)	First Cell	Last Cell
A	12	3.1	0.4	S1	S6
B	13	0.4	0.4	S1	S1
C	12	0.4	3.1	S2	S1

Table B.3: Optimal Cells per Sample

Appendix C

Additional ANCF Results

A comparison of the full spectra of the T-Liner at each of the tested RPMs can be seen in Fig. C.1. The spectra presented are for Microphone 13 which has a projected polar angle of 43.5°. The hardwall SPL is also included as a baseline for comparison. The hardwall SPL is shown in black and the T-Liner is shown in green. The measured SPL in decibels, dB, is shown on the vertical axis and the frequency in Hertz, Hz, is shown on the horizontal axis. The periodic spikes in the SPL correspond to the blade passing frequency (BPF) for a given fan speed. The BPF is a function of the speed of the fan, causing the frequency of the first BPF to increase as the speed of the fan is increased.

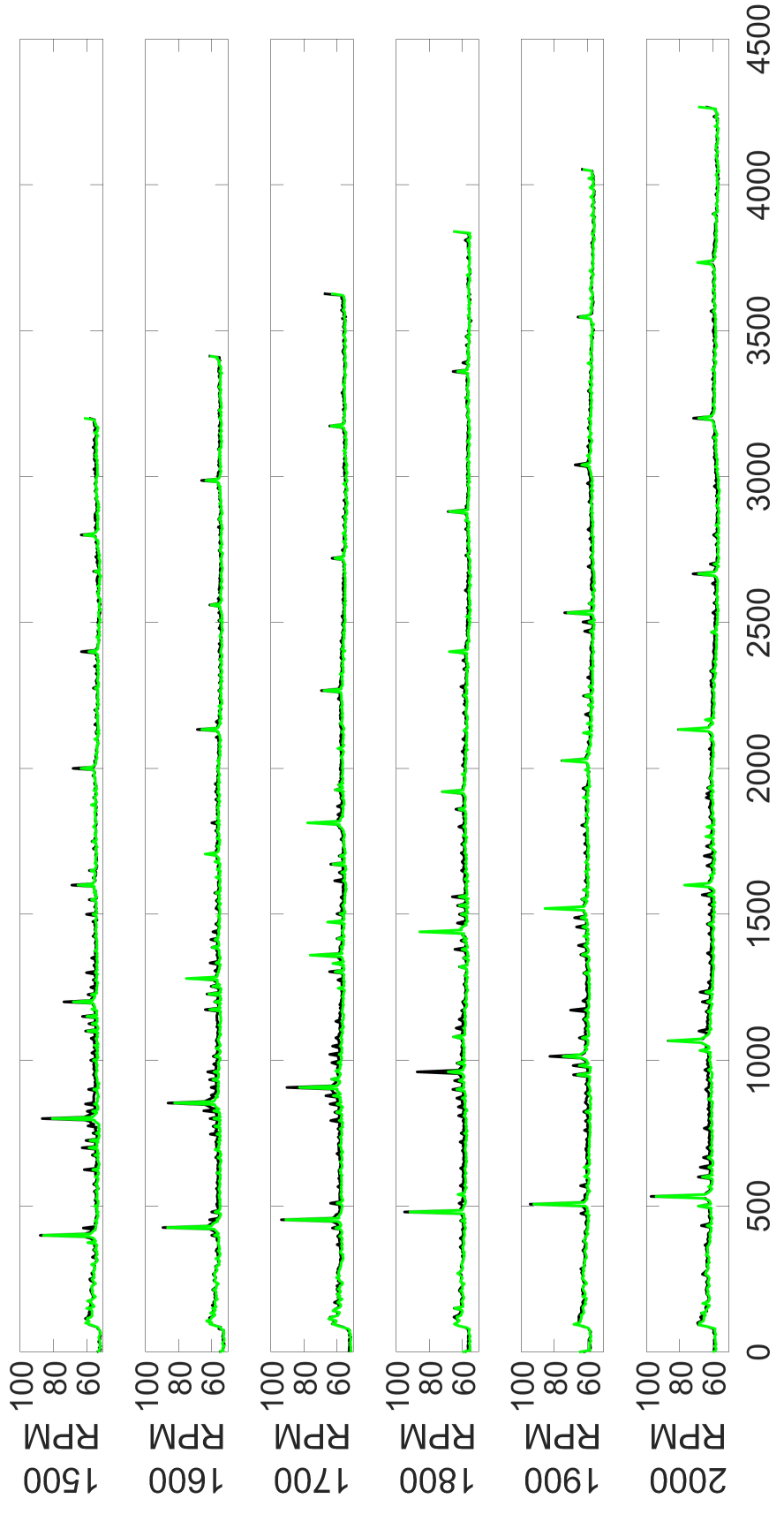

Figure C.1: Direction comparison of the hardwall and liner spectra for mic 13 at each RPM test point. The hardwall baseline results are shown in black and the liner results are shown in green.

Appendix D

Technology Readiness Level Systems

TRL Systems

The Technology Readiness Level (TRL) system is a metric used to estimate the maturity of a technology during its development. The earliest form of the system was a 7 stage system introduced by NASA in 1974. The current system is based on a revision in 1990 which expanded assessment criteria to include 9 stages [189]. Other agencies have developed similar systems based on the NASA TRLs. Most commonly seen in Europe is the European Space Agency's (ESA) Technology Readiness Level which uses the same general definitions as NASA. However, the assessment criteria used by the ESA are more detailed and outline numerous standards the technology must meet before being categorised at a particular level. A summary of the NASA and ESA systems is presented in Table D.1 and Table D.2 respectively. A more detailed description of the NASA system is provided by [190] and a more detailed description of the ESA system is provided by [191]. In this study, the NASA system is used as the ANCF has historically been assessed using this system.

Readiness Level	Definition	Explanation
TRL 1	Basic principles observed and reported.	Scientific knowledge generated underpinning hardware technology concepts/applications.
TRL 2	Technology concept and/or application formulated.	Invention begins, practical application is identified but is speculative, no experimental proof or detailed analysis is available to support the conjecture.
TRL 3	Analytical and experimental critical function and/or characteristic proof of concept.	Analytical studies place the technology in an appropriate context and laboratory demonstrations, modeling and simulation validate analytical prediction.
TRL 4	Component and/or breadboard validation in laboratory environment	A low fidelity system/component breadboard is built and operated to demonstrate basic functionality and critical test environments, and associated performance predictions are defined relative to the final operating environment.
TRL 5	Component and/or breadboard validation in a relevant environment.	A medium fidelity system/component breadboard is built and operated to demonstrate overall performance in a simulated operational environment with realistic support elements that demonstrates overall performance in critical areas. Performance predictions are made for subsequent development phases.
TRL 6	System/sub-system model or prototype demonstration in an operational environment.	A high-fidelity system/component prototype that adequately addresses all critical scaling issues is built and operated in a relevant environment to demonstrate operations under critical environmental conditions.
TRL 7	System prototype demonstration in an operational environment.	A high-fidelity engineering unit that adequately addresses all critical scaling issues is built and operated in a relevant environment to demonstrate performance in the actual operational environment and platform (ground, airborne, or space).
TRL 8	Actual system completed and "flight qualified" through test and demonstration.	The final product in its final configuration is successfully demonstrated through test and analysis for its intended operational environment and platform (ground, airborne, or space).
TRL 9	Actual system flight proven through successful mission operations.	The final product is successfully operated in an actual mission.

Table D.1: TRL developed and used by NASA [190, 192]

Readiness Level	Definition	Explanation
TRL 1	Basic principles observed and reported	Lowest level of technology readiness. Scientific research begins to be translated into applied research and development.
TRL 2	Technology concept and/or application formulated	Once basic principles are observed, practical applications can be invented and R&D started. Applications are speculative and may be unproven.
TRL 3	Analytical and experimental critical function and/or characteristic proof-of-concept	Active research and development is initiated, including analytical / laboratory studies to validate predictions regarding the technology.
TRL 4	Component and/or breadboard validation in laboratory environment	Basic technological components are integrated to establish that they will work together.
TRL 5	Component and/or breadboard validation in relevant environment	The basic technological components are integrated with reasonably realistic supporting elements so it can be tested in a simulated environment.
TRL 6	System/subsystem model or prototype demonstration in a relevant environment	A representative model or prototype system is tested in a relevant environment.
TRL 7	System prototype demonstration in a space environment	A prototype system that is near, or at, the planned operational system.
TRL 8	Actual system completed and "flight qualified" through test and demonstration	In an actual system, the technology has been proven to work in its final form and under expected conditions.
TRL 9	Actual system "flight proven" through successful mission operations	The system incorporating the new technology in its final form has been used under actual mission conditions.

Table D.2: TRL developed and used by ESA [191]